Suppressing Delamination Through Vertically Aligned Carbon Nanotube (VACNT) Interleaves

By

ROBERT CHRISTOPHER WORBOYS

Department of Aerospace Engineering
UNIVERSITY OF BRISTOL

A dissertation submitted to the University of Bristol in accordance with the requirements of the degree of DOCTOR OF PHILOSOPHY in the Faculty of Engineering.

OCTOBER 2019

Word count: 41628

Abstract

The layered architecture, and lack of through-thickness reinforcement, has led to delamination being the most common failure mode in fibre reinforced polymer composites. A variety of strategies have been developed to suppress delamination, however the majority of these also cause degradations to the in-plane mechanical properties. Suppressing delamination requires the interlaminar fracture toughness (ILFT) of the composite system to be enhanced, so as to demand more energy for cracks to initiate, coalesce and propagate. Vertically aligned carbon nanotube (VACNT) interleaves have shown promising qualities as delamination suppressors, due to their extremely high localised areal densities, and desirable alignment, which results in bridging of the resin-rich interlaminar region.

The aim of this research is to understand how geometric characteristics of VACNTs, such as length and areal distribution, influence the ILFT enhancement, and hence, their delamination suppressive capabilities. Within the research, focus is placed on assessing the capabilities of VACNT interleaves as delamination suppressors in delamination-prone composite structures.

Mode I and Mode II ILFT tests are conducted on HexTow® IM7/HexPly® 8552, interleaved with VACNTs, with a selection of CNT lengths, areal densities, and areal distributions. Tensile tests are performed on VACNT interleaved, delamination-prone, tapered and notched specimens. All interleaved specimens are compared to an equivalent unmodified baseline. Fractography analysis, high speed camera footage, and computed tomography scans are performed on damaged specimens to determine their failure mechanisms and allow comparisons with an equivalent unmodified composite system.

Overall, VACNTs are found to suppress delamination, however their maximum toughening capabilities are limited to the secondary mode of failure of the host composite system, which, in this case, is intralaminar delamination. Distinguishing between an inter- or intra-laminar delamination dominated composite system is vital, before interleaves are selected as a delamination suppression technique. Cohesive elements with enhanced properties are shown to be a simple and effective method to model composite structures with VACNT interleaves.

DEDICATION

I would like to dedicate this thesis to Mum, Dad, Jenny and Beth for their loving support and belief throughout my PhD journey.

If it wasn't for you all, I would not be here, and for that I am eternally grateful.

The author wishes to acknowledge the support of Rolls-Royce plc through the Composites University Technology Centre (UTC) at the University of Bristol and the EPSRC through the ACCIS Centre for Doctoral Training grant, no. EP/G036772/1.

Acknowledgements

"Are you pleased that you chose to study a PhD?"

I have numerously been asked this question (mostly on a Friday evening pub trip), and during the last 3 years I have provided some dramatically varied answers. However, now, as I am coming towards the end of this marathon of a journey, I'm happy to state that my answer is unanimously positive. It should be highlighted that this would not be case without a select number of people, who deserve to be acknowledged for all of their efforts and kindness.

Firstly, I would like to thank my academic supervisors Ian Hamerton, Luiz Kawashita and Stephen Hallett, for sharing their wealth of knowledge and experience. I always felt valued and respected as a researcher, which has given me great confidence going forward.

I would also like to thank my industrial supervisor Rob Backhouse for his continual guidance and support in ensuring my ideas became reality. Our discussions have always sparked great ideas, which have evolved the project into something I am proud to call mine.

A huge thank you to the team at N12 Technologies (now wholly owned by NAWA Technologies) for not only supplying the VACNTs and supporting my work throughout, but for also allowing me to visit and use their facilities, when developing and fabricating my test specimens. I would especially like to thank Mackenzie Devoe and Christopher Gouldstone for their fantastic competency when I needed their assistance.

I'd like to thank our amazing lab support team: Steven Rae and Oliver Nixon-Pearson, whose assistance ensured my experiments went flawlessly. Furthermore, I would like to thank our marvellous technicians: Ian Chorley, Simon Ball, Guy Pearn and Richard Chaffey, whose expertise supported the manufacture and testing of all the samples described in this work.

For assisting my abundance of office issues, I'd like to sincerely thank the whole of the ACCIS support staff, with particular thanks going to Allison McIntosh-Smith, Paige Spicer, Sarah Hallsworth, Kathinka Watts and Helen Jones.

It has been a pleasure to be part of so many groups within the University during my time here. In particular, I would like to give thanks to all the members of my CDT cohort (especially Andrés Rivero, Aewis Hii, Tamas Rev and Vincent Maes) who have shared this long and arduous journey with me; my colleagues in the UTC, whose valuable knowledge has accelerated by understanding; and my flatmates and senior resident teams (Oliver Parks, Daniel Francis, Josh Hoole, Amber Knapp-Wilson, Chris Mayo and Sarah North), whose generous and caring nature have led to some life-long friendships. As Paul McCartney and John Lennon wrote: *"I get by with a little help from my friends"*, which I think is very apt for my time here at Bristol.

Finally, I would like state my everlasting gratitude to my family and girlfriend, Beth Hickton, for their enthusiasm and loving support. You have always kept me motivated, which ultimately got me over the finish line!

AUTHOR'S DECLARATION

I declare that the work in this dissertation was carried out in accordance with the requirements of the University's Regulations and Code of Practice for Research Degree Programmes and that it has not been submitted for any other academic award. Except where indicated by specific reference in the text, the work is the candidate's own work. Work done in collaboration with, or with the assistance of, others, is indicated as such. Any views expressed in the dissertation are those of the author.

SIGNED: ..... DATE: .....

TABLE OF CONTENTS

List of Tables

List of Figures

NOMENCLATURE

$[]_{2s}$	Doubly symmetric layup
$[]_s$	Symmetric layup
δ	Crosshead displacement
ρ	Density
σ	Gross tensile stress
σ_{II}	Pure Mode II cohesive stress
σ_I	Pure Mode I cohesive stress
a	Crack length
a_0	Initial crack length
a_e	Equivalent crack length
a_p	Pre-crack length
b	DCB and ELS specimen width
C	Compliance
E	Young's modulus
E_f	Flexural modulus
G	Strain energy release rate
G_C	Critical strain energy release rate
G_{IC}	Critical Mode I strain energy release rate
G_{IIC}	Critical Mode II strain energy release rate
G_{IIprop}	Propagated Mode II strain energy release rate

G_{Iprop} Propagated Mode I strain energy release rate

G_{prop} Propagated strain energy release rate

h Half-thickness of DCB or ELS specimen

I_1 Distance between the load application and ELS specimen centroid

L Specimen free length

P Applied load

S_{II} Pure Mode II cohesive strength

S_I Pure Mode I cohesive strength

T_g Glass transition temperature

η_G Through-thickness compression fracture toughness enhancement

η_S Through-thickness compression strength enhancement

vol % Weight percentage

wt % Volume percentage

Abbreviations

AR	Aspect Ratio
CB	Carbon Black
CF	Carbon Fibre
CFRP	Carbon Fibre Reinforced Polymer
CNF	Carbon Nanofibre
CNT	Carbon Nanotube
CT	Computed Tomography
CV	Coefficient of Variation
CVD	Chemical Vapour Deposition
DCB	Double Cantilever Beam
DWCNT	Double-Walled Carbon Nanotube
ELS	End Loaded Split
ENF	End Notched Flexure
EPD	Electrophoretic Deposition
FE	Finite Element
FRP	Fibre Reinforced Polymer
FT	Fracture Toughness
FVF	Fibre Volume Fraction
GFRP	Glass Fibre Reinforced Polymer
GNP	Graphene Nanoplatelets
IFSS	Interfacial Shear Strength
ILFT	Interlaminar Fracture Toughness
ILSS	Interlaminar Shear Strength

IR	Infrared
MWCNT	Multi-Walled Carbon Nanotube
OHT	Open Hole Tension
PA	Polyamide
PLA	Polylactic Acid
PMMA	Polymethyl Methacrylate
PTFE	Polytetrafluoroethylene
PVF	Polyvinyl Fluoride
SEM	Scanning Electron Microscope
SSA	Specific Surface Area
SWCNT	Single-Walled Carbon Nanotube
TGA	Thermogravimetric Analysis
TTC	Through Thickness Compression
TTR	Through Thickness Reinforcement
VACNT	Vertically Aligned Carbon Nanotube

CHAPTER 1

INTRODUCTION

1.1 Background

Composite materials have undergone a large-scale adoption in engineering applications over the recent decades, due to their attractive material properties and versatility. In particular, engineers seek to exploit their high specific stiffness and strength, as reported in Table 1.1, with the additional benefit of good corrosion resistance and fatigue performance. However, what separates composite materials from their metallic or ceramic alternatives, is the ability to tailor their material properties, thereby allowing structural optimisation based on the application requirements.

By definition, composites comprise of two or more elements, which when combined, are stronger than their individual constituent components. In engineering applications, these components come in the form of a reinforcement and a matrix, as illustrated in Figure 1.1. The main purpose of the reinforcement is to add stiffness and strength to the composite, while the

Table 1.1: Specific properties of some high-performance fibres in comparison with common metals [1].

Specific Properties	**Carbon (HM)**	***para*-Aramid (HM)**	**E-Glass**	**Aluminium**	**Steel**
Specific Modulus: E/ρ $(Nm/kg)^a$	256	80	28	26	27
Specific Strength: σ/ρ $(Nm/kg)^b$	1.2	2	0.78	0.05 - 0.23	0.04 - 0.27

ρ = Density, σ = Tensile Strength, E = Young's Modulus, HM = High Modulus.
[a] Also known as the stiff-to-weight-ratio.
[b] Also known as the strength-to-weight-ratio.

matrix protects the reinforcement against environmental and external loads, as well as enabling load transfer throughout. Reinforcement can be categorised into either continuous fibres, discontinuous fibres, or particulates. For the majority of high-performance engineering applications, reinforcement comprises of continuous fibres embedded into an organic polymer matrix. These are defined as fibre reinforced polymers (FRPs) and will be the primary focus of this research.

With the exception of randomly mixed fibres and braided fibres, fibrous reinforcement in composite materials is arranged in layered formations, with the surrounding matrix cohesively bonding layers together. This architecture is defined as a laminate and can be seen in Figure 1.1. For each layer (known as a ply), the direction of the fibres can be controlled, which can lead to significant anisotropic properties, *i.e.* directional dependent material properties, especially for uni-directional fibre reinforcement. The anisotropic behaviour allows engineers to design the composite layup, or the order in which the layers are placed, to ensure the greatest strength in the directions of the highest expected load. As a result, the efficiency of the composite laminate relative to other homogeneous alternatives, such as metals, is improved.

The layered architectural structure associated with composite materials means that there is an inherent weakness between the fibrous layers, known as the interlaminar region. The lack of reinforcement in the through-thickness direction means that the through-thickness stiffness and strength of fibre reinforced polymers (FRPs) are an order of magnitude lesser than their in-plane equivalents. This is a consequence of the inability of the low strength resin rich interlaminar regions to withstand interlaminar stress and therefore micro-cracks begin to form. If these stresses are not reduced, the micro-cracks will eventually coalesce to form a continuous crack that separates the composite laminate layers in a process known as interlaminar delamination.

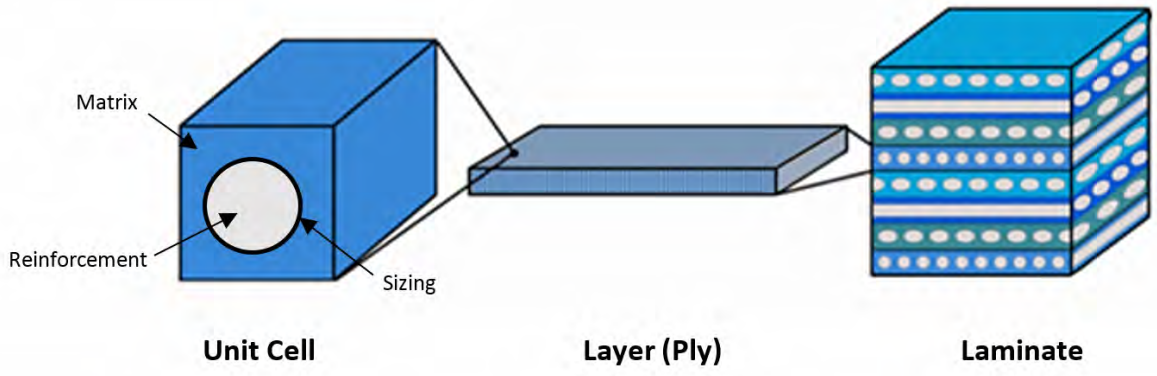

Figure 1.1: Schematic of the constituents and architecture of typical composite materials. Figure adapted from [5].

1.1.1 Composite fracture and delamination

There are multiple fracture modes associated with composite materials, which arise depending on the loading conditions, composite constituents and fabrication quality. Examples of these fracture modes, as illustrated in Figure 1.2, include translaminar crack progression (fibre breaking) and transverse or longitudinal intralaminar matrix cracking. However, owing to the vast difference in strength between the matrix and the fibres, for the majority of load cases, composites are susceptible to interlaminar delamination more than any other fracture mode. The next most common fracture mode is intralaminar delamination, whereby cracks propagate through the fibrous layer, but still remain parallel to the lamination plane. This requires additional energy to debond and pull the fibres out of the matrix (termed 'pull-out') and hence is not as commonly observed as interlaminar delamination. Therefore, unless specified otherwise, 'delamination' refers to interlaminar delamination for the remainder of this research.

Delaminating cracks can propagate through three fundamental modes, as illustrated in Figure 1.3, however for most of the load cases found in engineering structures, delamination growth is a combination of the three, known as mixed-mode delamination. In order to characterise delamination and, in particular, a material's ability to resist delamination, a parameter called the strain energy release rate (G) is identified. This is defined as the rate at which energy is dissipated as the material undergoes fracture, and the strain energy release rate can be calculated at the delamination front for each of the fundamental fracture modes.

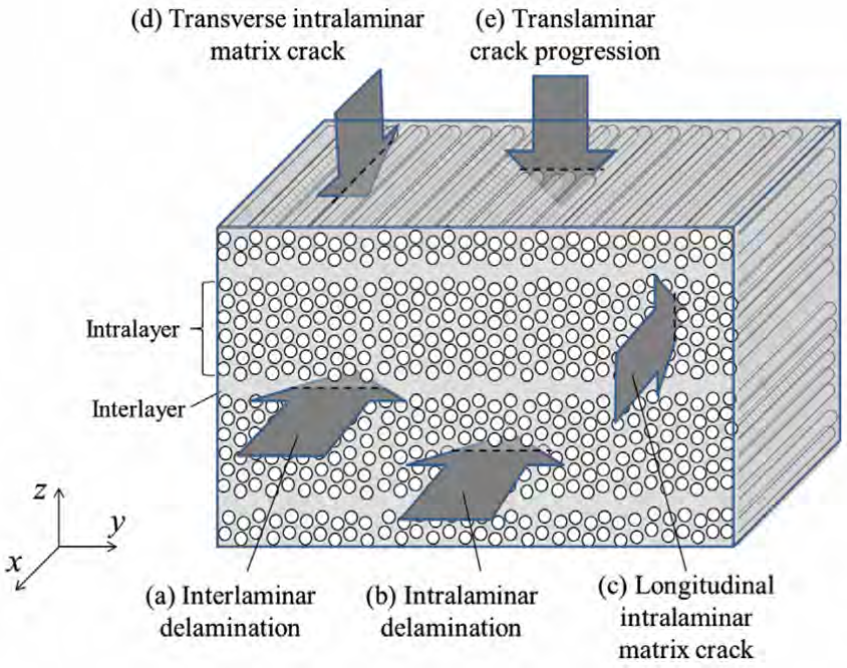

Figure 1.2: Schematic of fracture modes in an unmodified FRP laminate [6].

In order to estimate when a material will fracture, the required strain energy release rate for a crack to grow, known as the critical strain energy release rate (G_C), must be evaluated for each fundamental fracture mode. For composites, these values are material properties, known as the modal interlaminar fracture toughness, and can be measured through standard experimental tests. Once known, delamination fracture will occur when the strain energy release rate at the delamination crack front is equal or in excess of the critical value, *i.e.* when:

$$G \geq G_C \tag{1.1}$$

Such a material property is of particular interest when modelling a composite material, as it will enable engineers to predict the loads required to initiate fracture as well as the initial failure location.

1.2 Motivation

1.2.1 Sources of delamination

Interlaminar delamination occurs in a wide variety of loading conditions, which induce large levels of interlaminar stresses within the composite laminate. As extensively reviewed by Wisnom [47], delamination prone structures consist of those that are subjected to through-thickness loading, or those that have geometries which promote interlaminar stresses. Examples include structures with curved or tapered geometries, discontinuities such as ply-drops or free edges, impacted composites, and notched laminates. Other studies have also shown the onset of delamination being induced through a variety of processes, including interlaminar residual stresses caused

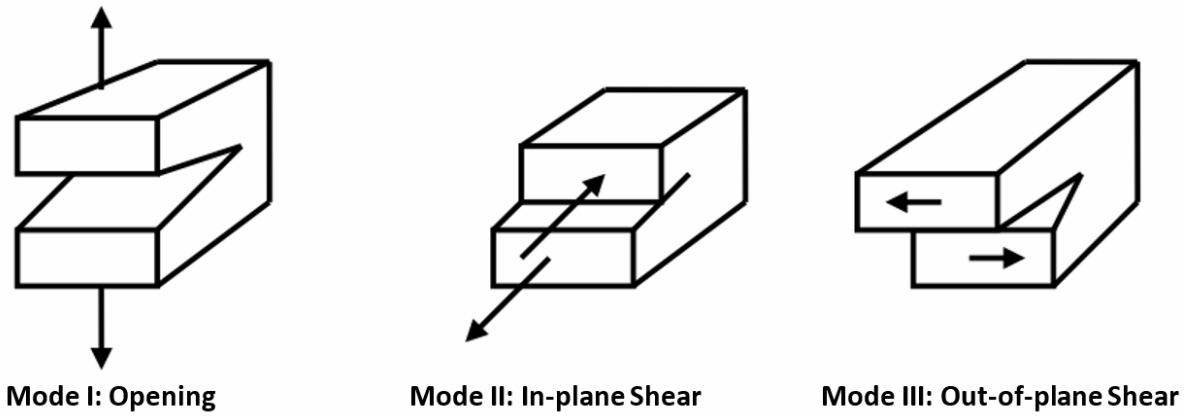

Figure 1.3: Schematic of the three fundamental fracture modes for a composite material. Figure adapted from [7].

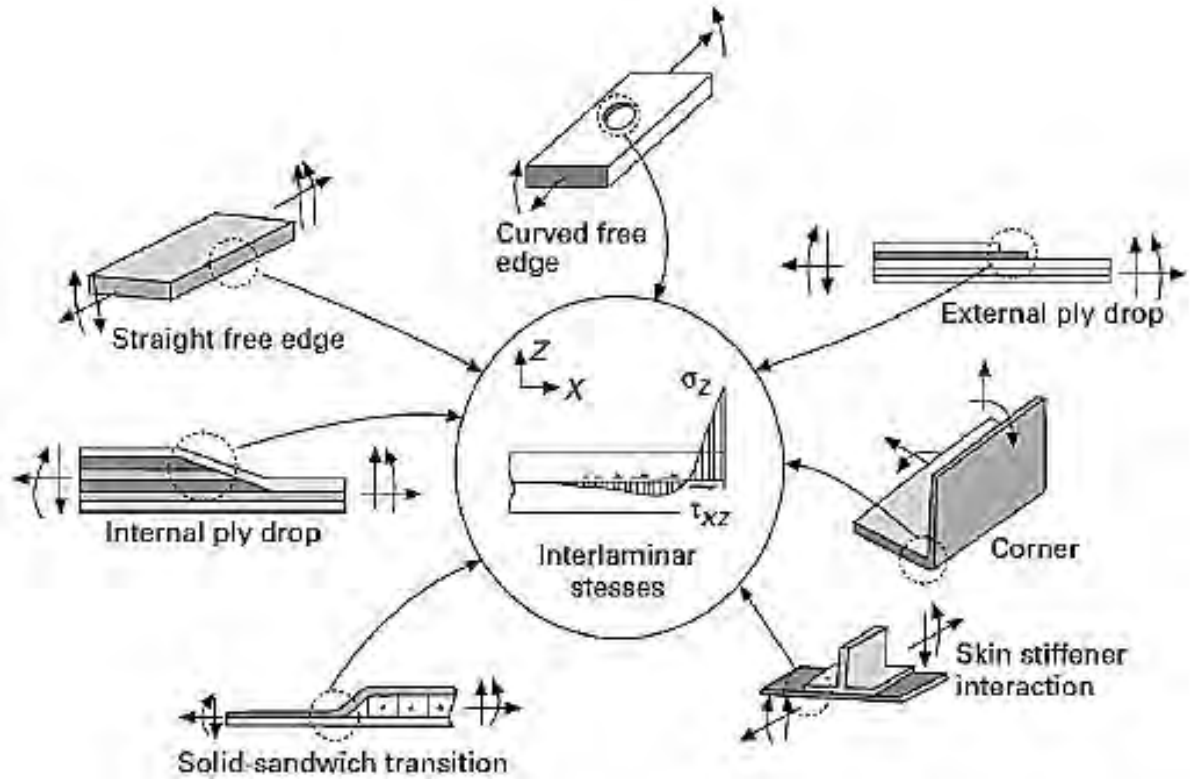

Figure 1.4: Sources of delaminations at geometric and material discontinuities [8].

by environmental conditions [48], manufacturing defects [49], and damage through machining procedures, *e.g.* drilling [50].

For all of these cases, as illustrated in Figure 1.4, it has been discussed that delamination is the limiting factor influencing the composite strength [47]. Experimental and numerical studies support this claim through showing evidence of a significant decrease to the tensile, flexural and compressive mechanical properties [51–53], when a delamination is present. With such dramatic knockdowns, safety critical industries, for instance the aerospace industry, apply strict safety requirements to their composite structures. These include, 'no growth policies' and an immediate structural integrity examination for composites laminates with delaminations detected [54]. Subsequently, if parts do not meet the strict damage tolerance requirements, they must be immediately repaired or replaced at great financial and laborious cost [55].

1.2.2 Industry trends

It is well reported that the current generation of civil aircraft, *i.e.* Airbus A350 XWB and Boeing 787, owe around $50-55\%$ of their total structural weight to composites [9]. Composite adoption within the aerospace industry has been a growing trend in recent years, as can be seen in Figure 1.5, with the aim of driving down structural weight and reducing fuel consumption.

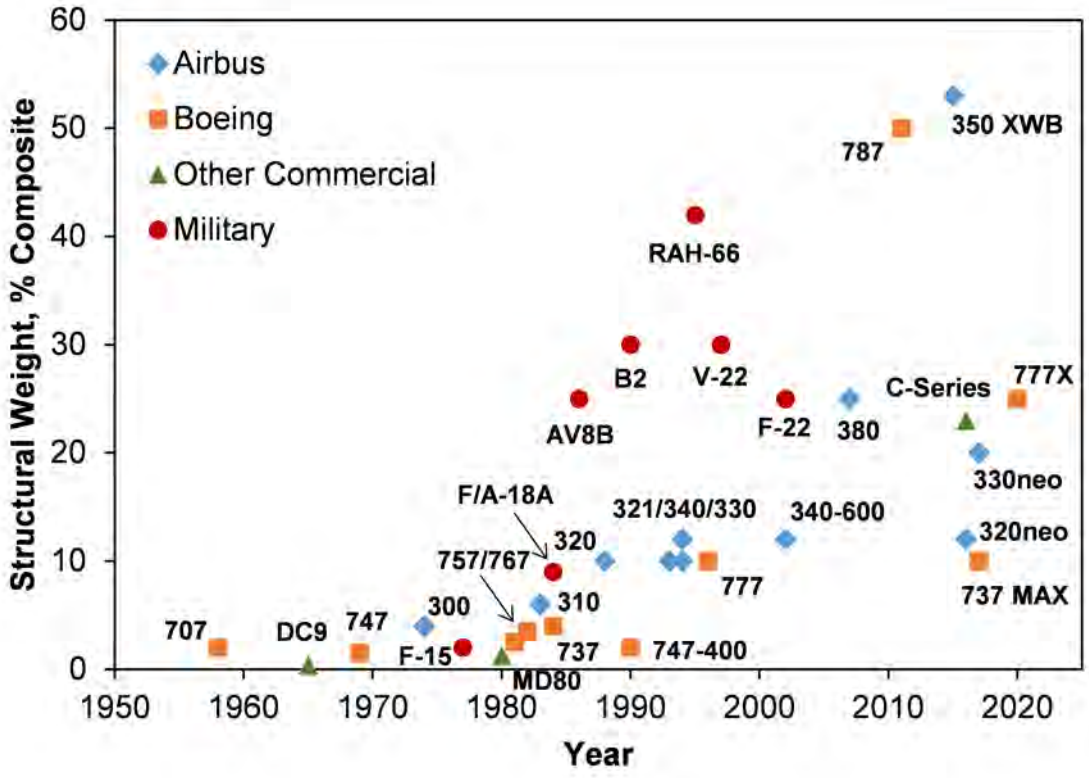

Figure 1.5: A graph showing the increasing growth of composite use in aircraft over the years [9].

The components initially transitioning from metals to composites have been those loaded predominately in-plane and exposed to moderate environmental conditions. Areas susceptible to out-of-plane loading, for example impacts (from bird-strikes, hailstones, tool-drops, *etc.*), have either yet to be replaced, covered in metallic or ceramic alternative materials, or have been purposely over-designed, thereby adding large amounts of parasitic weight to the aircraft. Therefore, it is believed by the author that the poor through-thickness strength and fracture toughness associated with composite materials will result in further adoption stagnating. If this is to be avoided, and the efficiency of the next generation of aircraft is to be increased, the fracture toughness of composite materials must be improved.

1.2.3 Research outline

This research will focus on methods to improve the fracture toughness of composite materials. As discussed in Section 1.1.1, this can be done through increasing the critical strain energy release rate (G_C) of the material, or in other words, increasing the required energy for a crack to initiate and propagate through the structure. For composites, cracks will tend to initiate by delamination, therefore, focus will be placed on techniques to suppress delamination. This will be achieved

through introducing other obstacles into the system to hinder or resist crack growth, thereby requiring more energy to delaminate.

Before an appropriate delamination suppression technique is selected, an in-depth literature review, which summaries existing techniques, shall be constructed. This review will cover both the well-established and state-of-the-art methods, commenting on the advantages and disadvantages of each. Z-binder, fibre-modifier, and matrix-modifier through-thickness reinforcement methods shall be included along with their suitable applications. The review will identify areas of novelty and subsequently conclude on the aims and objectives that will be considered in the remainder of the research.

CHAPTER 2

LITERATURE REVIEW OF TECHNIQUES FOR SUPPRESSING DELAMINATION OF ADVANCED COMPOSITE MATERIALS

2.1 Introduction

A wide variety of techniques have been developed for suppressing delamination in advanced composite materials. This chapter will provide a summary of these methods, including the fracture toughness (FT) enhancements and limitations associated with their application.

Overall, the delamination suppressing techniques described in this review can be categorised into three themes: z-binders, fibre modifiers, and matrix modifiers. These themes, along with examples of delamination suppressive approaches, can be seen in Figure 2.1. This diagram portrays the fundamental structure of this review.

The chapter will conclude with a brief summary, highlighting areas of unresolved research, which shall later lead on to the research aims and objectives, and subsequent thesis chapter breakdown.

2.2 Delamination Suppression Methods

2.2.1 Z-binders

Z-binder delamination suppression methods involve a macro-scale z-binder being inserted through the thickness of the composite laminate to create a bridging zone. This z-binder can come in the form of a pin, fibre, or thread and is designed to generate traction forces to resist any crack opening (Mode I) or shearing (Mode II) behaviour. Under Mode I conditions, z-binder pull-out, elastic deformation, and rupture contribute to the increased energy requirement to propagate a crack. On the other hand, crack growth in Mode II conditions is suppressed by z-binder elastic

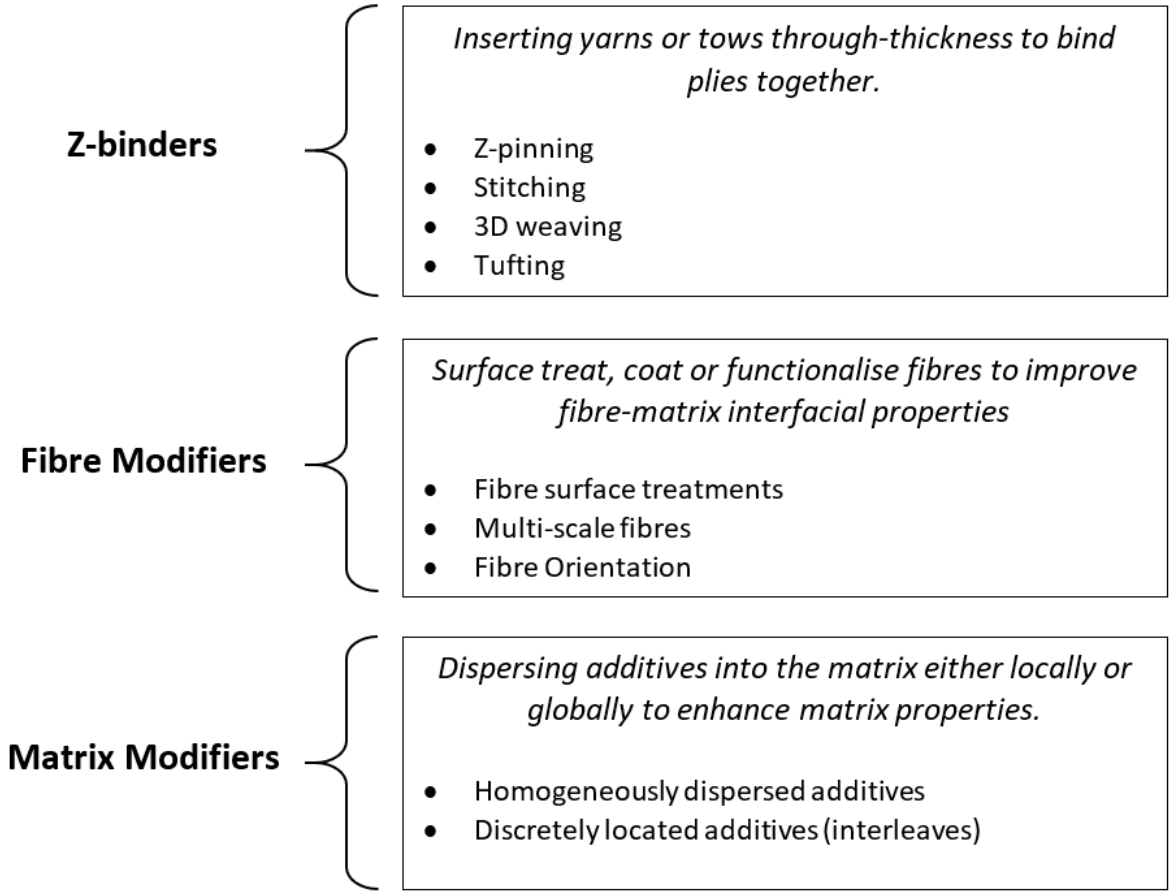

Figure 2.1: The literature review structure with examples of approaches to suppress delamination in composite materials.

shear deformation, pull-out, shear rupture, and snubbing. The latter is an energy dissipation process, whereby lateral forces push the z-binders into the surrounding host composite material. Reactive forces from the composite resist any lateral deformation of the z-binder, and as a result, extra energy is required for a crack to grow.

A number of z-binder techniques have been used to suppress delamination in composites, including z-pins, stitching, 3D weaving, braiding, and knitting [12]. This review shall focus on the first three, due to their more extensive use in delamination suppression applications.

2.2.1.1 Z-pinning

Z-pins consist of fine nail like structures, as seen in Figure 2.2, which are commonly made from titanium, steel or fibrous carbon composite. With a diameter in the range of 0.2 – 1.0 mm, z-pins are designed to locally bind plies together through a combination of friction and adhesion. The pins are normally inserted through an ultrasonic assisted z-fibre machine (UAZ) with pin volume content in the range of 0.5 – 4.0%.

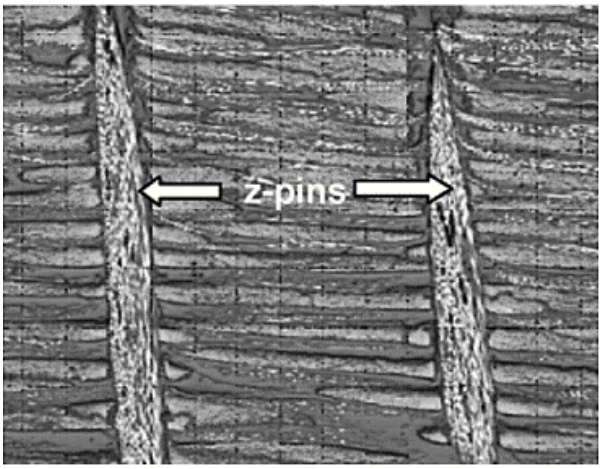

Figure 2.2: An SEM image of z-pins in composite prepreg [10].

Currently, z-pinning is the most common z-binder through-thickness reinforcement technique for prepreg applications. Z-pinning offers a substantial improvement in interlaminar fracture toughness (ILFT) and impact damage tolerance; In a review by Mouritz [10], it was reported that for every 0.5% of z-pin volume content, the Mode I FT doubled, while the Mode II FT increased by 75% (Figure 2.4a). Moreover, the post impact damage area was observed to decrease by between $19-64\%$ for z-pin reinforced laminates, depending on the laminate thickness and impact energy [10]. Compressive mechanical properties were also enhanced as the bridged plies were found to be more stable and hence less likely to buckle.

2.2.1.2 Stitching

Stitched fibre reinforced laminates involve sewing high-strength thread through the thickness of dry fibrous ply layers. Industrial scale machines are able to sew intricate patterns at variable areal densities and insertion angles in order to bind the fabric layers together. Three of the most common stitching patterns are modified lock stitch, lock stitch and chain stitch. These are illustrated in Figure 2.3. Owing to its minimal crimping of the in-plane fibrous layers, and hence preserved in-plane properties, modified lock stitch is the most common for components with large in-plane loads. Once the dry fibre layers are stitched, the binded system is infused with liquid resin using conventional processing methods, such as resin transfer moulding (RTM) or resin film infusion [11].

Stitching has been demonstrated to provide substantial improvements to the Mode I ILFT, with reports showing that the modified lock stitch and double-yarn orthogonal-stitch provides the greatest improvements [56]. A positive correlation between the stitch areal density and the Mode I ILFT enhancement has also been determined, as can be seen in Figure 2.4b [12, 56]. ILFT has been shown to be dependent on stitch material and pattern, as well as increase with stitch diameter [11]. Conversely, Mode II enhancements are not as clear, with different studies

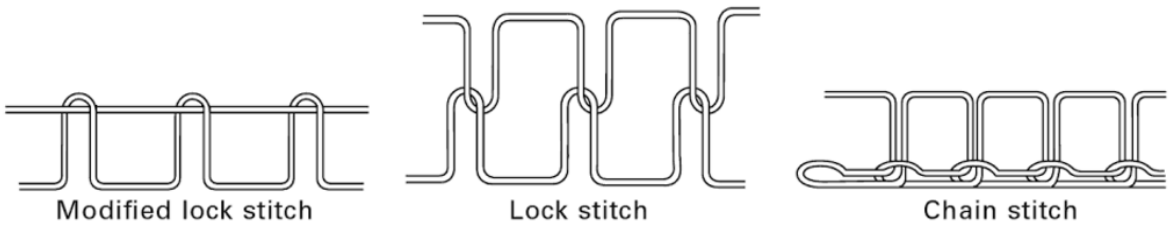

Figure 2.3: Schematic of the most common stitch patterns [11].

showing improvement, degradation or not effect at all after stitching [57]. Contrasting with the behaviour found for Mode I ILFT, it was concluded by Mouritz *et al.* [57], that the Mode II shear strength increased with the inclusion of low density stitching. However, at high densities, stitching degraded the shear properties below that of an unstitched baseline laminate [57]. The reasoning for this will be explained in Section 2.2.1.5.

2.2.1.3 Tufting

Tufting is a variant of the stitching method, which only requires a single thread (the tuft) and needle. The technique involves inserting a threaded needle through a dry fabric preform and then retracting the threaded needle in the opposite direction to the insertion. Frictional forces between the thread and dry fabric preform hold the tuft in place, thereby preventing the tuft from slipping during the retraction step. This results in a loop forming on the back face of the dry preform as can be seen in Figure 2.5. The advantage of tufting compared to stitching is that the tufts are held in low tension, which results in the in-plane property degradations generally being less in tufted composites than in stitched composites. Furthermore, tufting only requires access

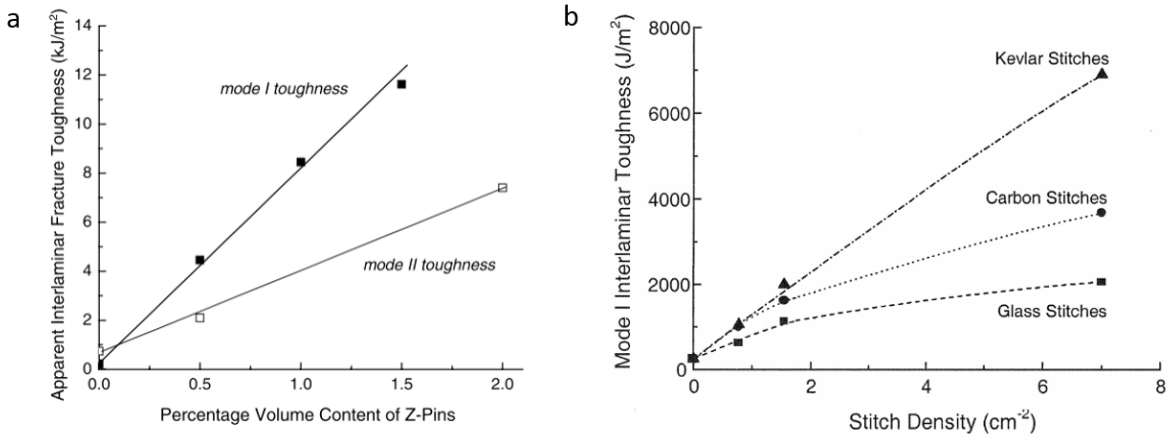

Figure 2.4: (a) The effect of Z-pin content on the Mode I and Mode II interlaminar fracture toughness [11]; (b) The effect of stitch density on the Mode I interlaminar fracture toughness for a variety of stitching materials [12].

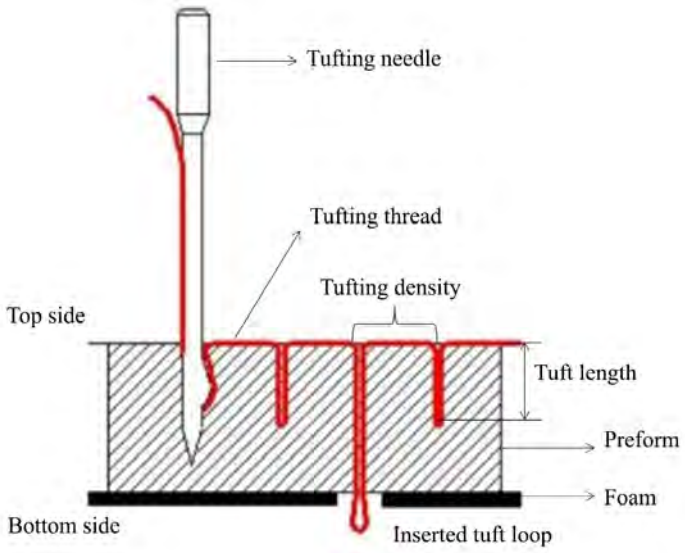

Figure 2.5: Schematic of the thread arrangement in a fully tufted preform and partially tufted preform [13].

to one side of the dry fabric preform, which significantly eases the manufacturing process.

Tufting has been shown to significantly improve the Mode I and Mode II fracture toughness for carbon fibre fabric infused with epoxy resin. For example, Treiber has reported a 400% and 140% increase in G_{IC} and G_{IIC} respectively, for CFRP laminates tufted with carbon sewing thread [58]. Furthermore, Dell'Anno has reported a 200% increase in G_{IC}, but this was also found to induce a 10% reduction in in-plane tensile strength [59].

Liu *et al.* reported degradations in the tensile strength of a tuft thread, due to the insertion process [13]. One method that was found to reduce tuft strength degradations was to partially insert the tufts through the laminate thickness. An example of such a tufting arrangement can be seen in Figure 2.5. The reasoning for the greater strength degradation in fully inserted tufts is the greater friction effects between the tuft and preform when the tuft is inserted. It is therefore expected that partially tufted laminates will outperform fully tufted laminates with respect to delamination suppression, however no literature has yet been found to support this prediction.

2.2.1.4 3D weaving

3D weaving is an adaptation of the conventional single layer weaving process. Similar to its single layer predecessor, 3D woven fabrics use looms to weave two fibrous yarns, termed the warn and weft. However, in contrast with regular woven fabrics, 3D weaving uses additional looms to interlace z-binder yarns perpendicular to the in-plane warp and weft yarns. This produces a 3D-fibre reinforced structure as can be seen in Figure 2.6.

Although any fibre type can be theoretically woven, carbon and glass are the most common for

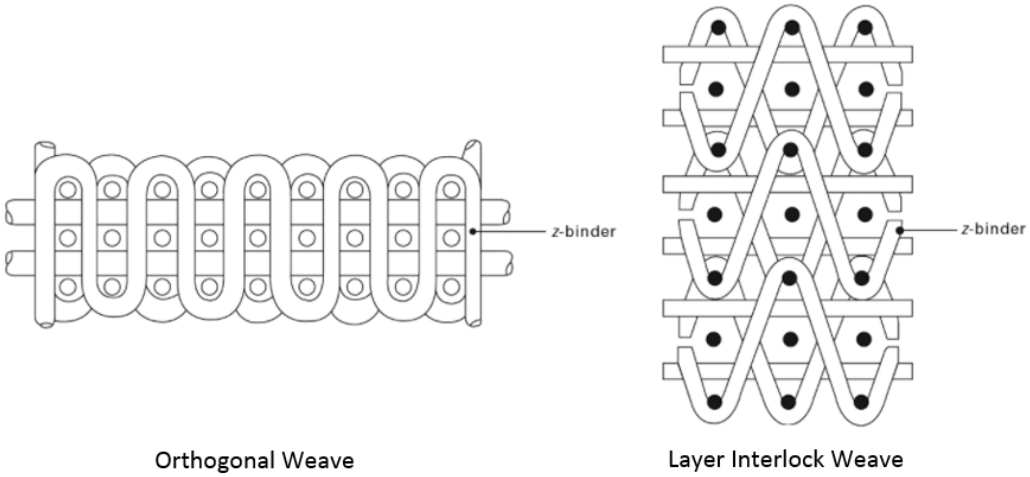

Figure 2.6: Schematic of the cross-section of the most common weave patterns [11]

structural applications, due to their high strength and low cost. These thin continuous filament z-binder yarns can be woven to make multiple architecture types, with layer interlocking and orthogonal weave being the most common. These patterns are shown in Figure 2.6. Similar to stitching, once the dry fibre is woven, it is infused with liquid resin and cured.

The obtainable ILFT enhancements from 3D weaving are comparable to that from z-pinning for Mode I conditions [11] (see Figure 2.7). Contrastingly, under Mode II conditions, the ILFT has been experimentally found to provide much lower enhancements [60]. The Mode II ILFT improvements are sourced from the woven z-binders aiding with crack arrest and deviation, as

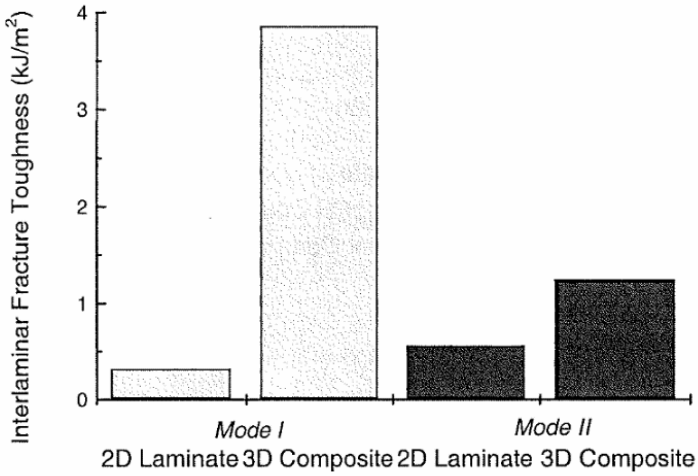

Figure 2.7: The Mode I and Mode II interlaminar fracture toughness for 2D and 3D woven composites [12].

well as allowing for loads to be transferred through-thickness as the crack approaches [61]. These mechanisms provide much less of a contribution towards the fracture toughness enhancement than fibre pull-out or crack bridging, which are associated with Mode I fracture. Therefore, the overall Mode II ILFT is lower.

2.2.1.5 Limitations with z-binders

While the previously mentioned z-binder reinforcement techniques provide structural integrity through-thickness, they also disturb the fibre architecture in-plane. Subsequently, this leads to defects and the in-plane mechanical properties of the laminate decreasing. The extent of fibre disruption is dependent on the diameter of the z-binders, areal density and the weave and stitch patterns. For example, modified lock stitch (Figure 2.3) and orthogonal weave (Figure 2.6) have been developed with the aim of reducing fibre crimp, and hence minimising in-plane property degradation.

A selection of z-binder defects are displayed in Figure 2.8(a-d). These include fibre breakage, fibre crimping and fibre waviness caused by the insertion of the z-binder into uncured prepreg or dry fabric. Such behaviour has shown to result in reductions in elastic and mechanical strength properties, with studies on z-pins showing a reduction of $5-15\%$ for tensile strength, compressive strength and bending strength and stiffness, when at 4% z-pin volume content [10].

Microscopy has shown that resin rich regions form around the z-binders, which lead to the onset of early matrix cracking and hence a crack source for delamination initiation. At high concentrations, resin pockets around fibres have been found to connect, forming channels and provide a crack growth path (Figure 2.8c). Along with the fact that the mismatch in thermal expansion properties between the z-binders and the surrounding material causes micro-interfacial cracking during cure, this limits the volume fraction at which z-binders can be incorporated.

Swelling is a process whereby the fibre volume content of the reinforced laminate is decreased in response to the incorporation of z-pins. Observed by Chang *et al.* [62], it was postulated that swelling is induced by the fibre disruption and the rigid z-binders resisting the plies from compacting together under pressure, which leads to larger volumes of resin within the interlaminar regions. This was found to accelerate fatigue-induced damage, particularly in tensile conditions, while the compressive fatigue-life was found to deteriorate due to the progressive rotation of the fibres around the z-binder, when loading cyclically. The additional rotation promoted failure through fibre micro-buckling and kinking during compressive load regimes. Overall, Chang *et al.* determined that the fatigue-life for z-pinned laminates reduced by approximately a third under both loading conditions [62].

More recent studies have investigated the influence of z-binder diameter on the in-plane [10], flexural [63], and interlaminar properties [64]. Overall, it has been shown that for a given volume content, the thinner z-binders outperform those with larger diameters. This has been attributed to the lesser localised damage and disruption associated with the thinner z-binders. It

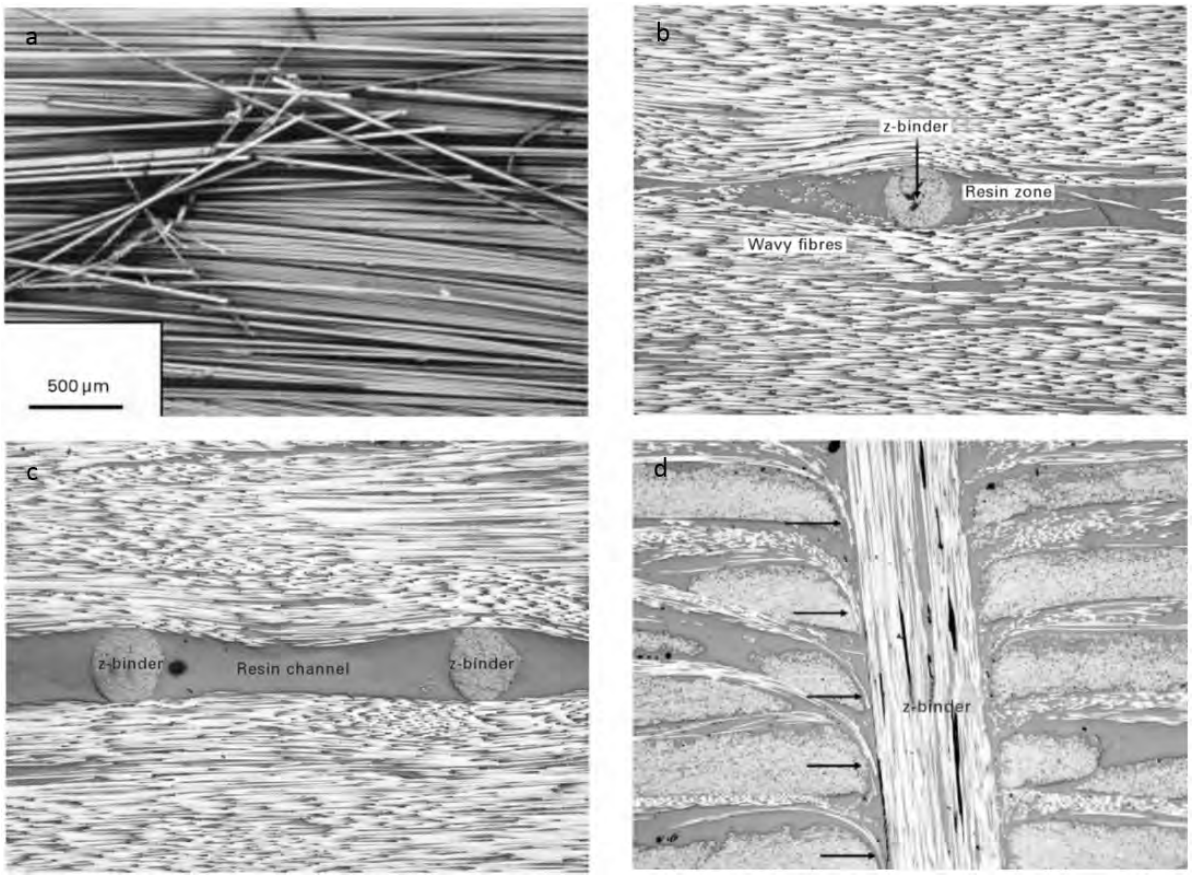

Figure 2.8: SEM images of (a) fibres broken through stitching, (b) fibre waviness around a z-binder, (c) resin rich regions joining to form a resin channel in a z-pinned composite, (d) fibre crimping from z-pin insertion [11].

is therefore believed by the author that the next generation of z-binders are likely to be thinner, potentially at the micro- or nano-scale in order to optimise performance.

2.2.2 Fibre modifiers

2.2.2.1 Fibre surface treatment

Untreated fibres produce composites with a low interlaminar shear strength (ILSS), due to their inert surface leading to poor bonding with the surrounding matrix [65]. Therefore, the rationale behind surface treating fibres is to improve fibre-matrix adhesion properties. Adhesion can be enhanced through physical means, *e.g.* increasing the fibre surface roughness to increase surface area and number of contact points, or chemical means, whereby the fibre surface is coated in an organic polymer functional group, which reacts with the matrix and creates a strong interfacial bond. Most surface treatment methods result in these modifications happening simultaneously.

Surface treatment methods can be categorised into either oxidative treatments or non-

oxidative treatments, depending on whether they involve an oxidation step. The oxidation process can take place in a gas- or liquid-phase and can be applied either chemically, electrochemically or through catalytic oxidisation. Examples of non-oxidative treatments include carbon pre-coating, plasma treatment, gamma treatment, and rare earth treatment [65].

Oxidation treatment methods produce acidic functional groups on the fibre surface. The treated surface properties are influenced by the concentration of the oxidative medium, fibre type, treatment time and temperature [65]. Albertsen *et al.* investigated the ILFT of CFRPs with four different wet oxidation surface treatment levels [14]. Overall, the ILFT at crack initiation was found to increase significantly with fibre surface treatment (Figure 2.9), due to the increase in fibre-matrix bond strength. On the other hand, the Mode I ILFT at crack propagation was found to be a maximum at an intermediate level of surface treatment due to a considerable reduction in fibre bridging when at high surface treatment levels. Furthermore, fibre surface treatment was found to transform failure type from the fibre surface (adhesive failure) into the matrix (cohesive failure).

Non-oxidative methods, such as plasma or gamma treatment, exposes the fibre to high levels of energy, thereby allowing the removal of surface contaminants; the increase in surface energy, which promotes wetting of the fibre with the matrix; the depositing of functional groups for chemical reactions between the matrix and fibre interface and; the etching of the fibre to increase surface roughness [65].

Tiwari *et al.* exposed carbon fabric to three doses (100, 200 and 300 kGy) of gamma radiation, inserted these treated fibres into resin, and tested under interlaminar shear stress conditions [15]. SEM images (Figure 2.10), showed clear increases in fibre roughness with increased radiation exposure. Furthermore, the treated fabric with a dose of 300kGy absorbed 22.8% more resin compared to the untreated fibres. The interlaminar shear strength (ILSS) was found to increase

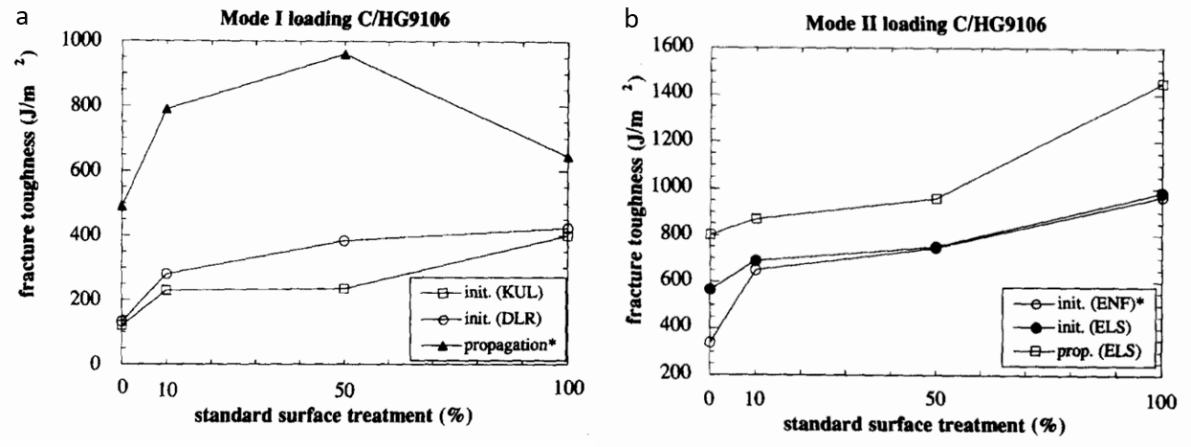

Figure 2.9: The influence of surface treatment on the interlaminar fracture toughness under (a) Mode I and (b) Mode II conditions [14].

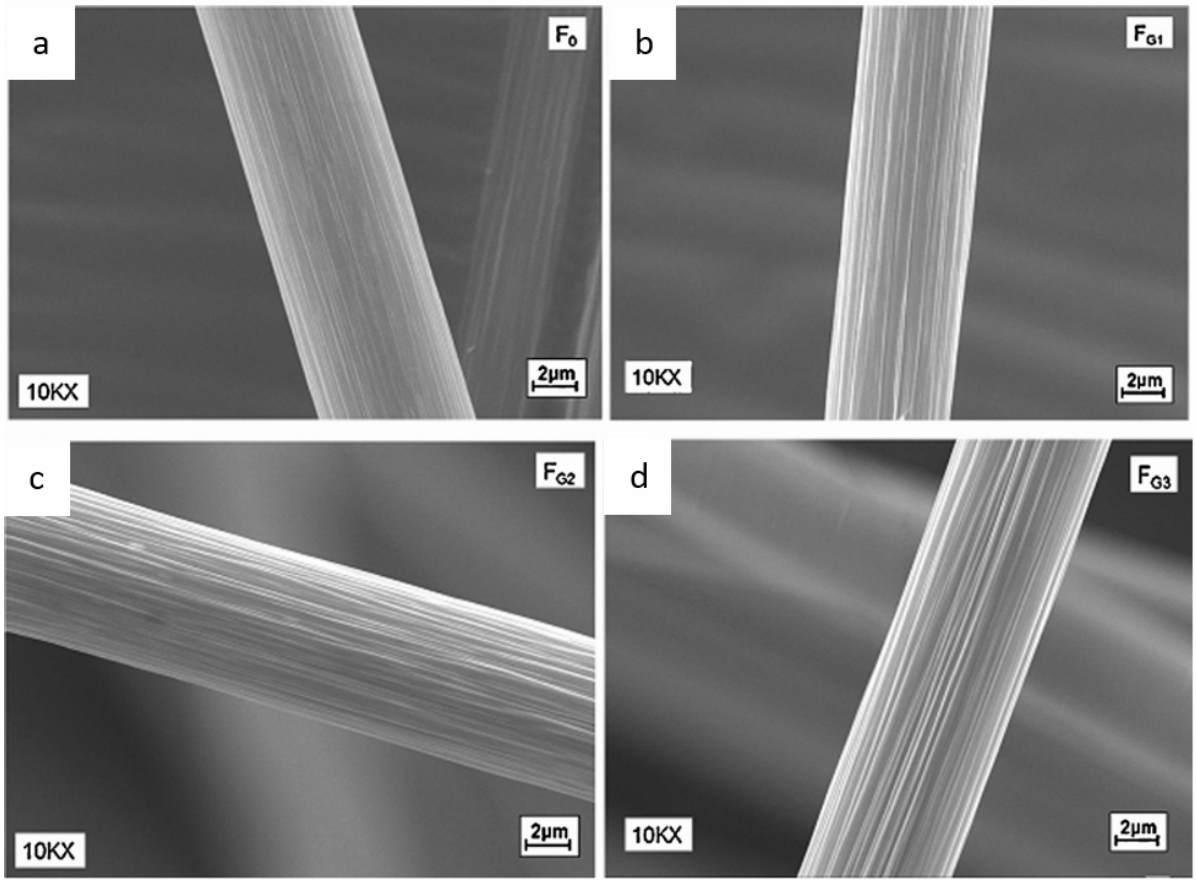

Figure 2.10: SEM images of (a) an untreated fibre and (b-d) fibres gamma treated with 100-300 kGy doses respectively [15].

with radiation dose, with a 60% increase in ILSS being measured for the 300 kGy dosed fabric.

2.2.2.2 Multi-scale fibres

Multi-scale fibres consist of attaching (or grafting) carbon nanotubes (CNTs) on to the surface of the fibre in order to enhance interfacial shear and impact strength. An illustration of this technique (also known as 'fuzzy fibres') can be seen in Figure 2.11. These radially aligned CNTs (RACNTs) anchor the fibres to the surrounding matrix, thereby requiring more energy for fibres to pull away from the matrix, or for cracks to propagate within the matrix. A more in-depth discussion of the toughening mechanisms associated with multi-scale fillers, such as CNTs, can be found in Section 2.2.3.

Four different techniques have been developed to graft CNTs on to fibres. These include; *(i)* direct growth of CNTs on to the fibres; *(ii)* electrophoretic deposition (EPD) of CNTs on to the fibre surfaces; *(iii)* chemical reactions between functionalised CNTs and the fibres and *(iv)* coating of the fibres with CNT-containing sizes [66]. Early studies, such as by Thostenson *et al.* [17], grew the

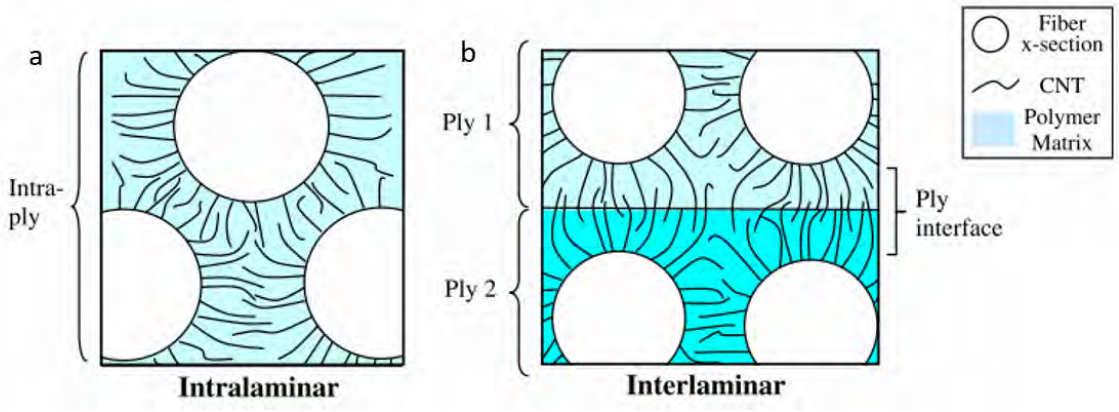

Figure 2.11: An illustration of the multi-scale fibre technique for reinforcing the (a) intralaminar properties and (b) the interlaminar properties of an FRP composite [16].

CNTs through a standard chemical vapour deposition (CVD) technique after initially coating the fibres in a metal catalyst (see Figure 2.12). The high temperatures associated with this technique resulted in concern about the mechanical degradation of the carbon fibres. Subsequently, a variety of studies were conducted to investigate the influence of CNTs on fibre properties, from either the CVD growth process or other CNT attachment techniques. Investigated parameters included pre-treatments [67], temperature [68], catalysts [68] and hydrocarbon sources [69]. These studies predominantly concluded that processing parameters must be tailored to minimise fibre degradation and therefore optimise structural performance.

Studies investigating the ILFT of multi-scale fibre composites have reported considerable enhancements through grafting fibres with CNTs. Wicks *et al.* [70] and Kepple *et al.* [71] have reported a 76% increase (see Figure 2.16) and 50% increase in the Mode I ILFT respectively. Neither study discussed the Mode II behaviour, however it was shown that the in-plane strength properties were also enhanced by approximately 5% [70]. Mathur *et al.* discovered that the obtainable enhancements from multi-scale fibres to the laminate flexural strength and flexural modulus was dependent on the fibre type, with 2D multi-scale woven cloth showing the greatest improvements [72]. The flexural strength and flexural modulus were also shown to increase with CNT weight percentage (wt%) deposited, however at lower CNT concentrations (0.05 wt%), all composites underperformed relative to their non-grafted fibre equivalents.

Under shear conditions, studies have focussed on the interfacial properties of CNT grafted fibres, with interfacial shear strength (IFSS) improvements of single fibres reported to be above 150% [73]. This has been attributed to the increased surface area, good wettability of the CNT grafted fibres, local stiffening of the epoxy at the fibre-matrix interface induced by the CNTs and the mechanical interlocking between the CNTs and the matrix [66, 74, 75]. Little work has been published on the interlaminar shear strength or Mode II ILFT of multi-scale composite systems; Garcia *et al.* reported a 69% enhancement in ILSS for a multi-scale woven fibre preform

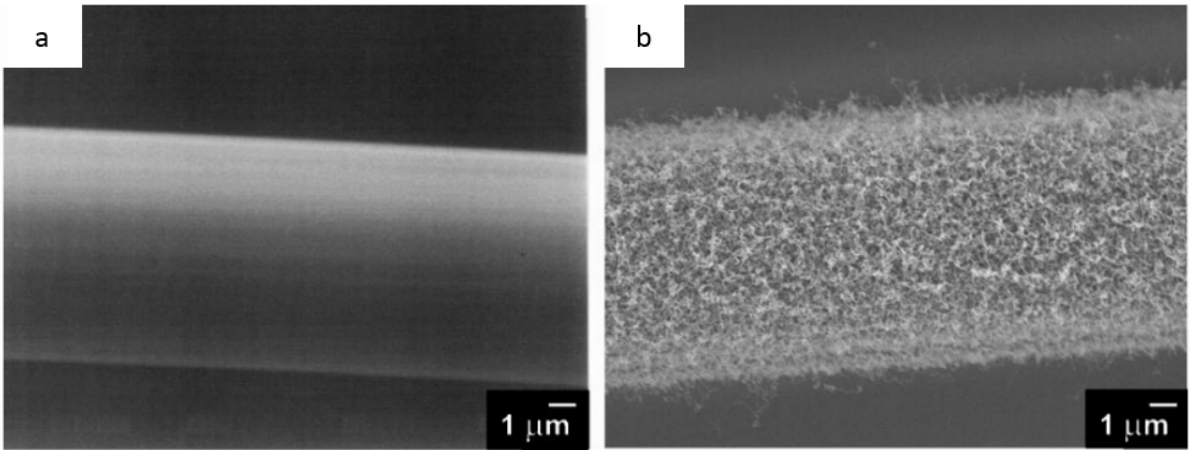

Figure 2.12: SEM images of (a) an unmodified fibre and (b) a fibre with CNTs grafted onto the surface through a CVD technique [17].

composite system [16], however it is believed by the author that no other sources have been published to support this finding.

For all of the studies mentioned thus far, the primary fibrous systems have been made from carbon, however it has be shown that CNTs can also be grown on glass and ceramic fibres through an injection CVD (ICVD) method [76] or chemical reactions between functionalised CNTs and fibres [77]. The latter technique was used by Eskizeybek *et al.* to chemically graft CNTs on to glass fabric and measure the effects on the Mode I ILFT [77]. Fractography analysis showed that the ILFT enhancements ($\approx 160\%$) were attributed to crack bridging and crack migration away from the fibre-matrix interface and into the surrounding matrix, instead of the interfacial region.

More recent studies investigating multi-scale fibres have grafted other multi-scale carbon derivative structures on to fibres, including carbon black [78] and graphene [79], however, due to their lower aspect ratios and surface areas relative to CNTs, the reported material enhancements are not as high [80]. Furthermore, a focus has been placed on upscaling the production processes of multi-scale fibres to increase yield and reduce cost [81]. Additional work will need to be concentrated on optimising the production parameters to achieve greater property enhancements, whilst simultaneously minimising fibre damage.

2.2.2.3 Fibre orientation

The energy required to delaminate a fibre reinforced polymer (FRP) is influenced by the orientation of the fibrous plies surrounding the fracturing interface. Such a dependency occurs because the stress distribution at the interface is dependent on the anisotropic properties of the plies, with residual thermal stresses becoming particularly important due to the difference in expansion coefficient between the fibres and the matrix.

Interfaces with same fibre orientations will exhibit nesting behaviour, with fibres migrating

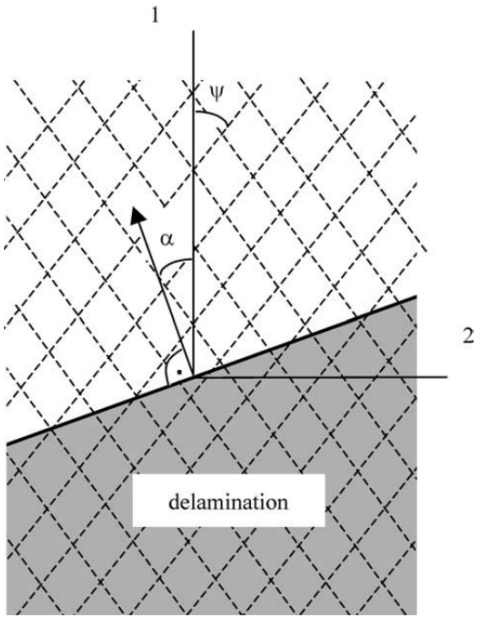

Figure 2.13: Schematic of the top view of a delaminating interface showing the reinforcement (dashed lines) of adjacent plies, the principal reference frame (1, 2) associated with the symmetry axes, and delamination front (solid line). The orientation of the fibres are characterised by angle ψ and the direction of delamination growth is signified by angle α [18].

between adjacent plies and bridging across the interface. In general, fibre nesting will suppress delamination because the bridging fibres must be pulled out when the delaminating crack propagates. This pull-out process dissipates additional energy and thus results in an increase in the interlaminar fracture toughness. On the other hand, interfaces with dissimilar fibre orientations will not exhibit fibre nesting behaviour.

In order to characterise failure of uni-directional FRPs with dissimilar ply orientations, two angles are commonly defined: α and ψ. These are illustrated in Figure 2.13; α is the angle between the delamination growth direction and the principal axis, while ψ is the angle between the fibre direction and the principal axis.

While studies investigating the influence of fibre orientation on interlaminar fracture toughness have shown contradictory results [18], a common finding is that FRPs with dissimilar ply orientations show additional failure mechanisms when delaminating, compared to uni-directional interfaces. For example, Blondeau *et al.* observed a stick-slip load response for DCB specimens with anti-symmetric ($\psi°/-\psi°$) fibre orientations [19]. This indicated that delamination suppressive mechanisms were present. It was observed through fractography analysis that the delaminating cracks migrated into the plies in an anti-symmetric pattern and formed fibre band regions that extended across the width of the specimen (see Figure 2.14). These fibre bands were found to be able to dissipate between two to four times more energy than the baseline uni-directional specimen.

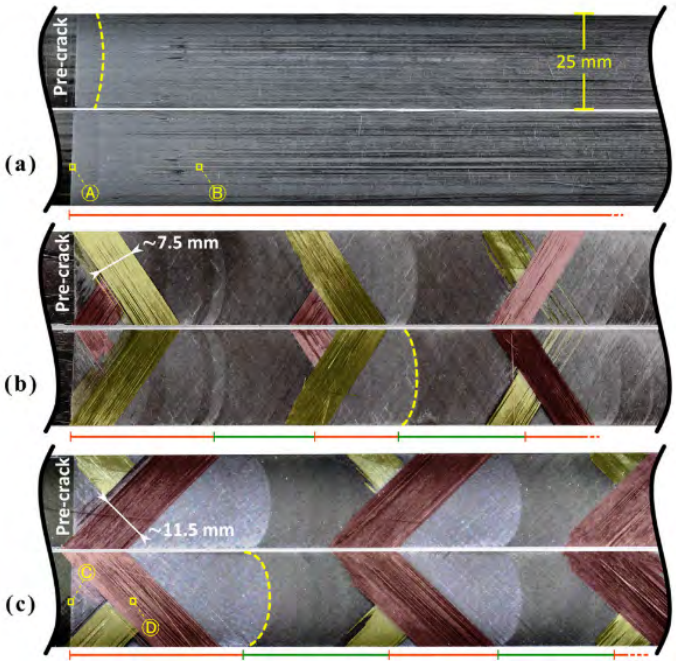

Figure 2.14: Fracture surface of DCB specimens with fibre orientation, ψ, at the initial delamination interface (a) UD, (b) $60°/-60°$ and (c) $45°/-45°$ [19].

Saravanakumar *et al.* also reported observing cracks being guided into the plies surrounding the delaminating interface [82]. In their test programme, specimens with a $0°/0°$ interface measured the lowest fracture toughness. The authors suggested that this was because the crack was not deviated away from its original path and continued to run parallel to the fibres. However, when the fibre orientation was altered to either $45°$ or $90°$, the cracks would deviate into the plies and deflect with the fibre alignment. Subsequently, intralaminar mechanisms such as crack tip diversion and crack branching were observed, which absorb further energy as the crack front propagates. This led to Saravanakumar *et al.* measuring an 87% increase in G_{IC} for a $0°/45°$ interface compared to a $0°/0°$ orientation.

Crack migration, wherein cracks transition from one ply interface to another, has been reported in multiple literature sources involving laminates with dissimilar fibre orientations [20, 82, 83]. Early literature empirically suggest that crack migration occurs when the difference in fibre angle across a delaminating interface exceeds $33.5°$ in Mode I [84] and $7.5° - 10°$ in Mode II [85]. Saravanakumar *et al.* found that DCB specimens with $0°/90°$ and $90°/90°$ interfaces exhibited crack migration mechanisms, while those with $0°/0°$ interfaces and $0°/45°$ interfaces did not [82]. Herraez *et al.* illustrated that specimens under Mode II conditions are more susceptible to crack migration due to the damage zone being oriented into the plies (see Figure 2.15). This led to the fracture toughness at initiation being the same regardless of the ply orientation, while the energy dissipated during crack propagation increased with ply angle [20].

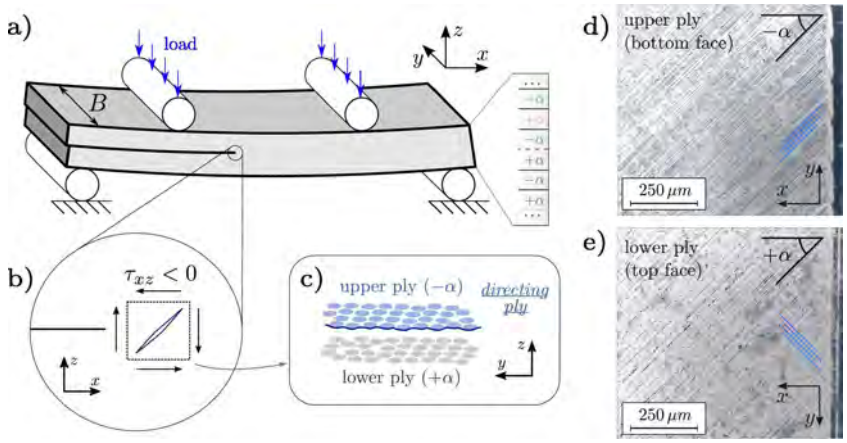

Figure 2.15: (a) A schematic of a 4ENF setup, (b) the shear stress component at the crack tip, (c) illustration of the preferential delamination plane at the bottom face of the upper ply (directing ply), and the fracture surfaces of one specimen with a $45°/-45°$ interface corresponding to the upper ply (d) and the lower ply (e) [20].

Shokrieh *et al.* showed that the interface fibre angle has a significant effect on the steady-state interlaminar fracture toughness as well as the bridging zone length [83]. For example, DCB specimens with a $0°/0°$ interface showed the longest bridging length due to good penetration of two adjacent layers of the delamination interface. Shokrieh *et al.* also found that increasing the interface fibre angle, causes the fibre bridging length to decreased, and so more energy is required to peel-off fibres from the fracture surface. This resulted in the interlaminar fracture toughness of the $0°/0°$ interface being the least.

2.2.2.4 Limitations with fibre modifiers

2.2.2.4.1 Surface treatment

As briefly discussed in the previous sections, the main limitation with fibre modifying methods is associated with the adverse effects on the fibre itself, after attempting to strengthen the fibre-matrix interfacial bond. For example, fibre etching methods, such as plasma etching or gamma radiation, inherently remove a proportion of the fibre surface to increase surface roughness, which reduces the fibre load bearing capabilities. Li *et al.* showed that high and prolonged doses of gamma radiation can lead to a fibre surface roughness reductions [86], while Jang and Yang drew a similar conclusion with plasma etching [87]. This weakens the fibre-matrix interface, and as a result has been shown to reduce the tensile strength of a single T300 carbon fibre by 8% [88].

Excessive oxidation surface treatment has been shown to result in pitting of the fibre surface, which again leads to the degradation of mechanical properties. Wu *et al.* found a linear reduction in fibre tensile strength with oxidation time (Figure 2.16a) [21], due to this pitting behaviour. Moreover, Tiwari *et al.* found a 40% reduction in fibre tensile strength after an oxidation period of

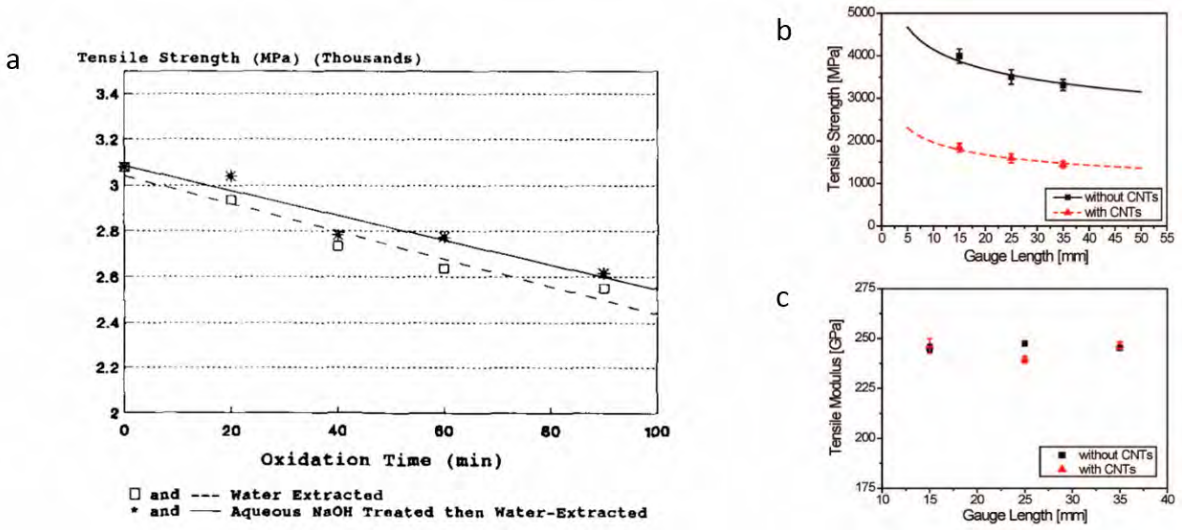

Figure 2.16: The influence on fibre tensile strength from (a) oxidation exposure time [21] and (b) from grafting with CNTs [22]; (c) The effect on fibre tensile modulus from grafting with CNTs [22].

three hours [89]. Therefore, the extent of ILFT enhancements, and hence delamination resistance, is limited to the required fibre strength for its application.

2.2.2.4.2 Multi-scale fibres

To reinforce fibres through CNT grafting, it is desirable to have strong anchoring interactions between the CNTs and the matrix. This maximises the stress transfer between the fibres and matrix, while also minimising damage during handling. To achieve high adhesion, strong chemical bonds must form at the surface of the fibre, which lead to fibre damage and fibre strength reduction concerns. In common with other surface treatments, the CNT growth and attachment process results in local oxidation or gasification exposure to the fibres, which may cause damage. This is of particular concern for carbon fibres as the catalysts commonly used in grafting production dissolve carbon and so etch away the fibre surface [66]. Subsequently, Qian *et al.* found that the tensile strength of fibres decrease by up to 55% when grafted with CNTs (see Figure 2.16b) [22]. On the other hand, the tensile modulus has been found to be dependent on the fibre core properties and so is not significantly affected by CNT grafting [22, 71].

The extent of fibre damage has been found to be dependent on fibre type, fibre pre-treatment, CNT growth conditions, and grafting density [66]. However, poor adhesion between the CNT and matrix and short CNT lengths have resulted in the multi-scale composite underperforming relative to an equivalent composite with unmodified fibres [90, 91]. Other grafting techniques including electrophoretic deposition (EPD) [92], CNT solution in fibre sizing [93], and chemical grafting [94] have shown promise in avoiding fibre damage. Unfortunately, these techniques

suffer with little control of the orientation of the CNTs, which is one of the key contributors to improving FT; CNTs tend to lay parallel to the primary fibre, reducing their anchoring potential [66]. CNT-fibre bond strength and CNT dispersion over the fibre are also areas of concern [93, 94].

Overall, it has been shown that the mechanical performance of grafted fibres is dependent on the CNT structure, length, density and alignment. Optimisation of these parameters must be determined in order to avoid property degradation. This was recently highlighted by Zhang *et al.*, who measured a reduction in IFSS of 37.5% by grafting CNTs on to fibres [75]. Numerical models from the same study indicated that the CNTs acted as stress "re-distributors", both relocating and enhancing the stress concentrations at the end of the grafted CNTs. Such a behaviour has not been previously discussed, showing that there is still a lot to understand before multi-scale fibre composite properties can be predicted.

2.2.3 Matrix modifiers

A common precursor to delamination is matrix cracking, whereby cracks initiate in the interlaminar or intralaminar regions, grow, and coalesce at the ply interface. Therefore, delamination resistance is strongly dependent on the FT of the matrix.

Polymer matrix modifiers work by inserting additives into the matrix to form a nanocomposite or multi-scale composite (see Figure 2.17). These micro-scale or nano-scale additives (also termed ‘inclusions‘ or ‘fillers‘) can be categorised into either *(i)* homogeneous dispersion or *(ii)* discrete placement, and will be covered in the upcoming sections. For either of these categories, the energy dissipation mechanisms, which result in the FT of matrix modified composites increasing, remain the same. These have been listed below:

- *Debonding of the additive from the matrix:*
  The differential stiffness between the additive and the matrix means that they will deform differently upon loading. This will lead to an interfacial shear stress developing and subsequently the additive debonding away from the matrix when the stress exceeds the critical interface strength.

- *Inelastic matrix deformation and void growth around the debonded additive:*
  Around the debonded additives, voids will form. Tri-axial stress concentrations at the newly developed void crack tips will result in the acceleration of plastic deformation of the matrix, which subsequently leads to new surface formations and the void size increasing. These new surface formations result in additional energy dissipation.

- *Crack pinning and deflection:*
  Cracks tend to grow in the path of least resistance. If an inclusion is obstructing this path, the crack will be forced to deviate. This requires a greater driving force to redirect the crack front and an increased fracture surface area is generated, which accumulatively increases energy dissipation.

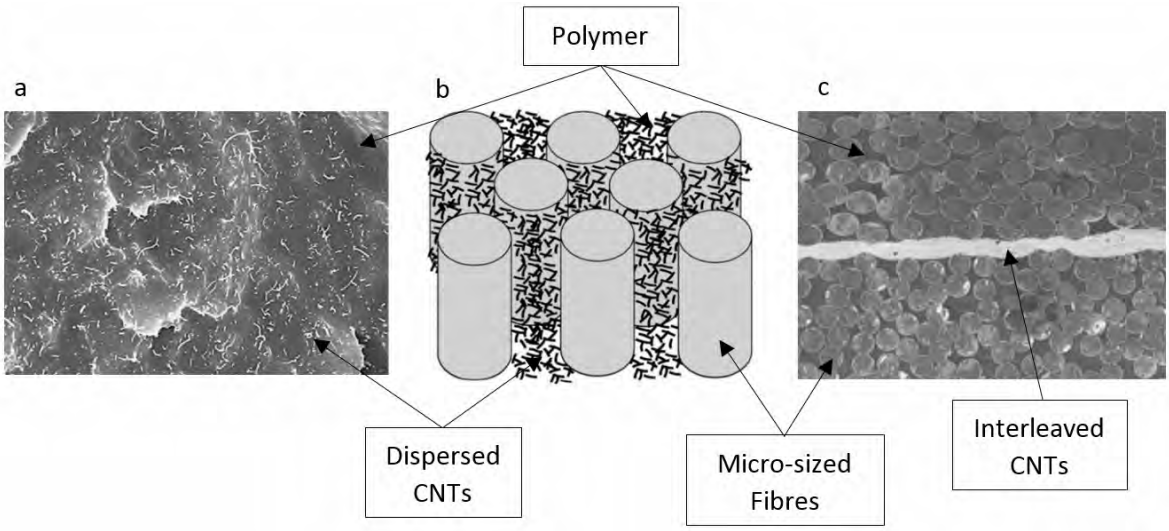

Figure 2.17: An example of a nanocomposite with CNTs dispersed into epoxy resin [23], and a multi-scale composite with CNTs either (b) homogeneously dispersed into the matrix of a FRP system [24], or (c) interleaved into an FRP system [25].

- *Additive pull-out and crack bridging:*
  In common with the z-binder techniques discussed in Section 2.2.1, matrix modifying additives can bridge cracks. This process is shown in Figure 2.18. Rafiee *et al.* have shown that mixing the resin with high aspect ratio or 2D geometry, *e.g.* graphene, is more effective at promoting crack deflection and bridging behaviour [95]. This is due to the fact that higher aspect ratios result in great amounts of crack bridging, crack deviation and available filler pull-out length.

- *Additive rupture:*
  If the interfacial bond strength between the additives and surrounding matrix exceeds that of the additives itself, it will rupture. Rupture requires less energy than pull-out and therefore, the number of additive ruptures should be minimised [96, 97]. Snubbing, as mentioned in Section 2.2.1, can have a large effect on the onset of additive rupture, with the filler orientation being a primary contributor for dictating the proportion of additive pull-out to additive rupture.

- *Telescopic pull-out (MWCNTs only):*
  For additives that have multiple walls, *e.g.* MWCNTs, pull-out can occur between the walls of the additive. For this to occur, the outer wall must rupture and remain adhered to the matrix, while the inter-walls slide away. The breaking of the covalent bonds between the walls provides a secondary source of energy dissipation, which toughens the matrix.

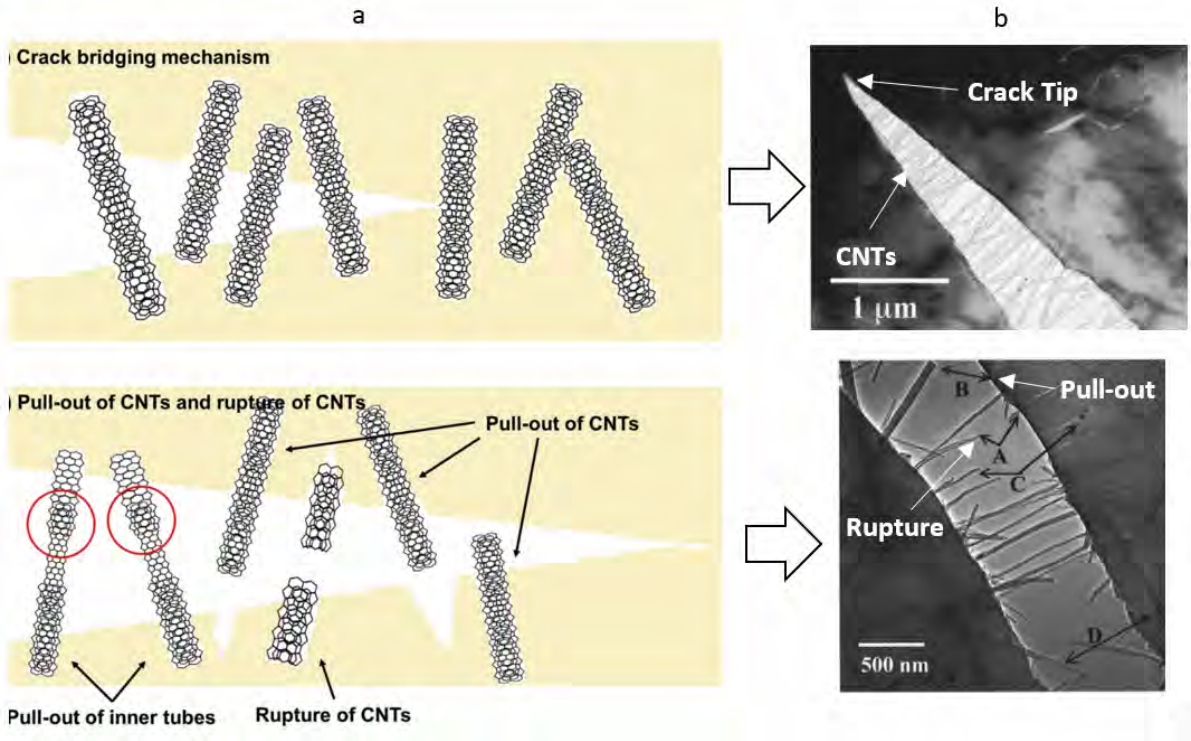

Figure 2.18: (a) Schematic of the energy dissipating mechanisms involved with matrix modifiers [23] with (b) TEM images showing bridging near the crack tip, additive rupturing and pull-out [26].

The contribution that each of these energy dissipating mechanisms has on the total FT of a matrix modified material was determined by Hsieh *et al.* [98]. Overall, additive pull-out and debonding were found to be the most prevalent. Therefore, the most effective delamination resistant methods should priorities these mechanisms.

2.2.3.1 Homogeneous dispersion

A vast variety of additive types have been homogeneously dispersed into epoxy resin with the aim of improving the ILFT. Early studies showed that dispersing elastomeric toughening agents into an epoxy-graphite composite system resulted in an 8-fold increase in ILFT [99]. This was attributed to the elastomer impeding cross-links, and thereby increasing the mobility between polymer chains and the total energy dissipation through the breaking of covalent bonds. Other additives, which have also demonstrated substantial toughness enhancements when dispersed into polymer matrix systems, include, thermoplastics [100], rubbers [101], and epoxidised soybean oil (ESO) [102]. Unfortunately, these materials result in large degradations in mechanical properties, such as tensile strength, tensile modulus and glass transition temperature (T_g) [103, 104]. As can be seen in Figure 2.19a, Yee and Pearson discovered that the tensile

modulus of epoxy linearly decreased with rubber content when homogeneously dispersed [27]; Although the FT was found to increase by an order of magnitude, it came at the price of a 33% reduction in stiffness.

Silica particulates [105], nanoclays [28] and carbon fillers [30, 106] have also shown great potential as matrix modifiers, with large FT enhancements being attributed to the energy dissipating mechanisms outlined in Section 2.2.3. As can be seen in Figure 2.19b, the advantage with these alternative additives is they do not inherently reduce the in-plane mechanical properties of their polymer host. Instead, studies have reported increases in stiffness, strength, T_g and flexural properties [107], along with FT.

As well as additive type, geometric size and shape have also been shown to influence a filler's FT enhancement capabilities. Multiple studies investigating and comparing similar additives in both the micro- and nano-scale have inferred that additives at the nano-scale offer greater FT enhancements than similar micro-scale variants [108–110]. The FT dependency on additive scale supports the conclusion drawn by Rafiee *et al., i.e.* inclusions with a higher aspect ratio and surface area are more effective at promoting crack deflection and bridging behaviour [95]. Taking this into consideration, additives which have very high aspect ratios, *e.g.* nanosheets, nanotubes, and nanofibres, have received vast amounts of interest as delamination-resistant fillers [107]. Out of all filler materials, carbon fillers, *e.g.* CNTs, CNFs, GNPs, and carbon black (CB), have attracted the most attention as they not only offer substantial mechanical enhancements, but also multi-functional capabilities with high thermal and electrical conductivity, and good chemical stability. Carbon fillers also require much lower concentrations to achieve similar enhancements compared to clay or silica additives [107]. With this in mind, the remainder of this section shall focus on carbon-based nano-fillers and how their characteristics influence the extent of FT improvement.

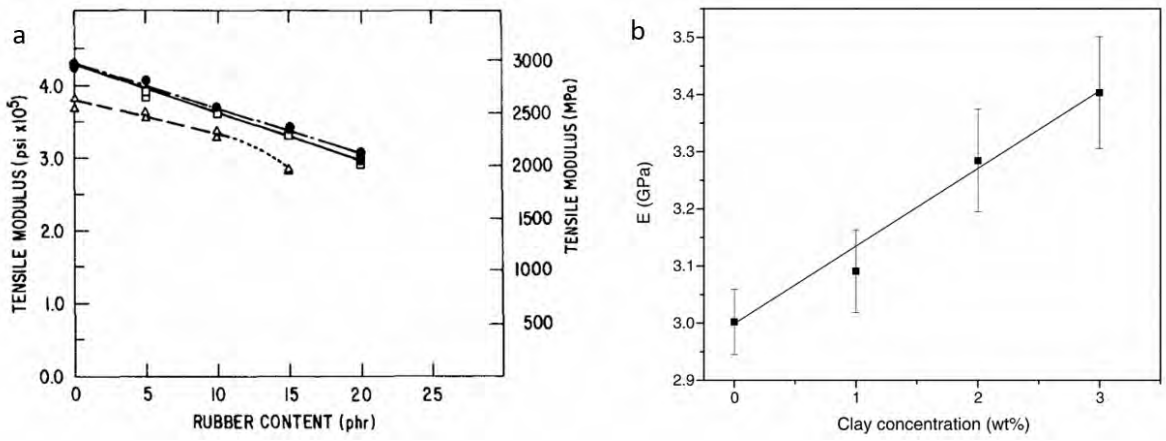

Figure 2.19: The dependence of Young's modulus on the (a) rubber content of three different rubber additives in an epoxy resin [27] and (b) clay content in epoxy resin [28].

2.2.3.2 Homogeneously dispersed carbon nano-fillers

A summary of the Mode I FT enhancements, for a variety of homogeneously dispersed carbon nano-fillers in epoxy resin, is displayed in Table 2.1. The stated percentage enhancements have been calculated relative to the equivalent neat epoxy resins, which were also reported in the same sources. The table has been separated into 'influential factors' in order to aid with this discussion. In general, these factors affect the contribution from each of the toughening mechanisms outlined in Section 2.2.3 and will now be individually discussed.

Filler geometry - aspect ratio and specific surface area

Multiple carbon filler types have been used to toughen epoxy resin with differing levels of success. These include carbon nanotubes (CNTs), carbon nanofibers (CNFs), graphene nano-platelets (GNPs) and carbon particulates (known as carbon black (CB)). As mentioned in the previous section, geometric parameters including aspect ratio (AR) and specific surface area (SSA), are highly influential towards FT improvements. Hernandez-Perez *et al.* recorded an order of magnitude difference in FT enhancement when using randomly dispersed CNTs with a higher AR [112], while Rafiee *et al.* attributed the greater FT enhancement from dispersed GNPs to their superior SSAs [95]. As discovered by Hsieh *et al.* [98] and later observed by Hernandez-Perez *et al.* [112], additive pull-out is the dominating toughening mechanism for these matrix modified systems. Therefore, fillers with a greater matrix bonded surface area require more energy to oppose interfacial forces as they are pulled out. Furthermore, a greater surface area is also more efficient at transferring stress between the filler and matrix, reducing the likelihood of filler debonding.

Fillers with a higher AR have also been shown in influence the extent of crack deflection. Fractured surfaces have been reported to be quantifiably rougher for high AR fillers, due to the increased distortion in the crack path as it deflects further away from the fillers [112]. For FRPs, the increased filler aspect ratio has been observed to lead to greater amounts of filler entanglement with primary fibres, which obstructed crack propagation along the fibre interface and thus increased the FT [34].

Filler dispersion, functionalisation and interfacial strength

One of the most important factors dictating the mechanical performance of matrix modified composites is dispersion quality. Dispersion quality refers to both the distribution of the fillers and the extent of filler damage during the dispersion process. An in-depth discussion on the limitations of dispersion can be found in Section 2.2.3.5.

There are multiple techniques to homogeneously disperse additives into a resin system including ultrasonication, shear mixing, calendaring, ball milling and extrusion [116]. The choice

Table 2.1: The influential factors associated with carbon nano-fillers on the Mode I fracture toughness.

Influential Factor	Ref.	Nano-filler Type	Wt(%)	Mode I FT Enhancement (%)
Filler Geometry - Aspect Ratio and Surface Area	[95]	MWCNT	0.1	66
		GNP	0.1	126
	[106]	CB	0.1	18
		DWCNT	0.1	17
	[111]	CNF	0.1	10
	[112]	MWCNT (HAR)	1	130
		MWCNT (LAR)	1	13
Filler Dispersion, Functionalisation and Interfacial Strength	[113]	DWCNT	0.5	31
		DWCNT-NH2	0.5	43
		MWCNT	0.5	#
		MWCNT-NH2	0.5	29
Filler Concentration	[113]	SWCNT	0.1	23
		SWCNT	0.3	12
		DWCNT	0.1	17
		DWCNT	0.3	31
		MWCNT	0.1	22
		MWCNT	0.3	23
Filler Orientation	[114]	MWCNT (R)	0.5	21
		MWCNT (A)	0.5	45
		MWCNT (R)	1	76
		MWCNT (A)	1	120
	[115]	CNF (R)	1.0*	850
		CNF (A)	1.0*	1100
		GNP (R)	1.0*	460
		GNP (A)	1.0*	740

** These are vol% rather than wt%*

 # High viscosity disabled degassing - composite contained numerous voids

HAR - High Aspect Ratio
LAR - Low Aspect Ratio
R - Randomly Aligned
A - Aligned transversely to the crack front

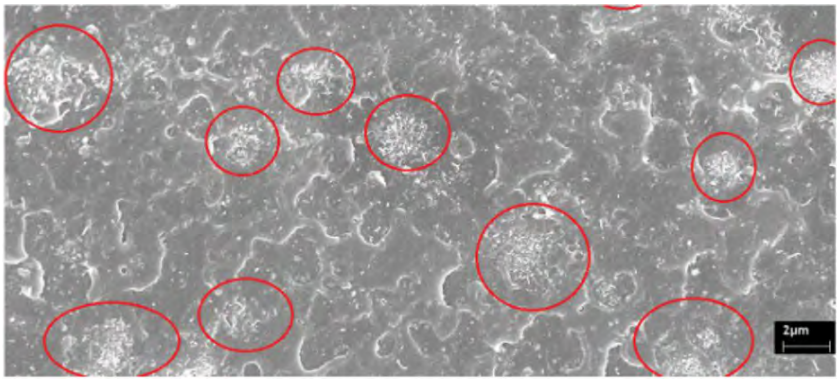

Figure 2.20: SEM image of CNTs within a PVB matrix, red circles indicating CNT agglomeration [29].

will depend on the matrix system involved, and the acceptable amounts of filler damage. A major challenge with dispersion techniques is to prevent filler agglomeration, whereby the additives cluster together because of Van der Waal attractive forces. This clustering behaviour, as seen in Figure 2.20, significantly lowers the filler's reinforcement efficiency; Fillers are able to slide past each other rather than pulling away from the surrounding matrix, an event that requires substantially less energy [117].

An abundance of studies have commented that the FT of a matrix modified system is subject to the dispersion technique adopted [113, 118, 119]. One common method to improve dispersion is to functionalise the filler surface with oxygen containing groups, such as carboxyl or hydroxyl groups [34], or with amino groups, such Amine or Azanide [30, 113]. These groups have been shown to facilitate the exfoliation of CNT bundles and increase solubility within the resin [120]. However, care must be taken with these methods as they require strong acids, which can create filler defects and can decrease their aspect ratios.

Functionalised fillers also have the benefit of improving the interfacial properties with the matrix. Gojny *et al*. functionalised the surface of CNTs using Azanide (NH_2) and measured the FT with respect to a neat resin and one with unmodified CNTs [113]. The functionalised fillers were found to increase the FT by up to 10% compared to a similar unmodified filler, and over 40% compared to the neat resin. This was attributed to both the improved filler dispersion and the greater interfacial strength. The study concluded that functionalisation methods need to be tailored to avoid excess damage to the filler and prevent a tendency for filler rupture over pull-out, which results in lesser strain energy dissipation.

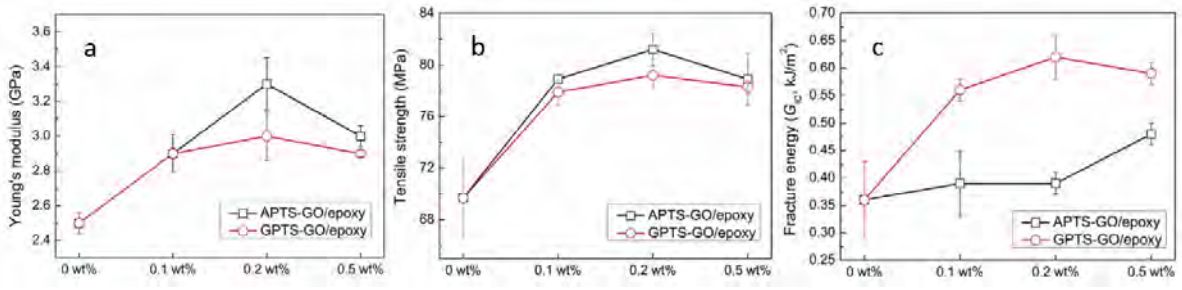

Figure 2.21: The mechanical properties of neat epoxy and epoxy composites contain various weight contents of re-functionalised graphene oxide (GO): (a) Young's modulus, (b) ultimate tensile strength and (c) Mode I critical strain energy release rate (G_{IC}) [30].

Filler concentration

In general, FT enhancements increase with filler concentration as the accumulation of energy dissipating events increases. However, there is a limit, whereby the FT no longer increases with filler concentration, but instead plateaus or decreases. This behaviour can be observed in Figure 2.21, which shows the effect on modulus, strength and FT, when the content of graphene oxide (GO) in epoxy is increased. The reasoning for this is related to filler dispersion and agglomeration, which will be described further in 2.2.3.5.

Filler orientation

The final factor influencing the FT enhancements in homogeneously dispersed matrix modified composites is the orientation of the fillers. It was concluded in Section 2.2.3, that to maximise FT, fillers should prioritise pull-out and debonding mechanisms, as these provide the greatest contributions toward the overall energy dissipation [98]. To optimise these mechanisms, fillers should be aligned transversely to the propagating crack, so as to bridge the fractured surface. For homogeneously dispersed fillers, alignment can be achieved through magnetic [114] or electrical fields [115]. It has been shown by Ma *et al.* that MWCNTs aligned transverse to the crack front increases the Mode I FT by over 100% relative to random alignment [114]. Moreover, Landai *et al.* and Wu *et al.* (of the same research group) have measured approximately a 30% and 60% improvement in Mode I ILFT by aligning CNFs [111] and GNPs [121] perpendicular to the crack front respectively.

For these aligned techniques to be the most effective, the fillers must be orientated so as to bridge the crack plane. If the crack plane is unknown, then unaligned, randomly distributed fillers are recommended for increasing the FT of the composite. However, with respect to delamination, the crack plane is already known to be parallel to the fibres and so, similarly to the z-binder alternatives, the optimum orientation will be in the through-thickness direction.

2.2.3.2.1 Homogeneously dispersed carbon nano-fillers in hierarchical reinforced composites

Hierarchical reinforced composites (HRC) are materials that have reinforcement at multiple scales. One example includes the multi-scale fibres discussed in section 2.2.2.4.2. This section will focus on another common form of HRC found in engineering applications, namely, homogeneously dispersed nano-fillers within fibre reinforced polymers. Such a HRC is illustrated in Figure 2.17b.

Reinforcing HRCs with homogeneously dispersed nano-fillers can be achieved through multiple methods. One example, as done by Borowoski *et al.* [122], is to infuse resin with the dispersed nano-fillers into a dry fibre preform, however this method requires the viscosity of the reinforced resin to be sufficiently low.

Similar to nano-composites, the challenge with homogeneously reinforcing HRCs is ensuring uniform dispersion and strong interfacial bonds between the nano-fillers and the matrix. However, a challenge unique to HRCs, is to encourage beneficial interactions between the fillers and fibres, while avoiding interfacial degradations between the matrix and the fibres. For instance, Srivastava *et al.* observed that with a 3 wt% of MWCNTs in a CFRP system, fibre bridging and matrix tensile cracking increased compared to a baseline laminate [123]. Along with other filler energy dissipating mechanisms (as listed in section 2.2.3), such as filler bridging and filler pullout, an overall fracture toughness improvement of 44% in Mode I and 29% in Mode II was measured. On the other hand, Wichmann *et al.* measured no appreciable difference in fracture toughness when the FRP system was mixed with a variety of CNTs; even when the CNTs were oriented to encourage bridging [124]. Their suggested reason was because the fibre-matrix interfacial strength dominates the fracture toughness measurement, and because the CNTs did not encourage further matrix bridging, no improvement in the fracture toughness was detected after the CNTs were introduced. Seyhan *et al.* found that randomly oriented CNTs inhibited fibre nesting and fibre bridging between the ply interfaces [125]. This resulted in a reduction in Mode I propagation fracture toughness, which is highly dependent on fibre bridging effects. Seyhan *et al.* further found that in Mode II, which is prone to hackle formations, the CNTs acted to arrest the crack by preventing the expansion of micro-cracking within the matrix rich interfacial areas between the plies. It was suggested that the CNTs increased the hackle formation, which led to a 8% increase in initiation fracture toughness, because of the increased friction between the delaminated surfaces.

These studies have shown that it is important to account for the influence of nano-fillers on the fibre bridging behaviour, and matrix-fibre interfacial properties.

When comparing the improvements between the Mode I and Mode II fracture toughness by homogeneously dispersing CNTs into a FRP system, Quan *et al.* measured six times greater improvement in Mode II compared to Mode I [126]. Fractography analysis showed that under Mode II the process zone is around six times greater in Mode II than in Mode I. As a result, surfaces of failed Mode II specimens were found have a greater increase in nanotube breaking,

crack deflection and matrix micro-cracks compared to their baseline equivalents.

As previously mentioned, studies investigating homogeneously dispersed nano-fillers in HRCs have reported that two influential factors that result in improvement in ILFT, are the quality of the dispersion of the fillers and bond strength between the fillers and the matrix. In order to improve both of these factors, a common technique is to functionalise the surface of the fillers. For example, it is common to enhance fracture toughness properties with carbon nano-fillers through functionalising the fillers with amino (-NH_2) or carboxylic (-COOH) functional groups. These groups both reduce the likelihood of filler clustering, while also improving interfacial bond strength to their host matrix. For instance, Mujika *et al.* measured the Mode II ILFT of four CF/EP specimens that were dispersed with functionalised and non-functionalised CNTs [127]. In the study, all but the functionalised CNT specimens showed no to little improvement in the fracture toughness. This was attributed to the poor dispersion and weaker filler bonding associated with the non-functionalised CNTs. A similar conclusion was also found by Godara *et al.* [128] and Ashrafi *et al.* [129].

2.2.3.3 Discretely located matrix modifiers (interleaves)

An alternative to distributing matrix modifiers homogeneously throughout the matrix, is to concentrate them locally in regions that are prone to damage. As discussed in chapter 1, the layered architecture of FRP composite materials leads to interlaminar delamination being the dominant failure mode. Therefore, concentrated reinforcement will be most effective if located in the resin rich interlaminar region.

Interleaving is a technique of inserting additional material between the ply interfaces in order to inhibit crack growth and therefore increase the ILFT of the laminate. This method only modifies a localised region and should therefore has a lesser influence on the global laminate properties relative to the homogeneous dispersion technique.

Interleaving can be classified into three groups: particle, film, and fibrous interleaving [130]. Particle interleaving commonly comes in the form of dried thermoplastic particulate powders that are uniformly sprinkled onto the prepreg surface and pressed to embed to the prepreg system. These particle interleaved prepreg plies are then stacked on top of each other to form the architecture illustrated in Figure 2.22a. The toughening mechanisms associated with these particles include particle deformation and debonding, crack-tip shielding, matrix yielding, and crack deflection [130, 131].

Film interleaving involves inserting a partially cured polymer film with a defined thickness between plies to increase the interlaminar thickness (see Figure 2.22b). These films can be either the same polymer as the host composite [32], or different [31], providing the two polymers are compatible. Both thermoplastic and thermoset film interleaves have been investigated with respect to their FT enhancement capabilities. In general, thermoplastic films offer greater ductility and increased toughness, however, they also result in a reduction to in-plane mechanical

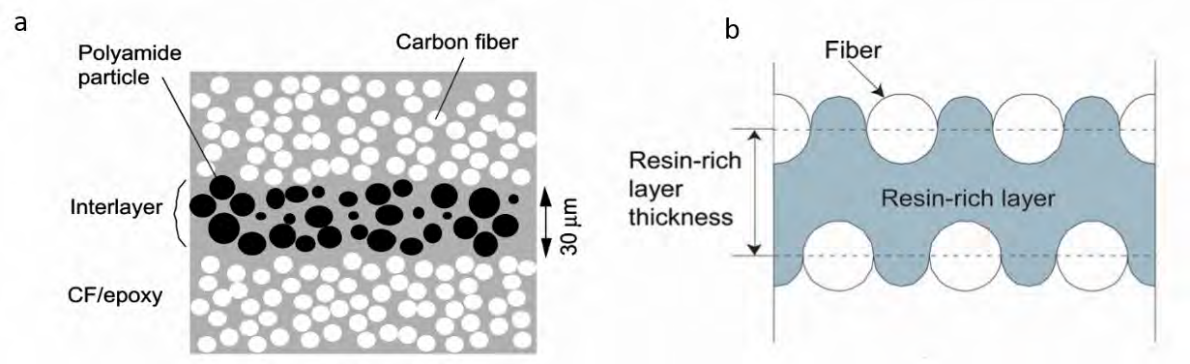

Figure 2.22: Schematic of the cross-section of (a) a particle interleaved composite [31] and (b) a film interleaved composite [32].

properties and lower thermal performance.

The FT of film interleaves has been shown to increase with film thickness up to a limit of approximately 0.1mm [132]. Increasing film thickness also has detrimental effects on the laminate, namely, lowering the global stiffness, strength and altering the global fibre volume fraction of the laminate. In order to account for this, additional plies are normally included, which increases the laminate weight. More recent studies have therefore adopted discrete interleaf strips, so as to minimise in-plane mechanical property losses, while simultaneously enabling control and manipulation of delamination damage [133].

Fractography studies have indicated that the extent of resin film interleaf deformation determines the improvement in toughness [134, 135], with shear deformation generally being substantially higher than through-thickness deformation. This suggests that further reinforcement is required through the insert thickness in order to improve the G_{IC} properties. Yasaee *et al.* compared a variety of interleaf configurations under Mode I [136] and Mode II [133] conditions. These interleaf inserts consisted of pure thermoset and thermoplastic resin films, randomly oriented chopped aramid fibres, and E-glass/epoxy glass. All inserts were 10mm wide and demonstrated a significant increase in G_{IC} and G_{IIC} compared to unmodified baselines. It was concluded that the increased inter-ply thickness only marginally contributed to the critical Mode I ILFT. Instead, the ability to mechanically link plies together was the dominating factor for improving ILFT of a composite material.

The influence of ply thickness on the ILFT was also studied by Hojo *et al.* [32]. In their work, it was suggested that a thicker interface formed from interleaving does not contribute to the Mode I interlaminar properties because the process zone size is very small. This referenced process zone is a region located in front of the crack tip, where stress concentrations at the crack tip lead to damage and small crack formations in the process region. Hojo *et al.* further suggested that the process zone is much greater in Mode II conditions. Fractography analysis on the surface of failed Mode II specimens showed that interfaces with a larger thickness had greater plastic

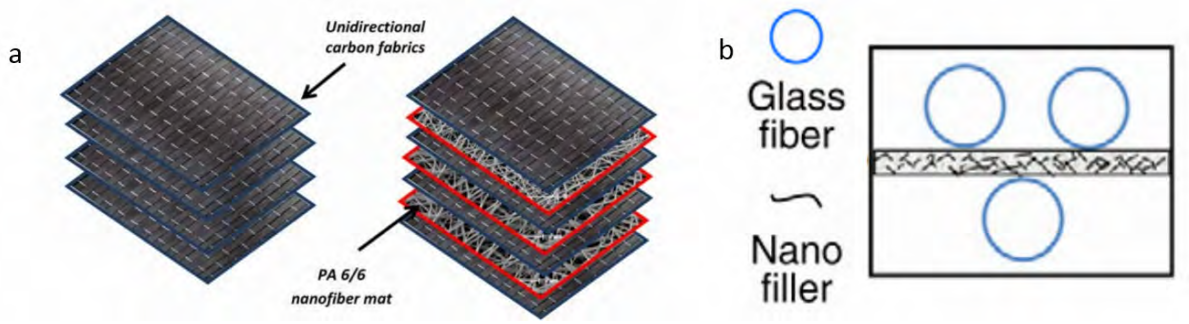

Figure 2.23: Example schematics of nano-fibre interleaving methods including (a) nano-fibre veil interleaves [33] and (b) randomly dispersed nano-fillers in a polymer film [34].

deformation in the form of hackle markings. It was this larger plastic deformation that led to the greater Mode II fracture toughness measurements for laminates with a thicker interface. Cheng *et al.* further showed that as the interlayer thickness increases beyond the plastic zone diameter, a crack will no longer propagate along the interface between fibre layers and the host matrix, but will remain in the resin rich region, resulting in a cohesive failure [137].

More recently, interleaving techniques have focused on using fibrous reinforcement to bridge the gap between plies and therefore improve the interleaf's ability to bind plies together. While chopped microscale fibres have shown significant improvements to Mode I FT [136, 138], the majority of fibrous material used in interleaf applications have been in the nanoscale. These lower scale fillers minimise disruption to the fibre architecture and avoid substantial increases in laminate thickness.

Nanoscale fibrous material commonly comes in the form of nanotubes [36], nano-fibrilmats [139], and nanofibres [135, 140]. Examples of these configurations can be seen in Figure 2.23 and Figure 2.17c. In common with homogeneously dispersed nano-fillers, all of these fibrous interleaf systems dissipate energy and thereby enhance the composite's FT through the mechanisms described in Section 2.2.3.

Multiple thermoplastic materials have been used for nano-fibrous interleave reinforcement including nylon [139], polyamide [140] and polycaprolactone [141]. However, with superior mechanical properties and the ability to create an electrical or thermal conductive network through-thickness, carbon-based nanoscale fibrous interleaf materials offer multi-functional capabilities, which have attracted a wide variety of research for both structural and electrical enhancement applications [142]. Carbon also offers greater thermal stability than thermoplastics, allowing for interleaves to be used in elevated temperature environments. Furthermore, the lack of compatibility and strong interaction between thermoplastic nano-fibres and epoxy introduces processing difficulties [143]. For these reasons, the remainder of this section shall focus on the delamination suppressing behaviours associated with carbon-based fibrous interleaves.

2.2.3.4 Discretely located carbon nano-fillers (interleaves)

Carbon nano-filled interleaves can be categorised into two groups, depending on how the carbon fillers are incorporated into the layup process. These include, dry transfer and film transfer. Dry transfer uses methods similar to that described for particle interleaves, *i.e.* spraying [144], sprinkling [145] or pressing [38], to deposit the dry fillers on to the prepreg surface. In contrast, film transfer involves initially manufacturing a fibrous veil [146] or dispersing carbon fillers into a polymer film [147] to later transfer to the prepreg surface as an extra layer during the layup process. The advantage with the latter is that the hazardous nano-fillers are contained, improving their handleability and processability.

Table 2.2 outlines previous literature, which investigates the Mode I and Mode II FT enhancements through interleaving carbon-based interleaves within FRP systems. Similar to Table 2.1, the reported literature has been grouped into 'influential factors' to aid with the discussion. While substantially less work has been published on FT enhancements from nano-filled interleaves, similar conclusions about their toughening capabilities can be shared with the homogeneous dispersion alternatives. These factors are individually considered below:

Filler geometry - aspect ratio and specific surface area

A variety of carbon-based fibrous fillers have been interleaved into composite laminates, however due to their superior AR and SSA, CNTs and CNFs have been the most extensively investigated for FT enhancement applications. When interleaving GFRPs with nano-filled resin films, Zhu *et al.* discovered that long CNTs offered the greatest enhancement to both the Mode I and Mode II FT [34]. SEM images of the fractured surface indicated that this was caused by the greater extent of nano-filler pull-out and crack bridging mechanisms [34]. The higher AR nano-fillers were also found to cause the most entanglement with the primary fibres to effectively obstruct interlaminar crack propagation. Liu *et al.* measured the greatest FT enhancements when interleaving with a combination of polyamide (PA) particles and MWCNTs [35]. This combination increased the filler AR and SSA relative to each individual filler component, resulting in an 127% increase in G_{IC} from additional bridging effects (see Figure 2.24).

Table 2.2: The influential factors associated with carbon nano-fibrous interleaves on the Mode I and Mode II fracture toughness.

Influential Factor	**Ref.**	**Nano-filler Type**	**Wt (%)**	**Mode I FT Enhancement (%)**	**Mode II FT Enhancement (%)**
Filler Geometry - Aspect Ratio and Surface Area	[35]	PA	20	50	-
		MWNT	20	-23	-
		PA-MWNT	20	127	-
	[34]	CNF	0.5	39	49
		CNT (HAR)	0.5	52	74
		CNT (LAR)	0.25	79	91
Filler Dispersion, Functionalisation and Interfacial Strength	[148]	CNT (NF)	-	104	-
		CNT- H_2SO_4/KnO_4	-	100	-
	[34]	CNF (NF)	0.5	30	39
		CNF-GPS	0.5	39	49
Filler Concentration	[36]	CF	10#	41	-
			20#	100	-
			30#	36	-
	[135]	CF	10#	50	50
			20#	50	50
			30#	0	4
Filler Orientation	[140]$	Veil (R)	20	-	100
		Veil (AP)	20	-	50
		Veil (AT)	20	-	75
	[38]	VACNT	-	50 / 150*	200

** This is for different host FRP systems.*
 # This is the area density (g/m^2) of CNFs at the interlayer.
$ This is not a carbon-based nano-fibrous veil system.

HAR - High Aspect Ratio
LAR - Low Aspect Ratio
NF - Non-functionalised
R - Randomly Aligned
AT - Aligned transversely (but in-plane) to the fibres
AP - Aligned parallel to the fibres

Filler dispersion, functionalisation and interfacial strength

Unlike homogeneously dispersed nano-fillers, nano-filled interleaves do not require uniform dispersion to achieve FT enhancements. The exception to this is for low concentrated nano-filled resin film interleaves, whereby filler agglomeration (see Figure 2.24a) has been found to result in detrimental effects to the FT [35]. A limited number of studies have also investigated functionalisation of the nano-fillers within the interleaves, however, rather than for aiding dispersion, functionalisation is aimed at improving the interfacial properties of the fillers and matrix. Results range from having no influence [148] to a marginal increase [34], however this is still an area in need of further research.

Filler concentration

In general, nano-filler concentrations within interleaves are able to be much greater than for homogeneous dispersion, due to the dispersion not being a critical factor [149]. The reasoning for this will be discussed in more depth in Section 2.2.3.5.

It is believed by the author that, as of yet, no study has investigated the influence of interleaf nano-filler concentration with respect to FT enhancement. The closest studies involve micro-scale carbon fibres (CF) that were deposited on to FRP prepreg surfaces through sprinkling or spraying [36, 135]. These studies have shown that the areal density of CFs can be optimised to gain the greatest interlaminar strength and toughness properties. Prior to the optimum CF interleaf areal density (20 g/m^2), the FT was found to increase due to a 'zig-zag' crack propagation through the

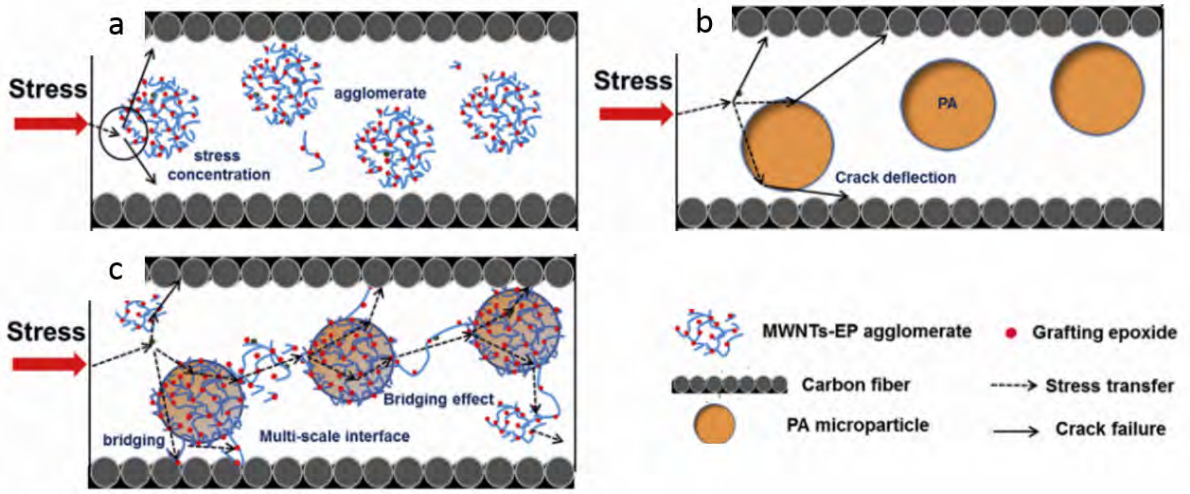

Figure 2.24: Schematic of fracture in the interlaminar region of composites with different interleave types: (a) EP/PES/MWNTs-EP interleaf; (b) EP/PES/PA interleaf; (c) EP/PES/PA-MWNTs-EP interleaf [35].

interleaved interlaminar region (see Figure 2.26(b-c)) [36]. This more torturous crack path led to a greater fracture surface area and hence further energy dissipation. As the volume fraction of the CFs within the interlayer remained constant (≈ 10%), the increased CF areal density resulted in a higher interlaminar thicknesses, peaking at more than 200 μm [36]. Although this interlaminar thickness will substantially increase the overall laminate thickness, the thicker interface was also found to better contain the crack, further increasing the FT through additional bridging and pull-out mechanisms. However, when the CF areal density exceeded 20 g/m^2, the FT measured dramatically decreased due to crack deflection away from the interleaved region. This will be discussed further in Section 2.2.3.5.

Filler orientation

The majority of nano-filled interleaf systems mentioned thus far have consisted of randomly oriented fillers, however, as discussed in Section 2.2.3.2, the most effective fillers should be oriented so as to bridge the crack plane. For nano-filled interleaves bridging the interlaminar region, this orientation will coincide with z-binders described in Section 2.2.1, *i.e.* through the laminate thickness.

Investigating the FT enhancement from electrospun fibril veils, Stahl *et al.* discovered that veils with a greater amount of fibres bridging the interlaminar region (random in this case), provided the highest FT enhancements [148]. Unfortunately, owing to the fibrous length far exceeding the interlaminar thickness, veils are limited in their bridging capabilities. In contrast, the length of CNTs can be tailored through their growth conditions to match the interlaminar region. This has led to an upcoming interleaf research field known as vertically aligned carbon nanotubes (VACNTs).

Pioneering work by Garcia *et al.* has developed a method to grow and mechanically transfer VACNTs on to the surface of prepreg using a roller [38]. In their study, substantial FT enhancements were measured for both Mode I and Mode II conditions, with later work showing that in-plane properties are not compromised [150]. Complementary numerical models investigating VACNTs have suggested the potential increase of more than six times the critical Mode I FT enhancement relative to z-pins [96], signifying great promise for future research.

2.2.3.5 Limitations with matrix modifiers

2.2.3.5.1 Homogeneously dispersed matrix modifiers

As discussed in the previous section, a limitation associated with homogeneously dispersed matrix modifiers is from the filler dispersion quality. High quality dispersion can be described as a uniform filler distribution, with fillers that have not been damaged during the dispersion process. This filler architecture has been shown to produce the greatest enhancements to a nano-composite's mechanical properties [118].

Filler damage is a consequence of harsh processing methods, such as extensive shear mixing or the usage of harsh acids for functionalisation purposes. These processes can lead to a reduction in filler AR or the introduction of filler defects, thereby reducing their mechanical properties and ability to dissipate energy [151, 152].

The uniformity of the filler distribution is limited by the selected filler concentration and filler AR. At higher filler concentrations, the average distance between filler particles is reduced and so the Van der Waal attractive forces rise [153]. This results in an increased tendency for filler agglomeration. Fillers with larger ARs, *e.g.* SWCNTs and GNPs, also suffer with an increased tendency to agglomerate. It was observed by Gojny *et al.* [113] that the concentration for maximum Mode I FT enhancement lowers, for fillers with higher ARs; In their study, it was measured that Mode I FT enhancements for DWCNTs stagnated at 0.3 wt%, while higher AR SWCNTs were limited to only 0.1 wt%. This was attributed to the increased likelihood of filler entanglement and the shorter average distance between high AR fillers. Therefore, increasing the filler's AR limits the maximum filler concentration before agglomeration occurs.

The maximum filler concentration is also limited by the manufacturing process adopted. Filler incorporation has been shown to increase resin viscosity [154] and therefore, for composite processes including RTM or infusion, the FT enhancements are limited to the maximum resin viscosity that circumvents excess voids and incomplete matrix infusion [155, 156]. Other manufacturing concerns involving homogeneously dispersed fillers involve the consolidation process, with fears that an increased viscosity will alter the interlaminar thickness [66]. Not only does interlaminar thickness influence the ILFT measurements, but also the in-plane properties, with significant degradations measured for tensile strength, tensile modulus and flexural modulus (see Figure 2.25b) [37].

Fillers with a greater AR or greater concentration have been seen to suffer more from filtration effects through the fibres [155, 157]. This can result in localised filler segregation and depletion, which leads to concentration gradients within the composite [66]. Fibre filtration effects have shown to align the fillers in the direction of the fibres, which, for delamination suppression purposes, is the most inefficient direction [66].

2.2.3.5.2 Discretely located (interleaf) matrix modifiers

A limitation associated with discretely located matrix modifiers (interleaves) is their influence on geometric properties and in-plane mechanical properties. For example, Li *et al.* measured a significant increase in interlaminar thickness as areal density of CFs fillers were increased (see Figure 2.25a) [36]. While it has been shown that increasing the interlaminar thickness will increase the FT of a composite laminate [132], it will also lead to substantial increases in the overall laminate thickness and severe structural assembly challenges. Moreover, increasing the interlaminar thickness can lead to degradations to in-plane properties.

Another limitation with interleaved systems is associated with compatibility between the interleaf and the host composite. Multiple studies have described crack deflection behaviours, which restricts the FT enhancements measured from interleaving. For instance, it was discussed in Section 2.2.3.4 that when increasing the areal density of CF interleaves, Li *et al.* discovered that the FT decreased after exceeding 20 g/m^2 [36, 135]. Images of the fractured DCB specimen edge showed the crack transiting away from the interleaf and into the adjacent ply (see Figure 2.26d). The crack then propagated through the ply for the remainder of the test. It was proposed that the reasoning for the loss in FT enhancement after a CF areal density of 20 g/m^2 was due to a weaker interface between the interleaf and ply, compared with the interleaf alone. A similar behaviour was observed by Hojo *et al.* (Figure 2.26a) [31], Daelemans *et al.* [140], Ning *et al.* [158] and more recently by Ni *et al.* [159]. These studies were conducted on differing interleaf and the composite host systems, which shows that the interaction between the interleaf and host composite needs to be accounted for when designing toughened interleaved hybrid composite systems.

2.3 Summary and Unresolved Research Areas

In summary, this review has described three themes of delamination suppressing methods, namely, z-binders, fibre modifiers, and matrix modifiers. While each technique has been shown to be effective at improving the ILFT of a composite laminate, they also have unique limitations, which dictate their suitability for different applications.

In general, for all of the themes discussed, there is a compromise between FT enhancement and the conservation of in-plane mechanical properties; z-binders have been reported to offer the greatest FT enhancements in both Mode I and Mode II conditions, however their severe insertion procedures lead to fibre disruption and damage; fibre modifiers dramatically improve

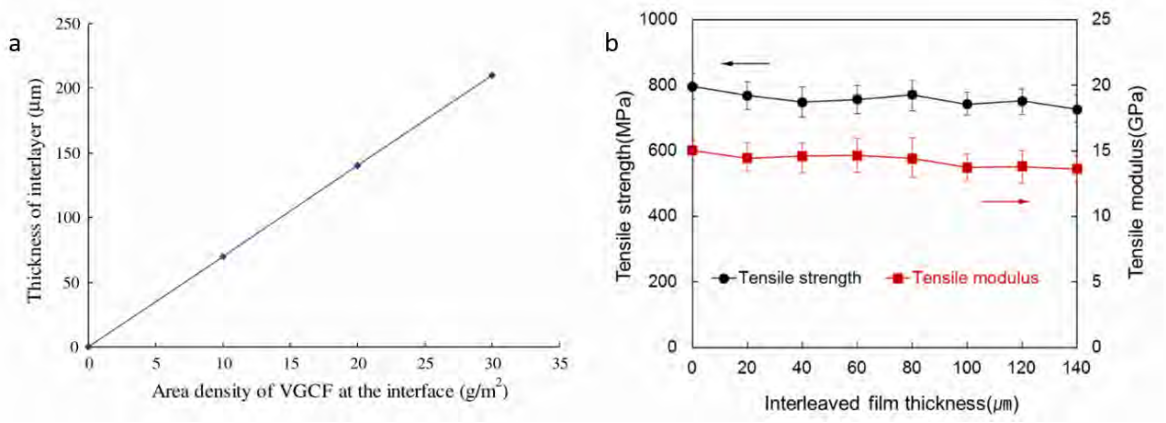

Figure 2.25: (a) The relationship between area density of CF nano-filler interleaves and the interlaminar thickness [36] and (b) the effect of polymer interleaf film thickness on the tensile strength and tensile modulus [37].

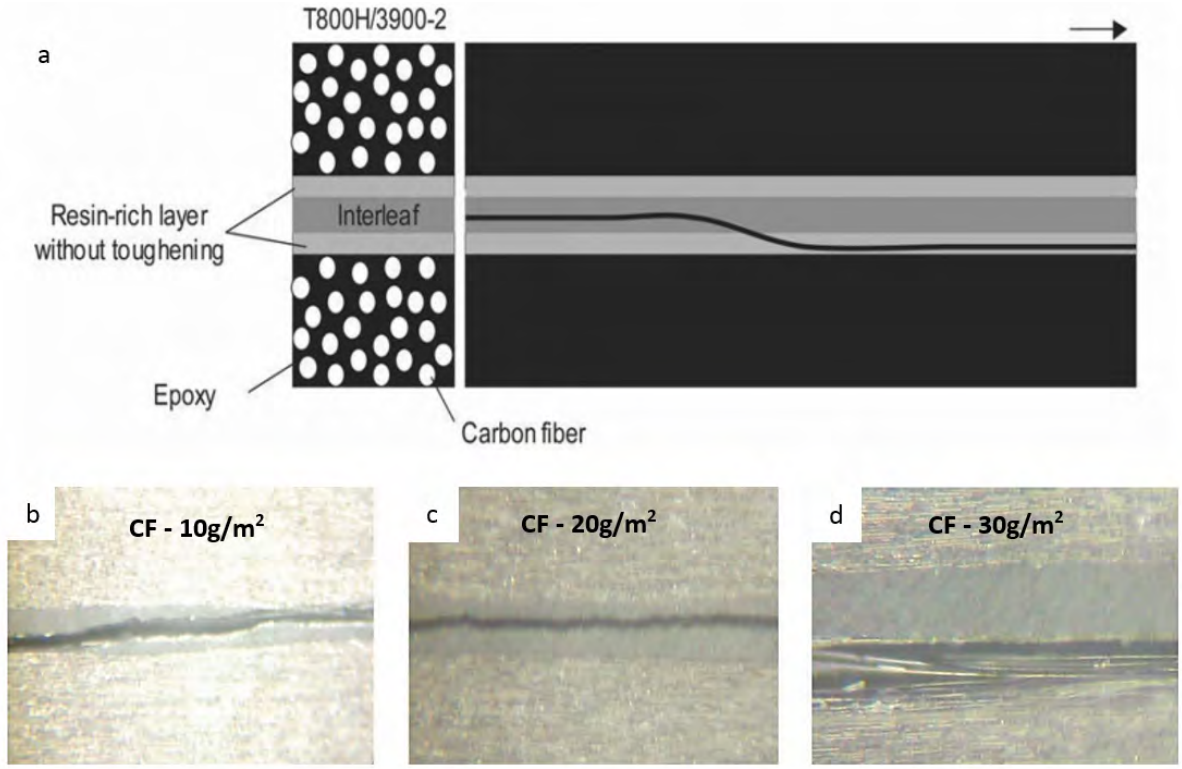

Figure 2.26: (a) A schematic of a crack propagating from the interleaf into the ply-interleaf interfacial region [31] and microscope images of the crack propagation through CFRP laminate with CF interleaf concentrations of (b) 10 g/m^2; (c) 20 g/m^2; (d) 30 g/m^2 (images taken 10 mm from a crack initiator) [36].

the interfacial properties between the fibre and matrix, however, in doing so, also leads to fibre damage and additional stress concentrations; matrix modifiers enhance the weakest component of the composite, *i.e.* the matrix, through introducing additional energy dissipating mechanisms, however, can increase matrix ductility or initiate premature cracks, which degrade in-plane properties. As the majority of engineering applications require a balance between toughness, strength and stiffness, these compromises limit the maximum available toughness enhancements.

Recently, carbon-based matrix modifiers have received the greatest amount of attention, due to their substantial FT improvements, without significant losses to in-plane performance. These techniques are also able to be implemented using a variety of manufacturing methods, at low expense, and with multi-functional opportunities available. This had led to some studies using matrix modifiers in conjunction with z-binders to further improve FT and minimise in-plane losses [160, 161]. Regardless of the incorporation method of the matrix additives, *e.g.* homogeneous dispersion or discrete location, a number of factors dictate the toughening benefits from adding matrix modifiers; filler geometry, filler dispersion, filler interfacial properties, filler concentration and filler alignment. Summarising the conclusions found in existing literature, it

can be concluded that to gain the optimum performance, a matrix modifying technique should utilise fillers that:

1. have a high aspect ratio and surface area;
2. are well dispersed within the matrix;
3. have a maximum concentration that avoids agglomeration;
4. improve interfacial properties but without encouraging filler rupture;
5. are aligned so as to bridge the fracture plane.

These characteristics are designed to promote filler pull-out and crack bridging, two energy dissipating mechanisms that have been shown to dominate FT enhancements in composite materials [98].

Comparing the Mode I and Mode II ILFT enhancements for identical nano-fillers applied either homogeneously or between plies (interleaves), Zhu *et al.* concluded that interleaving nano-fillers provides significantly greater improvements relative to dispersed nano-fillers [34]. The greater FT enhancements associated with interleaved composites were attributed with more nano-filler particles at the fracture surface, which resulted in increased energy dissipating events. Owing to filler agglomeration having a lower influence for interleaved composites, greater local filler concentrations could be achieved. Therefore, if the failure location is known, localised reinforcement provides a more efficient method for toughening a composite than homogeneous dispersion. Localised reinforcement has the additional benefit of having a lower influence on the global properties of the composite as the majority of the structure is unmodified.

For the majority of nano-filled interleaves, including the study by Zhu *et al.* [34], the fillers have been randomly oriented. Preliminary studies investigating the effect of aligning the fillers, so as to bridge the expected crack front, have shown substantial improvement to the FT. This has led to an emerging field known as vertically aligned carbon nanotubes (VACNTs).

2.3.1 VACNTs and interlaminar fracture toughness

The first study of VACNTs interleaves as ILFT enhancers was conducted by Veedu *et al.* [162]. In their work, it was shown that CNTs oriented in the through-thickness direction can exhibit gains of 348% and 54% in the Mode I and Mode II ILFT respectively. CNTs were grown on to the SiC woven fibre preform surface using a chemical vapour disposition (CVD) method. This process required high temperatures and reactive conditions, which, as shown by Zhang *et al.*, results in 40% drop in tensile properties in argon and 70% drop when in a vacuum environment [68]. Another technique developed by Garcia *et al.* enables a VACNT forest to be printed onto a pre-impregnated fibre epoxy system [38]. CNTs were grown on to a silicon substrate using CVD and later transferred to prepreg using a roller to mechanically press to the tacky prepreg surface

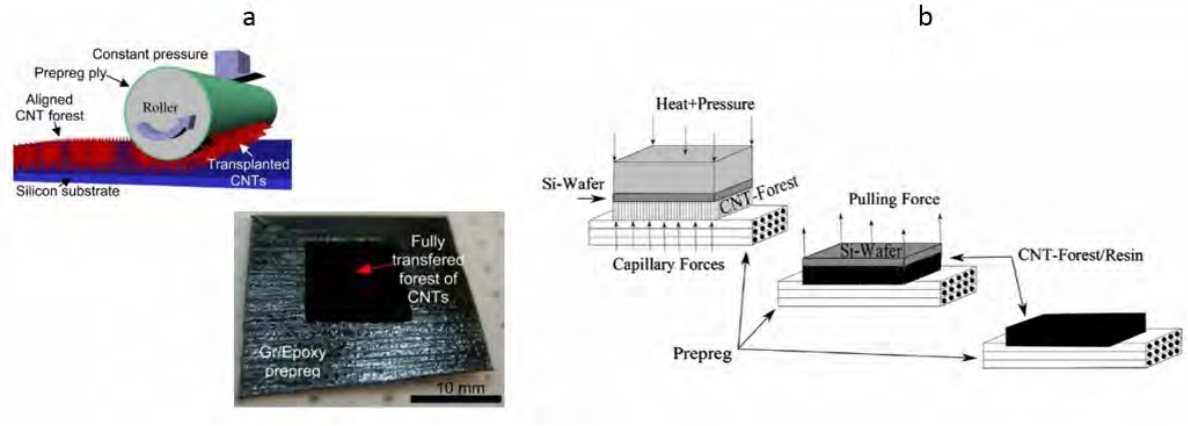

Figure 2.27: An example of VACNTs being transferred to prepreg using (a) a mechanical roller [38] and (b) a combination of heat and pressure [39].

(see Figure 2.27a). This not only maintained the orientation of the CNTs in the through-thickness direction, but also avoided the fibres being exposed to harsh conditions, thereby minimising degradation of the fibre dominated properties. Overall, Garcia *et al.* reported a 50 – 150% increase in the Mode I and 200% increase in Mode II fracture energies. It should be noted that the Mode II evaluation was conducted on HexTow® AS4/HexPly® 8552 (AS4/8552), which measures a value of 1000 – 1150 J/m^2 in its unmodified form [163]. For comparison, this value is similar to that reported by Garcia *et al.* for their nanotube interleaved laminate.

More recent studies have used a combination of heat and pressure to transfer VACNTs from a substrate on to the prepreg surface (Figure 2.27b) [39, 159]. This reduces the likelihood of shear forces, which would lead to VACNT misalignment. For example, Ni and Wardle investigated the Mode I and Mode II interlaminar fracture micro-mechanisms, when AS4/8552 is reinforced with aligned carbon nanotubes [159]. Despite being conducted on the same host laminate, their results were very different to those reported by Garcia *et al.*; interlaminar fracture toughness was measured to be 6% less than the unreinforced baseline for Mode I and no different when tested under Mode II conditions. This was attributed to a crack bifurcation process, whereby the crack deflected to the less tough intralaminar region and propagated parallel to the VACNT interface.

Currently, VACNT interleaving is still at an immature stage, particularly with regards to how the VACNT characteristics influence the ability to suppress delamination and understanding the benefits of VACNTs in more complex delamination-prone structures. For example, one advantage of working with CNTs is the ability to tailor their geometric shape and global densities through the modification of the synthesis conditions, *e.g.* catalyst type, temperature, time, water introduction, and reaction support materials [164]. Through synthesis tuning research, it has been shown that increasing CNT density increases the shear and axial modulus [165, 166], compressive strength [167] and energy absorption [168] of the raw VACNT forest. This is due to the increased Van der Waals interactions and increased support from the neighbouring nanotubes [169]. However, to

date, no studies have investigated how the VACNT density influences the mechanical properties when interleaved into an FRP material. Numerical studies have predicted that an increase in the CNTs density, length, and interfacial shear strength could lead to a higher Mode I FT of composite laminates [96, 170], however this has not yet been verified by experimental results.

As well as dispersing the VACNTs homogeneously, nanotube distributions can also be applied discretely. For example, additional steps to the manufacturing procedure enables the VACNTs to be printed or deposited in user defined patterns. Interleaf patterning has already been achieved using techniques such as inkjet printing [171], film casting [172], masking [173], and laser etching [174]. Although the printing transfers have been high quality, their applications have been limited to electrical improvements through constructing geometrically complex and highly conductive networks. Structural improvement studies on patterned interleaves have been focussed on thermoplastics, such as Polylactic Acid (PLA) and Polymethyl Methacrylate (PMMA), for the interleaf material. These studies have aimed at preserving in-plane mechanical properties and weight, whilst simultaneously improving the interlaminar fracture toughness of the laminates [171, 172]. Overall, selective deposition of the PMMA interleaf through an inkjet extrusion technique has shown that the distribution of the interleaves influences the interlaminar fracture toughness of the laminate through increasing the complexity of the crack path [171]. While the interleaf pattern did not improve the fracture toughness to the same extent as a continuous PMMA film (17% and 58% less for G_{IC} and G_{Iprop}, respectively), only an eighth of the interleaf material was required, thereby drastically reducing the parasitic weight and in-plane losses.

Another patterned interlaminar reinforcement technique was reported by Narducci *et al.* [175]. In the study, PLA thermoplastic was cast on the surface of prepreg using a laser-cut patterned mask and tested under Mode I and Mode II conditions. Under both conditions, the patterned interleaf showed a greater fracture toughness relative to a continuous PLA film equivalent. A significant contribution to the interface toughness was the formation of resin pockets around the PLA, which led to a non-uniform resin layer thickness. This non-uniformity encouraged fibre waviness and nesting, adding additional toughening mechanisms and resulted in the measured Mode I and Mode II fracture toughness being greater than a continuous PLA film interleaf. Narducci *et al.* also discovered that applying interleaves to multiple interfaces rather than at a singular layer was found to increase the Mode I and Mode II fracture toughness, through promoting fibre bridging and interaction between plies. This occurred for both the patterned and continuous interleaved specimens [172]. Although it has been proven that nanotubes can be grown vertically in a patterned formation [173, 174], no studies have been conducted on how patterned VACNTs effect the interlaminar fracture toughness of an FRP material. Ni *et al.* have densified VACNT columns in a patterned arrangement through applying a compressive load to buckle the VACNTs [176]. This technique was found to increase the short-beam shear strength by 7%, with increased crack diffusion and intralaminar, as well as interlaminar, damage resulting in further energy dissipation. In the study, the buckled and densified interleaved specimens

showed ≈5% increase in shear strength compared to non-buckled VACNT interleaved specimens. Unfortunately, no discussion of this result was provided. The author concluded by stating that investigations on patterned VACNT features would be in the scope of future work.

2.3.2 Reinforcing delamination prone composite structures

Another area, as identified by the author, which lacks in-depth research is delamination suppression in delamination prone structures. Two examples of such structures include tapered structures and open hole tension structures. These are individually discussed below:

2.3.2.1 Tapered structures

Composite tapering, *i.e.* changing laminate thickness along its length, offers further mass reduction opportunities, as well as allowing designers to satisfy strict geometric requirements. Examples of tapered composites can be found in aircraft wings, helicopter and turbine blades, and fly wheels [40]. The most common method for tapering a composite is through gradually terminating plies internally along the length (Figure 2.28) [40]. Here, the terminated, or 'dropped', plies are surrounded by continuous sub-laminates, known as the core and belt. Upon surpassing the terminated plies, these adjacent continuous plies connect, leaving a triangular resin pocket ahead of the terminated ply. The resin pocket shape is dictated by the amount of symmetry between the surrounding core and belt continuous plies.

Literature has shown that tensile loaded tapered specimens tend to fail through interlaminar delamination between the continuous and discontinuous ply interfaces [177–179]. During loading, these interfaces experience interlaminar shear stress and through-thickness compression [180], with a maximum at the terminating ply end, which decreases towards the thick section [179, 181]. In contrast, the thin section experiences through-thickness tension [182]. This behaviour is attributed to the residual stresses in the continuous plies, which promote ply straightening to

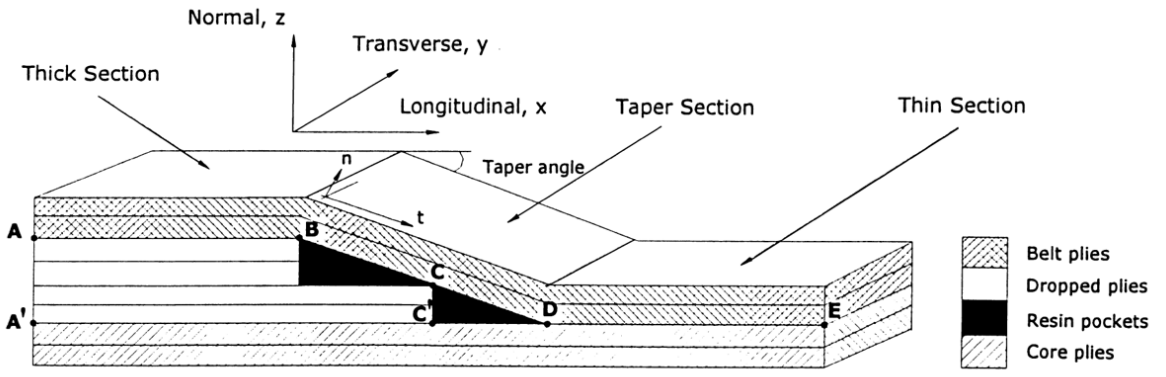

Figure 2.28: Schematic of tapering a composite with internally dropped plies [40].

their original shape and is increased with asymmetry in the layup [182]. Opening stresses are maximal at the tip of the resin pocket and decrease towards the thinner section [183].

Research into tapered specimens can be categorised into three main themes. The first corresponds to the identification of parameters affecting the tapered laminate mechanical properties. Such studies have shown that tensile strength is sensitive to ply-drop separation distance and hence tapering angle [180, 183, 184], the number of plies dropped at one location [185, 186], fibre type [187] and the ply stacking sequence [178, 186, 188].

The second theme focusses on the identification of the failure mechanisms associated with tapered laminates, which enables the prediction of when and where delamination first initiates through finite element models. Experimental studies have shown that under tension, cracks initiate at the tip of the resin pocket and propagate towards the ply termination through the continuous-discontinuous ply interfaces [186, 189, 190]. This happens in predominately Mode II conditions. Numerical studies have shown experimental consistency with respect to the onset load and growth of delamination [43, 189], with approaches focusing on interlaminar stress estimation around the ply-drop and the application of suitable failure criterion [178]. Fracture parameters, such as strain energy release rates, have also be estimated [189].

The final theme involves methods of modification of tapered composite structures to increase strength through suppressing delamination. Multiple strategies have been investigated to achieve this including homogeneous resin modification [190], ply modification [187], and interleaving the continuous-discontinuous ply interfaces [191, 192]. For example, Helmy *et al.* added nano-clay fillers to the bulk resin and compared the tensile fatigue strength to an unmodified epoxy baseline for multiple layup configurations [190]. While the failure mode did not change with nano-clay addition, the fatigue life improved by over 50% for certain conditions. Nano-clay also resulted in the resin becoming more brittle, thereby increasing laminate stiffness and lowering the ultimate failure strain.

An alternative to altering the resin is to modify the plies to reduce the size of the resin pocket, and hence the region of weakness ahead of the terminating ply. Khan *et al.* achieved this through chamfering the ply ends *via* abrasion with fine grit-sized media [187]. Overall, this technique was found to increase the tensile strength by $15-41\%$ compared to unchamfered plies, depending on the stacking sequence and number of plies dropped at the same location. Chamfered plies were also found to change the mode of failure from delamination to fibre dominated.

As interlaminar delamination is the most common mode of failure for tapered specimens, a selection of studies have focused on interleaving the interfaces between the discontinuous and continuous plies with tougher systems. For example, Llonas *et al.* interleaved the ply-drop region with a film adhesive with the aim of suppressing delamination [191]. While the delamination onset load was increased by 14% with the inclusion of the film interleaves, it was found to be highly dependent on the stacking sequence, with some layups not exhibiting any significant strength improvements. Gouldstone *et al.* also investigated interleaving a ply-drop to suppress

delamination, however, instead of an adhesive film, VACNTs with a nominal length of 15 μm were used [192]. The aim was to utilise the orientation or the CNTs to bridge the resin pocket ahead of the terminating ply. Both baseline and interleaved uni-directional tapered specimens were loaded in a Mode II condition through a 3-point bend fixture. Overall, a 5% increase in failure load was observed, with the failure mode shifting from delamination to intra-ply failure and fibre breakage.

2.3.2.2 Open hole tension structures

In order to incorporate composites into complex engineering structures, cut-outs must be made, such as holes or notches, to connect components, allow internal access or integrate additional systems to the structure.

It is well documented that a notch will result in stress concentrations, with stresses being elevated in close proximity to the notch edge [193]. The ductile behaviour associated with metals leads to a crack blunting phenomenon, which reduces the local stresses and thereby stabilises the failure event. Advanced composite materials on the other hand, commonly fail in a brittle fashion, and therefore require other mechanisms to suppress catastrophic failure, once the local stresses around the notch exceed that of the local strength. Examples of these mechanisms include matrix splitting, delamination, fibre pull-out, and fibre rupture.

The notched tensile strength of an advanced composite material has been shown to be dependent on the laminate size and thickness [194–196], notch geometry [194, 197], ply stacking sequence [197–199], ply thickness [194, 196, 200], and machining quality [201]. An extensive experimental programme on the tensile strength of quasi-isotropic notched laminates, when hole diameter, ply thickness, and laminate thickness were varied, was conducted by Green *et al.* [194]. The study concluded that not only did the strength change when the open hole tension (OHT) specimen dimensions were modified, but also the mode of failure; overall, three failure modes were observed, defined as brittle (fibre dominated failure with little sub-critical damage), pull-out (fibre dominated failure with extensive sub-critical damage), and delamination (matrix dominated failure). It is the latter case that is of greatest interest to this study.

During their investigation, Green *et al.* monitored the damage steps leading to failure for each specimen configuration. Initially, sub-critical isolated damage around the hole and free edges was observed in the forms of delaminations and matrix cracking. Additional loading led to delamination growth, which was found to propagate repeatably along a specific ply interface towards the specimen edge. This subsequently resulted in the structural integrity of the laminate being lost. The failure sequence observed by Green *et al.* [194] and supporting numerical work by Hallett *et al.* [2] indicates that the composite notched strength can be enhanced, if delamination is suppressed.

Suppressing delamination for a notched composite has been investigated using a variety of techniques. For example, stitched composites have been shown both experimentally and

numerically to reduce the stress concentration factor (SCF) around a notch [202, 203], with stitch density and stitch pattern being found to influence the laminate strength [204, 205]. However, as discussed in section 2.2.1.5, the stitching process damages the fibre architecture, commonly leading to reductions of in-plane properties [206] and fatigue life [207].

Interleaving notched composite laminates has also been investigated as a means of suppressing delamination. These studies have evaluated the obtainable enhancements in tensile strength [208], compressive strength [150, 209] and the residual tensile strength of bolted CFRPs [210]. While all studies reported strength increases, the magnitudes vary significantly ($5-45\%$). It is believed by the author that this can be attributed to the relative interleaf material properties and the inherent contribution that delamination has on the failure sequence.

2.3.3 Key literature for this research

Table 2.3 summarises the most relevant literature discussed in section 3.1. The intention of this table is to provide a resource that can easily be digested for comparing conclusions. Chapter 8 will utilise this table for commenting on how the research conclusions found in this Thesis have expanded upon the state of the art on vertically aligned carbon nanotube (VACNT) interleaves.

2.4 Research Aims, Objectives and Thesis Overview

2.4.1 Research aims and objectives

The aims of this research are to *(i)* evaluate how CNT characteristics influence the ability to suppress delamination in a vertically aligned carbon nanotube (VACNT) interleaved FRP composite system and; *(ii)* assess the effects of interleaving delamination-prone composite structures using VACNTs. For the former, CNT parameters, which have been predicted numerically to affect the Mode I ILFT, *e.g.* CNT length and density, shall be experimentally examined under Mode I and Mode II conditions. The latter will involve two structures that, when unmodified, are known to fail through delamination. In order achieve these aims the following objectives must be satisfied:

1. experimentally measure the Mode I and Mode II interlaminar fracture toughness for VACNT interleaved FRP composites with a variety of CNT characteristics;

2. experimentally measure the tensile strength of a selection of delamination-prone structures to determine whether VACNTs provide delamination suppressive traits;

3. use fractography techniques on all tested specimen configurations to observe the mode of failure and reasoning for any discrepancies in measured material properties;

4. develop simple finite element (FE) tools to validate the experimental findings and indicate whether VACNTs can be captured through homogeneous cohesive elements;

Table 2.3: Key papers related to the work conducted in this research.

Author	Year	Host System	Major Findings
Tong et al. [170]	2008	-	Numerical results reveal that the MWCNT's length, density, and maximum pull-out displacement, as well as the interfacial friction shear stress, are important parameters affecting the delamination toughness.
Garcia et al. [38]	2008	AS4/8552	Measured a 50-150% increase in Mode I ILFT and a 200% increase in the Mode II ILFT when interleaving with VACNTs.
Blanco et al. [96]	2009	AS4/8552	Numerically predicted a six times increase in Mode I FT toughness from VACNT interleaves relative to Z-pins.
Li et al. [36]	2009	T700S/2500	When VGCF interleaf density exceeded 20g/m^2, cracks would transition from the interlaminar region to the adjacent ply. This led to a decrease in the Mode I fracture toughness. It was proposed that the reasoning in the loss in FT enhancement was due to the weaker interface between the interleaf and the ply compared with the interleaf alone.
Falzon et al. [39]	2013	T700/M21	Measured a 31% increase in Mode I and 162% increase in Mode II ILFT when interleaved with VACNTs.
Ni et al. [159]	2019	AS4/8552	Measured a 6% drop in FT in Mode I and no change in FT in Mode II when interleaved with VACNTs. Observed the crack bifuricating into the intralaminar region.
Zhang et al. [171]	2018	977-2-35-12KHTS-268-300	Selective deposition of the PMMA interleaf through an inkjet extrusion technique showed that the distribution of the interleaves influences the interlaminar fracture toughness of the laminate through increasing the complexity of the crack path. The interleaf pattern did not improve the fracture toughness to the same extent as a continuous PMMA film (17% and 58% less for GIC and GIprop, respectively), only an eighth of the interleaf material was required.
Narducci et al. [175]	2018	Skyflex	PLA thermoplastic was cast on the surface of prepreg using a laser-cut patterned mask and tested under Mode I and Mode II conditions. Under both conditions, the patterned interleaf showed a greater fracture toughness relative to a continuous PLA film equivalent. A significant contribution to the interface toughness was the formation of resin pockets around the PLA, which led to a non-uniform resin layer thickness. This non-uniformity encouraged fibre waviness and nesting, adding additional toughening mechanisms and resulted in the measured Mode I and Mode II fracture toughness being greater than a continuous PLA film interleaf.
Narducci et al. [172]	2018	Skyflex	Applying interleaves to multiple interfaces rather than at a singular layer was found to increase the Mode I and Mode II fracture toughness, through promoting fibre bridging and interaction between plies. This occurred for both the patterned and continuous interleaved specimens
Ni et al. [176]	2020	AS4/8552	VACNT interleaf arrays were densified through applying a compressive load to buckle CNT columns. Buckled VACNTs were found to increase short beam shear stength by 7% and increase the double edge-notched tension strength by 25%. SEM images showed that cracks were forced into the intralaminar region by the densified VACNTs.
Green et al. [194]	2007	IM7/8552	Found that the failure mode of OHT specimens is dependent on the laminate thickness, width and hole size. The failure modes observed include delamination, pull-out and brittle.
Gouldstone et al. [211]	2014	AS4/8552	Found a 5% increase in tensile failure load by interleaving a tapered specimens with VACNTs with a length of 15μm. The failure mode was found to shift from delamination to intra-ply and fibre breakage.
Guzman et al. [150]	2016	AS4/8552	Measured a 30% increase in tension bearing (bolt pullout) strength and a 14% increase in open hole compression strength when specimens were interleaved with VACNTs.

5. develop or adapt manufacturing methods for fabricating VACNT interleaved FRP composites to modify the VACNT interleaf characteristics and reduce interlaminar defects.

2.4.2 Thesis overview

In order to achieve the stated aims and objectives, the thesis is separated into two themes. The first concentrates on the Mode I and Mode II ILFT enhancements from interleaving with a variety of VACNT configurations. Parameters include CNT length, areal density and distribution. The second theme investigates using VACNTs in delamination-prone applications. Focus is placed on the mechanical enhancements, mode of failure and whether VACNTs can be accurately captured using cohesive element modelling. A breakdown of the chapters can be found below:

Part 1: The influence of CNT geometric parameters on suppressing delamination.

Chapter 3 - Investigates the effect of CNT length on the Mode I and Mode II interlaminar fracture toughness of a VACNT interleaved CFRP.

Chapter 4 - Investigates the effect of interfacial layup and the number of interleaved interfaces on the Mode I and Mode II interlaminar fracture toughness of a VACNT interleaved CFRP.

Chapter 5 - Investigates the effect of CNT density and distribution on the Mode I and Mode II interlaminar fracture toughness of a VACNT interleaved CFRP.

Part 2: Suppressing delamination in delamination-prone composite structures.

Chapter 6 - Investigates using VACNT interleaves as a method of suppressing delamination in tapered CFRPs.

Chapter 7 - Investigates using VACNT interleaves as a method of suppressing delamination in notched CFRPs.

Chapter 8 - Summarises the key findings from the research and recommends directions for future work.

Where possible, each chapter has been written in a standalone format, so as to add convenience to the reader. Exceptions to this are when test methods are repeated or when findings from one chapter directly contribute to or complement another. Therefore, each chapter contains its own abstract, introduction and conclusion, which are designed to justify and summarise the chapter's contribution.

CHAPTER 3

THE EFFECT OF NANOTUBE LENGTH ON THE INTERLAMINAR FRACTURE TOUGHNESS OF VACNT INTERLEAVED COMPOSITES

Abstract

Carbon fibre reinforced polymer laminates are interleaved with vertically aligned carbon nanotubes (VACNTs), with a selection of nanotube lengths, ranging from $7-40$ μm. Prior to the layup process, VACNTs are embedded into an epoxy resin film (thickness - 50 μm) in order to facilitate manufacture. All specimens are tested experimentally using double cantilever beam (DCB) and end loaded split (ELS) methods, to measure the Mode I and Mode II interlaminar fracture toughness, respectively. Interlaminar fracture toughness was found to be insensitive to nanotube length, with all tested VACNT configurations exhibiting a $17-20$% increase in Mode I and a $12-15$% increase in Mode II, relative to baseline samples containing no VACNT interleaves. Fractography analysis showed that cracks deflect away from the VACNTs, causing intralaminar delamination fracture, which maps closely the VACNT film topology. Intralaminar cracks were seen to propagate through the fibre-matrix interface, indicating that the fibre-matrix interfacial properties are the limiting factor for this reinforcement technique. It is therefore believed by the author that the measured fracture toughness enhancements are the effective intralaminar fracture toughness properties for the CFRP system (HexTow® IM7/HexPly® 8552).

3.1 Introduction

This chapter aims to develop an understanding of the micro-mechanism behaviours involved with VACNT interleaved composite laminates. Mode I and Mode II experimental tests will be performed on aerospace grade carbon epoxy laminates, which are interleaved with a selection of VACNTs lengths. To complement these mechanical tests, fractography analysis will be conducted to further develop an understanding of the failure mechanisms present. This will not only validate the behaviour seen by Ni and Wardle [159] (as discussed in section 2.3.1), but also indicate whether primary nanotube characteristics affect the fracture process, as suggested numerically by Blanco *et al.* [96].

A key limitation of all of the CNTs mentioned thus far is their safety risks, especially during transportation and manufacture, prior to the laminate being cured. Carbon nanotubes are very easily ingested into the body, with studies showing carcinogenic tendencies, particularly in the lungs [212]. As a result, the nanotube manufacturing processes must take place in environmentally controlled facilities. Such facilities are expensive to implement and maintain, therefore deterring large scale industrial adoption. All of the VACNTs mentioned in this study have been supplied (as Nanostitch^{TM}) by N12 Technologies, Inc., Somerville USA, with the raw nanotubes have been embedded in 8552 resin film. This allows for easier and safer handling during manufacture.

In order to determine the contribution that the additional resin has on the interlaminar fracture toughness relative to the VACNTs, a secondary pure resin film interleaf baseline will also be tested in Mode I and Mode II conditions. This resin interleaf will increase the thickness of the interface, which as discussed in section 2.2.3.3, will increase the interlaminar properties of the laminate, particularly under Mode II conditions. The interlaminar property increase is a result of the increase in plastic deformation when the interface thickness exceeds the process zone diameter. As a result, testing laminates with resin interleaves will suggest the contribution of increasing the interface thickness through the VACNTs, relative to other toughening effects. To ensure that the interface thickness is the same, the thicknesses of the resin film and the VACNT interleaves used are equal.

3.2 Experimental Methodology

3.2.1 Materials

The Mode I and Mode II interlaminar fracture toughness specimens were made of HexTow® IM7/HexPly® 8552 prepreg (Hexcel Composites, Duxford, U.K.). Each were laid up by hand and autoclaved using the monolithic cure cycle stated in the product data sheet [3]. Unmodified, 8552 resin film interleaved, and 8552 resin film with embedded VACNTs interleaved specimens were manufactured. All specimens were manufactured as a plate, with interleaves introduced as a 25

mm wide strip at the centremost ply interface, as shown in Figure 3.1. All interleaves involved an 8552 resin film with nominal thickness of 50 μm. VACNTs came in the form of multi-wall carbon nanotubes (MWCNTs). CNTs were grown through a proprietary continuous chemical vapour deposition (CVD) process [213, 214], with nominal lengths of 7 μm, 11 μm, and 40 μm. These were then embedded into the 8552 resin film surface through a combination of heat and pressure. Table 3.1 shows the nanotube properties as stated by the supplier.

3.2.2 Mode I fracture toughness

3.2.2.1 Mode I laminate fabrication

In order to ascertain the Mode I critical strain energy release rate G_{IC}, the double cantilever beam (DCB) test was selected. DCB specimens consisted of 32 plies ($\approx$ 4 mm thickness), which were cut using a water-cooled diamond saw to 160 mm x 20 mm, as illustrated in Figure 3.2. These dimensions were chosen so as to comply with ASTM-D5528 standards for a unidirectional

Table 3.1: Geometric properties of the VACNTs investigated in this chapter (prior to resin film embedment).

Form *(-)*	**Length** *(μm)*	**Diameter** (nm)	**Areal Density** *(mg/cm^2)*	**Population Density** *($CNTs/cm^2$)*
MWCNTs	7/11/40 ± 4	12	0.03	3.20E+09

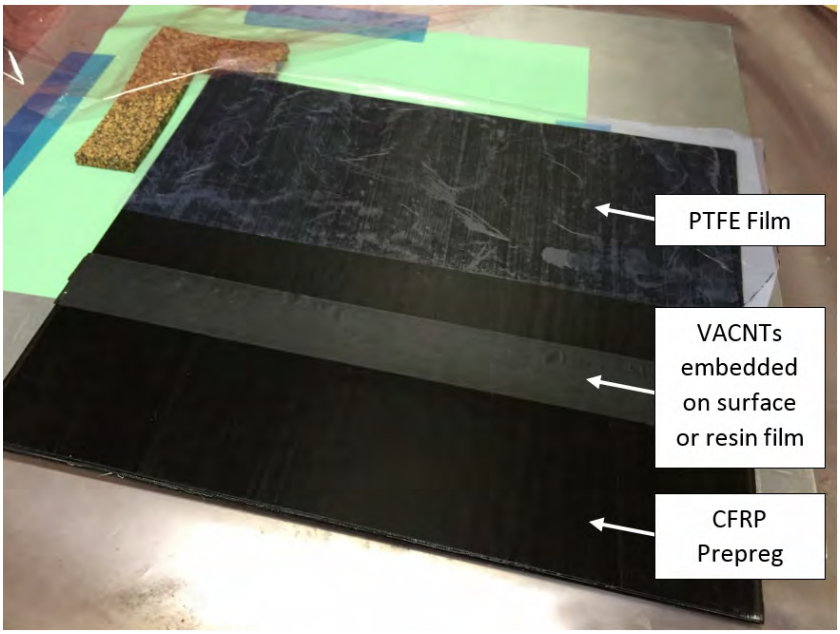

Figure 3.1: Photograph of the laminate mid-plane, interleaved with a strip of VACNTs embedded into 8552 resin film.

fibre reinforced polymer (FRP) [215]. All plies were unidirectional, apart from the two centre-most, which were offset at ±5° in order to minimise fibre bridging. Specimens were selected to be thicker than the minimum required thickness specified by the standards (3 mm), to account for the nano-reinforcement. At the mid-plane of the laminate, a 12 μm thick PTFE film was introduced to initiate a crack. This film was positioned so as to form an initial crack length (a_0) of 50 mm. The VACNT reinforcement was introduced at the mid-plane of the laminate, 25 mm from the PTFE film and spanned a total distance of 25 mm.

The opening load was applied through steel piano hinges, which were adhesively bonded to the composite using 3M DP490 EPX adhesive (cured for 7 days at 20°C). In order to gain the best adhesion properties, the specimens and hinges were grit blasted and cleaned in the regions where the adhesive was applied.

3.2.2.2 Mode I fracture testing

DCB testing was conducted using a calibrated Shimadzu test machine with a 1 kN load cell. Loads were applied at an opening displacement rate of 2 mm/min. All specimens were pre-cracked between 3-5 mm from the polytetrafluoroethylene (PTFE) film, so as to eliminate elevated initiation strain energy release rate values, caused by resin pockets around the thick PTFE film. In order to increase visibility of the crack front, one side of the specimens was painted with a thin

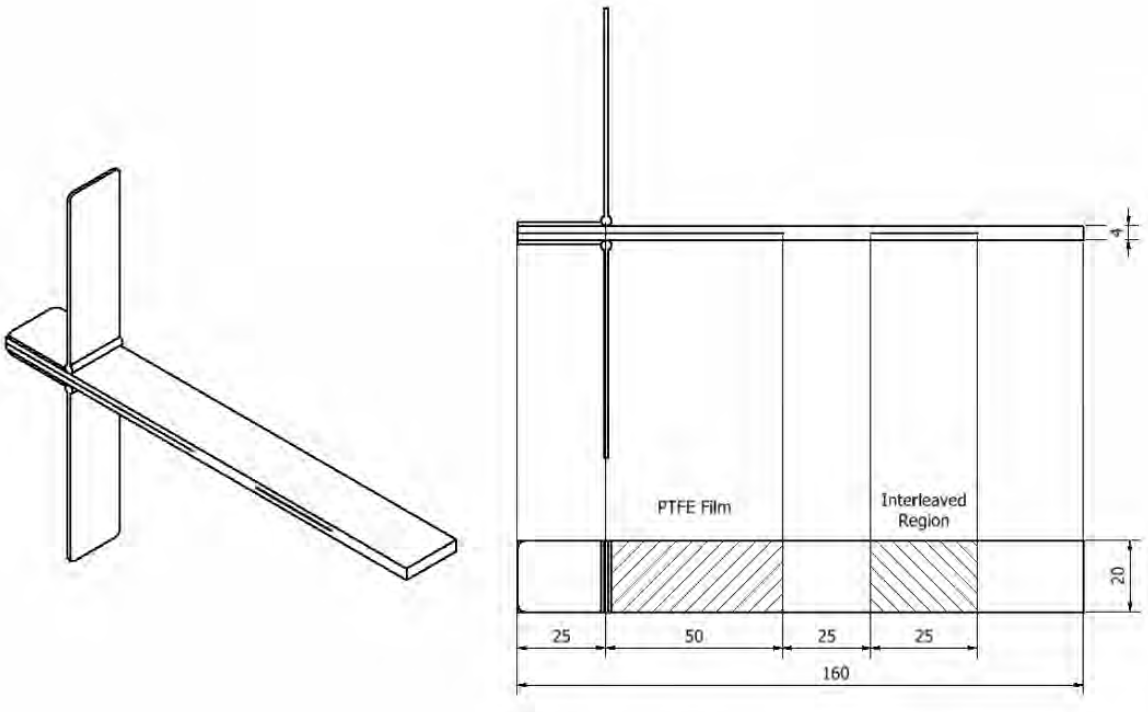

Figure 3.2: Geometric dimensions of the DCB specimens (all dimensions in mm).

layer of white correction fluid and a light source was used to illuminate the surface. A ruler was drawn on to the side surface, at 5 mm increments until a total crack length of 120 mm was reached, to monitor the crack front position with time. Every test was recorded using an iMETRUM video gauge (iMETRUM, Bristol, UK) with crack tracking software activated. Two pieces of black neoprene rubber were adhered to both surfaces of each specimen, with white tracking speckles applied with an iMETRUM stamping kit. The video gauge was synchronised with the Shimadzu test machine to take images at a frequency of 5 Hz, along with the corresponding load and displacement; this test setup is shown in Figure 3.3. A total of five replicates for each interleaf type were tested for fracture toughness assessment and comparison.

In order to convert the mechanical data to a strain energy release rate value, G_{IC}, the modified beam theory (MBT) method was adopted. As described in the ASTM-D5528 standards [215], the Mode I critical strain energy release rate is determined through Equation 3.1 at each crack length, a.

$$G_{IC} = \frac{3P\delta}{2b(a + |\Delta|)} \tag{3.1}$$

where P is the applied load, δ is the crosshead displacement, b is the specimen width, a is the crack length, and Δ is a correction factor.

The correction factor, Δ, accounts for any rotation about the crack front. It is determined experimentally by generating a least squares plot of the cube root of the compliance ($C^{1/3}$), *i.e.* the cube root of the ratio between crosshead displacement and applied load ($(\delta/P)^{1/3}$), as a function of the crack length. This will result in a linear relation in the form of Equation 3.2:

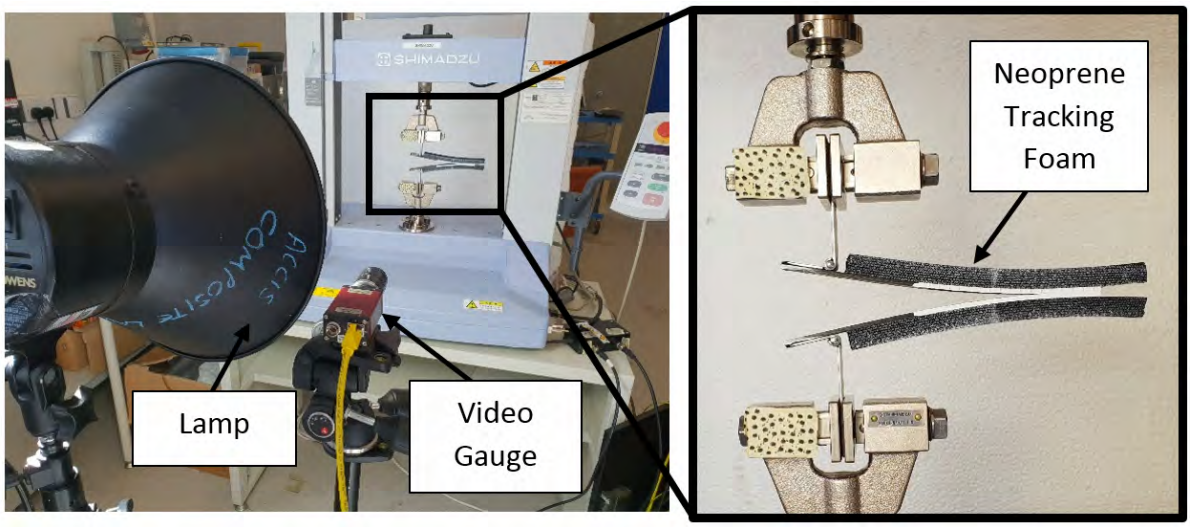

Figure 3.3: Photograph of the DCB experimental setup.

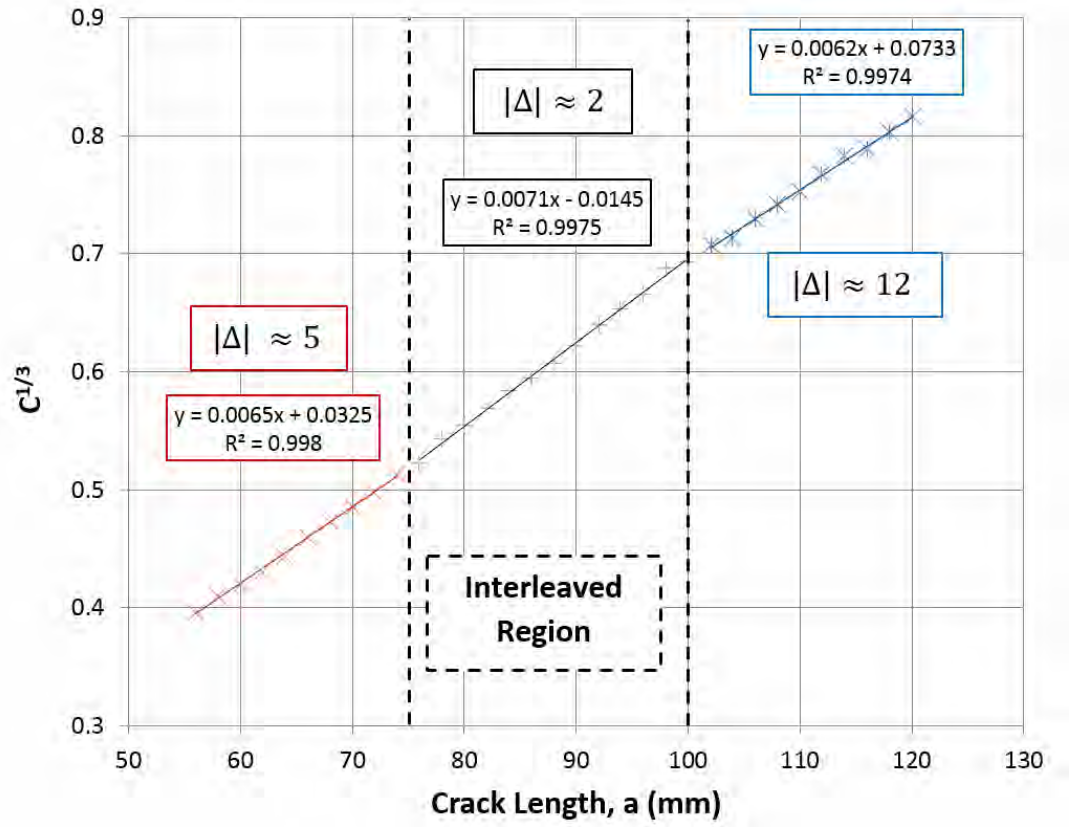

Figure 3.4: Example of a typical compliance calibration plot used to calculate the correction factor, Δ. Interleaved region annotated to highlight how Δ varies along the length of the specimen, justifying discretisation of the strain energy release rate calculation.

$$C^{1/3} = ma + d \tag{3.2}$$

where C is the compliance, a is the crack length, m is the gradient on the linear best-fit line and d is the intercept of the linear best-fit line.

The correction factor, Δ, is defined as the ratio of $-d/m$ and, as shown in Figure 3.4, changes depending on being in the interleaved or non-interleaved regions. Therefore, the compliance calibration method was applied discretely at each of the individual regions along the mid-plane.

3.2.3 Mode II fracture toughness

Multiple methods have been developed for determining the Mode II critical strain energy release rate, G_{IIC}, with the three point end notched flexural (3ENF) test being the most favoured. Such as test commonly results in an unstable crack propagation behaviour [216]. Alternatives such as four point end notched flexural (4ENF) or end loaded split (ELS) tests offer more crack growth stability through specific loading conditions. Consequently, for this study, ELS has been selected as it has been standardised by the International Organization for Standardisation [217].

3.2.3.1 Mode II laminate fabrication

In common with the DCB specimens described previously, ELS laminates consisted of 32-ply unidirectional HexTow® IM7/HexPly® 8552, with the centre-most plies offset by ±5° to minimise fibre bridging along the crack plane. Specimens were cut using a water cooled diamond saw to 20 mm x 200 mm so as to comply with the ISO/DIS 15114 standards [217]. A 12 μm PTFE film was used as the crack initiator and was placed at the mid-plane. This film was positioned to initiate an initial crack length, a_0, of 60 mm, with all interleaves starting another 25 mm away. The geometric dimensions of the ELS specimens can be observed in Figure 3.5.

Shear loads were applied through a piano hinge adhesively bonded using 3M DP490 EPX adhesive (cured for 7 days and 20°C). In order to promote a strong bond, the surfaces of the specimens were grit blasted and cleaned.

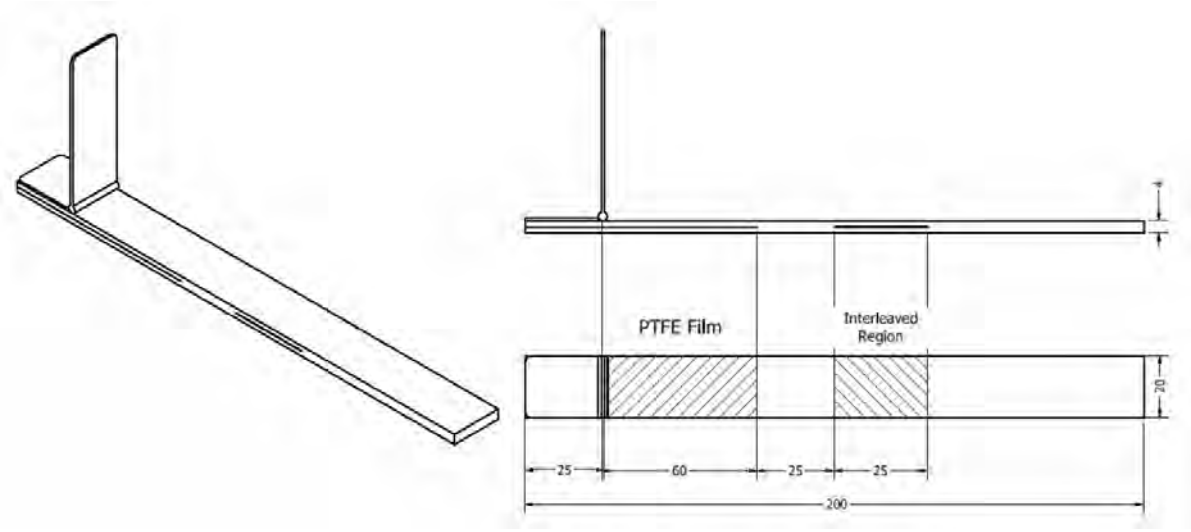

Figure 3.5: Geometric dimensions of the ELS specimens (all dimensions in mm).

3.2.3.2 Mode II fracture testing

A schematic and photograph of the ELS test set-up can be seen in Figure 3.6. Loads were applied through a displacement control of 2 mm/min using a calibrated Instron 8872 testing machine with a 5 kN load cell. Tests were stopped when the crack extended to the clamp.

All specimens were pre-cracked prior to testing in order to eliminate elevated Mode II initiation strain energy release rate (G_{IIC}) values, caused by resin pockets around the thick PTFE film. The ISO 15114 standards [217] suggest that in order to obtain stable crack growth behaviour, the inequality, as shown in Equation 3.3, must be satisfied:

$$a/L \geq 0.55 \tag{3.3}$$

where, as shown in Figure 3.6, a is the crack length and L is the specimen free length. (This inequality was derived by Williams [218]).

Therefore, fixing the gauge length, L, to the end of the interleaf region, *i.e.* a = 110 mm, and following Equation 3.3, a minimum pre-crack length, a_p, of at least 61 mm is required for theoretical stable crack growth. Unfortunately, this pre-crack length was not sufficient, however an iterative process found that an 80 mm pre-crack length achieved repeatable stable crack propagation. During both the pre-cracking and testing procedure, the torque wrench was set to 8 Nm to the ensure there was equal pressure on all specimens.

During testing, it was immediately evident that observing the crack tip is extremely difficult. Therefore, in order to avoid subjective decisions regarding the crack location, the corrected beam theory method was chosen. This method states that the equivalent crack length, a_e, can be calculated through Equation 3.4.

$$a_e = \left[\frac{1}{3}(2bCh^3E_f - (L + \Delta_{clamp})^3\right]^{1/3} \tag{3.4}$$

where a_e is the equivalent crack length, b is the specimen width, C is the compliance, $2h$ is the specimen thickness, E_f is the specimen flexural modulus, L is the specimen free length and Δ_{clamp} is the clamp correction factor.

The flexural modulus E_f and clamp correction factor Δ_{clamp} are determined through the compliance calibration method. This method required a pristine calibration specimen, with a hinge bonded to the opposite end of the crack initiator. The specimen is then loaded sequentially to 200 N when at a specimen free length, L, of 110 mm - 85 mm, decreasing in 5 mm increments. For each value of L, the corresponding compliance C was plotted. When the cube root of the compliance is taken, a linear relationship can be described in the format shown in Equation 3.5.

$$C^{1/3} = nL + e \tag{3.5}$$

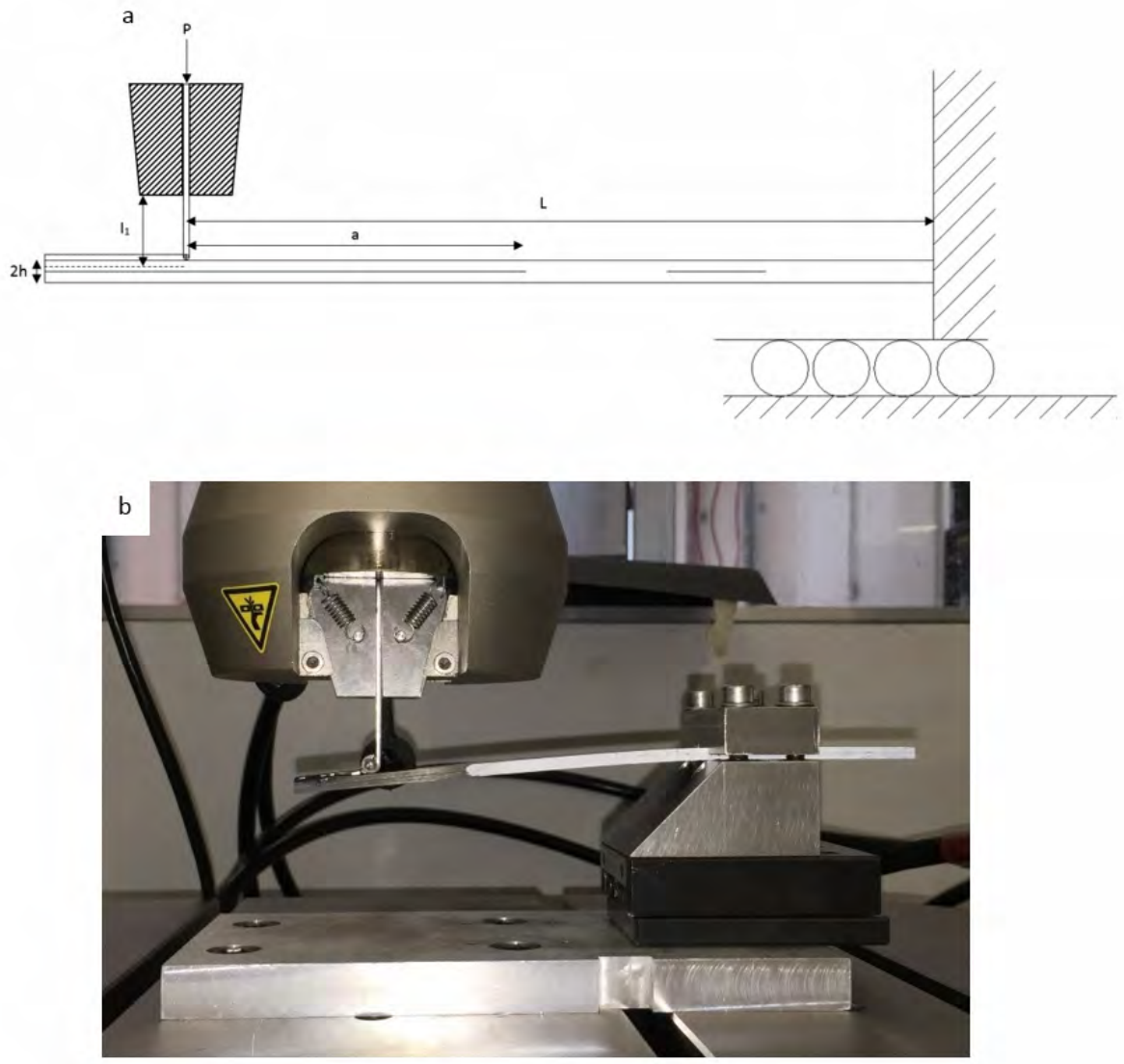

Figure 3.6: (a) Schematic of the ELS experimental configuration and (b) a photograph of the ELS experimental setup.

where C is the compliance, L is the specimen free length, n is the gradient and e is a constant, equivalent to the vertical axis intercept of the best-fit linear relationship.

The flexural modulus E_f can be deduced from the gradient n, as can be seen in Equation 3.6, while the clamping correction factor Δ_{clamp} is defined as the ratio of $-e/n$.

$$E_f = \frac{1}{2b(hn)^3} \tag{3.6}$$

It should be noted that due to the sparse number of calibration points along the specimen, the clamping correction factor Δ_{clamp} was assumed to be constant throughout. Although, the

Mode I analysis has shown that this will not be the case, Equation 3.4 shows that the Δ_{clamp} is dominated by the free length L. Furthermore, owing to the orientation of the VACNTs, the difference in flexural modulus caused from the nanotubes will be lesser when under a shear loading condition rather than an opening load.

As shown in Equation 3.7, the Mode II critical strain energy release rate, G_{IIC}, can be determined once these values have been established.

$$G_{IIC} = \frac{9P^2a_e^2}{4b^2h^3E_f} \tag{3.7}$$

This equation was derived with the assumption that the loads are applied directly at the beam centroid, however in reality, the gripping clamps are located a distance I_1 away from this point. To account for this, the following correction factors must be applied. These were suggested by Williams [218] and are stated in Equations 3.8 and 3.9.

$$\theta_1 = \frac{3\left[15 + 50(\frac{a}{L})^2 + 63(\frac{a}{L})^4\right]}{20\left[1 + 3(\frac{a}{L})^3\right]} \tag{3.8}$$

$$\theta_2 = -3\left(\frac{L}{a}\right)\frac{1 + 3(\frac{a}{L})^2}{1 + 3(\frac{a}{L})^3} \tag{3.9}$$

where θ_1 and θ_2 are the loading position correction factors, accounting for large displacement and hinge effects.

This enables a corrected Mode II critical strain energy release rate, $G_{IIC(Corrected)}$, to be determined, as seen in Equation 3.10.

$$G_{IIC(Corrected)} = G_{IIC}\left[1 - \theta_1(\frac{\delta}{L})^2 - \theta_2(\frac{\delta I_1}{L^2})\right] \tag{3.10}$$

where δ is the crosshead displacement, and I_1 is the offset distance between the loading application at the clamps and the mid-plane of the specimen beam. All of the G_{IIC} values stated in the remainder of this research are the corrected values.

Overall, a total of five replicants were tested for each configuration, as well as one calibration specimen.

3.2.4 Fractography

The aim of fractography analysis in this study was to *(i)* determine whether the VACNTs engage with the fibres and remain vertical post cure and *(ii)* understand how the VACNTs affect the fracture mechanisms when embedded in a composite material. For all VACNT interleaved specimens, scanning electron microscopy (SEM) was performed, while the unmodified baseline and specimens containing resin film interleaves were analysed through optical microscopy alone.

Both pristine and fractured specimens were cut using a water-cooled diamond saw. All fractured specimen configurations mentioned in this chapter were imaged from the three views outlined in Figure 3.7. Please note, 'surface view' corresponds to the internal fractured surface. Pristine images were captured predominantly from 'transverse view' as this was found to show the fibre-nanotube engagement the most clearly.

Before imaging was conducted, specimens were ground and polished to a fidelity of at least one micron. Both the unmodified and 8552 film interleaved specimens containing interleaves were viewed using a Zeiss Axio Image 2 microscope at magnification levels of x50 to x500. The VACNT interleaved specimens were viewed using a Verios^{TM} XHR SEM (FEI, Oregon, USA) at magnification levels of x75 to x25000 and a voltage acceleration of 500V.

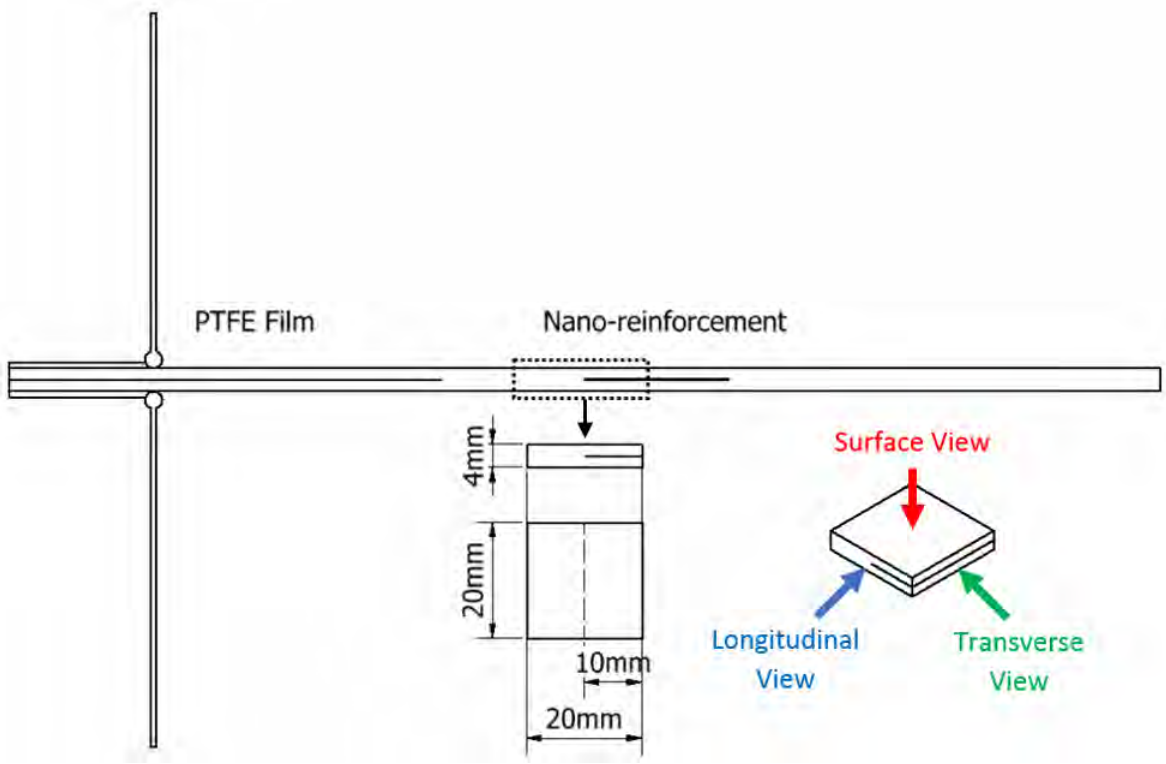

Figure 3.7: Schematic of a SEM specimen cut from a DCB specimen with definitions of the three views analysed in this research: longitudinal, transverse, and surface.

3.3 Results and Discussion

3.3.1 Microscopy: nanotube-fibre engagement

A selection of optical microscope and SEM images taken of pristine specimens containing 40 μm VACNTs are shown in Figure 3.8(a-c). It is evident from the images that the CNTs do not engage with the fibres throughout the laminate. Instead, there are a number of 'resin pockets' *i.e.* resin-rich areas, as annotated in Figure 3.8a, which provides an opportunity for cracks to by-pass the VACNTs. Furthermore, SEM images show asymmetry between the nanotube-fibre interfaces as seen in Figure 3.8b, with one nanotube-fibre interface more resin rich than the other. This is intrinsic to the manufacturing method, involving embedding VACNTs into the surface of the resin film and thereby creating an asymmetric film interleaf.

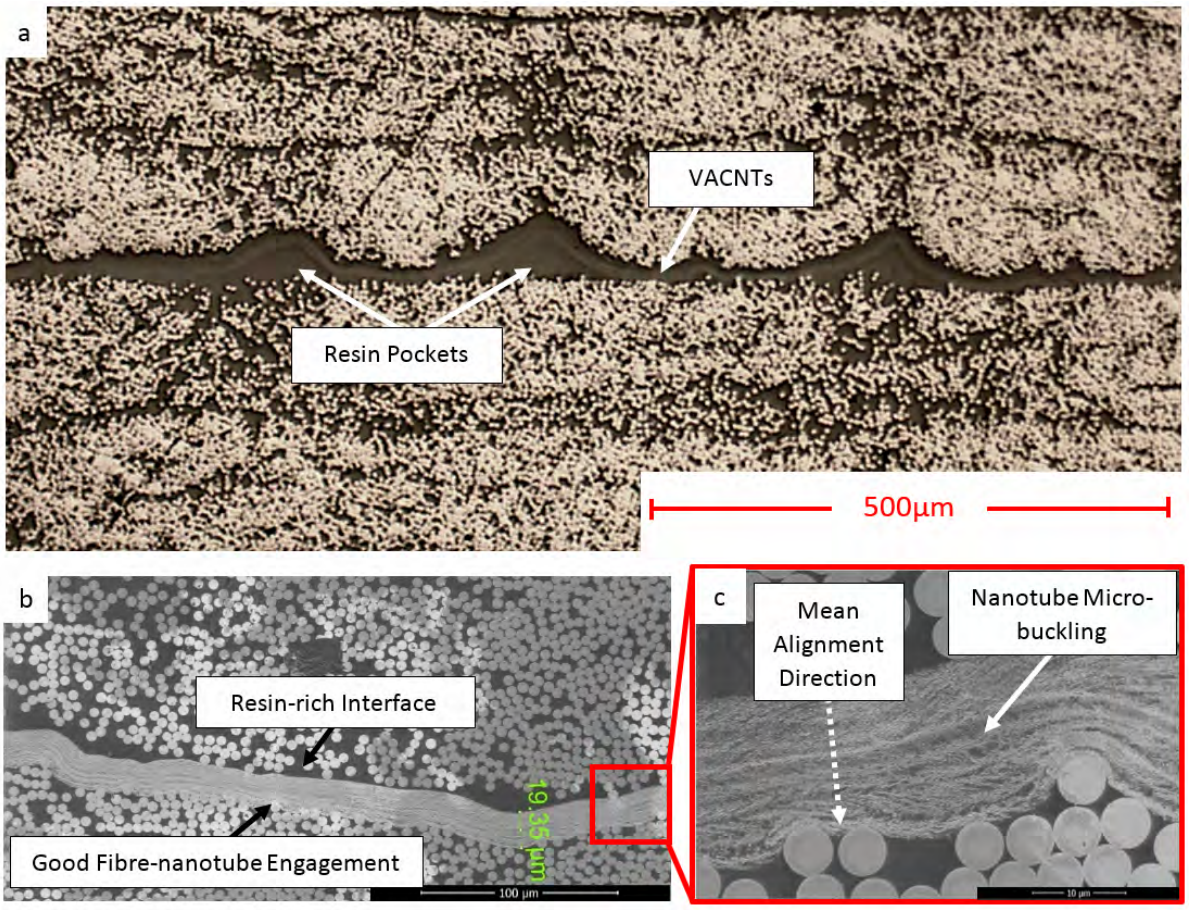

Figure 3.8: (a) Optical microscope image of resin pocket formations after cure, (b) SEM image showing asymmetry in nanotube-fibre engagement, and (c) SEM image of nanotube alignment direction and evidence of VACNT micro-buckling.

As a result, modification of the curing conditions, *e.g.* longer dwell, higher pressures, *etc.*, may be required to optimise the engagement process of the nanotubes with the carbon fibres through allowing greater levels of resin bleed. Otherwise, micro-cracking of the resin rich interface between the fibres and nanotubes may lead to a premature source of failure.

Figure 3.8c shows that the CNTs have a consistent alignment direction, although with evidence of nanotube micro-buckling. Such a behaviour has been also seen by Cao *et al.* [219], when placing nanotubes forests under cyclic compression. Overall, nanotube micro-buckling will lower the effective length of the nanotubes (> 50% in this case) and hence lower the available filler pull-out length. As reported by Rafiee *et al.* [95] and Blanco *et al.* [96], this will theoretically limit their energy dissipation capabilities.

The shorter nanotube length films (7 μm and 11 μm) did not appear to suffer from micro-buckling during cure, with their lengths remaining uniform throughout the panel. However, owing to their lower inertial properties relative to the longer nanotubes, there was a greater amount of film waviness within the resin rich regions, as seen in Figure 3.9.

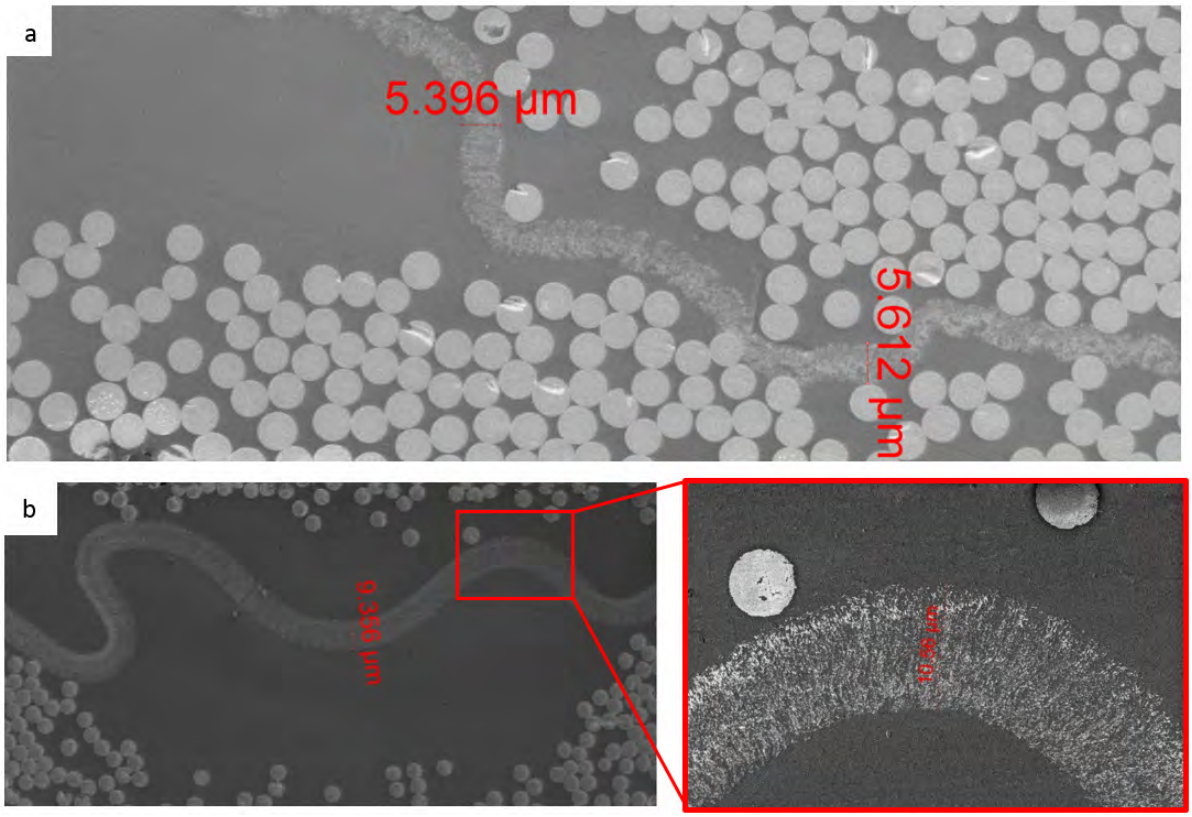

Figure 3.9: SEM images of (a) a pristine 7 μm VACNT interleaved interface surrounded by a resin rich region and (b) a pristine 11 μm VACNT interleaved interface surrounded by a resin rich region.

3.3.2 Mode I fracture toughness

3.3.2.1 Mode I fracture testing

A typical DCB load *versus* displacement plot for the baseline and interleaved specimens is shown in Figure 3.10. The position where the load diverges away from the baseline corresponds to the introduction of the VACNT interleaf. After this point, extra work must be done to propagate the crack. Apart from 2 out of 18 VACNT interleaved specimens, all samples showed stable propagation until the end of the interleaved region, where a large load drop repeatably occurred. Loads then slowly recovered to that of the baseline.

The average Mode I critical strain energy release rate, G_{IC}, recorded for each interleaved DCB specimen was compared against the unmodified baseline composite for the same crack lengths (this is shown in Figure 3.11). Prior to the interleaved region, all configurations measured a similar interlaminar fracture toughness, with initiation values at 210 J/m^2. This is comparable to multiple literature reports characterising HexTow® IM7/HexPly® 8552 [220–222]. Baseline in-

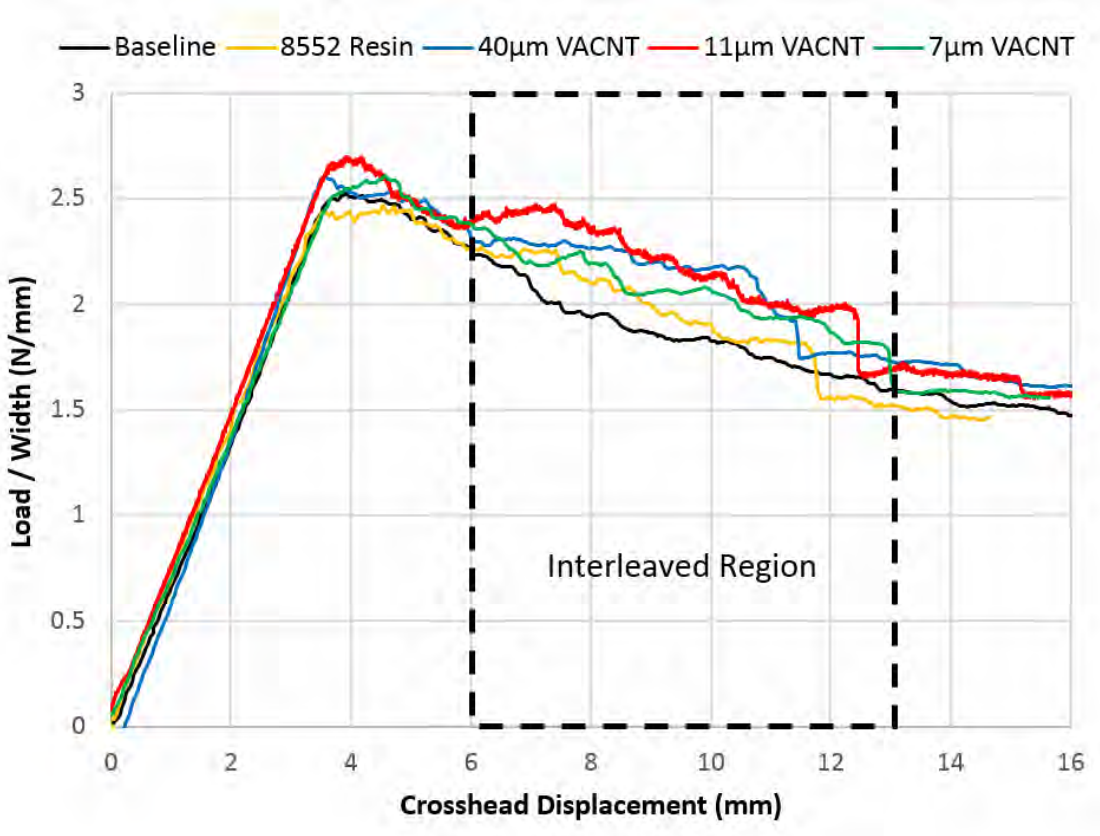

Figure 3.10: A typical DCB load *versus* displacement plot for an unmodified baseline IM7/8552, 8552 film interleaved IM7/8552, and vertically aligned carbon nanotubes interleaved IM7/8552 with a range of nanotube lengths.

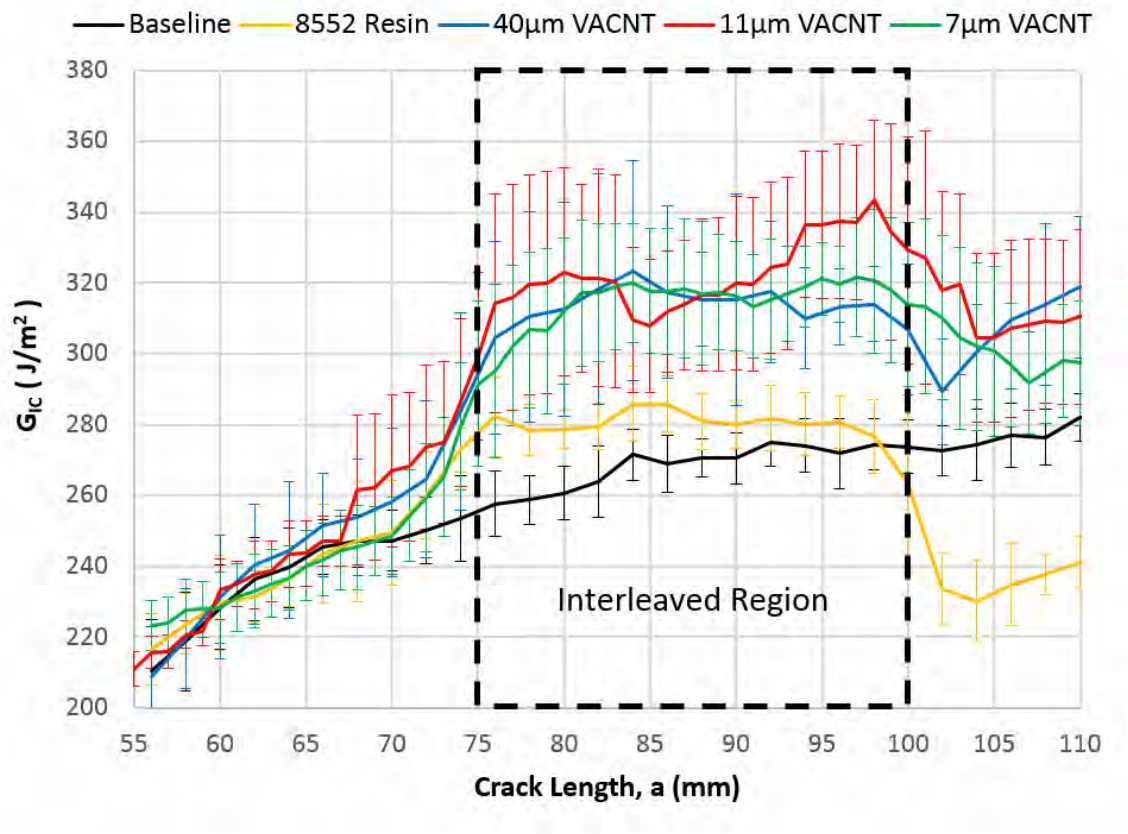

Figure 3.11: R-Curve for the Mode I interlaminar fracture toughness of an unmodified baseline IM7/8552, 8552 interleaved IM7/8552, and vertically aligned carbon nanotubes interleaved IM7/8552 with a range of nanotube lengths. Error bars signify ± one standard deviation away from the mean.

terlaminar fracture toughness values then began to rise steadily, a common behaviour attributed to fibre bridging [136]. At a crack length of approximately 85 mm, the propagated strain energy release rate, G_{Iprop}, reached a plateau of 275 J/m^2.

As the crack propagated through the interleaved region, the strain energy release rate of all interleaved specimens increased relative to the unmodified baseline composite. All five configurations were compared by calculating the area underneath the R-curve within the interleaved region, to yield the propagating strain energy release rate. Overall, the resin film interleaves were found to increase the Mode I propagation fracture toughness by 4.7% relative to the unmodified baseline composite, while the VACNT interleaved specimens all showed similar toughness gains at approximately 17 - 20%. The low enhancement from the resin film interleaf supports the conclusions by Hojo *et al.*, i.e. increasing the interface thickness does not significantly increase the Mode I fracture toughness. Therefore, it is clear that further fracture mechanisms, other than simply separating the plies, are present for the VACNT interleaved specimens, which are contributing to the increased Mode I fracture toughness.

The 8552-resin film interleaf measured a consistent interlaminar fracture toughness with little scatter between specimens. On the other hand, the crack growth through the VACNT interleaves were much less repeatable, with toughness values deviating between specimens by around ±10%. The reasoning for this will be explained through fractography analysis.

3.3.2.2 Mode I fractography

Initial inspections of the fractured specimens were captured through a combination of optical microscope and scanning electron microscopy (SEM). Figure 3.12a and Figure 3.12b show the fractured transverse view for the baseline and resin film interleaved DCB specimens respectively; both show predominately interlaminar failure across the specimen. The toughness enhancement

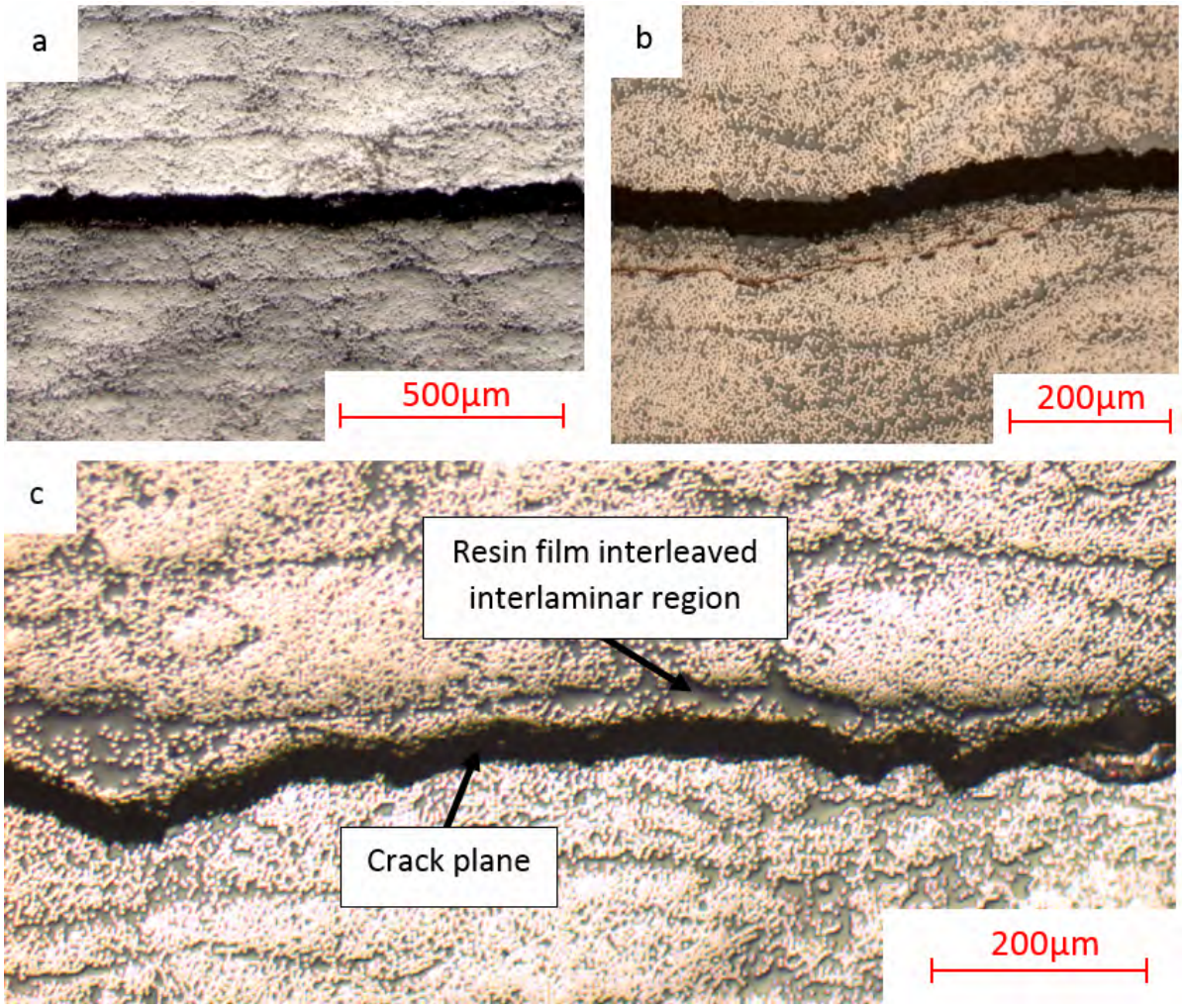

Figure 3.12: Transverse views of (a) typical interlaminar fracture for the baseline DCB specimens, (b) typical interlaminar fracture of the 8552 resin film interleaved DCB specimens and (c) evidence of intralaminar behaviour for the 8552 resin film interleaved DCB specimens.

measured for the resin interleaf is therefore attributed to the increased interlaminar thickness, which as shown by Masters and Sela *et al.* [132, 134], increases the fracture toughness by allowing greater amounts of matrix deformation. Additionally, owing to the low viscosity of the 8552 resin during cure, the excess resin bled into its surrounding plies, resulting in uneven interlaminar thicknesses. This not only resulted in the crack path propagating less uniformly, but also introduced some intralaminar failure, as seen in Figure 3.12c. The added complexity to the crack path is an additional reason for the increase in Mode I interlaminar fracture toughness.

Introducing VACNTs at the interlaminar region resulted in a predominately intralaminar delamination fracture mode, as seen in Figure 3.13. Literature investigations of the intralaminar properties of HexTow® IM7/HexPly® 8552 have measured a toughness of between 10 – 20% higher than the interlaminar value [134, 219], which is consistent with the fracture toughness plotted in Figure 3.11. The intralaminar fracture behaviour also agrees with the data reported by Ni and Wardle [159], which showed that the VACNTs cause the crack to bifurcate into the intralaminar region. However, while their work on AS4/8552 showed a reduction in Mode I fracture toughness, this study suggests an increase, equivalent to the difference between the interlaminar and intralaminar fracture toughness of the host laminate. This suggests that by reinforcing the interlaminar region with VACNTs, the localised interlaminar fracture toughness exceeds that of the intralaminar toughness and the crack bifurcates into the, now weaker, intralaminar region; this process can be observed in Figure 3.14.

Despite the majority of the fractured VACNT interleaved DCB specimens showing intralaminar delamination, some nanotube rupture was also observed, as shown in Figure 3.15. This additional fracture mechanism occurred when the crack transitioned between adjacent plies (see Figure 3.15b) and will locally increase the fracture toughness of the CFRP laminate. However, owing to its infrequently observed occurrence in the tested specimens, nanotube rupture will lead to greater levels of variability between sample results. No evidence of other interlaminar fracture mechanisms, *e.g.* nanotube pull-out, were observed in any of the specimens.

3.3.3 Mode II fracture toughness

3.3.3.1 Mode II fracture testing

A typical ELS load *versus* displacement plot for the unmodified baseline and interleaved specimens is shown in Figure 3.16. The majority of specimens were found to fracture in a stable manner throughout the test. It can be seen that as the crack enters the interleaved region, the load diverges away from that of the unmodified baseline, only returning back when the crack reaches the clamp.

The average critical strain energy release rate, G_{IIC}, of each interleaved ELS specimen was compared against the unmodified baseline, as shown in Figure 3.17. After pre-cracking, all configurations showed similar fracture toughness properties, with an initiation value at 530 ± 20 J/m^2. At a crack length of approximately 87 mm, the propagated strain energy release rate,

G_{IIprop}, reached a plateau at 600 ± 20 J/m^2. Other studies characterising HexTow® IM7/HexPly® 8552 estimated a Mode II critical strain energy release rate at initiation of between 550 and 1650 J/m^2 [222–225]. Although these values were measured through a variety of testing methods, such as ENF, 4ENF, and ELS, the large range indicates a great deal of uncertainty with this material property.

It can be seen in Figure 3.17 that as the crack reached the interleaved region, *i.e.* when a

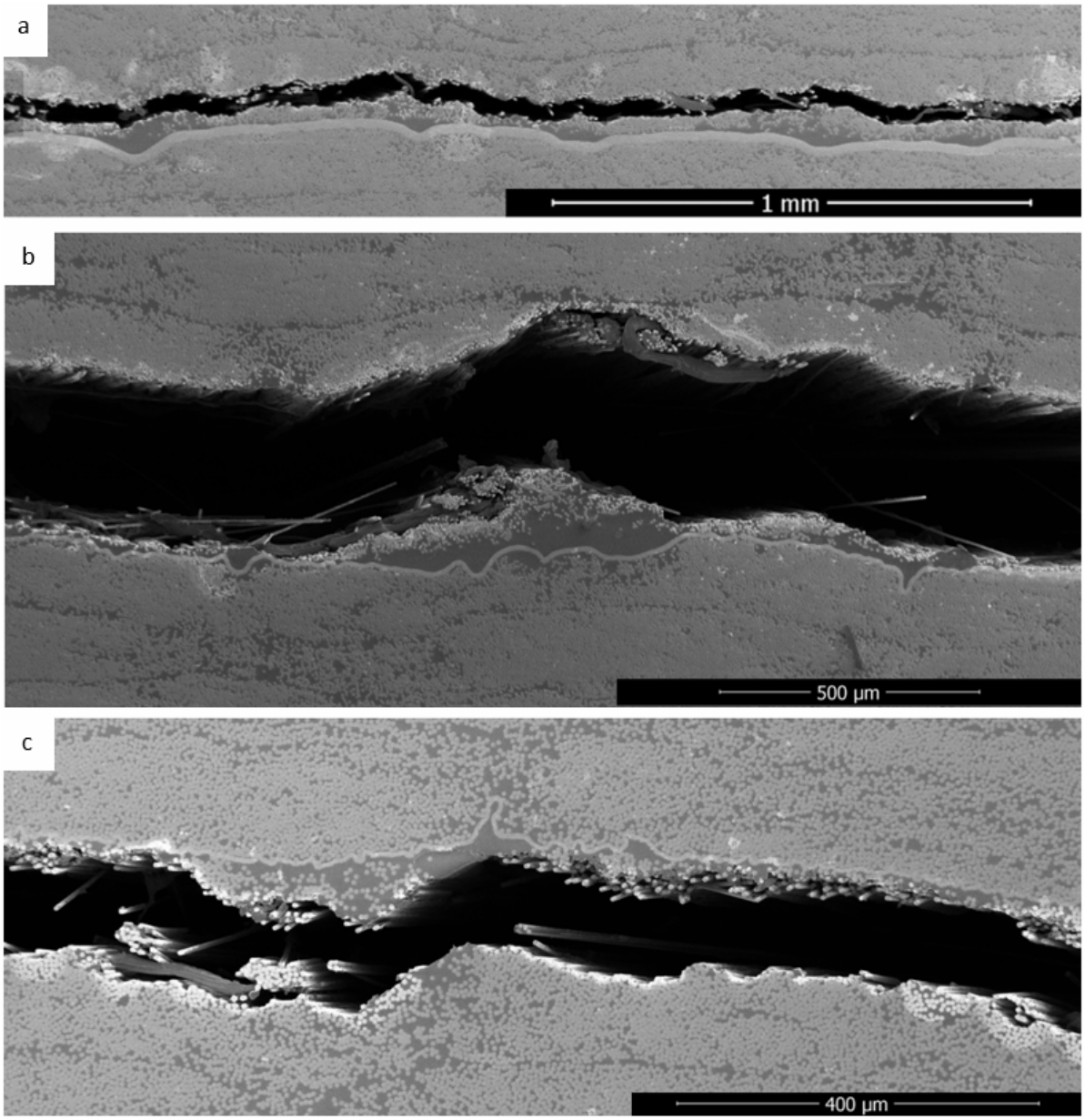

Figure 3.13: Transverse views of typical intralaminar fracture for (a) 40 μm, (b) 11 μm, and (c) 7 μm VACNT interleaved DCB specimens.

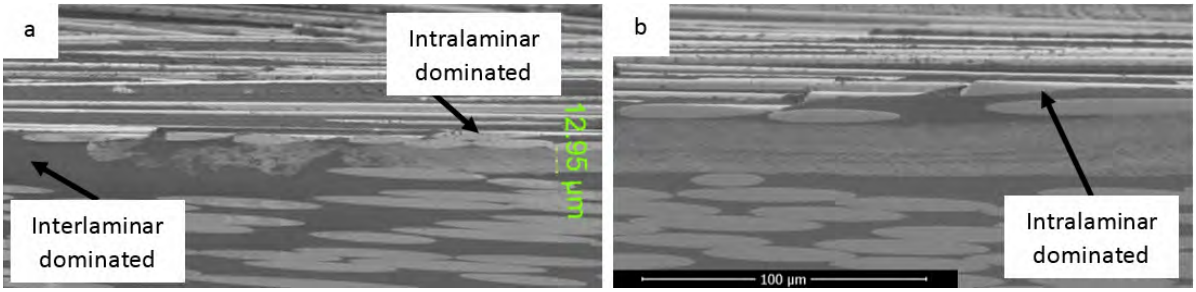

Figure 3.14: (a) Longitudinal view of the location of VACNT introduction where fracture transitions from an interlaminar to an intralaminar dominated failure mode; (b) Longitudinal intralaminar delamination within the interleaved region of the 40 μm VACNT interleaved DCB laminate.

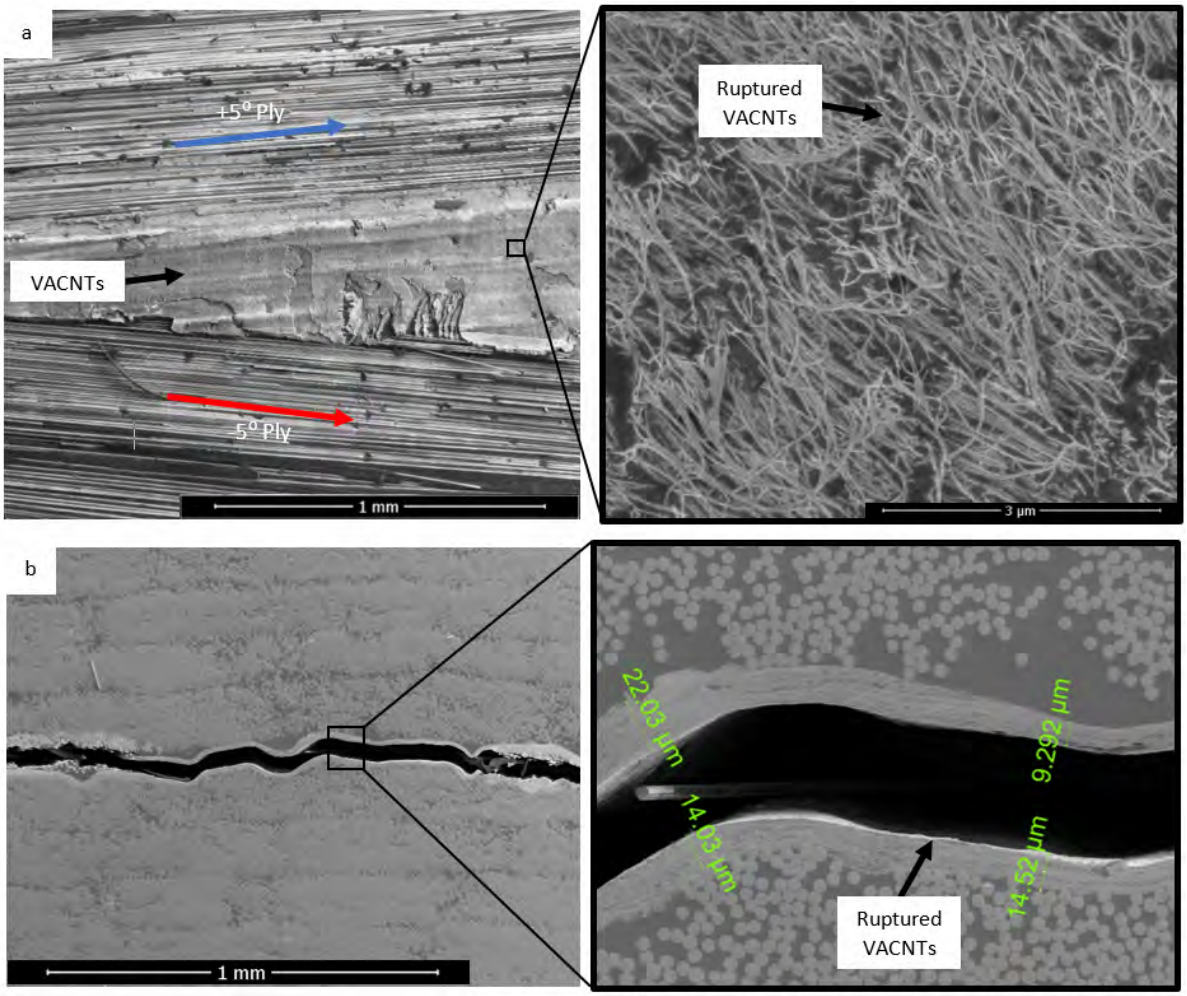

Figure 3.15: (a) Surface view and (b) corresponding transverse view of the 40 μm VACNT interleaved DCB specimen showing nanotube rupture.

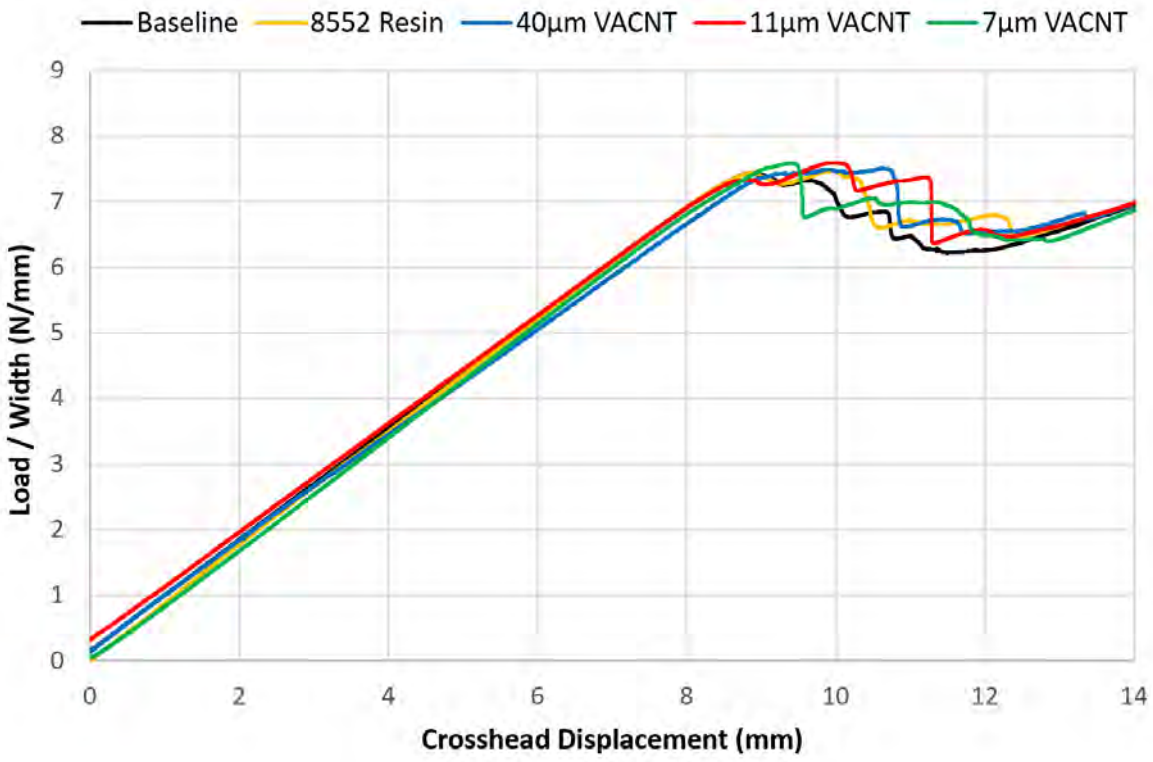

Figure 3.16: A typical ELS load *versus* displacement plot for the unmodified baseline, 8552 film interleaved and vertically aligned carbon nanotubes (VACNTs) interleaved with a variety of nanotube lengths within a host IM7/8552 laminate.

is 85 mm, the strain energy release rate of all interleaved specimens increased with respect to the baseline. Regardless of the interleave type, a similar enhancement in the interlaminar fracture toughness was measured. Overall, a propagation strain energy release rate, G_{IIprop}, of approximately 650 ± 10 J/m^2 was measured. This corresponds to an 8.3% increase in Mode II interlaminar fracture toughness relative to the unmodified baseline. Only a marginal difference was seen between the 8552-resin interleaf and VACNT interleaves, however, the resin interleaf was noticeably more stable and repeatable than the VACNT alternatives.

3.3.3.2 Mode II fractography

In common with the Mode I investigation, fractured specimen images were captured through a combination of optical microscope and scanning electron microscopy (SEM).

Figure 3.18a and Figure 3.18b show the typical interlaminar and intralaminar delamination fracture mode for the baseline and resin film interleaved ELS specimens respectively. Unlike in Mode I, the Mode II interlaminar fracture toughness enhancements of the resin film interleaved specimens are attributed to intralaminar mechanisms, such as fibre debonding and the crack

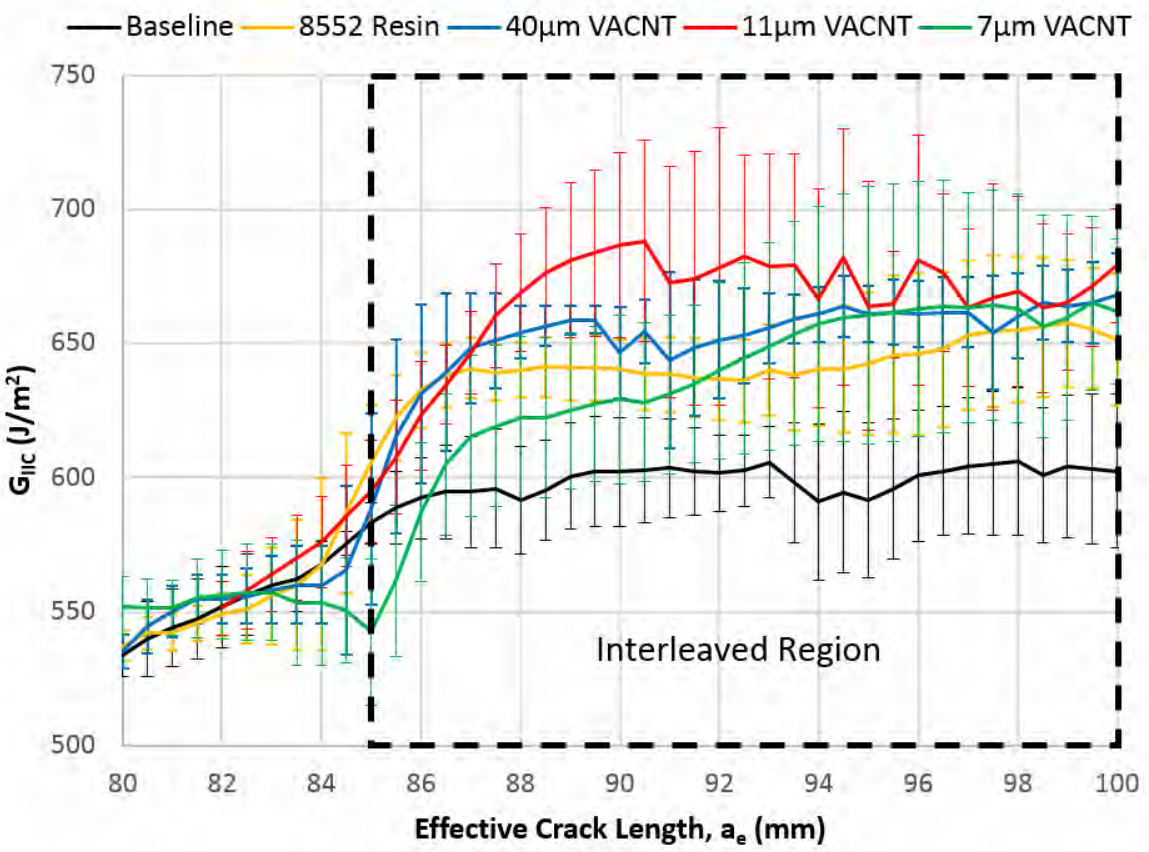

Figure 3.17: R-curve for the Mode II interlaminar fracture toughness of an unmodified baseline, 8552 film interleaved and vertically aligned carbon nanotube (VACNT) interleaved specimen with a variety of nanotube lengths within a host IM7/8552 laminate. Error bars signify ± one standard deviation away from the mean.

following a more tortuous path. This suggests that the process zone still exceeds the dimension of the thicker interface, as formed from the resin interleaf, and thus the crack cannot be contained at the interface when it enters the interleave region.

Within the VACNT interleaved specimens, nanotube pull-out was observed, as shown in Figure 3.19, however this was uncommon. Instead, failure was dominated through fibre pull-out, with an abundance of bare fibres and clean resin channels, surrounded by cusps. The clean appearance of the fibre surface, along with channels left by debonded fibres, suggests that the crack progressed across the fibre-matrix interface, as shown by Todo and Jar [226].

The transverse views of all VACNTs interleave configurations are shown in Figure 3.20. All three nanotube lengths showed similar behaviour to that exhibited by the resin film interleaf, namely, intralaminar delamination. Interestingly, these intralaminar cracks followed the topography of the nanotubes and this is particularly evident when observing around the resin

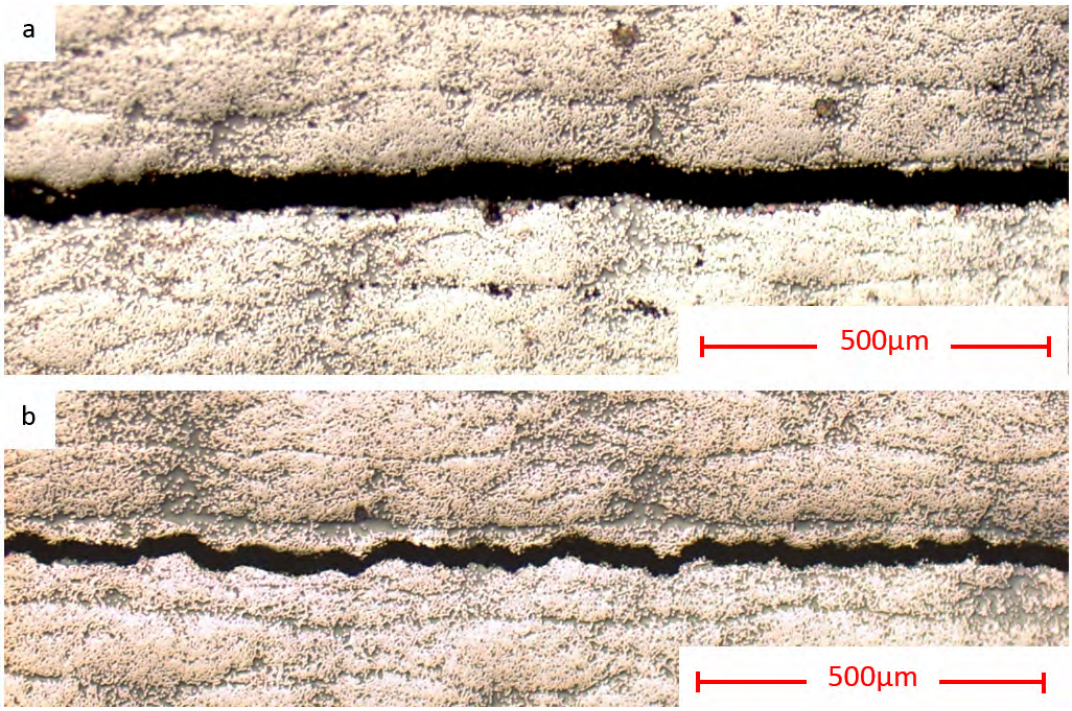

Figure 3.18: Transverse view of (a) typical interlaminar fracture for the unmodified baseline ELS specimens and (b) typical intralaminar fracture of the 8552 resin film interleaved ELS specimens.

pockets, which as mentioned earlier, resulted in non-uniform nanotube distributions along the specimen width. This observation suggests that the nanotubes increase the local stiffness in the interlaminar region, which in turn, increases the local strength. This stiffness enhancement diminishes with distance away from the nanotubes, and therefore cracks propagate at an offset distance from the reinforcement. The offset distance does not appear to be dependent on nanotube length and is similar to that observed in specimens containing the 8552-resin interleaf. Any fracture toughness increases from the VACNTs relative to the 8552-resin film, appears to be sourced from the infrequent nanotube pull-out regions and the more tortuous fracture paths, which results in a greater surface area, and therefore work to propagate the crack.

The insensitivity between interleaf configuration and interlaminar fracture toughness indicates that another, more dominant, effect is occurring as specimens fracture. Figure 3.21 shows an image of the 40 μm VACNT fracture path at a higher magnification, from which it can be seen that the crack follows the nanotube film topologies through breaking the fibre-matrix interfaces. Thus, the implication is that, in common with the Mode I study, the VACNT reinforcement capability appears to be limited by the fibre-matrix interfacial properties of the host laminate. A reasonable explanation for the 8% enhancement in G_{IIprop} mentioned earlier in this chapter is that this is attributed to the Mode II intralaminar fracture toughness of HexTow® IM7/HexPly® 8552. This value is dominated by the fibre-matrix interfacial properties and, to date, has not been reported for this CFRP system.

3.4 Conclusion

The Mode I and Mode II interlaminar fracture toughness of CFRP specimens have been investigated to determine the effects of introducing vertically aligned carbon nanotube (VACNT) interleaves into the interlaminar region. VACNTs with nanotube lengths of 40 μm, 11 μm, and 7 μm were embedded into a resin film, and transferred on to the surface of CFRP prepreg using a combination of heat and pressure. VACNTs interleaves were introduced as a strip located at the mid-plane interface of the laminate. The VACNT interleaved specimens were tested through double cantilever beam (DCB) and end loaded split (ELS) methods and compared to unmodified and resin film interleaved baseline specimens.

After curing, an abundance of resin pockets formed in the interleaved regions, attributed to insufficient resin bleed during cure. These resin rich regions led to waviness in the VACNT films, particularly for the shorter nanotube lengths, resulting in poor engagement between the nanotubes and the carbon fibres. The longer nanotubes suffered less with film waviness, due to their greater inertial properties, however micro-buckling was evident from the high autoclave pressures. A consequence of this was a reduction in the effective nanotube length of approximately 50%.

On average, the Mode I interlaminar fracture toughness enhancement was $17-20\%$ relative to the unmodified baseline equivalent and $12-15\%$ relative to the specimens containing resin film

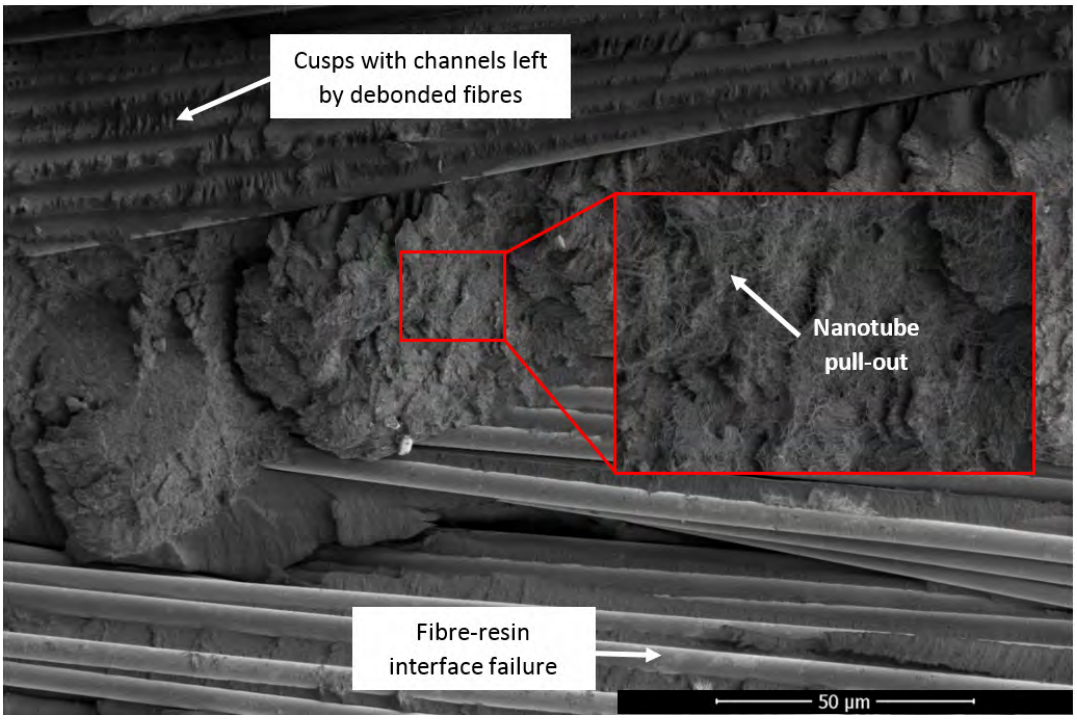

Figure 3.19: Surface view of fractured 40μm VACNT interleaved ELS specimen.

interleaves. Mode II interlaminar fracture toughness enhancements were 8 – 10% relative to the unmodified baseline, but no significant difference was measured with respect to the specimens containing resin film interleaves.

Fractography analysis has indicated that Mode I failure is dominated by interlaminar delamination for both the unmodified and resin film baseline specimens, but VACNT interleaved specimens are dominated by intralaminar delamination. Evidence of nanotube rupture was evident, but this was uncommon. Instead, when the crack reached the region containing the VACNT interleaf, the crack bifurcates into the ply and propagates parallel to the VACNTs. Similar behaviours were seen in the Mode II fracture, however, even the resin interleave baselines were found to cause predominately intralaminar delamination.

For both fundamental fracture modes, intralaminar delamination was found to be dominated by the fibre-matrix interfacial properties. Cracks were seen to follow the topology of the

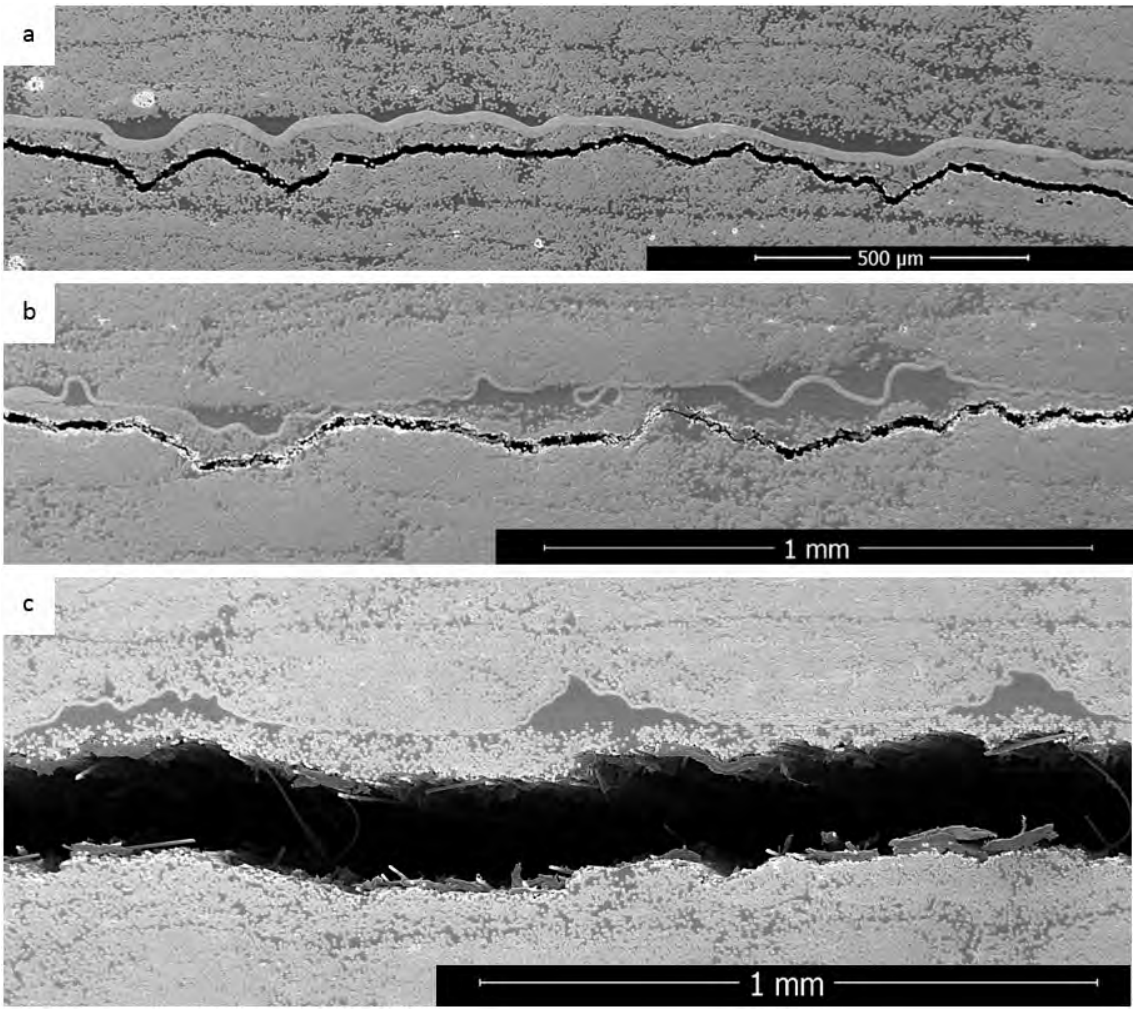

Figure 3.20: Transverse view of a typical intralaminar fracture for VACNT interleaved ELS specimens with (a) 40 μm, (b) 11 μm, and (c) 7 μm nanotube lengths.

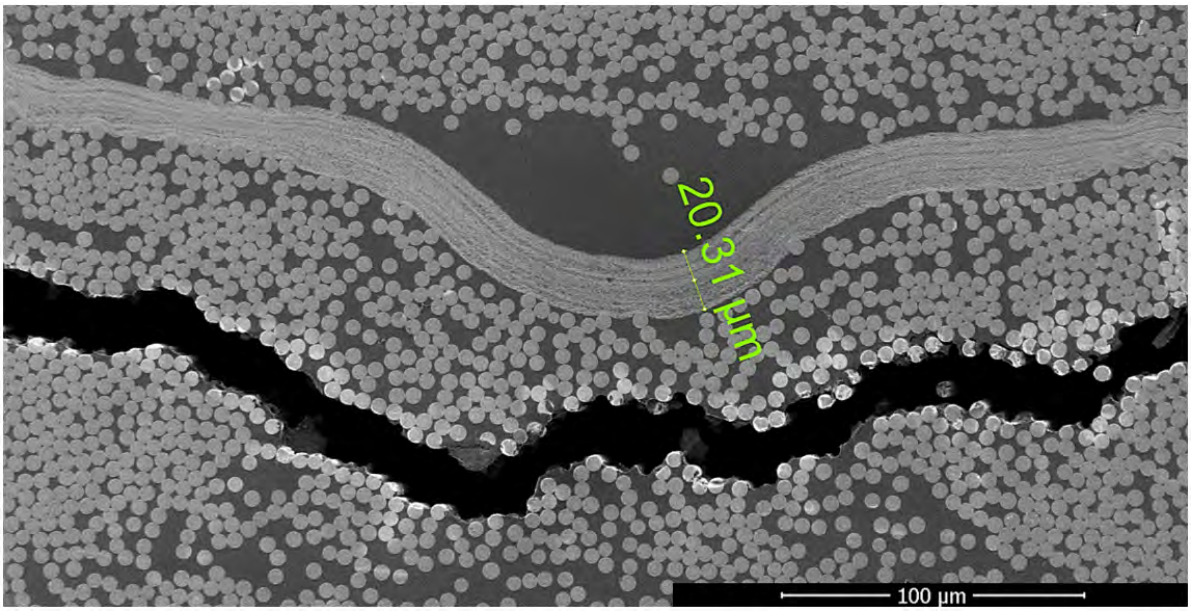

Figure 3.21: Magnified transverse view of 40 μm VACNT interleaved ELS specimen showing fracture through the fibre-matrix interface.

nanotubes, indicating a local stiffness and strength enhancement at the interlaminar region. This enhancement appears to be greater than the fibre-matrix interfacial properties of the host laminate, and as a result, crack propagation through the fibre-matrix interfaces becomes the subsequent mode of failure. All nanotube lengths tested appear to increase the interlaminar fracture toughness enough to result in this new failure mode. These tests are believed to yield the Mode I and Mode II intralaminar fracture toughness properties of HexTow® IM7/HexPly® 8552, which has not previously been reported for this composite system.

Prologue to Chapter 4

During chapter 3 it was concluded that introducing interleaves containing vertically aligned carbon nanotubes (VACNTs) into CFRP specimens resulted in the interlaminar fracture mode undergoing a transition from interlaminar delamination to intralaminar delamination. While the introduction of the interleaves did increase the fracture toughness properties of the composite, the maximum toughness enhancement was limited, with VACNT films of different nanotube lengths measuring the same fracture toughness in both Mode I and Mode II conditions. This limitation was attributed to the fibre-matrix interfacial properties of the host composite.

For all of the interlaminar fracture toughness tests conducted, the layup was uni-directional in order to comply with experimental standards [215, 217]. This methodology allows fibres to nest and bridge between plies, which introduces additional unwanted toughening mechanisms into the fracture toughness measurement. To avoid this, it is common practice to offset the plies immediately adjacent to the fracturing interface. For the tests performed in chapter 3, a $\pm 5^{\circ}$ fibre offset was selected. Although this subtle interface layup resulted in an interlaminar dominated delamination fracture mode within the non-interleaved regions, cracks migrated into the intralaminar region when the interleaves were introduced.

Chapter 4 will focus on understanding how the interlaminar fracture toughness of CFRP laminates, with increasing interfacial offset angles (defined as interface layups), is affected when interleaved with VACNTs. Literature suggests that increasing this angle offset will increase the fracture toughness in Mode II through introducing additional fracture mechanisms. To avoid extreme deviation from the test standards, the maximum angle difference between plies is limited to 30°. Efforts will be concentrated on measuring the toughness enhancement for each layup and the fracture mechanisms involved, commenting on any differences between each specimen configuration.

CHAPTER 4

FABRICATION PROCEDURES FOR IMPROVING FRACTURE TOUGHNESS AND QUALITY OF VACNT INTERLEAVED COMPOSITES

Abstract

This chapter investigates how the fabrication process for VACNT interleaved CFRP prepreg laminates can be modified to augment improvements in the interlaminar fracture toughness. Fibre orientations of the plies adjacent to the fracture plane, termed the interface layup, are modified to discourage intralaminar delamination and further increase the fracture toughness enhancements relative to an unmodified specimen. The examined fibre interface layup offset angles range between 10° and 30°. Increasing the interface layup offset angle is shown to not affect the Mode I interlaminar fracture toughness; however, the Mode II interlaminar fracture toughness increases. The fracture toughness enhancement from interleaving with VACNTs is found to be similar for all interfacial angles tested. Fractography analysis shows that for Mode I and Mode II conditions, the fracture mode undergoes a transition from interlaminar delamination to intralaminar delamination, when the crack reaches the interleaved region. Despite the interface layup changes, enhancements are still limited by the intralaminar fracture properties of the host laminate, dictated by the fibre-matrix interfacial properties rather than the interlaminar properties.

To improve nanotube-fibre engagement and reduce resin rich regions at the interleaved interface, the cure cycle was modified to allow more resin to bleed. The initial dwell was removed to lower the minimum viscosity of the resin. Scanning electron microscope (SEM) images showed superior nanotube-fibre engagement and reduced resin pocket formations for the modified cure cycle. Thermogravimetric analysis (TGA) showed that this increases the fibre volume fraction of the laminate, but not to a significant degree (< 1%).

4.1 Introduction

To measure the fracture toughness improvements arising from these TTR techniques, standardised experimental tests are commonly used on baseline and reinforced specimens. Examples of these tests include: double cantilever beam (DCB) [215], end loaded split (ELS) [217], and end notched flexure (ENF) [216] methods. In the test methodologies, specimen layups are specified as uni-directional, so as to make valid comparisons between composite systems. A uni-directional layup allows fibres to nest between plies, thereby bridging the interlaminar interface and introducing additional toughening mechanisms. As most engineering applications use multi-directional ply layups, *e.g.* quasi-isotropic, nesting does not normally occur, and so standard interlaminar fracture toughness tests are unconservative. To account for this, it is common practice to subtly offset the plies adjacent to the desired crack plane, *e.g.* by $\pm 5°$, to inhibit fibre bridging.

It is well known that delaminations grow preferentially along the direction of the fibres [227]. This has led the author to believe that the redirection and propagation of a crack during an intralaminar delamination fracture mode, will require more energy. Therefore, increasing the ply offset angle is believed to increase the difference between the interlaminar and intralaminar fracture toughness of a composite material, which would increase the maximum achievable fracture toughness enhancement of VACNT interleaved CFRPs.

In this chapter, the dependency between interface layup and interlaminar fracture toughness enhancements of VACNT interleaved Mode I and Mode II specimens will be investigated. Under small angles, it has already been shown that VACNT interleaves transition fracture from interlaminar delamination to intralaminar delamination; this limits the fracture toughness enhancements available. Efforts will be concentrated on the measurable fracture toughness enhancement for each layup and the fracture mechanisms involved, commenting on any differences between the laminate configurations. To prevent crack migration behaviour leading to the interleaved interface being bypassed, the maximum interface layup angle was limited to 30° ($\pm 15°$). Furthermore, in the region containing the interleaf, which has already been shown to be susceptible to intralaminar delamination, the interfaces adjacent to the fracture plane have also been interleaved. This should reduce the chance of crack migration occurring during the tests.

4.2 Methodology

4.2.1 Materials

All composite laminates in this chapter were fabricated from HexTow® IM7/ HexPly® 8552 prepreg and laid up by hand. Each laminate was autoclave cured using the monolithic cure cycle stated in the supplier's product data sheet [3]. To investigate the effect of the fibre orientation of the plies immediately adjacent the fracturing interface (termed interface layup in this chapter)

Table 4.1: Geometric properties of the VACNTs investigated in this chapter (prior to resin film embedment).

Form *(-)*	**Length** *(μm)*	**Diameter** *(nm)*	**Areal Density** *(mg/cm^2)*	**Population Density** *($CNTs/cm^2$)*
MWCNTs	40 ± 4	12	0.03	3.20E+09

on the Mode I and Mode II fracture toughness, two interleaved layups were manufactured: $[0_{15}, \pm 10, 0_{15}]$ and $[0_{15}, \pm 15, 0_{15}]$.

To reduce the chance of cracks migrating towards an adjacent interface, as seen by Laksimi *et al.* [84] [42] and Shi *et al.* [85], VACNTs were interleaved at three interfaces, corresponding to the interfaces with angled plies. It should be highlighted that this is different to the laminates investigated in chapter 3, which had only one interleaved interface. Interleaves were introduced at a crack length, a, of 75 mm and 85 mm for the DCB and ELS specimens, respectively. These can be seen in Figure 4.1.

The VACNT interleaves comprised of the same characteristics as the longest nanotubes described in chapter 3. For clarity, these have been described again in Table 4.1. VACNTs were grown through a proprietary continuous chemical vapour deposition (CVD) process [213, 214], with nominal lengths of 40 μm. VACNTs were then embedded into the surface of a 50 μm thick 8552 resin film using a combination of heat and pressure to produce the interleaved film system.

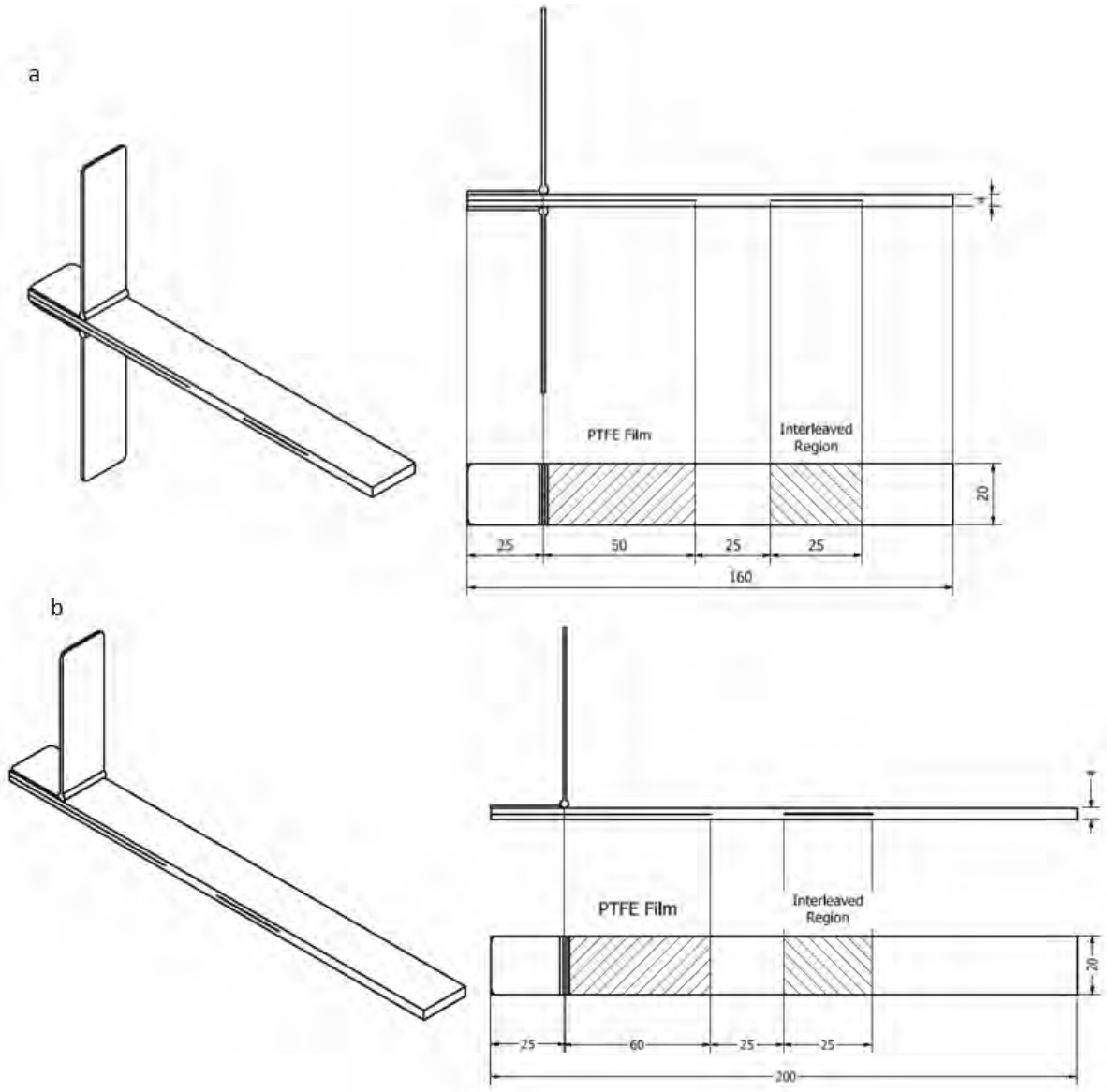

Figure 4.1: Geometric dimensions of (a) the interleaved DCB specimen and (b) the interleaved ELS specimen (all dimensions in mm).

4.2.2 Laminate fabrication and mechanical testing

To complement the work carried out in chapter 3 and to allow direct comparisons, the Mode I and Mode II interlaminar fracture toughness was determined through DCB and ELS tests, respectively. Specimens were fabricated and tested using identical geometric dimensions and testing conditions to that described in Section 3.2. At least three replicate samples were manufactured and tested for each layup described.

4.2.3 Fractography

Once fractured, specimens were cut, ground, and polished to at least 1 μm fidelity. The prepared cross-sectional surfaces were then viewed under a Zeiss Axio Image 2 optical microscope. Images were captured at x10 to x50 magnification. The aim of the fractography analysis was to determine whether altering either the interface layup, or the number of interfaces interleaved, influences the fracture mechanisms relative to that observed in chapter 3. That is, determining whether the crack still propagates in a predominantly intralaminar delamination fracture mode, or whether other toughening mechanisms and fracture modes are present.

4.3 Results and Discussion

4.3.1 Mode I fracture testing

Typical load *versus* displacement plots for DCB specimens with the centre-most plies at $\pm 10^{\circ}$ and $\pm 15^{\circ}$ angle offset are shown in Figure 4.2. Load-displacement curves directly taken from chapter 3 for an unmodified baseline and 40 μm VACNT interleaved DCB specimen are also included for comparison. Both of these earlier tests were performed with a laminate layup of $[0_{15}, \pm 15, 0_{15}]$ and with VACNTs interleaved at the fracture plane interface only.

Analysing Figure 4.2, it can be seen that, prior to the interleaf region, similar loads were measured for all specimens regardless of the interface layup. As the crack propagated into the interleaf region, *i.e.* when the crosshead displacement is approximately 6 mm, all interleaved specimens experienced a load rise, thereby deviating away from that of the unmodified baseline. This rise was similar in magnitude for all interface layups tested.

The corresponding R-curves for the averaged Mode I critical strain energy release rate, G_{IC}, can be seen in Figure 4.3. Overall, the fibre orientation does not appear to influence the critical strain energy release rate of the specimens, with all interface layups showing similar properties. For example, the strain energy release rate required for crack initiation was measured to be approximately 210 J/m^2 for all specimens. This finding supports the conclusion discussed in the review by Andersons and König for Mode I conditions [18]. In this review, it was stated that, "the effect of interface lay-up and delamination growth direction on the Mode I initiation toughness is moderate, if at all present".

Figure 4.3 also shows that as the crack propagates, the strain energy release rate of the baseline gradually rises, as a result of extra fibre bridging effects [136]. For the unmodified baseline specimen, this resulted in the interlaminar fracture toughness plateauing at 275 J/m^2. However, the VACNT interleaved specimens saw a fracture toughness enhancement when the crack entered the interleaved region (when $a > 75$ mm). This enhancement was similar for all specimen configurations tested regardless of their interface layup or the number of interfaces interleaved. When the crack was in the middle of the interleaved region, *i.e.* when $a > 85$ mm, all

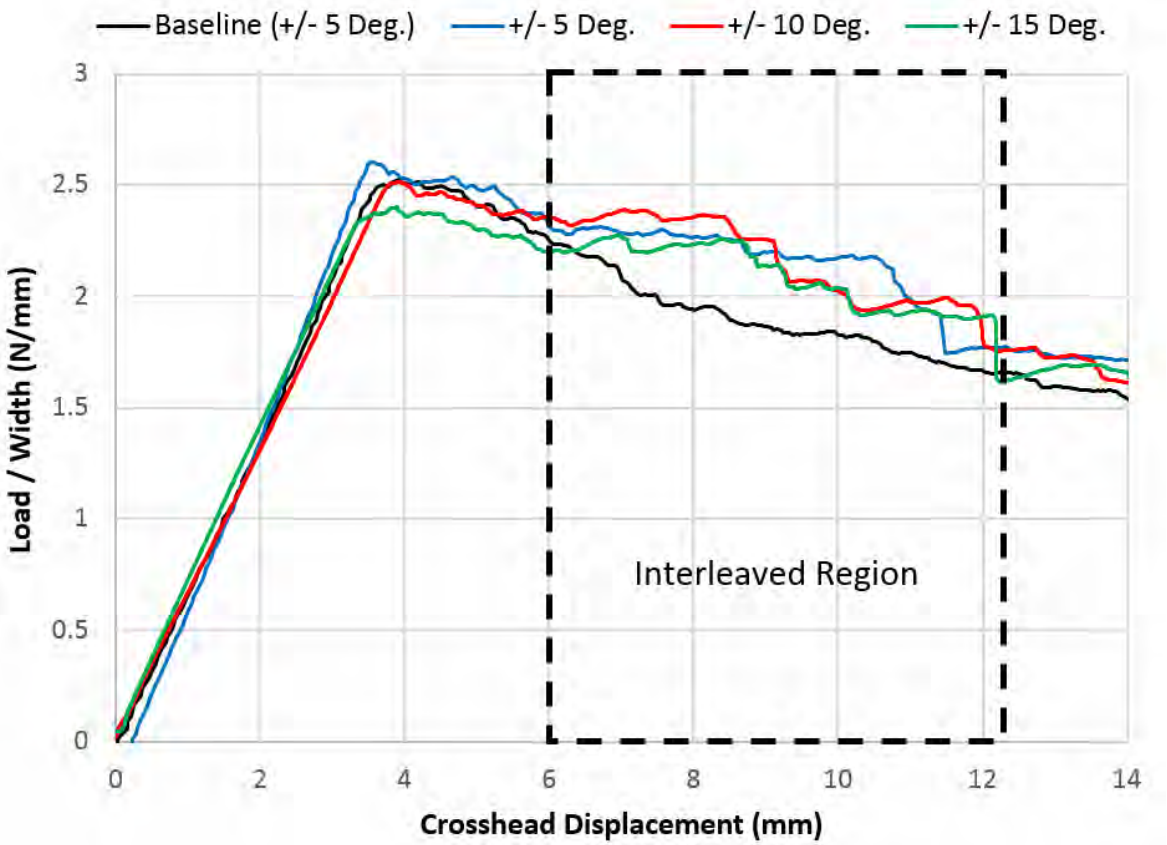

Figure 4.2: Typical load per unit width *versus* crosshead displacement plots for DCB tests with a selection of interface layups.

interleaved specimens measured an average strain energy release rate for crack propagation, G_{Iprop}, of approximately 320 J/m^2, or a 15 – 20% enhancement relative to the properties of the baseline specimen. It should be noted that a greater amount of scatter was observed for the interleaved specimens, however all showed a statistically significant difference when compared to the unmodified baseline specimen.

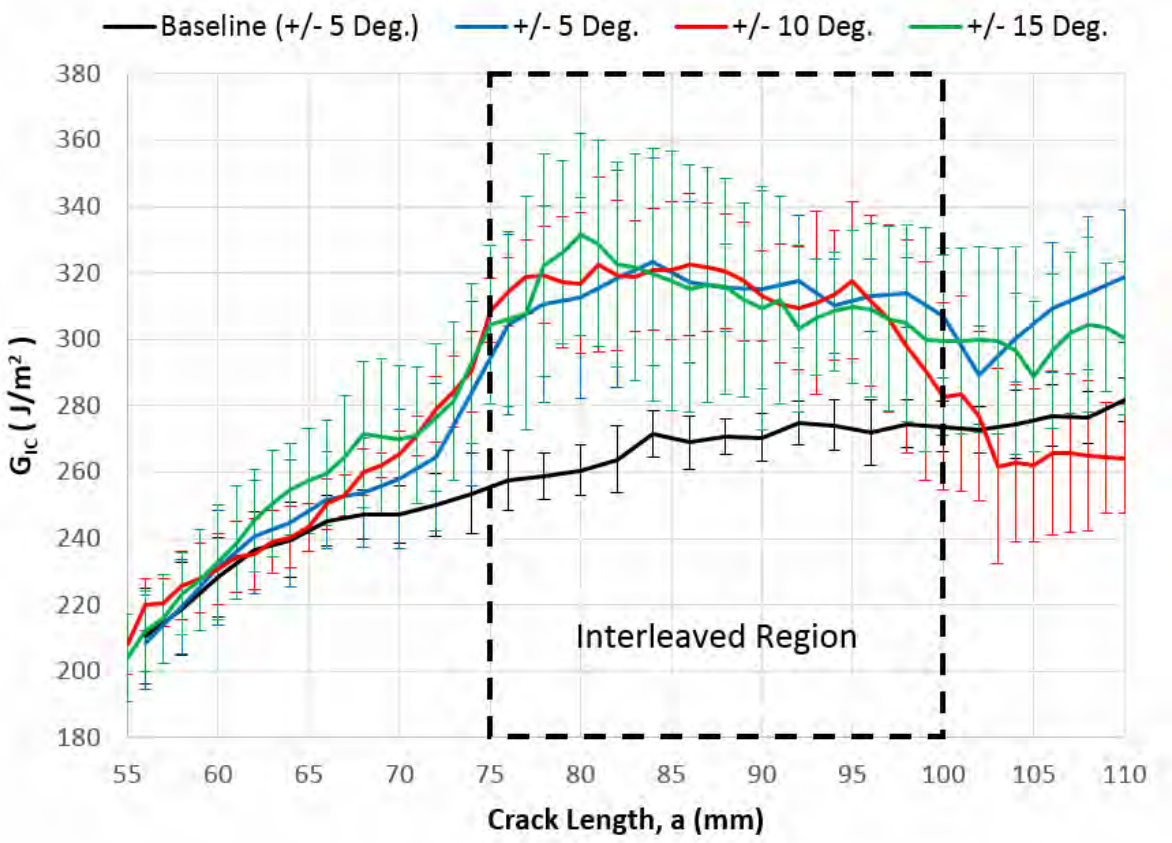

Figure 4.3: R-curves for Mode I critical strain energy release rate for DCB tests with a selection of interface layups. Error bars were taken at ± one standard deviation away from the mean.

4.3.2 Mode II fracture testing

Typical load *versus* displacement curves for interleaved ELS specimens with differing interface layups are plotted in Figure 4.4. In common with the Mode I analysis, the ±5° baseline and 40 μm VACNT interleaved specimens from chapter 3 have also been included for comparison. Comparing the load curves, it can immediately be seen that there is a dependency between the load required for crack initiation and the interface layup angle. The plots suggest that as the interface layup angle increases, so does the load required to initiate and propagate the crack. This supports the discussions and conclusions from Hwu *et al.* [228], Allix *et al.* [229], Lachaud *et al.* [230] and Andersons and König [18].

Despite the differing crack initiation loads, all tested specimens showed a load increase as the crack reached the interleave region. With the exception of the ±15° interface layup, cracks would then propagate in a stable manner through this region until reaching the clamp. It was observed that for the ±15° interface layup, the strain energy would build up as the crack reached, and was temporarily suppressed, by the VACNT interleaf. Once enough energy had developed,

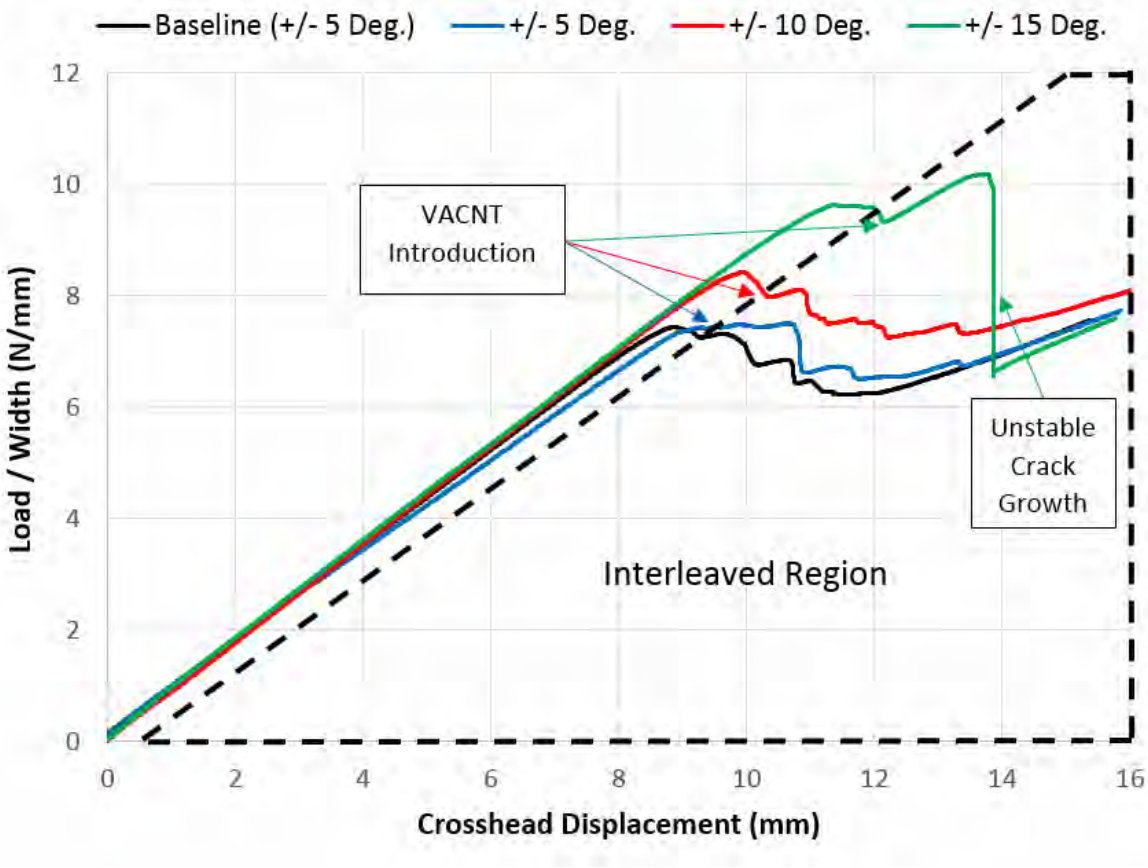

Figure 4.4: Typical load per unit width *versus* crosshead displacement plots for ELS tests with a selection of interface layups.

the crack would grow in an unstable manner to the clamp, evidenced by a sudden load drop.

The corresponding R-curves for each of the interface layups are plotted in Figure 4.5. It can be seen that similarly to the load plot, there is a relation between the interface layup and the fracture toughness, with the greater interface offset angle resulting in a heightened fracture toughness. G_{IIC} values at crack initiation was measured to be 0.55 J/m^2, 0.60 J/m^2 and 0.70 J/m^2 for the ±5°, ±10° and ±15° interface angle offset, respectively.

As the crack enters the interleaved region, *i.e.* when the crack length, a = 85 mm, the critical strain energy release rate rose for all interleaved specimens. Normalising the plots from Figure 4.5 relative to the G_{IIC} value at initiation, it can be seen that the percentage enhancement is approximately equal for all interface layups, at around 10% relative to the baseline. This has been plotted in Figure 4.6. With the exception of the ±15° interface layup, cracks propagated in a stable manner with specimens displaying this enhanced level of toughness. After approximately 5 mm into the interleaved region, the larger angle offset repeatably resulted in unstable crack growth all the way to the clamp.

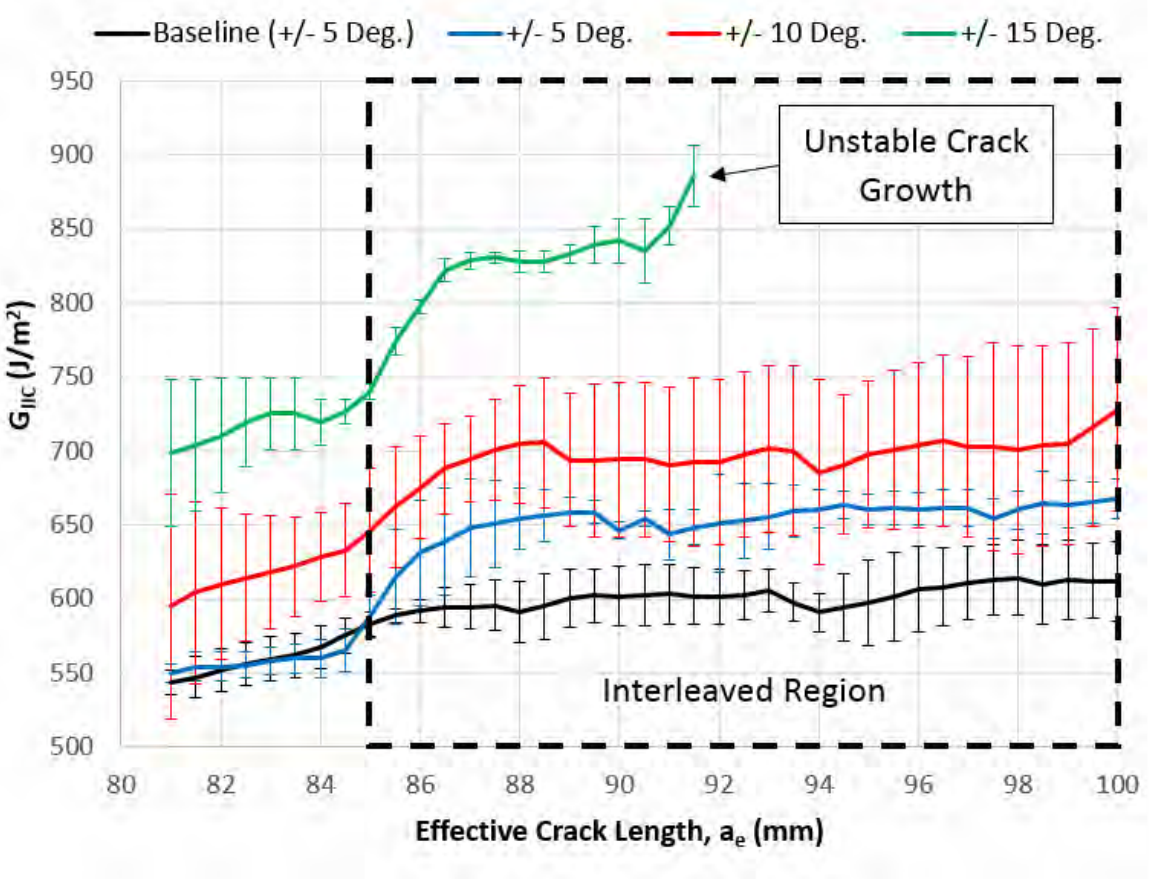

Figure 4.5: R-curves for Mode II critical strain energy release rate for ELS tests with a selection of interface layups. Error bars were taken at ± one standard deviation from the mean.

4.3.3 Fractography

To capture the fracture modes and mechanisms for each interface layup configuration, fractography analysis was conducted. Transverse views were taken within the unmodified and VACNT interleaved regions for the DCB and ELS test specimens. These images are shown in Figure 4.7 and Figure 4.8 for the DCB and ELS specimens respectively.

Analysing the optical microscope fractography images before and after the introduction of the interleaves, it can be seen that, in common with the findings in chapter 3, there is a transition between a predominantly interlaminar delamination fracture mode to an intralaminar delamination fracture mode. Despite three interfaces being reinforced with VACNTs, cracks were found to map the topology of the central interface, with little influence from the surrounding interleaves. No evidence of crack migration or intralaminar ply splitting was observed for any of the specimens examined. Higher magnification images showed that cracks propagated again through the fibre-matrix interfaces of the host laminate.

It is clear that the strain energy release rates, which are measured and plotted in Figure

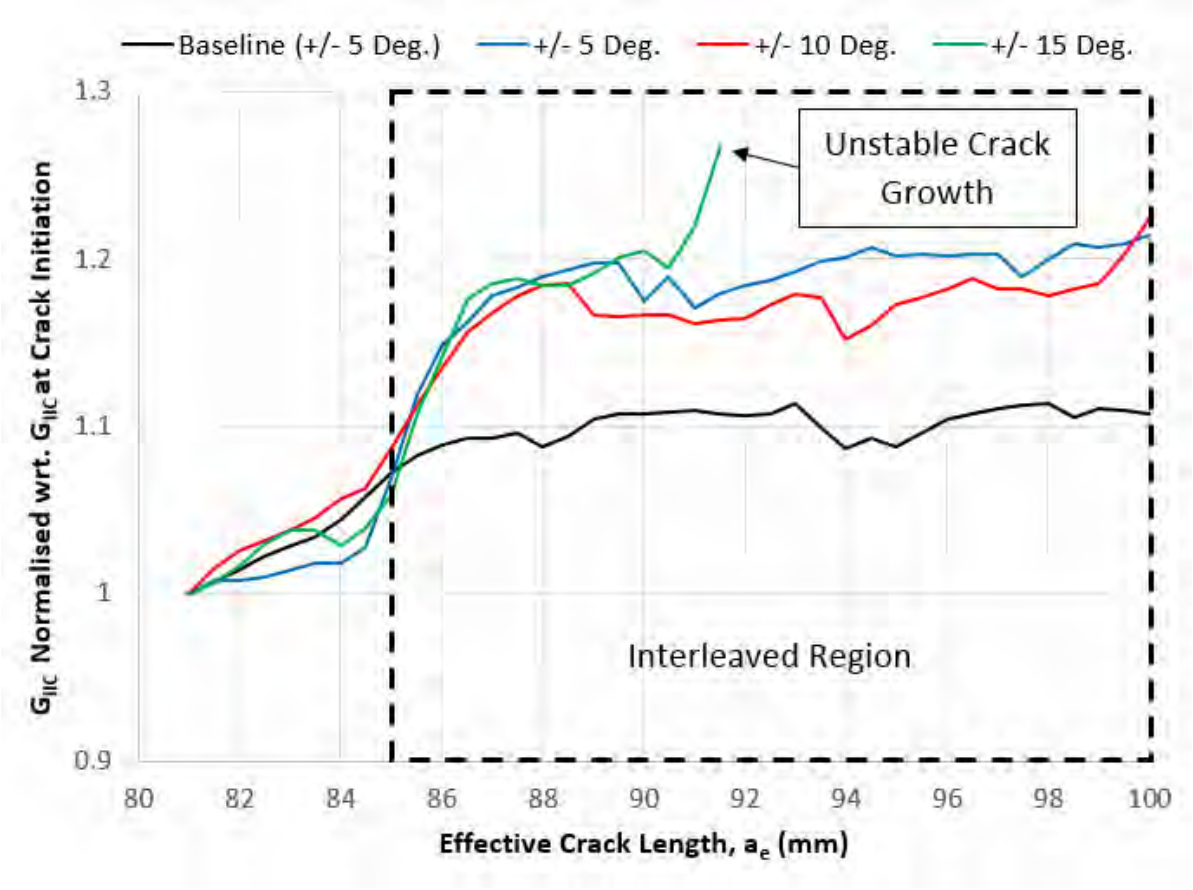

Figure 4.6: R-curves normalised with respect to G_{IIC} at initiation for Mode II critical strain energy release rate for ELS tests with a selection of interface layups.

4.3 and Figure 4.5, are again the material properties of the host IM7/8552 laminate. At the non-interleaved regions these correspond to the interlaminar fracture toughness, while at the interleaved regions, G_{IC} measurements equate to the intralaminar fracture toughness. The former is predominantly dictated by the 8552-resin properties, while the latter is predominantly determined by the fibre-matrix interfacial properties.

Overall, the mechanical tests and fractography analysis findings suggest that interleaving laminates with variable interface layup angles still leads to intralaminar dominated failure modes. This results in the fracture toughness enhancements being limited to the fibre-matrix interfacial properties of the host laminate. Furthermore, it is evident that for the interface layups investigated in this study, the difference between the interlaminar and intralaminar fracture toughness is similar. While greater fibre offset angles are likely to require more energy to propagate a crack through intralaminar delamination in Mode II conditions, unstable growth will be more frequent.

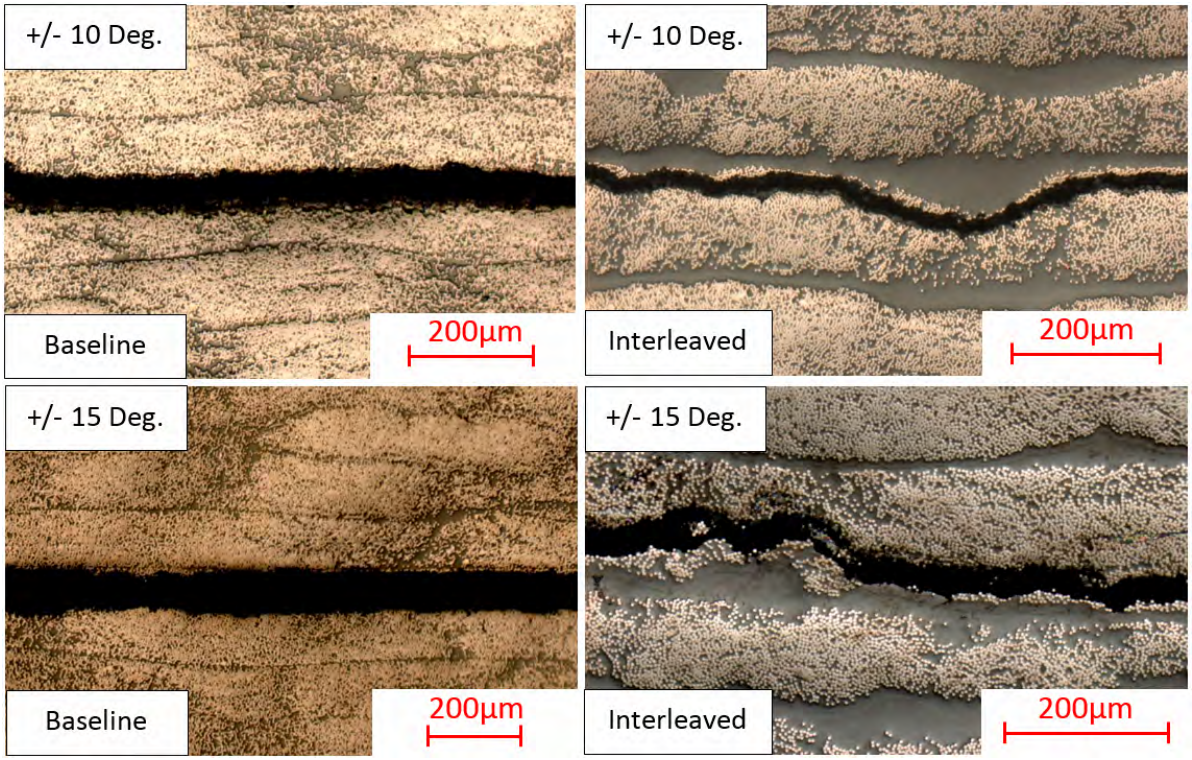

Figure 4.7: Transverse view from an optical microscope of fractured DCB specimens taken before and within the interleaf region for VACNT interleaved specimens with differing interface layups.

4.4 Conclusion

In conclusion, this study has investigated the effect that the interface layup has on the Mode I and Mode II interlaminar fracture toughness of an CFRP when interleaved with vertically aligned carbon nanotubes (VACNTs). Comparisons have been made between interleaved specimens with $[0_{15}, \pm 5, 0_{15}]$, $[0_{15}, \pm 10, 0_{15}]$ and $[0_{15}, \pm 15, 0_{15}]$ layups. On the whole, the Mode I interlaminar fracture toughness has been found to be independent of interface layup. However, under Mode II conditions, a dependency has been observed, with mechanical results showing that the Mode II interlaminar fracture toughness rises with interface layup angle for both the unmodified and interleaved regions. For all interface layups, VACNT interleaves were found to increase the Mode I and Mode II interlaminar fracture toughness by similar amounts, with fractography analysis showing that the fracture mode transitions from interlaminar delamination to intralaminar delamination. No crack migration or intralaminar ply splits were observed, and despite three interfaces being reinforced with VACNTs, cracks map the topology of the central interleaf film only. Unstable crack growth was witnessed for interface layups with larger angles under Mode II loading conditions.

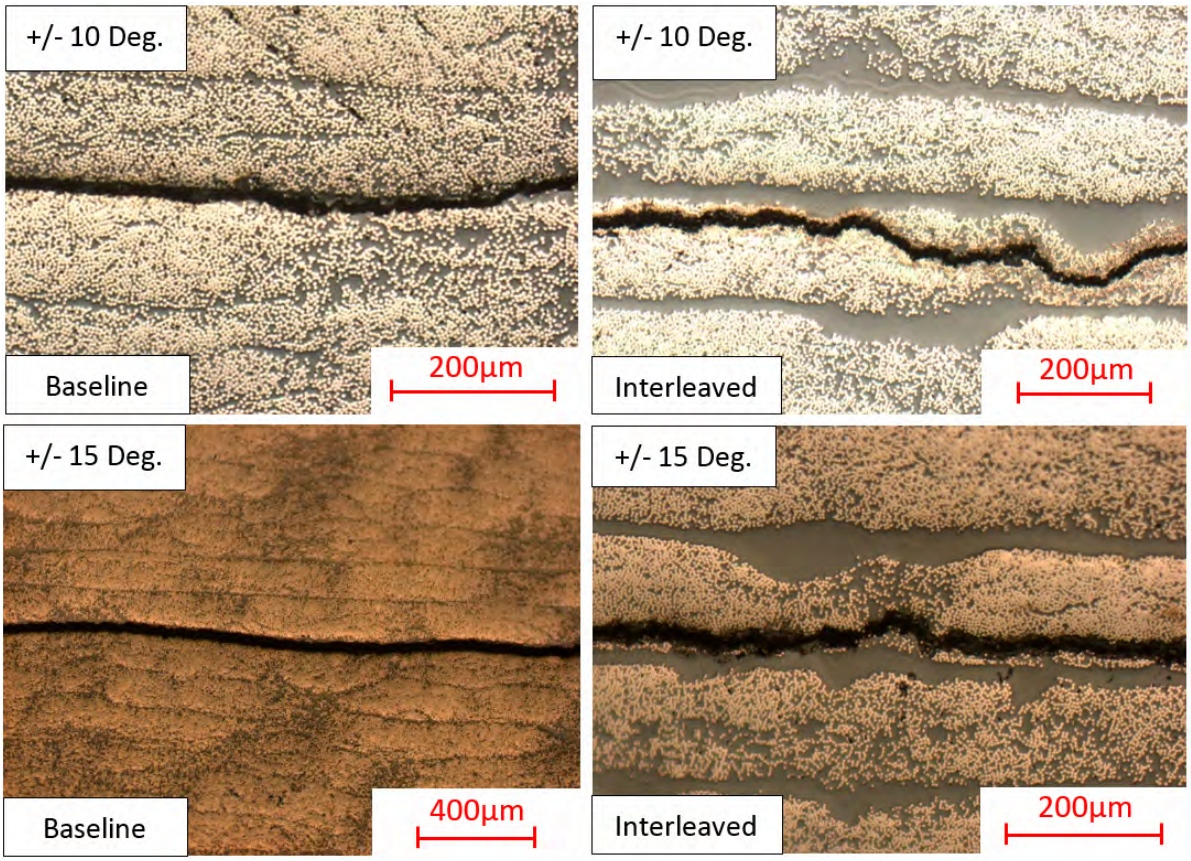

Figure 4.8: Transverse view from an optical microscope of fractured ELS specimens taken before and within the interleaf region for VACNT interleaved specimens with differing interface layups.

4.5 Fabrication Quality

4.5.1 Introduction

Microscopy and fractography images of the interleaved specimens fabricated thus far have revealed frequent interfacial resin rich regions, which have resulted in VACNT film waviness, variable interfacial thickness, and poor nanotube-fibre engagement. As all interleaved specimens have seen intralaminar dominated fracture behaviour, with cracks mapping the topology of the VACNT film, toughness properties have shown great scatter and hence less predictability. Furthermore, for other host composite systems where intralaminar behaviour is less prevalent, poor nanotube-fibre engagement introduces an interfacial weakness, which allows cracks to by-pass the reinforcement, as illustrated by Hojo *et al.* [32] and shown in Figure 4.9. Therefore, in order to avoid these issues, efforts were made to allow more resin to bleed from the system and reduce the frequency of resin pockets. Initially attempts were made to modify the bagging procedure, either by adding nylon peel-ply to the laminate surface or surrounding the laminate edges with a more porous cork to absorb extra resin during cure. Unfortunately, the laminates

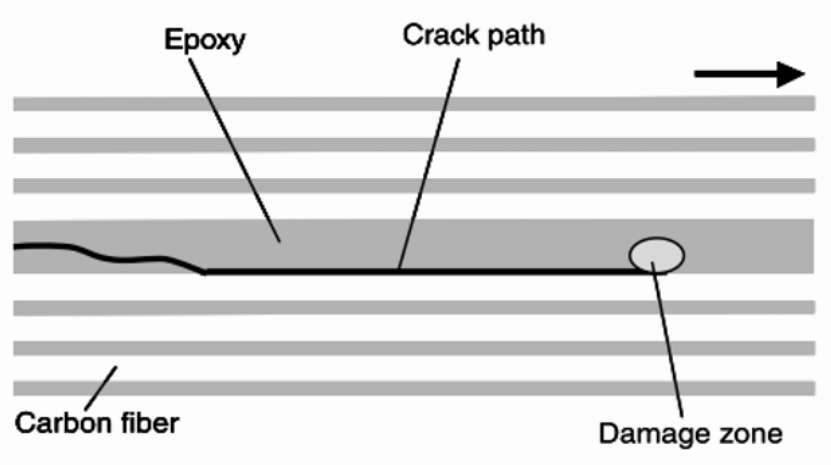

Figure 4.9: Illustrated schematic of crack path deviation to the interlaminar ply interface [32].

were too thick to allow for enough resin bleed and so focus was placed on subtly modifying the autoclave cure cycle instead.

4.5.2 8552 epoxy resin cure cycle modification

Allowing extra resin to bleed requires either additional pressure on the system, or the minimum viscosity of the resin to be lowered. To preserve the autoclave life, pressure was kept constant and attention was focused on lowering the resin viscosity instead.

It has been shown by Hubert *et al.* for 8552 resin [41], that the resin viscosity can be lowered in two ways, that is, either increasing the temperature ramp rate, or removing the dwell. Examples of these scenarios are plotted in Figure 4.10. To avoid large exotherms, changes to the temperature ramp rate were avoided. Instead, investigations were focused on removing the dwell from the cure cycle, which, as can be seen in Figure 4.10b, resulted in an undesirable increased viscosity due to the increased degree of cure.

The two cure cycles chosen for comparison are shown in Figure 4.11. Pressure and vacuum conditions were unmodified. To assess how the cure cycle affects the frequency of resin pocket formations and hence nanotube-fibre engagement, two uni-directional 100 mm x 100 mm x 4 mm CFRP laminates were manufactured using HexTow® IM7/ HexPly® 8552 prepreg. For each laminate, the central interface was identically interleaved with VACNTs with the same characteristics as that described in Table 4.1. The laminates were then separated and cured independently using one of the cure cycle conditions outlined in Figure 4.11. Once cured, each laminate was viewed under a scanning electron microscope (SEM) to compare the quality of the interface.

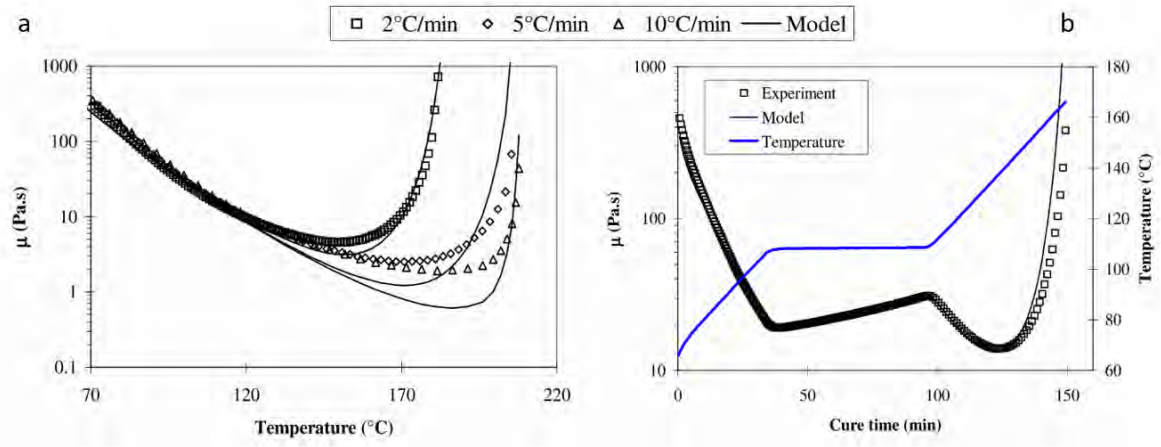

Figure 4.10: Images extracted by the work by Hubert *et al.* [41], which show the effect of (a) increasing the temperature ramp rate and (b) including a dwell into a cure cycle, on the viscosity of 8552 resin.

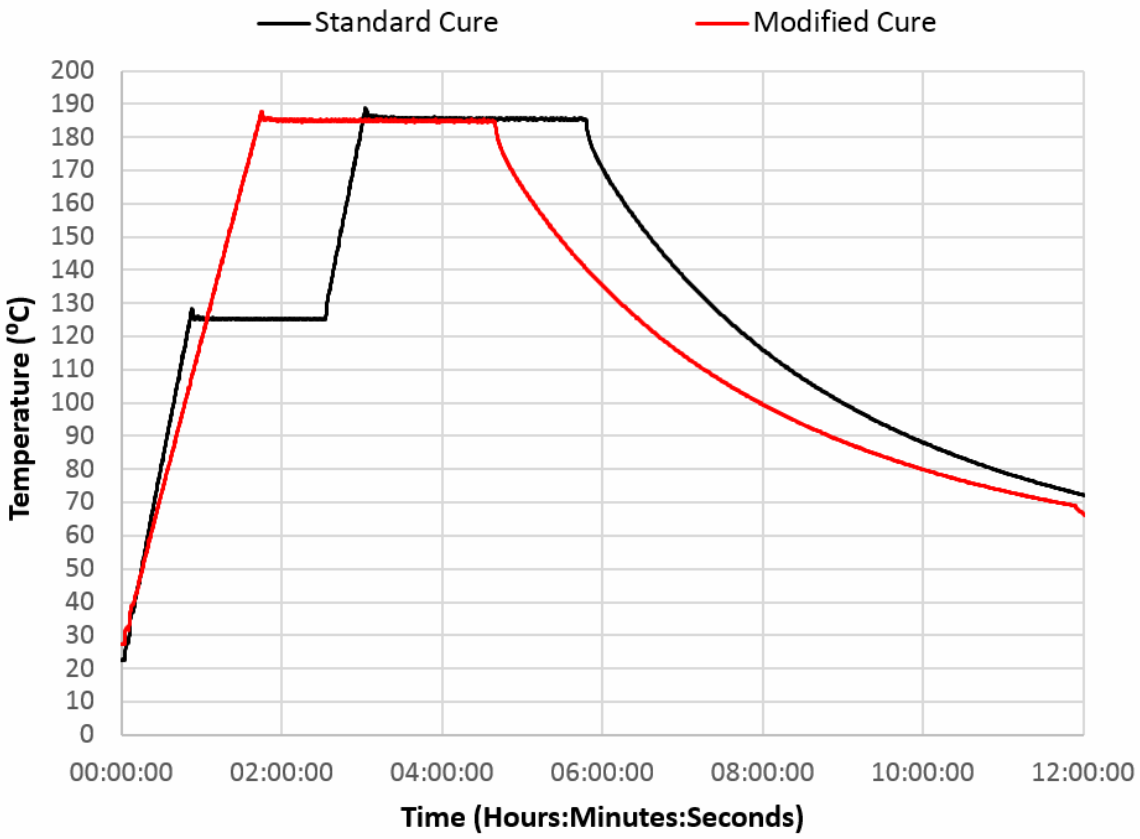

Figure 4.11: The temperature cure cycle for a standard cure cycle suggested by the supplier [3] and a modified cure cycle, which omits the initial temperature dwell.

4.5.3 Microscopy

To prepare samples for SEM imaging, the cured 100 mm x 100 mm composite laminates were cut using a diamond coated water-cooled saw, then ground and polished to at least 1 μm. Images were captured using a Hitachi TM 3030PLus SEM at a voltage of 5000V and magnification of x250. These have been collated in Figure 4.12.

Comparing the SEM images, it can be observed that the number of resin pockets, or resin rich regions, noticeably decrease for the modified cure cycle. Furthermore, the topology of the VACNT film meanders less when the resin pockets have dissipated. Overall, this leads to improved engagement between the nanotubes and the surrounding carbon fibres.

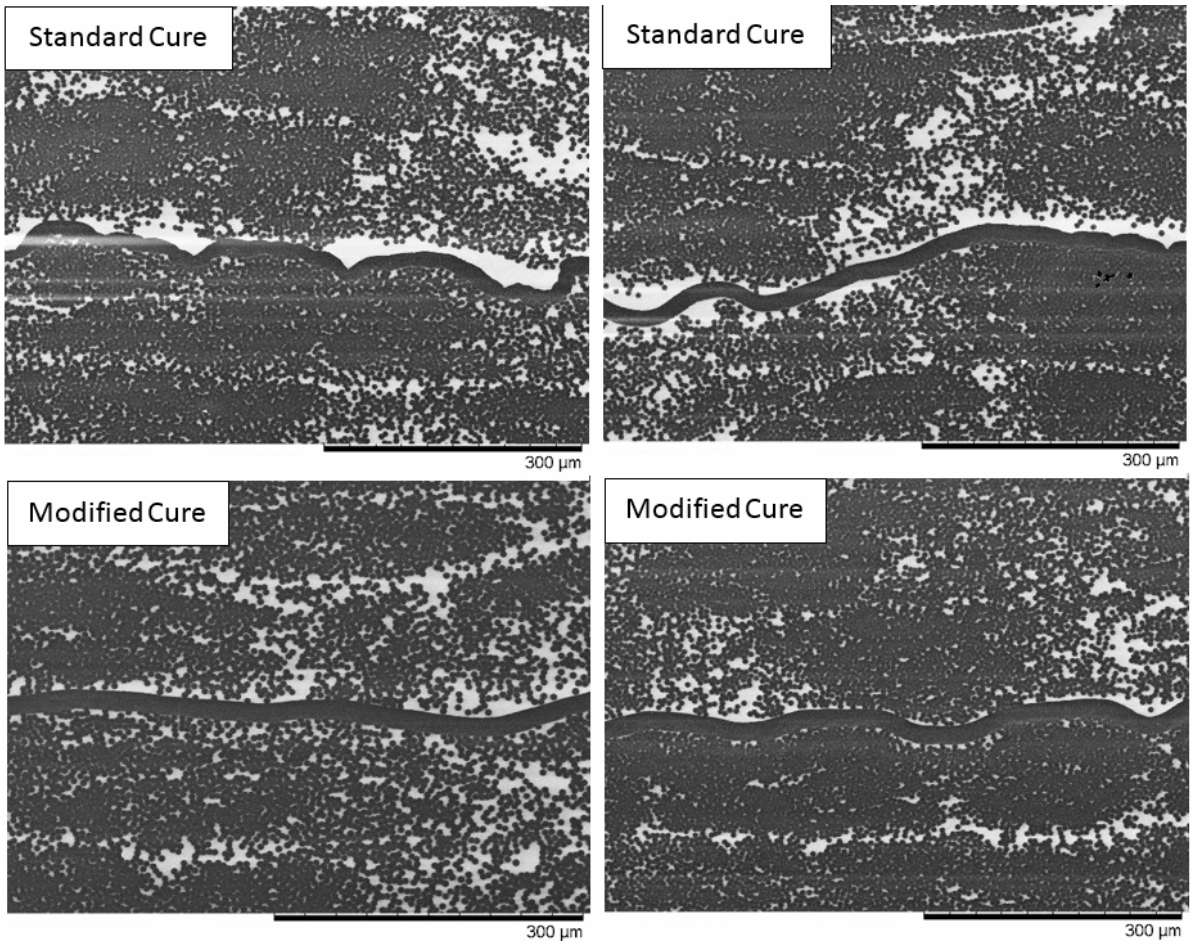

Figure 4.12: Transverse view SEM images taken of VACNT interleaved laminates, which have been cured using a standard cure cycle and a cure cycle whereby the initial dwell has been removed.

4.5.4 Fibre volume fraction modification

Improvements in nanotube-fibre engagement were achieved through removing the initial dwell from the cure cycle, which enabled more resin to bleed and thereby reduced the number of interfacial resin pockets. This bleeding behaviour occurs globally rather than locally at the central interface and is therefore likely to influence the fibre volume fraction of the whole composite.

To measure the extent to which the fibre volume fraction had been affected by the change to the cure cycle, a thermogravimetric analysis (TGA) method was adopted. Such a method has been shown as a viable equivalent to an acid digestion test, without being as labour intensive or requiring disposal of toxic waste materials [231]. The TGA method works through taking a small representative material sample ($< 50\ \mu g$) and exposing it to a linearly ramped temperature range to burn away all of the resin. This is done within an inert gas, in this case nitrogen, to prevent atmospheric reactions occurring at higher temperatures. The mass of the sample is monitored continuously through this process. At a certain temperature, the resin will burn off completely, leaving only the fibres remaining. Assuming that the density of the resin and fibres are known, the mass before and after the temperature ramp will enable the sample's fibre volume fraction to be determined through Equation 4.1.

$$Fibre\ Volume\ Fraction\ (\%) = \frac{V_f}{V_f + V_r} = \frac{m_f/\rho_f}{m_f/\rho_f + m_r/\rho_r} = \frac{m_f/\rho_f}{m_f/\rho_f + (m_c - m_f)/\rho_r} \tag{4.1}$$

where V is the volume, m is the mass and ρ is the density. While subscript f,r, and c correspond to the fibre, resin, and composite, respectively.

For this investigation, specimens originally cured with the standard or modified cure cycles were subjected to temperatures ramping between $30 - 1000°C$ at a rate of $10°C$/min. Once at $1000°C$, an isothermal dwell was conducted for 10 minutes to ensure the specimen reached the full environmental temperature. This procedure was also performed on an empty sample holder for calibration purposes. At least three replicants of each sample variant were tested to calculate an average.

Typical degradation of mass plots for laminates cured using the two cure cycles are shown in Figure 4.13a. From these curves it can be seen that for the modified cure cycle, the percentage mass of the remaining sample is more than that of the standard cure cycle. As expected, this suggests that a lower proportion of resin is in the modified cure composite system, as the lower viscosity resulted in more resin bleeding out.

On average, it was found that the mass reduced by 25% for samples cured using the standard cycle and 24% for samples cured using the modified cycle. Using the fibre and resin density values outlined in the suppliers material data sheet [3], and placing them into Equation 4.1, an estimated fibre volume fraction of 69% for the standard cure samples and 70% for the modified cure samples was determined (Figure 4.13b). These are slightly higher than that quoted by the

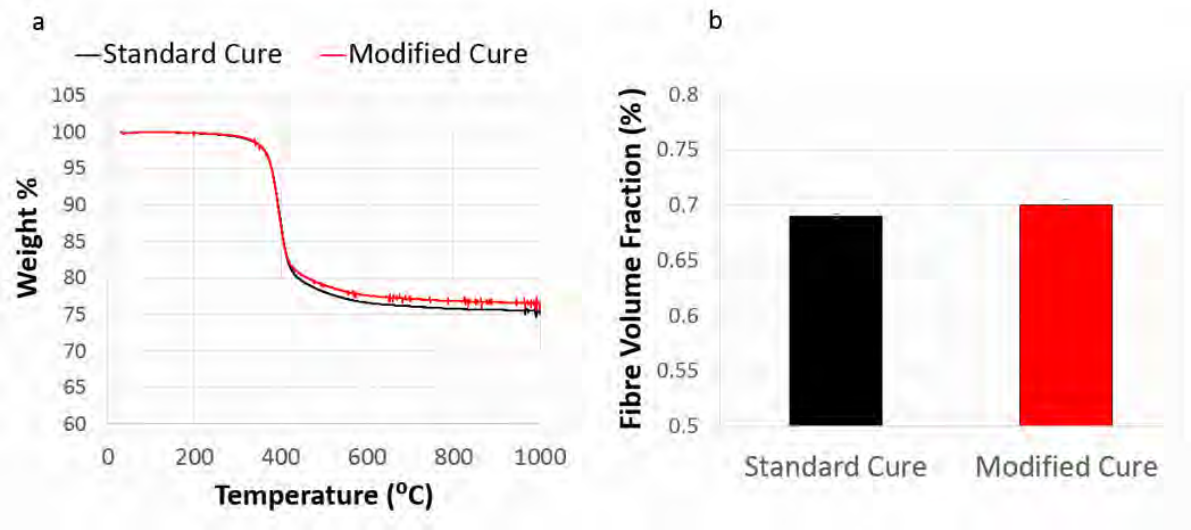

Figure 4.13: (a) The typical degradation in mass with temperature response for samples which were cured with an initial dwell (standard) or without an initial dwell (modified) during the cure cycle; (b) The corresponding fibre-volume fraction prediction for each specimen when using Equation 4.1.

supplier (67%), however absolute values were not in the scope of this study. What can be concluded is that the modification to the cure cycle does increase the fibre volume fraction, however the values are not significant (< 1%). This suggests that the resin rich regions at the central interface do not completely leave the composite system, but instead diffused into the surrounding plies. Therefore, to improve the interfacial quality and nanotube-fibre engagement, the dwell shall be removed from the autoclave cure cycle in subsequent studies.

Prologue to Chapter 5

In the research conducted thus far, it has been concluded that the interlaminar fracture toughness enhancement achieved from introducing VACNT interleaves into CFRP laminates is independent of nanotube length and interface layup. The cracks consistently migrate away from the interlaminar nanotube reinforced region into the intralaminar region and the extra energy required to do this is dependent on the intralaminar fracture toughness of the host laminate. Consequently, this limits the maximum achievable fracture toughness enhancements.

The VACNT interleaf films analysed in this study have all been embedded into a compatible host resin film prior to prepreg insertion. This eases fabrication and safety when handling. However, the extra resin results in poor nanotube to carbon fibre engagement and frequent resin rich regions, which give rise to interfacial weaknesses. It has been shown that these can be mitigated through subtle modifications to the cure cycle, aimed at reducing the resin viscosity, so that more resin can escape or diffuse into the rest of the laminate.

One major advantage of interleaving is the ability to modify the reinforcement distribution. For example, sensitive areas, such as notches or ply-drops, which inherently form weak discontinues, can be reinforced to reduce premature failure. Unfortunately, by introducing excess resin into the system and encouraging it to flow, the resin will disrupt the distribution of the nanotubes during cure. Therefore, to investigate how nanotube distributions influences the fracture behaviour of CFRP laminates, the fabrication process will be altered to enable the nanotubes to be placed accurately, without the need of the additional resin film. Measuring the nominal thickness of the interlaminar region in baseline specimens, the 11 μm nanotube length variant has been selected. This will enable bridging of the interlaminar region, without excessive nanotube micro-buckling. Moreover, an interface layup of $\pm 10^{\circ}$ has been chosen for all remaining fracture toughness specimens to encourage stable interlaminar crack growth throughout.

CHAPTER 5

The Effect of Nanotube Density and Distribution on the interlaminar fracture toughness of VACNT Interleaved Composites

Abstract

Carbon fibre reinforced polymer laminates are interleaved with VACNTs, which have a variety of nanotube densities and distributions. Three homogeneous VACNT interleaves with linearly separated densities, and four discretely distributed VACNT patterned interleaves, were experimentally tested through DCB and ELS methods to determine the Mode I and Mode II interlaminar fracture toughness, respectively. Patterned interleaves were transferred to prepreg through a novel masking and heated laminator method and were found to achieve good geometric tolerances. Fracture toughness was found to be independent of nanotube density with a $15-20\%$ enhancement in Mode I and a $5-10\%$ enhancement in Mode II conditions. All homogeneous interleaf configurations were found to cause crack deflection from the interlaminar to the intralaminar region. Additional fracture mechanisms, such as crack branching, were found to occur for the patterned interleaves, which led to some patterns, particularly for those with smaller feature sizes, measuring a fracture toughness exceeding that of a homogeneous interleaf. Patterned VACNT interleaves were also found to slow crack propagation in Mode I and stabilise crack growth in Mode II. This indicates that cracks may be able to be deflected in-plane, away from sensitive areas, such as laminate edges or notches, through strategic positioning of the interleaves.

5.1 Introduction

5.1.1 VACNT density

As concluded in section 2.3.1, no studies have investigated how the VACNT density influences the mechanical properties when interleaved into an FRP material. Therefore, in the first part of this chapter, VACNT films with a selection of VACNT densities will be interleaved into CFRP host laminates and will be subsequently tested under Mode I and Mode II conditions. Nanotube length will be maintained throughout at $11 - 15$ μm. Both pristine and fractured specimens will be visualised through scanning electron microscopy (SEM) to understand whether VACNT density influences *(i)* how the nanotubes engage with the fibres and *(ii)* the failure mechanisms at the interleaf region. The densities investigated are linearly separated, with the average equating to that of the VACNT interleaves in chapters 3 and 4.

5.1.2 VACNT patterning

Also concluded in section 2.3.1 was that no studies have been conducted on how patterned VACNTs effect the interlaminar fracture toughness of an FRP material. Therefore, in the second part of this chapter, CFRP laminates are interleaved with patterned VACNTs, with a surface coverage of 50%. The patterned VACNTs are transferred onto a prepreg surface using a similar masking technique to that reported by Narducci *et al.* [172] and Na *et al.* [173]. Scanning electron microscopy (SEM) is used on pristine specimens to capture the interleave transfer quality, and on fractured specimens, to understand the failure mechanisms present. For Mode I conditions, crack growth is recorded on both sides of the specimen to understand whether VACNTs influence the crack growth rate behaviour.

5.2 Methodology

5.2.1 Materials

The carbon fibre composite laminates in this chapter were manufactured out of HexTow® IM7/ HexPly® 8552 prepreg. Plies were laid up and cured using the modified monolithic cure cycle discussed in chapter 4. Three densities, four patterns and an unmodified baseline variant were manufactured for comparison under Mode I and Mode II conditions. This secondary baseline specimen was manufactured to account for the cure cycle and ply offset changes discussed in chapter 4. All configurations were manufactured as individual plates, with a 12 μm thick Polytetrafluoroethylene (PTFE) film inserted to initiate the crack. The VACNTs used in this chapter were grown using a proprietary continuous CVD process [213, 214], with catalytic and environmental conditions modified to achieve the correct nanotube height and densities. All

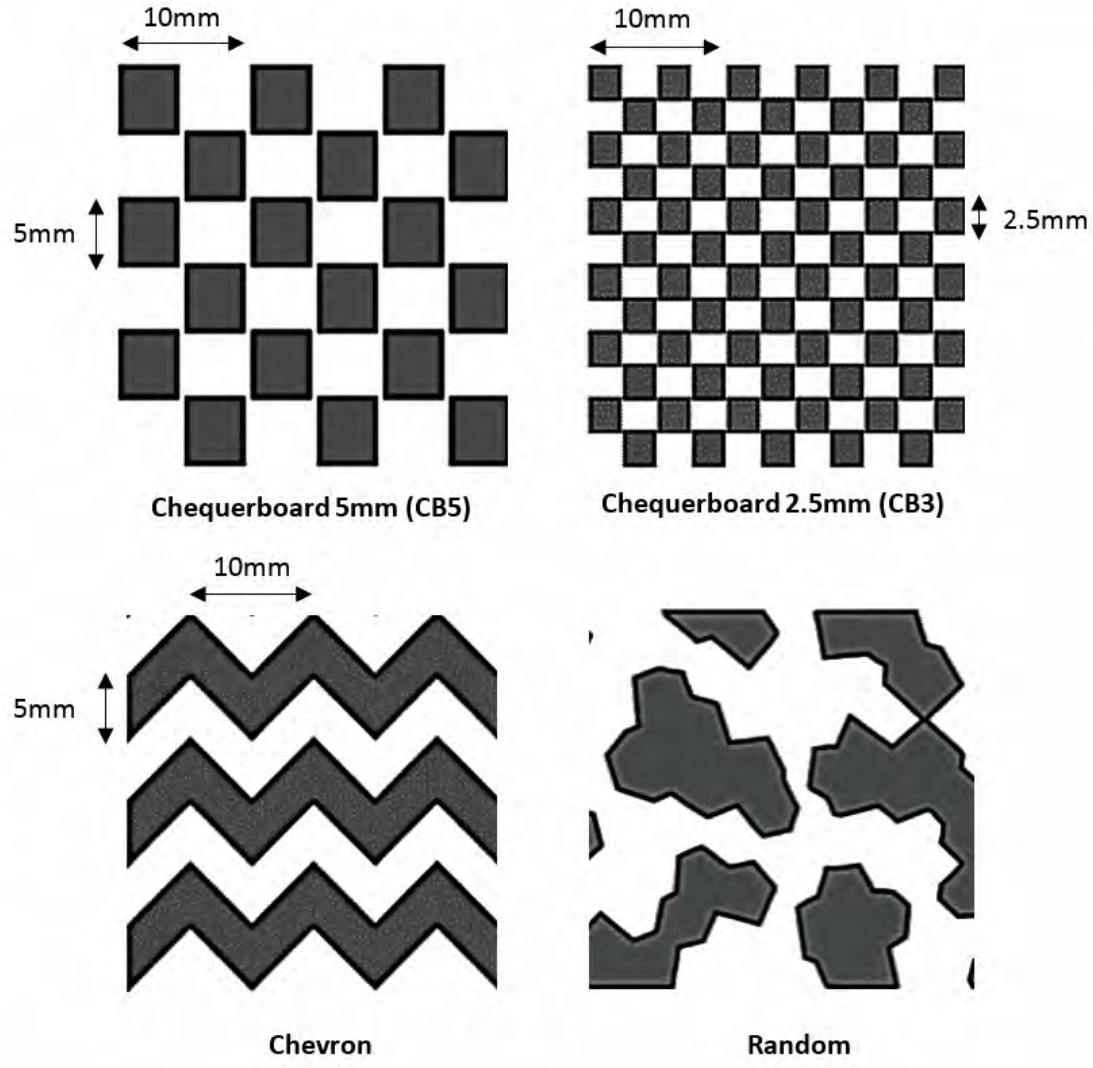

Figure 5.1: The four VACNT interleave pattern designs (30 mm x 30 mm) tested under Mode I and Mode II conditions.

VACNTs had a length of 11 μm, which, as discussed in chapter 4, was found to be the average interlaminar region thickness for IM7/8552.

The three densities selected in this study shall be defined as ‘low‘, ‘medium‘ and ‘high‘. The medium density corresponds to the same as that investigated in chapter 3 and chapter 4, while the low and high densities, corresponds to 50% below and above the medium density respectively. Table 5.1 shows all the nanotube properties evaluated in this chapter.

Four pattern designs were selected for investigation under Mode I and Mode II conditions. These are defined as ‘Chevron‘, ‘Chequerboard 5mm (CB5)‘, ‘Chequerboard 2.5mm (CB3)‘, and ‘Random‘. Each pattern design is illustrated in Figure 5.1. Patterns were selected to promote repeatability between tests, as well as capturing a variety of different features. For example, the

Chevron design consisted of alternating interleaf regions along the length, while the Chequerboard designs offer alternating interleaf regions along the width. Two Chequerboard designs were evaluated to investigate the influence of interleave reinforcement feature size on fracture behaviour; ahead of the crack tip, a process zone will form, whereby the elevated stresses at the crack tip will result in matrix micro-cracking and subsequently, a degradation in mechanical properties [232]. If the process zone is larger than the interleaf feature size, it is hypothesised that it will engulf the interleave reinforcement and as a result, reduce the mechanical property enhancements. Studies have suggested that the length of this process zone is approximately 1 mm in Mode I conditions and 4 mm in Mode II [232, 233], however this has only been determined analytically and numerically. Unfortunately, the manufacturing process, as discussed in the next section, only allowed for a minimum feature size of 2.5 mm, however this should still indicate whether feature size affects the fracturing behaviour and hence toughness measurements. The final pattern design, named 'Random', was developed with the aim of avoiding coupling effects between the interleave pattern and the ordered fibre orientation. It was created using a Voronoi generator package built into Matlab [234] to form a 2D pseudo-random mesh pattern as shown in Figure 5.2a. Elements of this mesh pattern were collated to create a patch pattern as shown in Figure 5.2b, with approximately 50% of the elements removed. This pattern was defined as 'Random', although some subjective decisions were made to ensure the pattern could be manufactured.

5.2.2 Mode I laminate fabrication

The Mode I critical strain energy release rate, G_{IC}, was obtained through DCB tests. As recommended by the ASTM-D5528 standards for a uni-directional FRP [215], specimens consisting of 32 plies ($\approx$ 4 mm thickness) were cut using a water-cooled diamond saw to 160 mm x 20 mm. All plies were uni-directional, apart from the two centre-most, which, as determined in chapter 4, had an offset of $\pm 10^{\circ}$ to minimise fibre bridging. At the mid-plane between the offset plies, a 12 μm thick PTFE film was introduced to initiate the crack. The film was positioned so as to ensure an initial crack length (a_0) of 50 mm. At a distance of 25 mm away from the PTFE film, the VACNTs interleaves were added and spanned a distance of 30 mm. The DCB specimen architecture is summarised in Figure 5.3.

The patterned VACNT interleaves described in Figure 5.1 were transferred using the process

Table 5.1: Geometric properties of the VACNTs investigated in this chapter.

Form *(-)*	**Length** (μm)	**Diameter** (nm)	**Areal Density*** (mg/cm^2)	**Population Density*** ($CNTs/cm^2$)
MWCNTs	11 ± 4	12	0.015 / 0.03 / 0.045	1.6 / 3.2 / 4.8 E+9

** The three densities stated correspond to the low / medium / high density VACNT variants.*

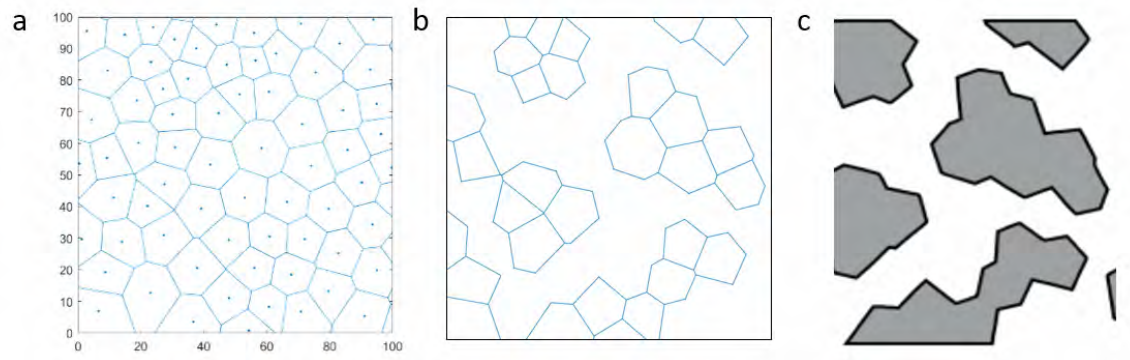

Figure 5.2: (a) Output from the Voronoi generator, (b) truncated design omitting approximately 50% of the elements and (c) the cutting outline determined by the Cricut Design Space Software [42].

described in Figure 5.4. Initially all pattern designs were imported into the Cricut Design Space software [42], whereby their outer geometries, as shown in Figure 5.1 and Figure 5.2c, were defined and cut from 25 μm thick release film using a Cricut Explore Air 2 (South Jordan, Utah, USA) [235] on an adhesive cutting board (Figure 5.4a). Once the cut patterns, or 'masks', were removed, they were aligned on the exposed prepreg surface (Figure 5.4b). VACNTs grown on a foil substrate were placed over the top of this masks (Figure 5.4c) and fed through a heated rolling laminator at 68°C and a feed rate of approximately 600 mm/min (Figure 5.4d). Once finished, the

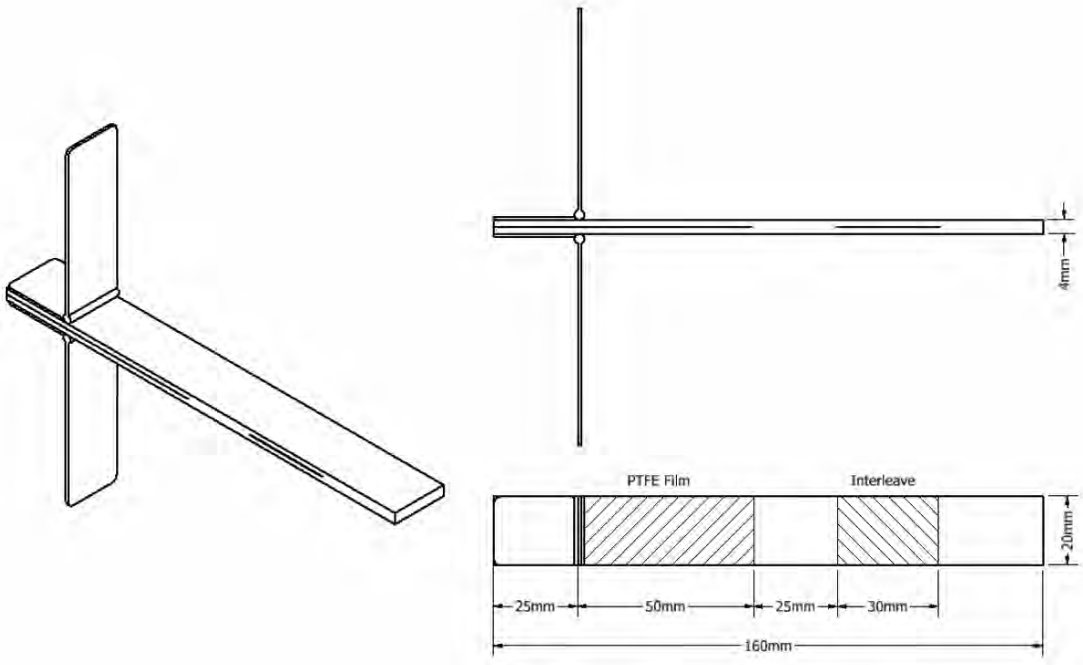

Figure 5.3: Geometric dimensions of the DCB specimens.

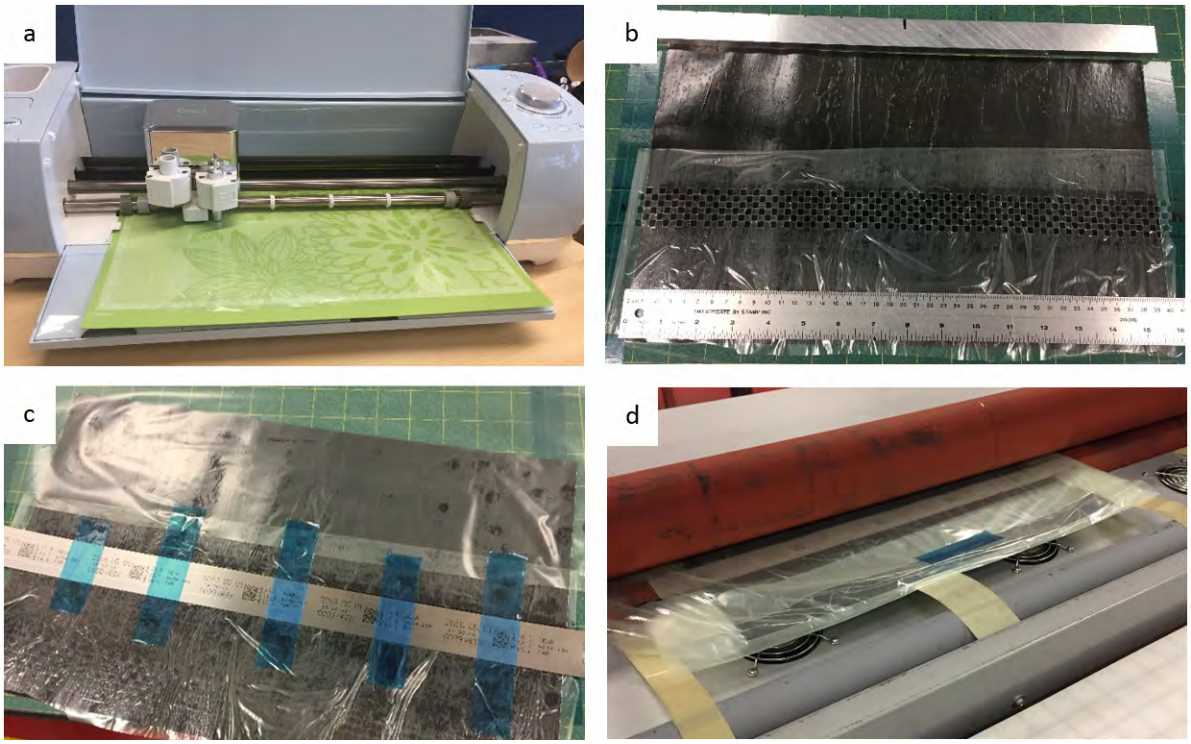

Figure 5.4: The process for manufacturing patterned VACNT interleaves onto prepreg: (a) Initially, patterns were cut out of 25 μm thick release film cutting using a desktop CNC machine on an adhesive cutting board. (b) Masks were positioned and placed over the exposed prepreg, before (c) the VACNT film was placed over the top; (d) The system was then fed through a heated laminator to transfer the nanotubes through to the exposed prepreg.

substrate and mask were removed to reveal the transferred nanotubes. Figure 5.5 shows all of the VACNT pattern designs when transferred to the exposed surface of the prepreg. Homogeneous VACNT interleaves used in the density study were transferred using a similar method as the patterned, however without the mask. VACNTs were instead directly placed on the exposed prepreg and placed through a heated laminator using the same feed conditions. Removal of the substrate revealed good nanotube transfer, with negligible carbon remaining on the substrate.

Opening loads on the DCB specimens were applied through steel piano hinges, which were adhesively bonded to the composite surface using 3M DP490 EPX adhesive, cured for 7 days at 20°C. Both the specimen surface and hinges were grit-blasted to ensure good adhesion.

5.2.3 Mode I fracture testing

Homogeneously distributed VACNT interleaved DCB specimens were tested in the same manner to that described in chapter 3, with 5 replicates taken for each configuration. As the patterned VACNT interleaves have non-uniform reinforcement across the width, it was expected that crack growth rate would vary on either side of the specimen. Therefore, for these tests, an iMETRUM

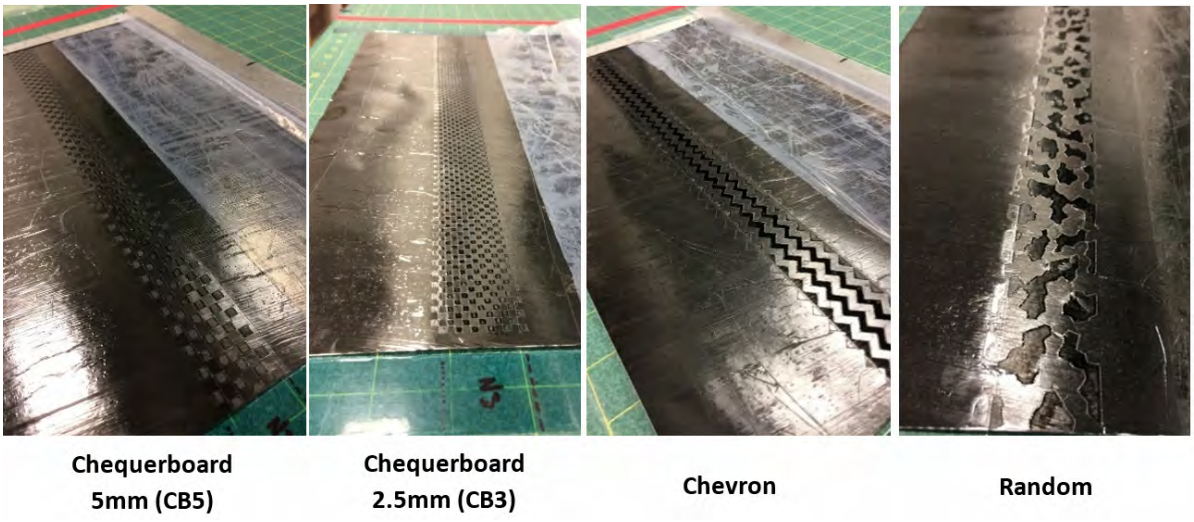

Figure 5.5: Examples of VACNT patterns transferred on to exposed prepreg.

video gauge (iMETRUM, Bristol, UK) was stationed either side of the specimen to monitor the differences in crack growth behaviour. White speckles and correction fluid were applied to both sides of the specimen to ensure good simultaneous tracking. Figure 5.6 shows both set-ups used in this chapter. For the patterned interleaved specimens, the Mode I critical strain energy release rate, G_{IC}, was calculated using the crack length data from one side of the specimen only. Calculation of the Mode I critical strain energy release rate was conducted using the same procedure outlined in chapter 3. At least 5 replicates were tested for each pattern design.

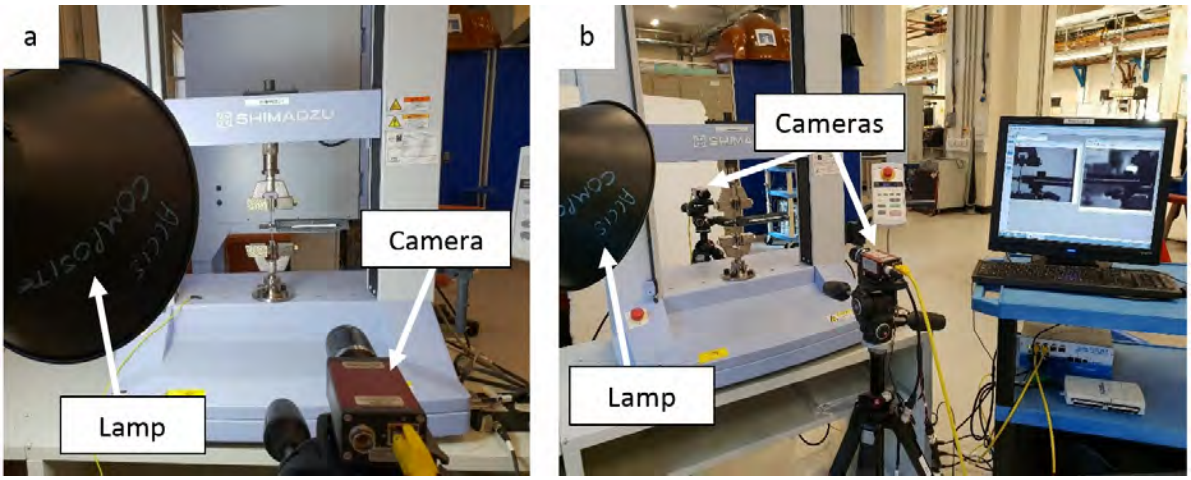

Figure 5.6: (a) DCB test set-up for homogeneous interleaf reinforcement and (b) a dual-camera setup for patterned non-uniform interleaf reinforcement.

5.2.4 Mode II laminate fabrication

In common with chapters 3 and 4, the Mode II critical strain energy release rate, G_{IIC}, was evaluated using an ELS testing configuration. Laminates consisted of 32 plies, all uni-directional apart from the two centre-most, which had an offset of $\pm 10^{\circ}$ to minimise fibre bridging along the crack plane. All specimens were laid up as a laminate plate and cut to 200 mm x 20 mm using a water-cooled diamond saw. Dimensions were selected to comply with the ISO/DIS 15114 standards [217]. PTFE film with a thickness of 12 μm was used to form an initial crack length (a_0) of 60 mm. Interleaves were introduced 25 mm away from the PTFE film and spanned a distance of 30 mm. The layout of the ELS specimens can be seen in Figure 5.7. Interleaf transfers were conducted using the same method as that described in Section 5.2.2.

Shear loads were applied through piano hinges bonded to the surface of the laminates using 3M DP490 EPX adhesive and cured for 7 days at 20°C. Prior to bonding, the surfaces of both the laminate and hinges were grit blasted and cleaned to ensure strong adhesion.

5.2.5 Mode II fracture testing

All ELS tests were performed with similar procedures to that described in chapter 3, with at least 5 replicates for each specimen configuration. Unlike for the DCB tests, patterned interleaf crack growth was not monitored visually due to difficulty in detecting the crack length during the test. In common with chapters 3 and 4, to avoid subjective determination of the crack length, the corrected beam method was adopted. An in-depth description of this method can be found in Section 3.2.3.2.

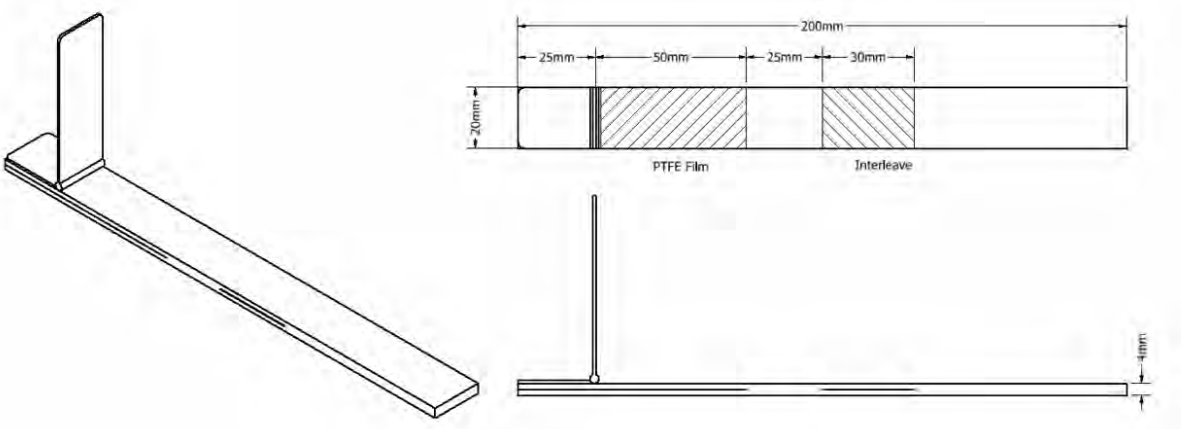

Figure 5.7: Geometric dimensions of the ELS specimens.

5.2.6 Microscopy and fractography

Scanning electron microscopy (SEM) was conducted on pristine and fractured specimens to assess the VACNT quality and to understand how the interleaf type affected the fracture behaviour. All specimens examined through SEM were cut using a water-cooled diamond saw to the dimensions outlined in Figure 5.8 and polished to a fidelity of one micron. Images were captured using a Verios^{TM} XHR SEM (FEI, Oregon, USA) at magnification levels of x70 to x7500 and a voltage acceleration of 500V.

5.3 Results and Discussion

5.3.1 Microscopy

5.3.1.1 VACNT density

Transverse views of the pristine low, medium and high density VACNT interleaves can be seen in Figure 5.9(a-c) respectively. Good nanotube-fibre engagement was observed for all specimens,

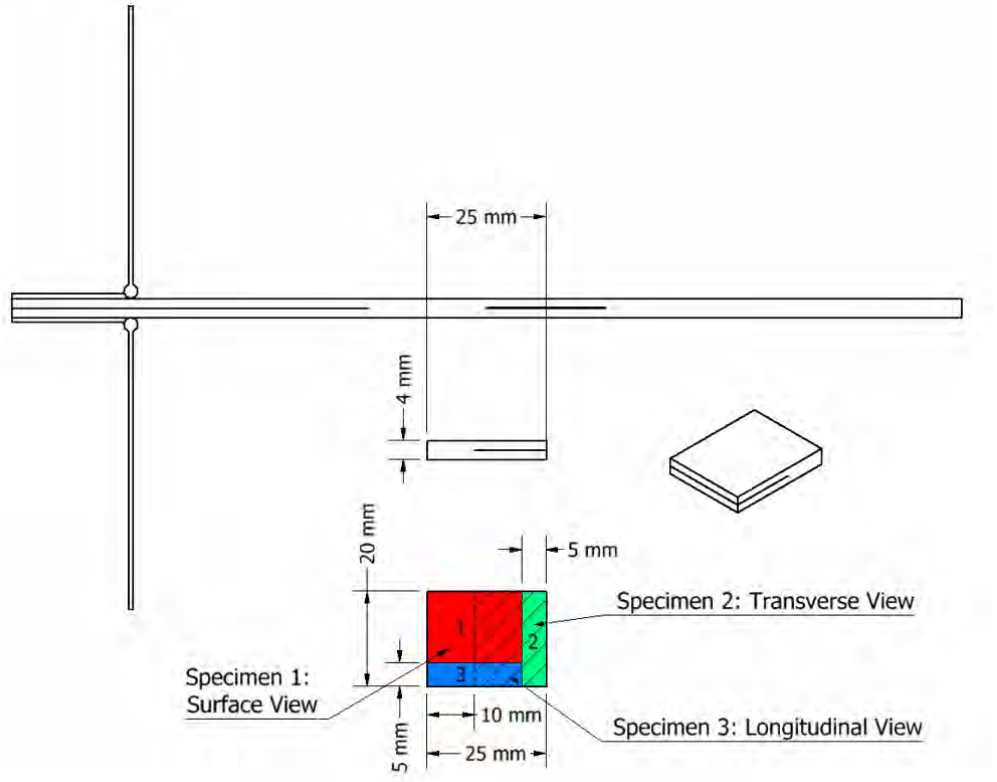

Figure 5.8: SEM specimen dimensions for a DCB specimen with the three views analysed: surface (1), transverse (2), and longitudinal (3).

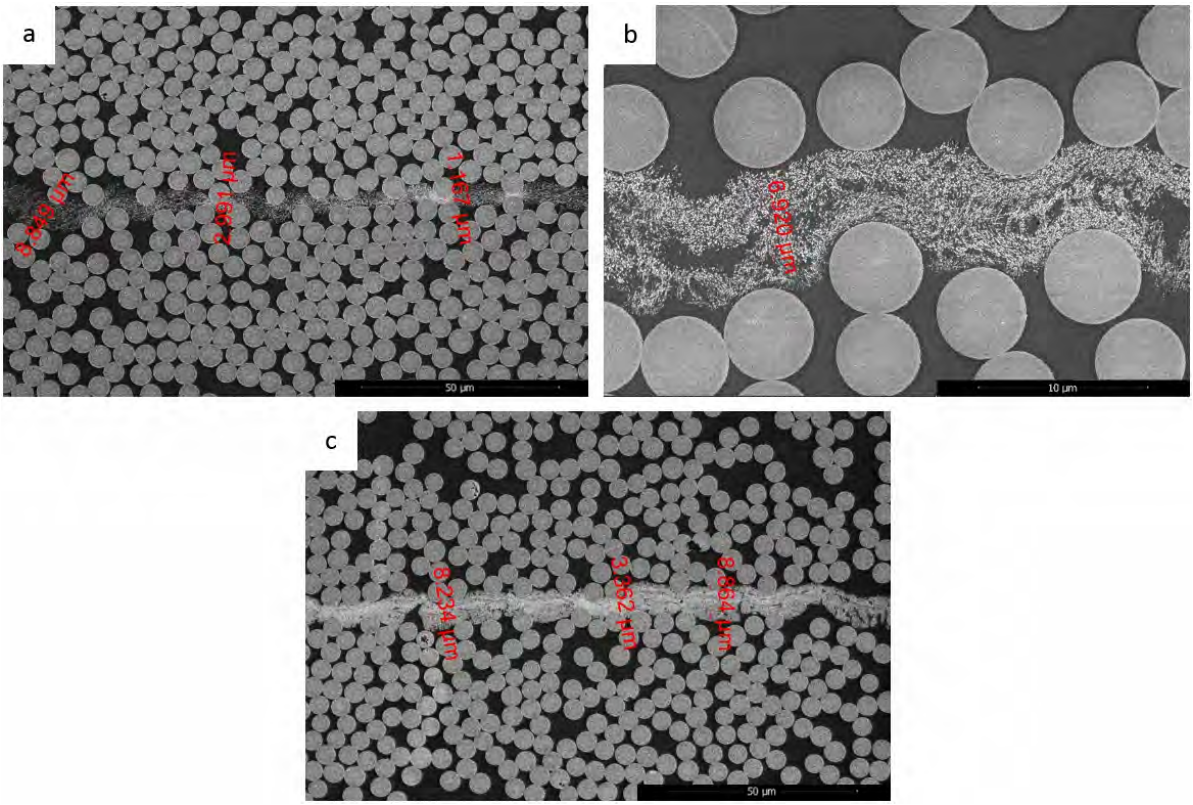

Figure 5.9: Transverse view SEM images of the interleaved interlaminar region with (a) low density, (b) medium density, and (c) high density VACNT interleaves.

with very little evidence of resin rich areas. The extent of nanotube buckling was found to be proportional to the density of the nanotubes, with the effective height loss being greatest for the low density VACNTs. This is believed to be a consequence of the low density VACNTs having the least resistance to deformation as concluded by Yaglioglu *et al.* [166].

5.3.1.2 VACNT patterning

A concern with the pattern manufacturing technique described in Section 5.2.2 was the feature size accuracy and edge quality of the VACNTs. As illustrated in Figure 5.10, the mask thickness will lead to some areas of contact loss between the nanotubes and prepreg during transfer. This will result in features becoming smaller than designed, as well as poor contact near the mask cut-out edges, leading to poor transfers and the potential for nanotube damage.

In order to assess the interleave quality, SEM images were captured of the areas where VACNT interleaves terminate across the specimen width. Figure 5.11(a-c) shows an example of this for a 'CB3' specimen. Overall, feature size was reduced by approximately 0.3 mm. VACNT termination was found to occur intermittently (see Figure 5.11b), with patches of nanotubes observed prior to final termination. However, little evidence of damage to either the nanotubes

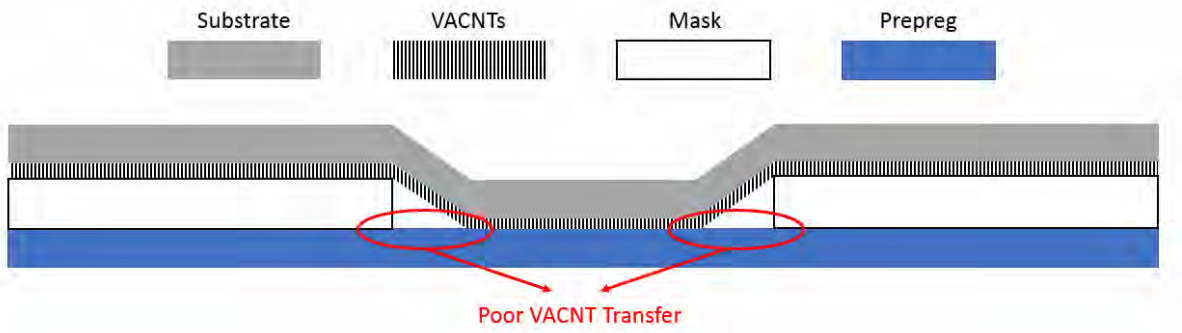

Figure 5.10: A schematic of the effect of mask thickness leading to curvature in the substrate and subsequently poor transfer at the edges of the mask cut-outs.

or fibre architecture was seen at the termination zone. Trials were conducted on thinner masks, however, their structural integrity was lost when removed from the adhesive cutting board.

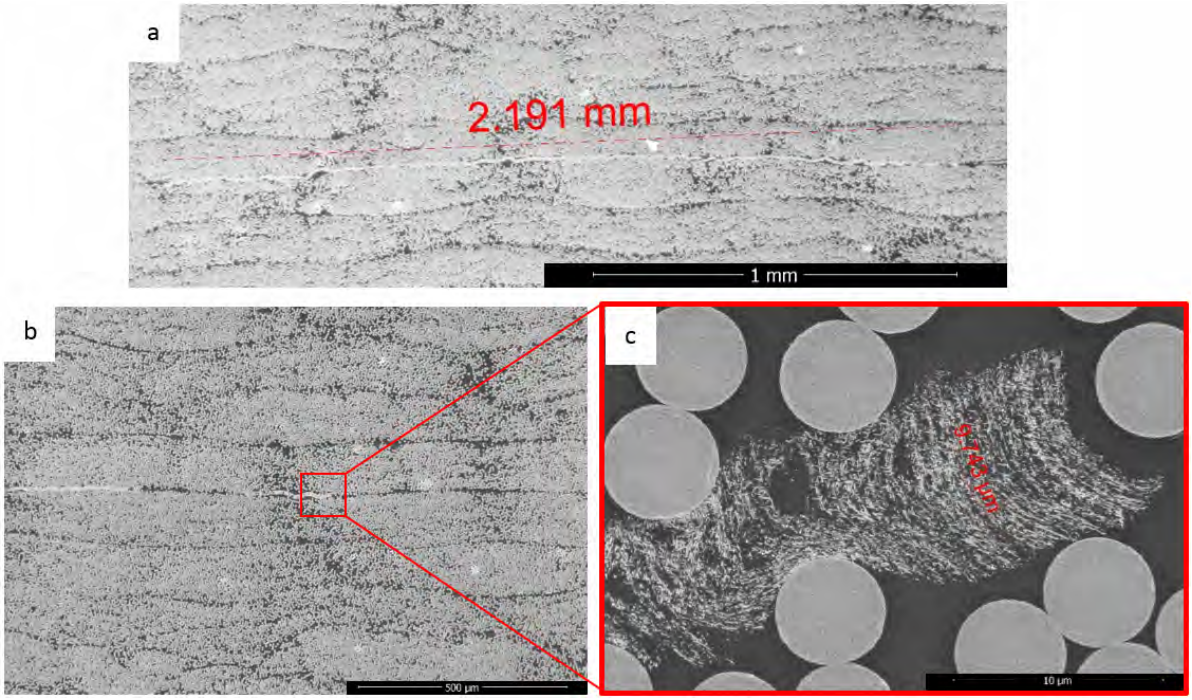

Figure 5.11: (a) The feature size of the transferred Chequerboard 2.5mm (CB3) interleaved specimen, (b) evidence of intermittent interleave termination for a Chequerboard 5mm (CB5) interleaved specimen with (c) a magnified end.

5.3.2 Mode I fracture testing

5.3.2.1 VACNT density

A typical load *versus* displacement graph of an unmodified baseline and each of the VACNT interleaves, with varying densities, are plotted in Figure 5.12. It can be seen that as the crack propagates into the interleaf region, the load diverges away from the baseline. Load enhancements were similar for all interleaf types tested. Upon surpassing the interleaf region, a sudden load drop led to the loads returning back to baseline values.

The average Mode I critical strain energy release rate, G_{IC}, for all of the tested specimens is plotted in Figure 5.13. All specimens showed similar crack initiation properties at ≈ 220 J/m^2, which supports the values reported in chapter 3 and 4. As the crack propagated, the fracture toughness for the baseline specimen rose due to fibre bridging effects, before reaching a plateau at ≈ 255 J/m^2 immediately before the interleave region at a crack length of 75 mm. For the unmodified baseline, this toughness remained constant for the remainder of the test. Although

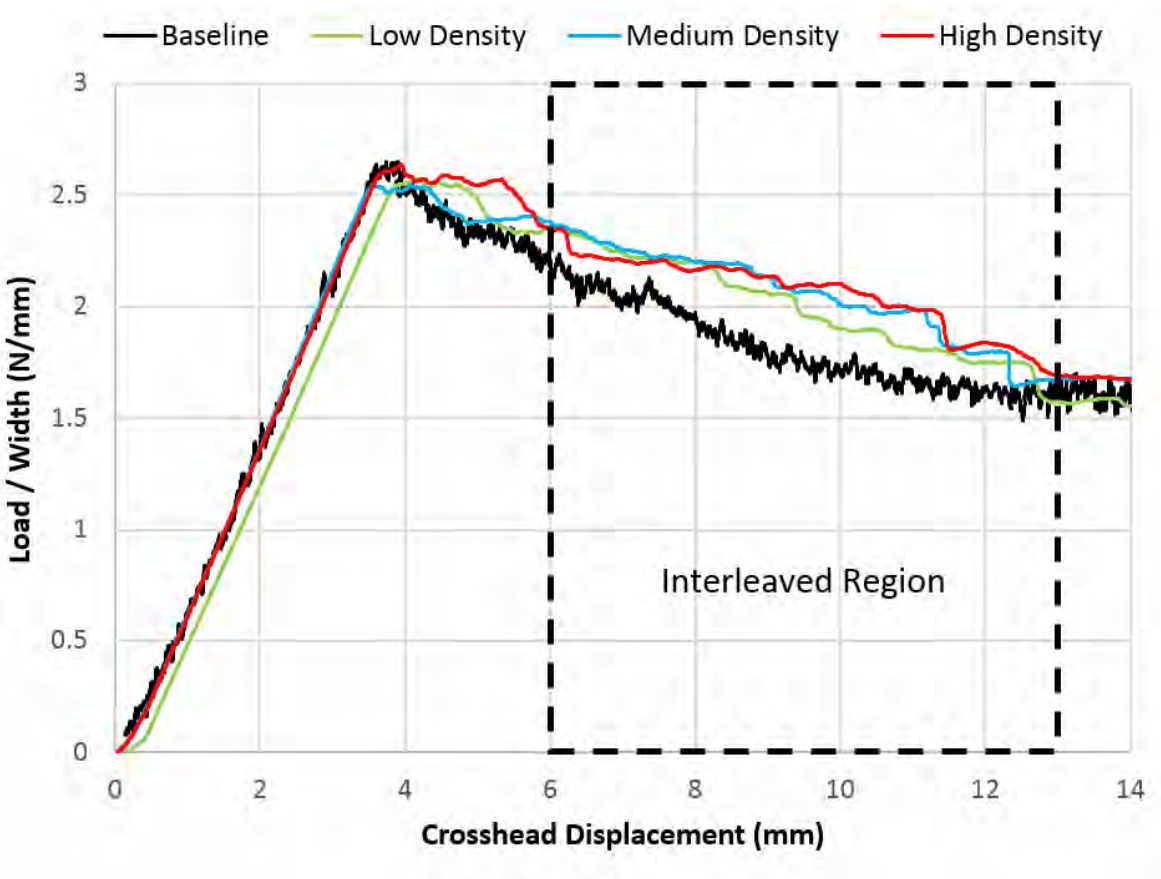

Figure 5.12: Load per unit width for a baseline, low density, medium density and high density VACNT interleaved IM7/8552 under Mode I conditions.

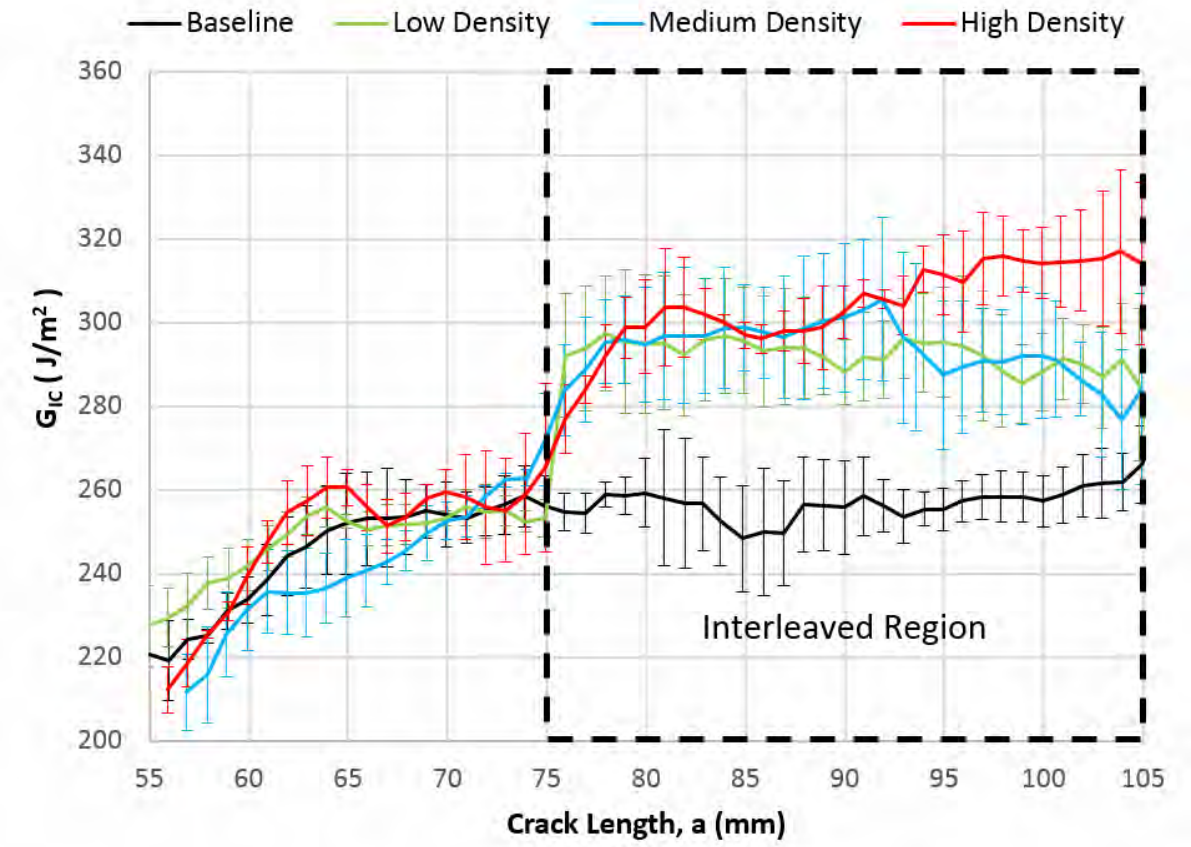

Figure 5.13: R-Curve for the Mode I interlaminar fracture toughness of a baseline, low density, medium density and high density VACNT interleaved IM7/8552. Error bars signify ± one standard deviation away from the mean.

this value is lower than that reported in chapter 3 (≈ 275 J/m^2), the difference is marginal and has been attributed to the change in central-ply offset; The larger offset angle reduces the amount of fibre bridging during crack propagation, thereby lowering the G_{IIprop} value.

All VACNT interleaved specimens exhibited a toughness growth at the interleaf region to ≈ 300 J/m^2. This equates to a $15-20\%$ improvement, which is similar to the behaviour observed in chapters 3 and 4 and independent of VACNT density.

5.3.2.2 VACNT patterning

5.3.2.2.1 Fracture toughness enhancement

Figures 5.15 - 5.17 show some typical load *versus* displacement plots with their corresponding R-curves for each of the VACNT patterns investigated. Regions of interleaf reinforcement can be clearly identified through load rises, while regions of interleave termination are accompanied by a sharp load drop. This translates to ordered patterns showing periodic toughness enhancements (Figure 5.15), while unordered patterns were found to exhibit inconsistent toughness profiles (Figure 5.16). Regardless, the peak toughness magnitudes were found to be similar to that of the homogeneous VACNT interleaves reported in Figure 5.13.

Figure 5.19 illustrates the toughness enhancement bands, *i.e.* the region that encompasses the maximum and minimum measured fracture toughness for all of the specimens tested with patterned interleaves. The bands have been divided between the unmodified region (when $a < 75mm$) and the interleaved region (when $a > 75mm$). It can be seen on the plot that in the interleaved region, the lower bound of the bands coincide with the baseline, while the upper bound range between 320-350 J/m^2. This suggests that the fracture toughness measured at the lower bounds coincide with interface regions that are unmodified, while measurements at the upper bound signifies regions where VACNTs are present at the interface.

Comparing the R-curves for the two chequerboard configurations tested (Figure 5.17), it appears that the smaller feature size results in a greater toughness enhancement, even exceeding that of a homogeneous VACNT film shown in Figure 5.13. The reasoning for this shall be discussed later in Section 5.3.3.2. The smaller chequerboard feature size also resulted in more uniform toughness enhancements during the interleaved region. This suggests that intermittent interleaf reinforcement has a similar effect to a homogeneous variant under Mode I conditions.

5.3.2.2.2 Crack growth rate

A typical crack growth rate profile for each of the VACNT interleaf pattern designs is plotted in Figures 5.18(a-d). Each plot shows the tracked crack length relative to the grip opening displacement for either side (defined ‘front‘ and ‘rear‘) of the specimen. For clarity, these side definitions are annotated in Figure 5.14. Overall, the crack growth rate was found to reduce as the crack enters the interleaf region as more work was required for it to propagate.

Prior to the crack entering the interleaved region, the crack growth rate was found to be equal on the front and rear sides of the specimen. This behaviour continued as the crack entered the interleaf region of the chequerboard patterns, however it diverged for the Chevron and Random interleaf design specimens. Figure 5.18e shows the 4 designs tested in this study with two cuts, illustrated as two dashed lines spaced at a specimen width (or 20 mm) apart. It can be seen that all designs, except Random, have a period which coincides with the specimen width. This explains

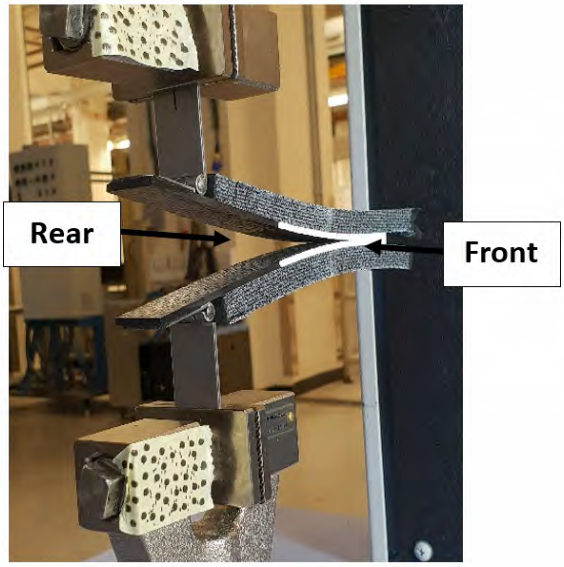

Figure 5.14: Side definition of a VACNT patterned interleaved DCB specimen during testing.

why no difference in crack growth rate was detected for the chequerboard designs, however it does not explain the behaviour measured in the Chevron design. The reasoning for this discrepancy is believed to be attributed to the manufacturing accuracy of the technique described in Section 5.2.2. Although the masks were cut to a high accuracy, the high length and low thickness of the mask film used resulted in difficulties when placing it in position on the exposed prepreg, and hence led to a reduction in the geometric accuracy of the VACNT pattern. Therefore, it is highly likely that the actual cutting planes of the 'Front' and 'Rear' sides followed a plane similar to the red and green lines illustrated in Figure 5.18e, rather than the red and black lines. This would mean that when the crack propagated through the interleaf region, one side of the specimen will consistently reach the VACNTs first and hence the growth rate will diverge. This scenario has been simulated and plotted in Figure 5.20. All points on this graph have been approximated from the values measured in Figure 5.18a, and the relationship between crack growth rate and opening displacement has been assumed linear. Comparing these two plots (Figure 5.18a and Figure 5.20), very similar behaviours can be seen. This suggests that geometric inaccuracies in the patterned interleaf are the cause of crack growth discrepancies between either side of the Chevron interleaved DCB specimens. For the 'Random' pattern, a crack growth divergence was also visible at the interleaf region, however a periodic behaviour was not observed due to the lack of periodicity in the pattern design.

Overall, these profiles indicate that crack behaviour can be controlled through the patterned architecture of the interleaves. For example, interleaf patterns could ensure cracks gradually deflect in-plane away from critical areas such as edges or notches.

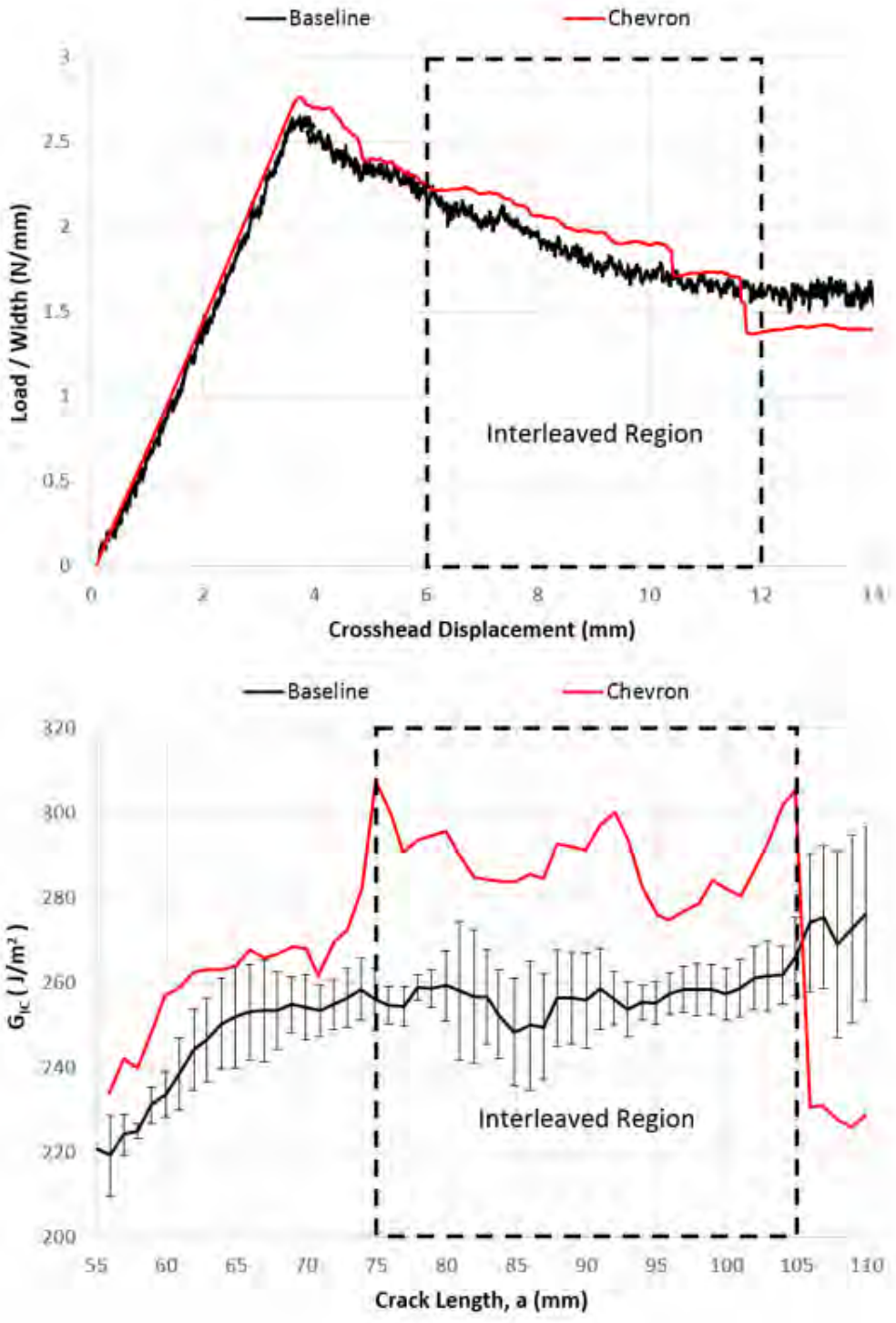

Figure 5.15: A typical load *versus* displacement plot and corresponding R-curve for a DCB specimen with a Chevron pattern VACNT interleaf.

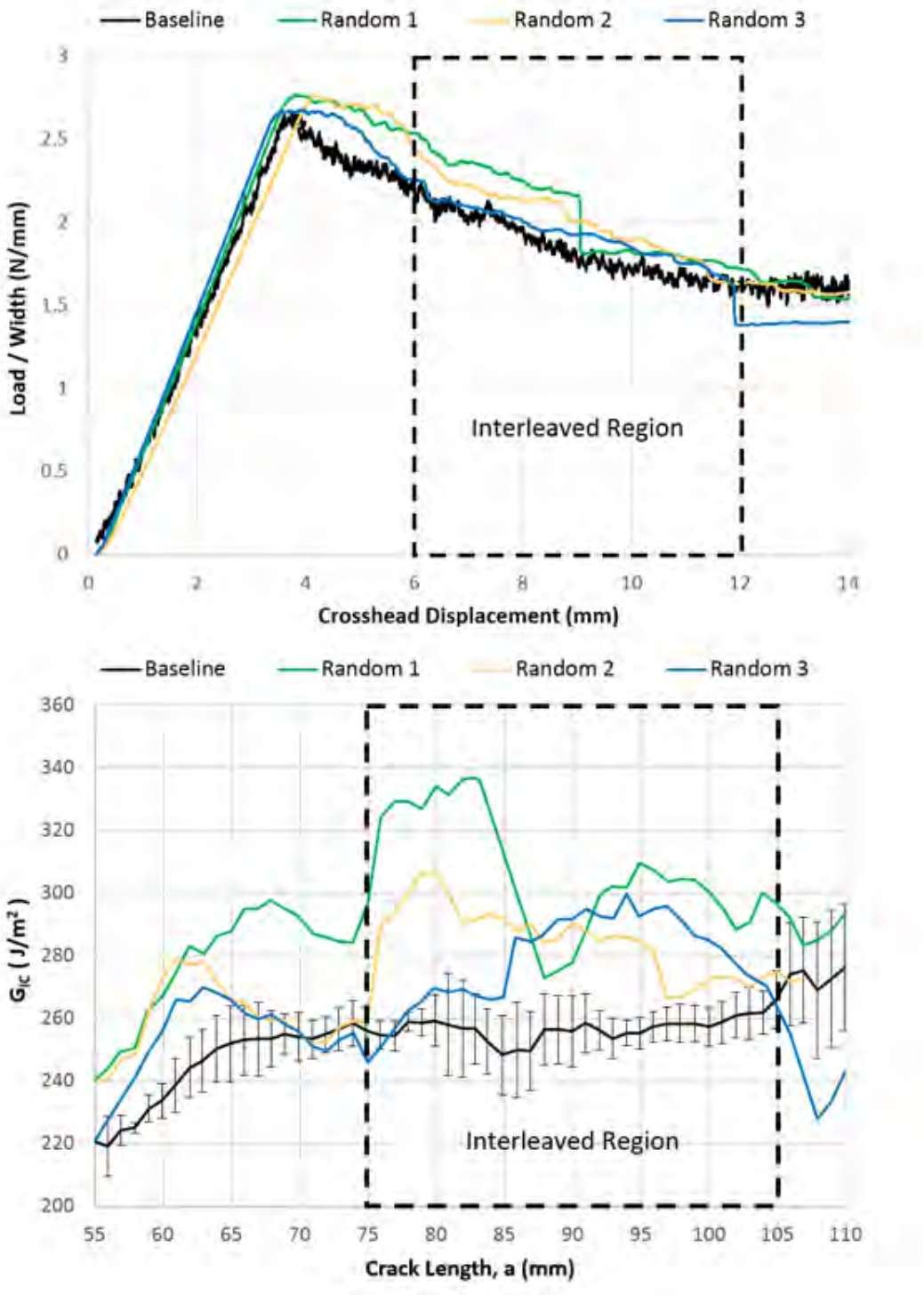

Figure 5.16: Typical load *versus* displacement plots and corresponding R-curves for a DCB specimens with a Random pattern VACNT interleaf.

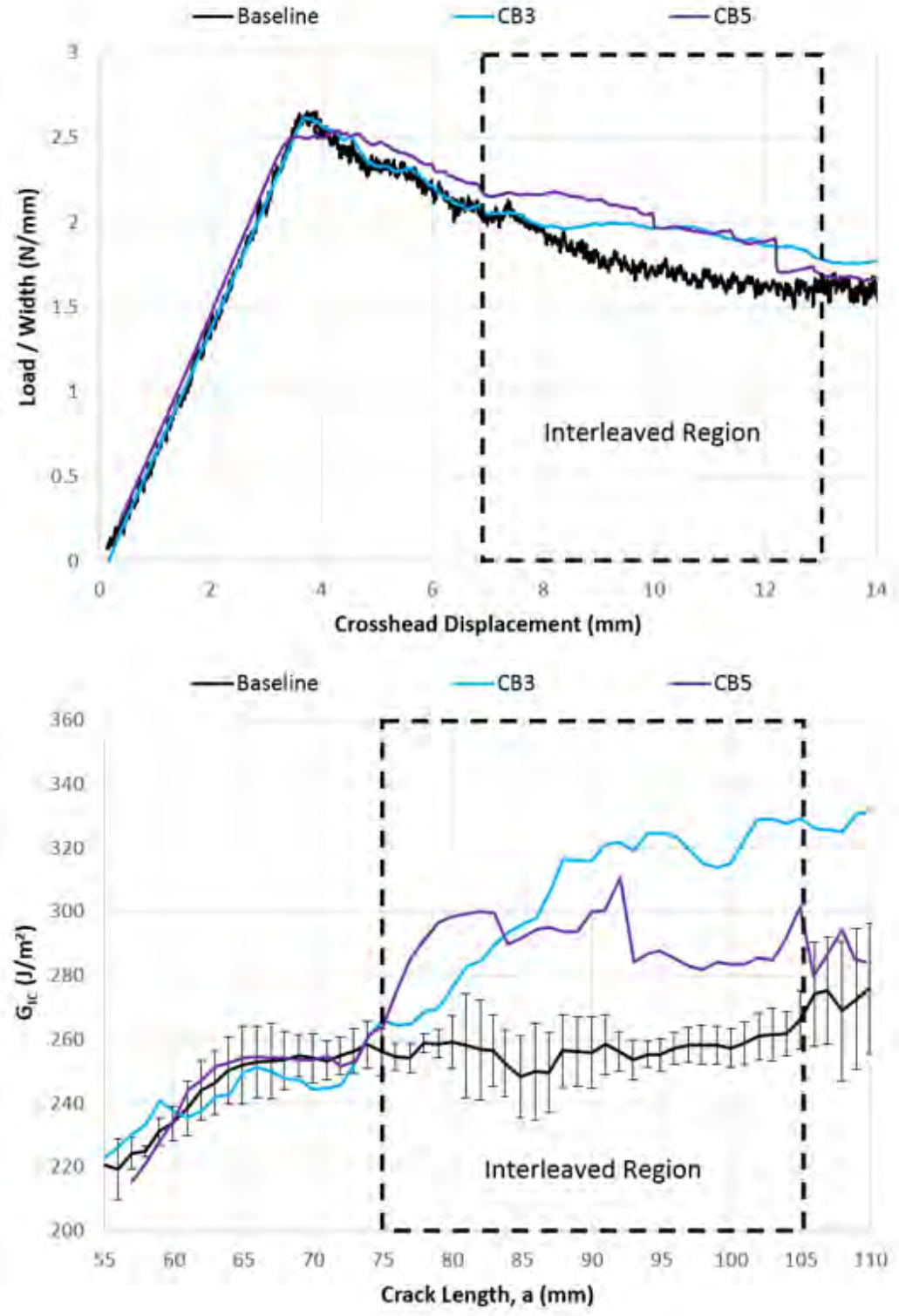

Figure 5.17: A typical load *versus* displacement plot and corresponding R-curve for a DCB specimen with VACNT interleaved Chequerboard patterns of 2.5mm (CB3) and 5mm (CB5) feature sizes.

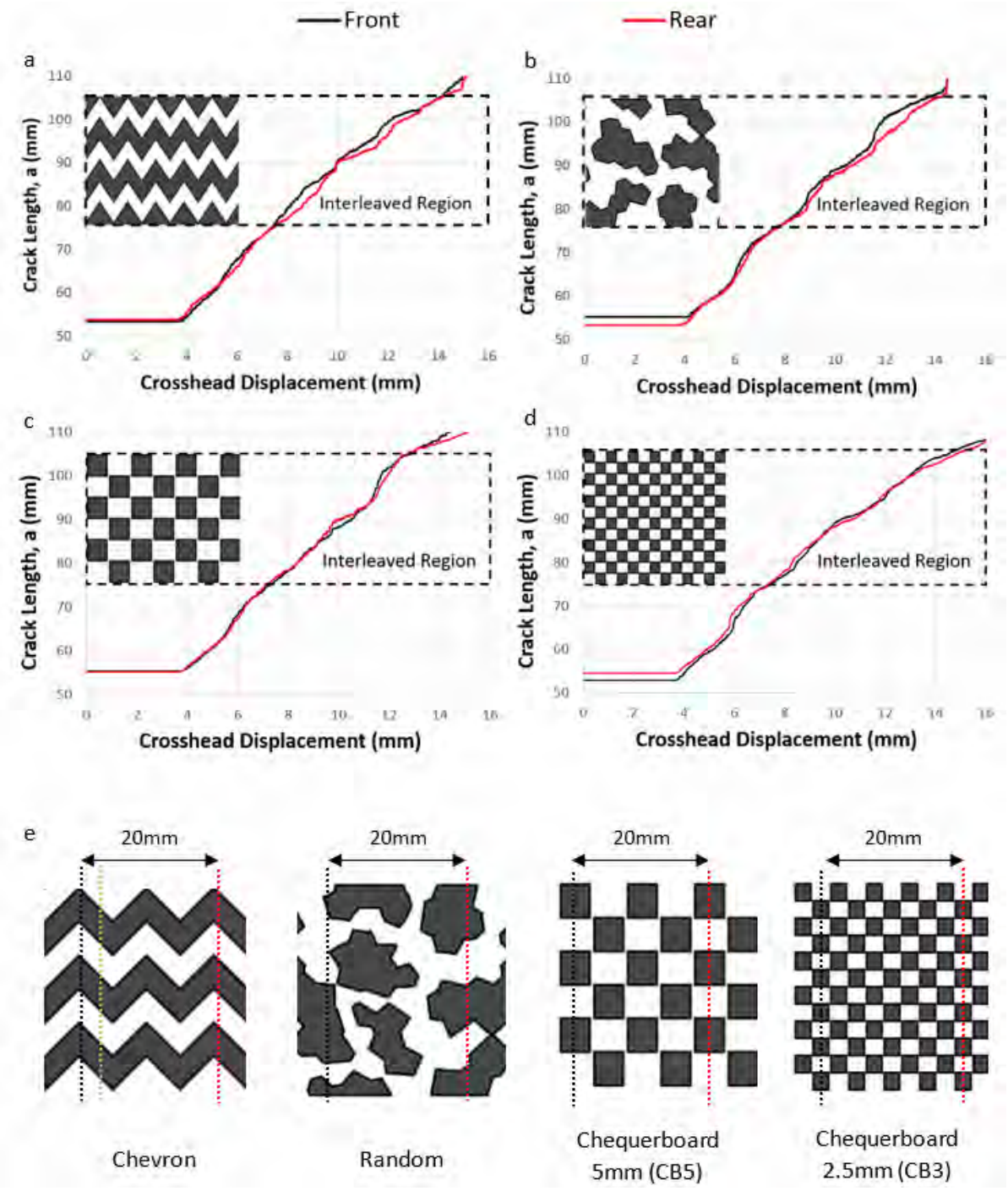

Figure 5.18: Crack growth profiles on the front and rear sides of the VACNT interleave patterns (a) Chevron, (b) Random, (c) Chequerboard (5mm), and (d) Chequerboard (2.5mm) tested under Mode I conditions. A schematic of the four interleaf patterns with dashed lines annotated to represent the cutting planes of a DCB specimen.

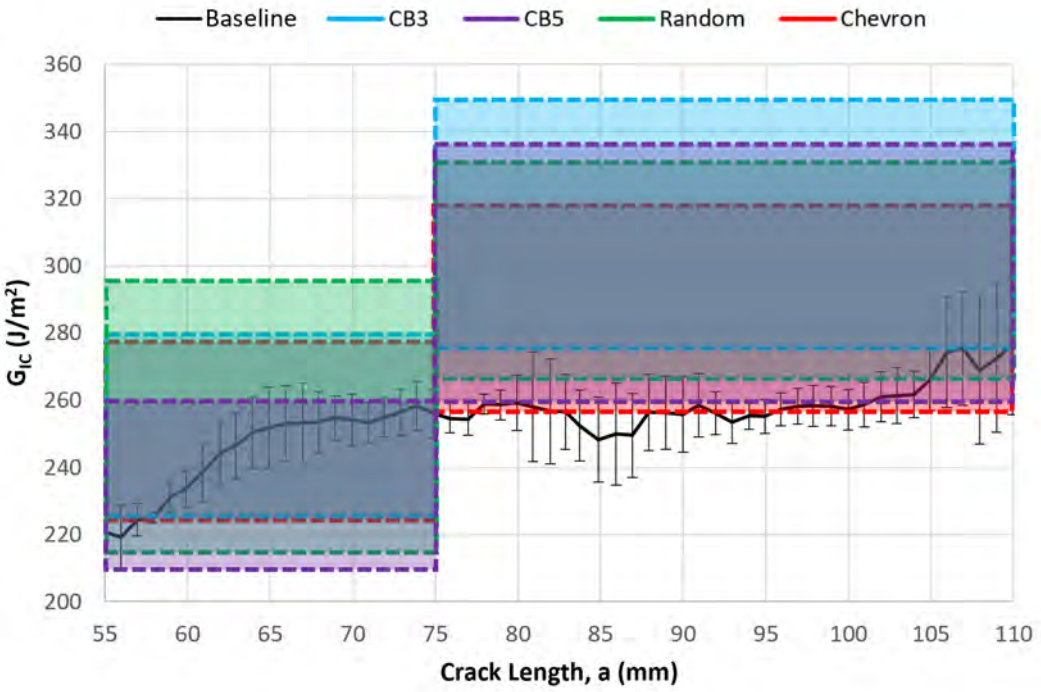

Figure 5.19: Mode I fracture toughness bands for DCB specimens with patterned interleaves.

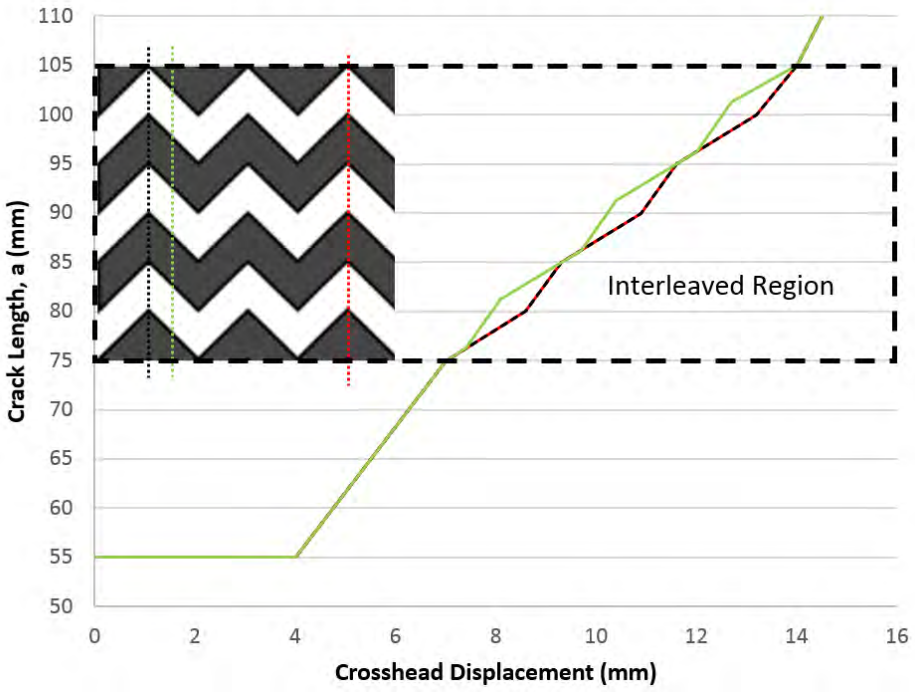

Figure 5.20: A representative example of the crack growth profiles in a VACNT interleaved DCB specimen, if cut at two different planes.

5.3.3 Mode I fractography

5.3.3.1 VACNT density

Capturing the longitudinal view at the VACNT interleaf initiation point, shown in Figure 5.21, it can be seen that the crack bifurcates from the interlaminar region into the intralaminar region, thereby by-passing the VACNTs. The crack then propagates parallel to the interleaf in a similar fashion to the VACNT interleaves previously reported in chapters 3 and 4.

Considering the transverse view at the interleaf regions, it was observed that intralaminar delamination occurred for every VACNT density tested. This can be seen in Figure 5.22. As discussed in chapter 3, evidence of the crack mapping the topology of the VACNT interleaf was again observed, however, owing to the reduced number of resin pockets, this was more subtle than previously seen. The less torturous crack path could be a factor influencing the lower absolute fracture toughness value measurement, reported in Figure 5.13. Occasionally, the crack

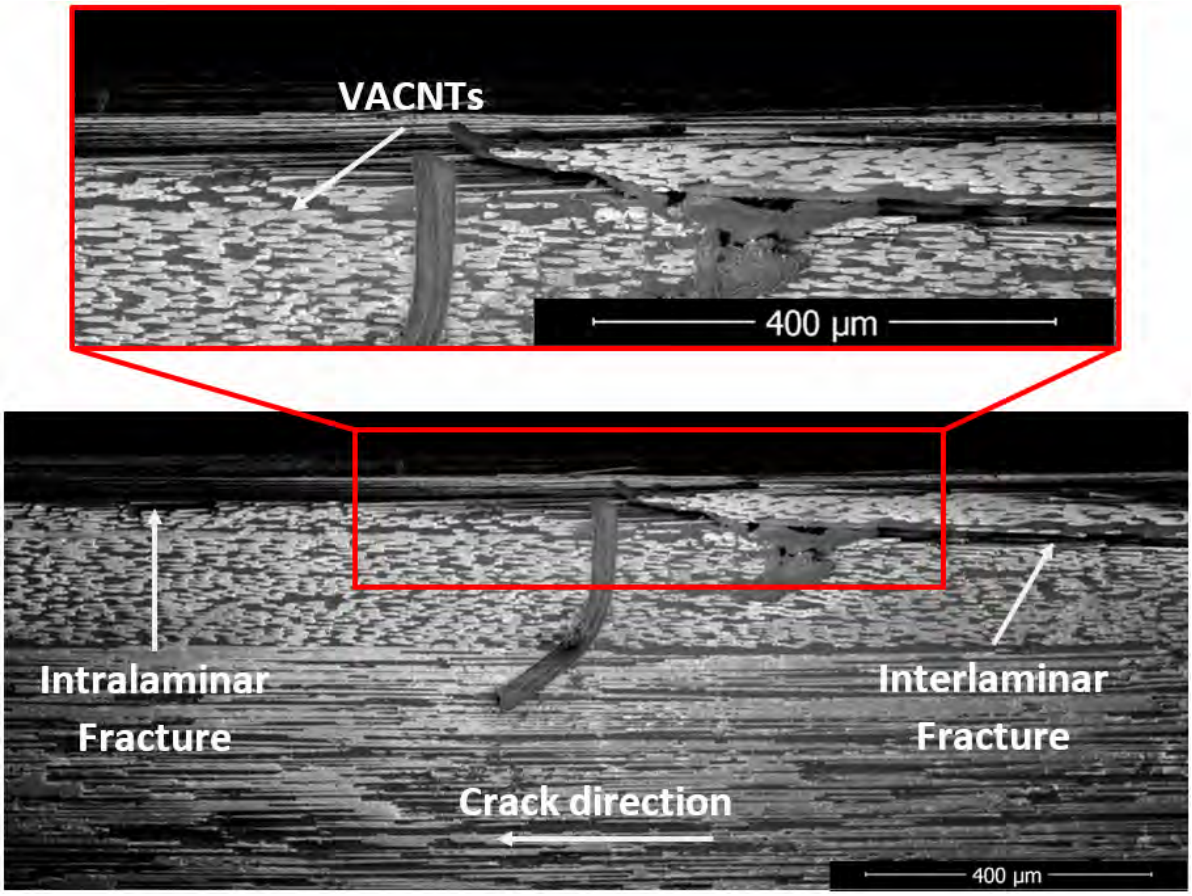

Figure 5.21: Longitudinal view SEM image of the medium density VACNTs showing the crack deflecting from the interlaminar to the intralaminar region through the introduction of the VACNT interleave film.

would propagate close to the interlaminar region, however it was found to propagate along the nanotube-fibre interface rather than pull-out or rupture the nanotubes as seen in Figure 5.22b and Figure 5.22c.

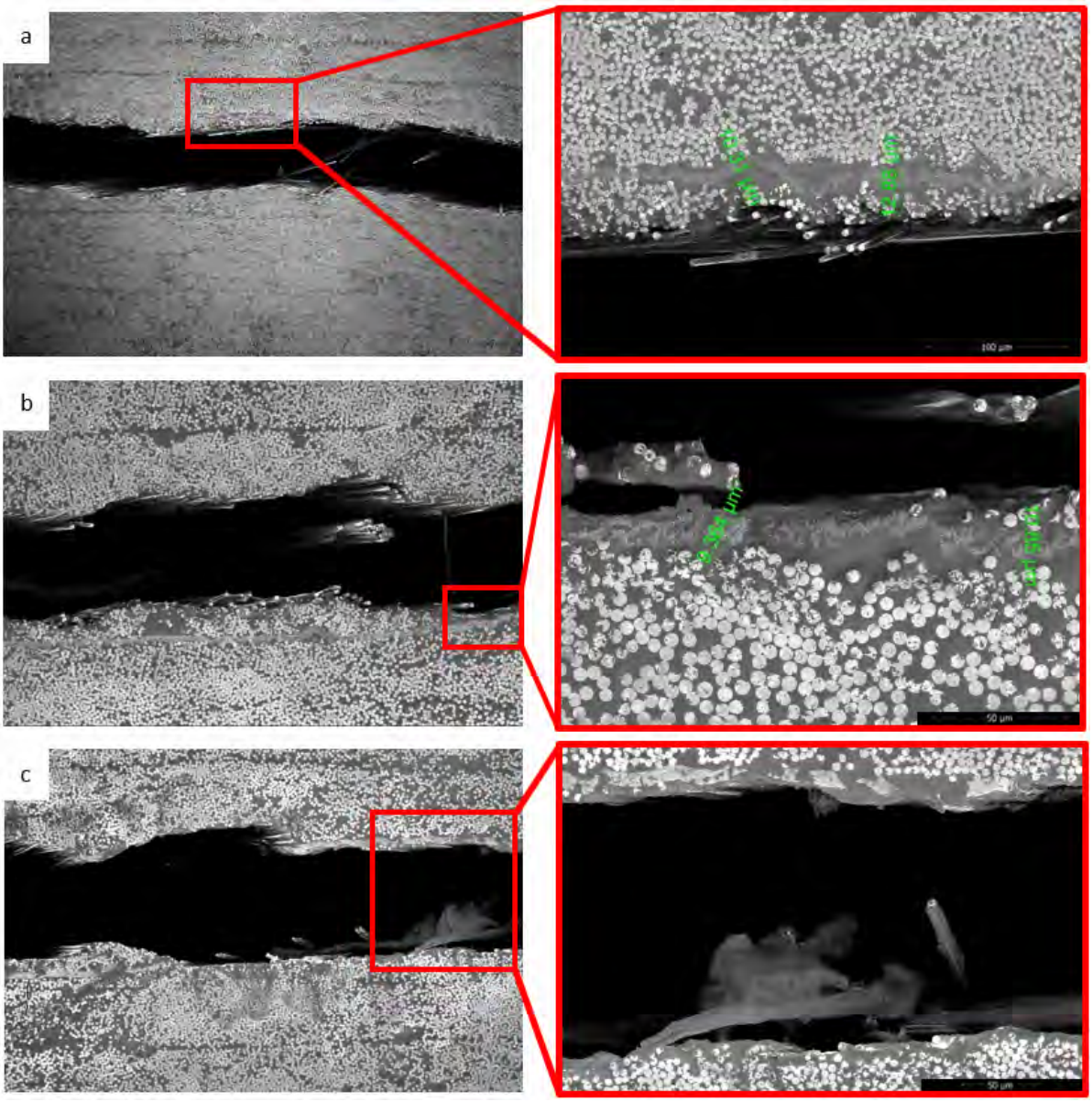

Figure 5.22: Transverse view SEM images of a typical intralaminar fracture within the interleaf region for (a) low density, (b) medium density, and (c) high density VACNT interleaved DCB specimens.

5.3.3.2 VACNT patterning

In common with all of the homogeneously distributed VACNT interleaved DCB specimens, fractography analysis captured intralaminar delamination within the patterned VACNT interleaved regions. However, unlike the homogeneous alternative, the discontinuous characteristics associated with the patterned interleaves led to crack branching features, *i.e.* a smaller crack disseminating from the main crack, as seen in Figure 5.23(a-b). This was found to repeatably occur at the locations where VACNTs were introduced. Such a mechanism will result in extra work being done through creating multiple fractured surfaces. Therefore, as the chequerboard pattern with smaller feature sizes (CB3) have more VACNT introduction points along its width, extra fracture surfaces are formed. This is one explanation for why the measured interlaminar fracture toughness of the Chequerboard 2.5 mm interleaved specimen exceeded that of the Chequerboard 5 mm and the homogeneously distributed VACNT interleaved specimens.

Despite the lack of order associated with the Random VACNT interleaf design, cracks were observed to propagate parallel to the fibre orientation, as seen in Figure 5.23c. This suggests that the crack growth direction is dominated by the orientation of the fibres rather than the interleaf shape, *i.e.* crack growth is still intralaminar dominated for patterned VACNT interleaved DCB specimens.

5.3.4 Mode II fracture testing

5.3.4.1 VACNT density

A typical load *versus* displacement plot for ELS specimens interleaved with VACNTs of differing densities is shown in Figure 5.24. For all configurations, the load per unit width increases linearly, before reaching a maximum around 8 N/mm, corresponding to crack growth initiation. As the crack propagates, the load decreases, before shortly rising again for the interleaved specimens. This corresponds to the location where the VACNTs are introduced. Here, the Mode II strain energy increases in the system, as the crack is momentarily suppressed. At the second load peak, the crack begins to propagate. Unlike the ELS tests previously discussed in this research, crack propagation was found to be unstable for the majority of the VACNT interleaved specimens.

The average Mode II critical strain energy release rate is plotted in Figure 5.25. Initiation was found to start around 620 J/m^2 for all specimens, before rising due to fibre bridging effects. Baseline specimens were found to plateau around 675 J/m^2. Mode II interlaminar fracture toughness tests completed by Yasaee *et al.*, found similar results for an unmodified baseline IM7/8552 prepreg system when tested under end notched flexure (ENF) conditions [223].

With the introduction of the VACNT interleaves, the interlaminar fracture toughness was found to increase to ≈ 710 J/m^2. This is equivalent to a $5-7\%$ increase in fracture toughness, slightly less than the resin embedded nanotube variant reported in chapter 3 and chapter 4. Furthermore, all nanotube interleaf specimens were found to fail in an unstable manner at the

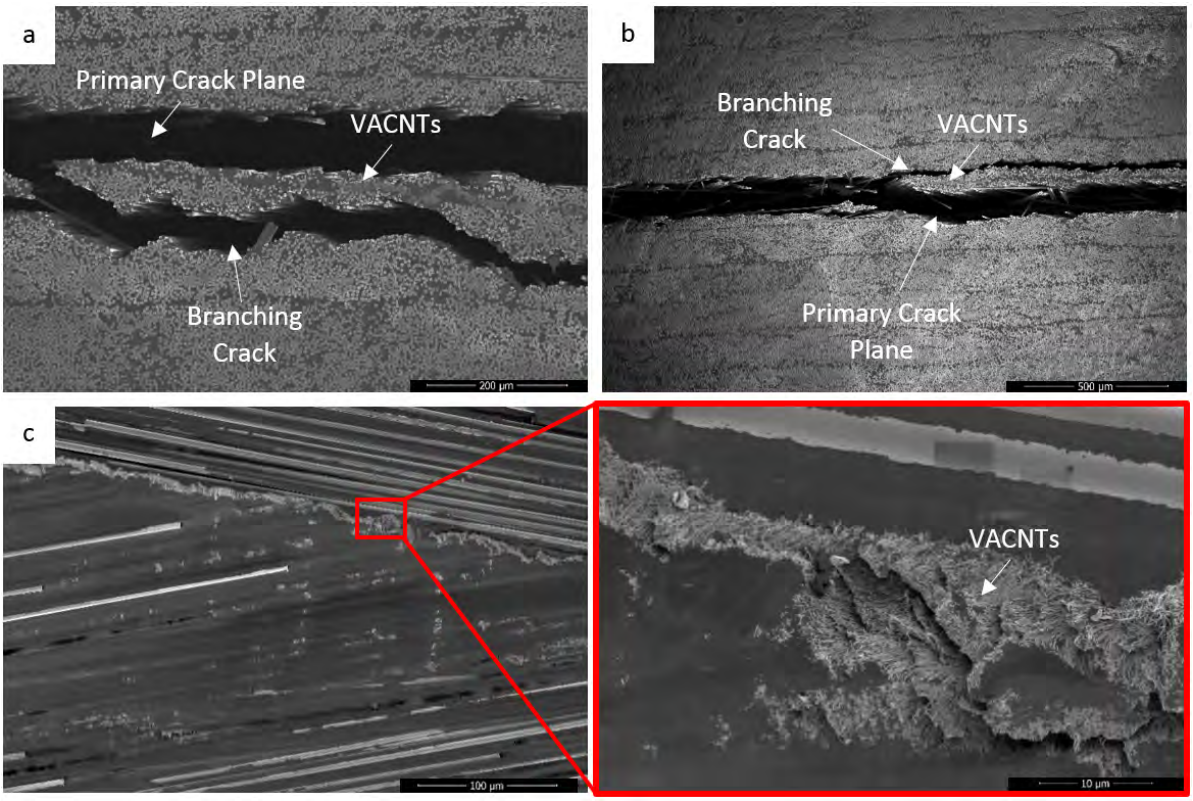

Figure 5.23: SEM images of fractured DCB interleaved specimens showing (a) transverse view of crack branching in a CB5 specimen, (b) transverse view of crack branching in a CB3 specimen, and (c) the surface view of the Random pattern showing failure parallel to the fibre orientation.

enhanced fracture toughness state. In some cases, this happened immediately after the interleaf was introduced and the strain energy rose, while others occurred after around 5 – 10 mm into the interleaved region.

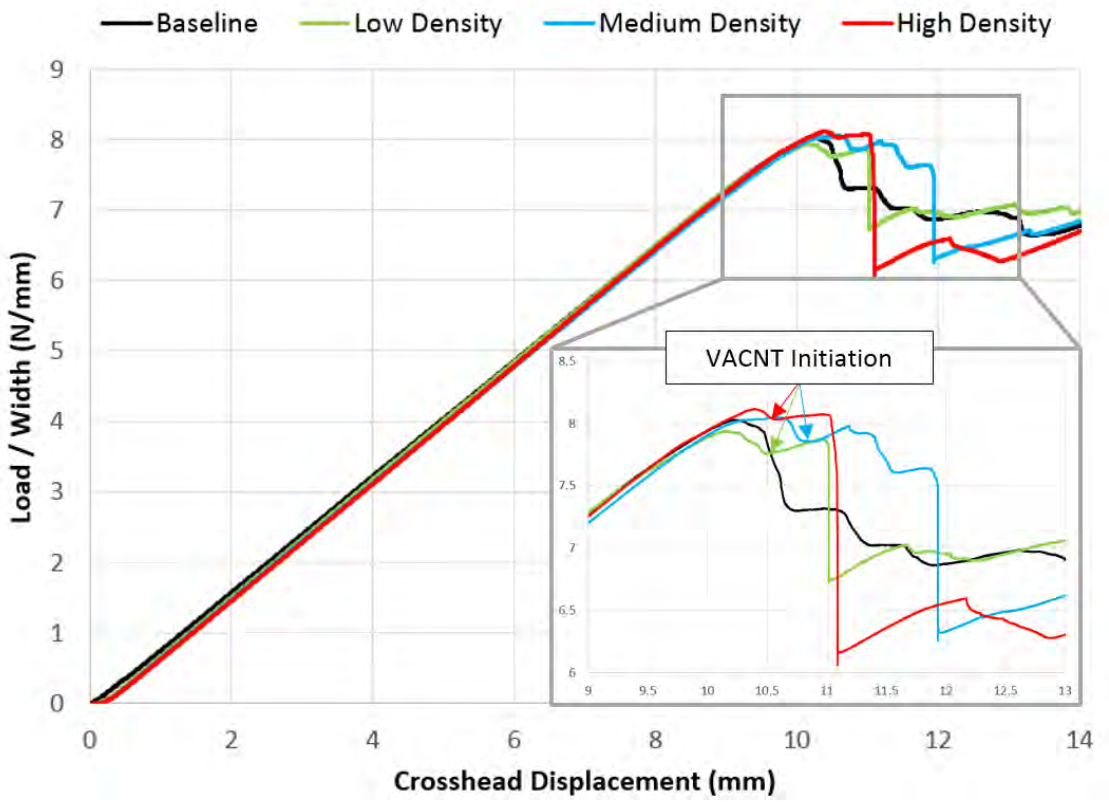

Figure 5.24: Load per unit width for a baseline, low density, medium density and high density vertically aligned carbon nanotubes interleaved IM7/8552 under Mode II conditions.

5.3.4.2 VACNT patterning

Figures 5.26 - 5.28 show typical load *versus* displacement plots with the corresponding R-curves for each of the VACNT interleaf pattern designs tested in Mode II conditions. In common with the Mode I experiments, VACNT interleaved areas can be distinguished through load and fracture toughness rises, while regions of interleaf termination are accustomed to load and fracture toughness drops. For the Chevron and Random patterns, the load drops occur in an unstable manner, while the Chequerboard patterns, particularly at the lower scales, were more stable during fracture. As these patterns have approximately the same nanotube areal density in the interleaved region as that of the 'low density' homogeneous variant, it appears that patterning of the VACNT interleaf can stabilise the crack growth behaviour. Therefore, interleaf patterning can increase the chance of detecting damage before it leads to catastrophic failure.

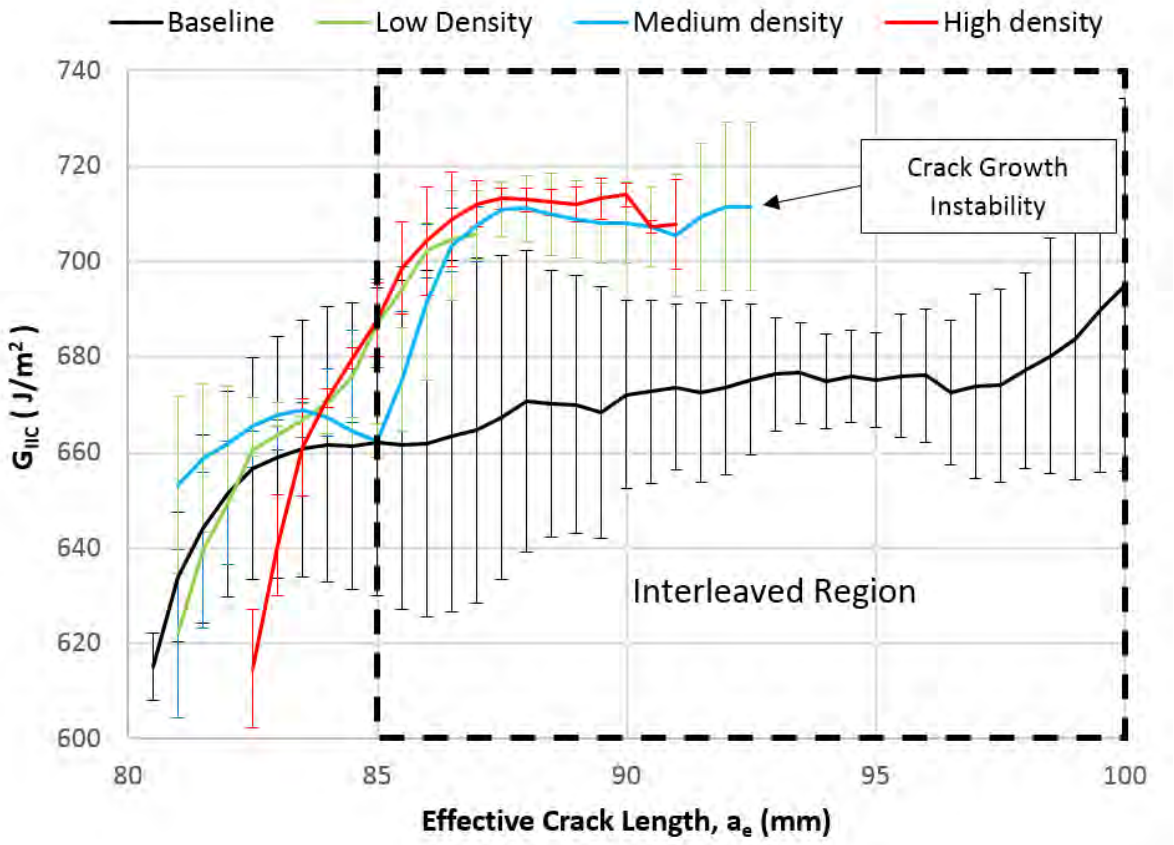

Figure 5.25: R-Curve for the Mode II fracture toughness of a baseline, low density, medium density, and high density VACNT interleaved IM7/8552. Error bars signify ± one standard deviation away from the mean.

5.3.5 Mode II fractography

5.3.5.1 VACNT density

Transverse view images, as shown in Figure 5.29, were taken shortly after the point of instability, at a crack length of 95 mm, for all specimen configurations. Similar features to that seen in chapter 3 and 4 were observed, *i.e.* intralaminar delamination at the interleave region (Figure 5.29(a-c)), whereby cracks map the VACNT topology (Figure 5.29b) and propagate through the fibre-matrix interface (Figure 5.29d). Along with the data reported in Section 5.3.4.1, this suggests that as the crack reaches the VACNT interleave, it is temporarily suppressed. Then, as the loading continues, strain energy begins to build until reaching a value which exceeds the critical strain energy release rate for intralaminar fracture ($\approx 5-10\%$ above that for interlaminar fracture), and the crack deflects into the intralaminar region. This value is dictated by the interfacial properties between IM7 carbon fibre and 8552 epoxy resin. At the heightened energy

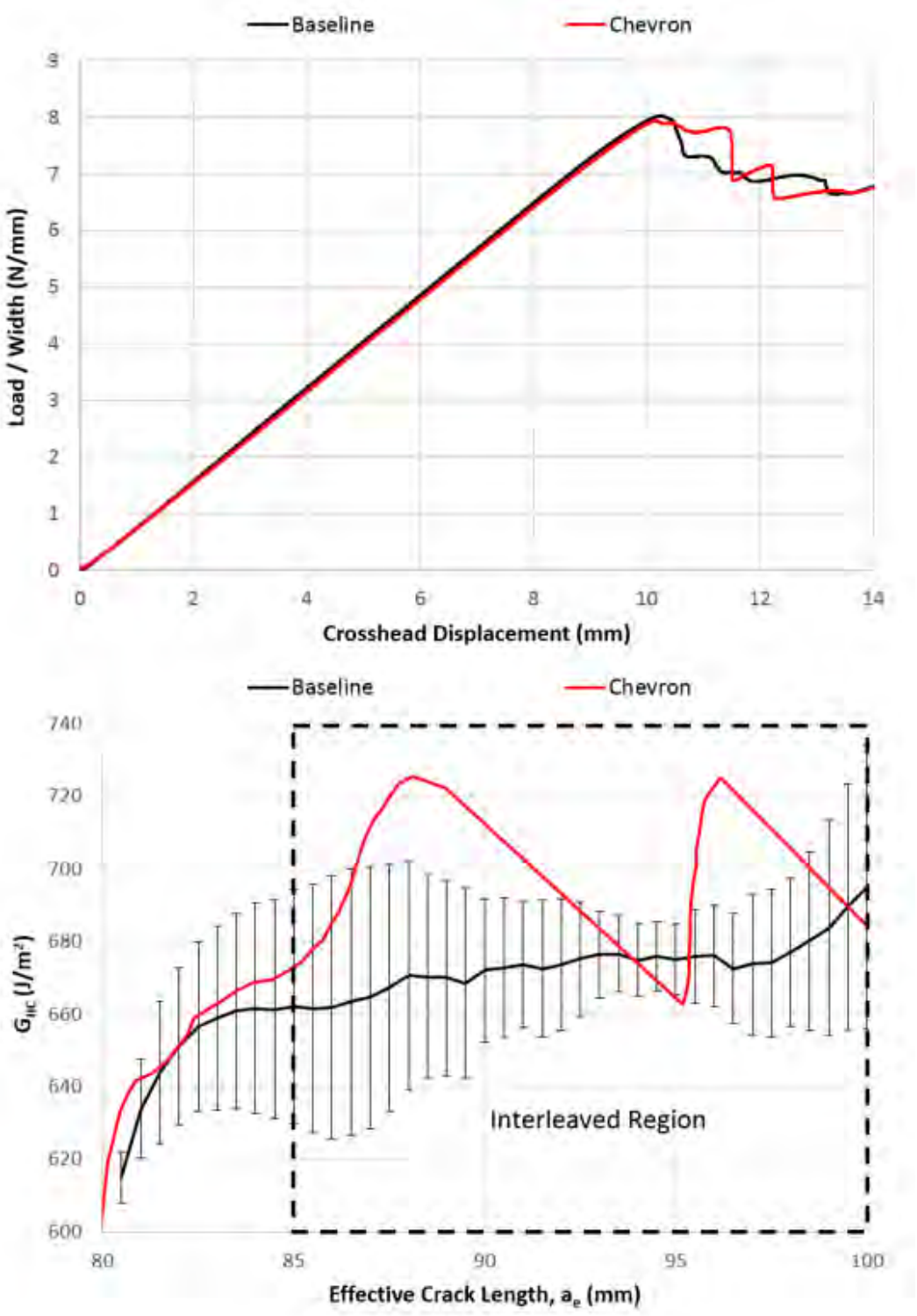

Figure 5.26: A typical load *versus* displacement plots and corresponding R-curve for an ELS specimen with Chevron VACNT interleaf.

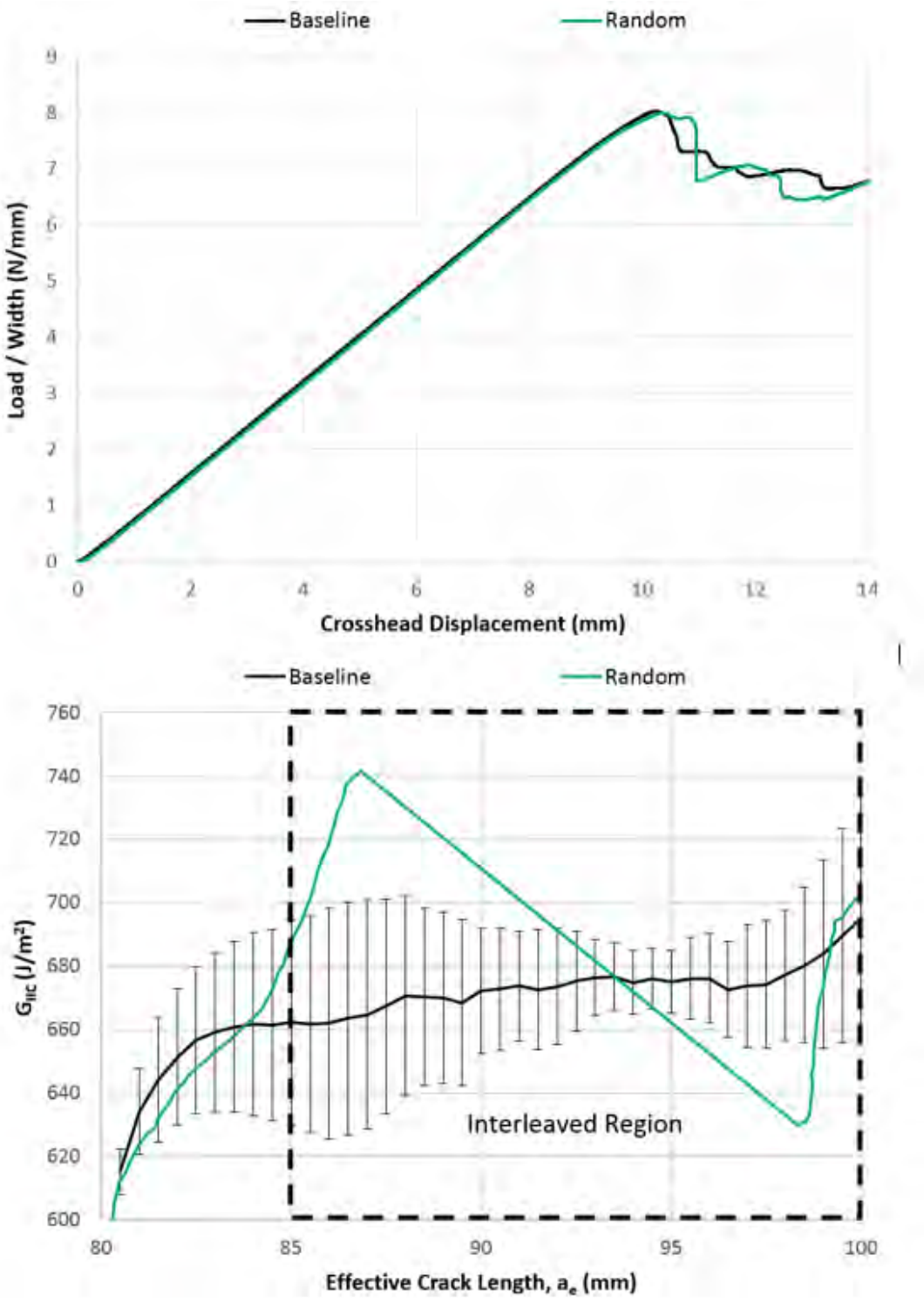

Figure 5.27: A typical load *versus* displacement plot and corresponding R-curve for an ELS specimen with Random VACNT interleaf.

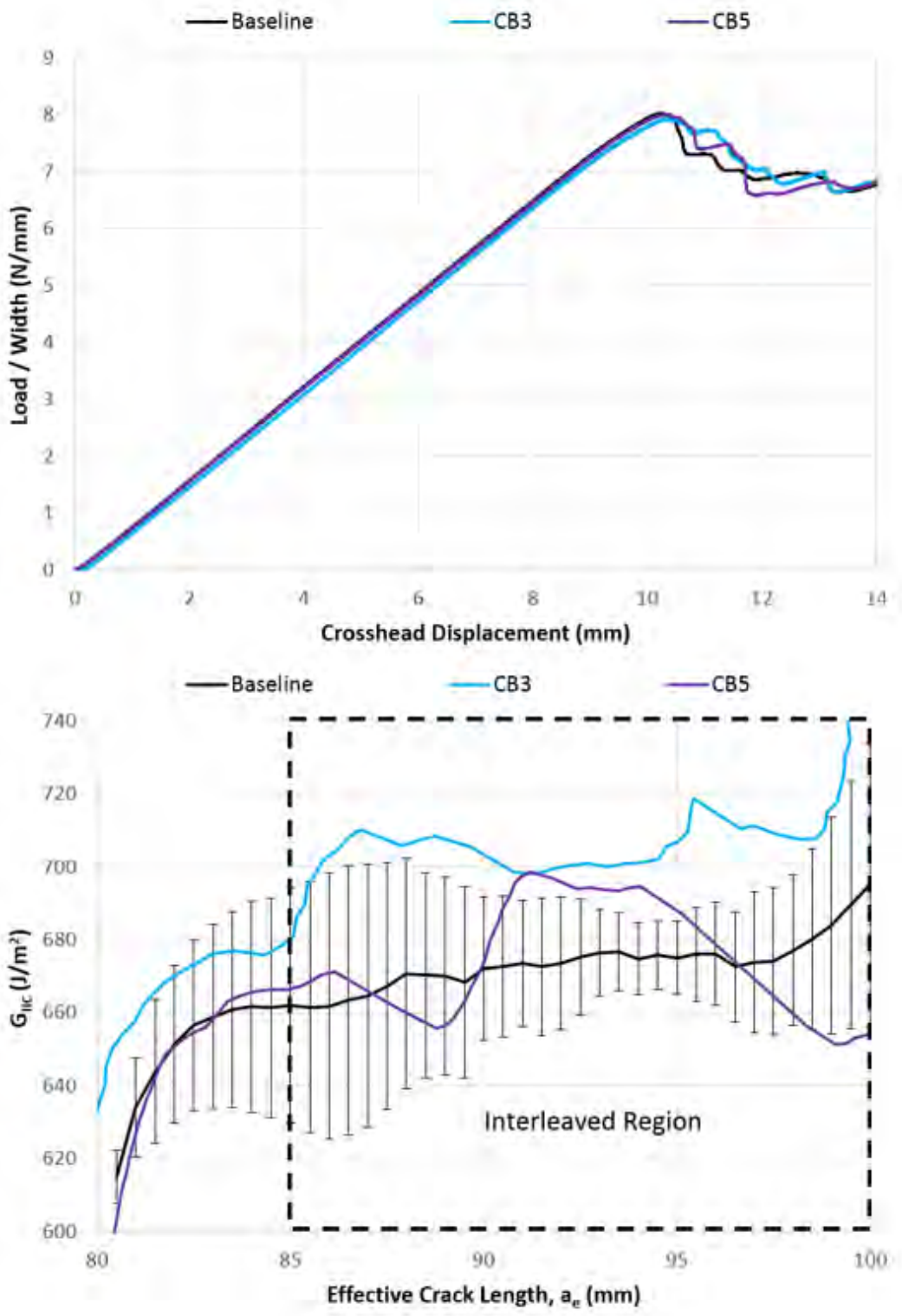

Figure 5.28: A typical load *versus* displacement plot and corresponding R-curve for an ELS specimen with Chequerboard VACNT interleaves with 2.5mm (CB3) and 5mm (CB5) feature sizes.

level, the stability criteria defined by Williams for interlaminar fracture [218] breaks down and cracks propagate in an unstable manner.

5.3.5.2 VACNT patterning

A selection of SEM images from the fractured ELS specimens with patterned VACNT interleaves can be seen in Figure 5.30. Unlike the Mode I specimens, no crack branching was observed for any of the specimens. Failure at the interleaf region was dominated by intralaminar fracture (Figure 5.30(a-b)), with evidence of crack deflection showing the transition between interlaminar and intralaminar delamination at the location of VACNT introduction (Figure 5.30c). Surface view images (Figure 5.30d) show a transition between cohesive interlaminar failure at the non-interleaved region, to fibre debonding failure, commonly associated with intralaminar delamination [236], at the VACNT interleaved region.

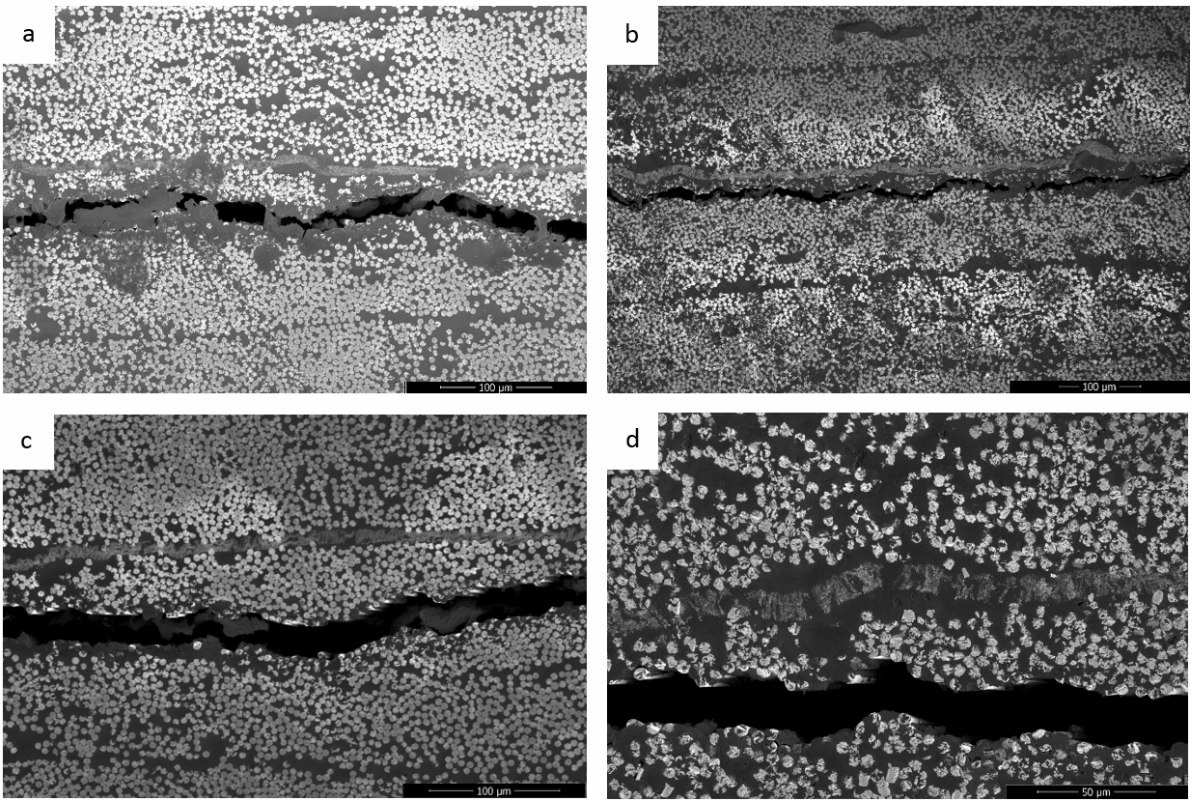

Figure 5.29: Transverse view SEM images of typical intralaminar fracture for (a) low density, (b) medium density, and (c) high density VACNT interleaved ELS specimens; (d) A magnified image of the medium density fracture shows fibre-matrix interfacial failure during delamination.

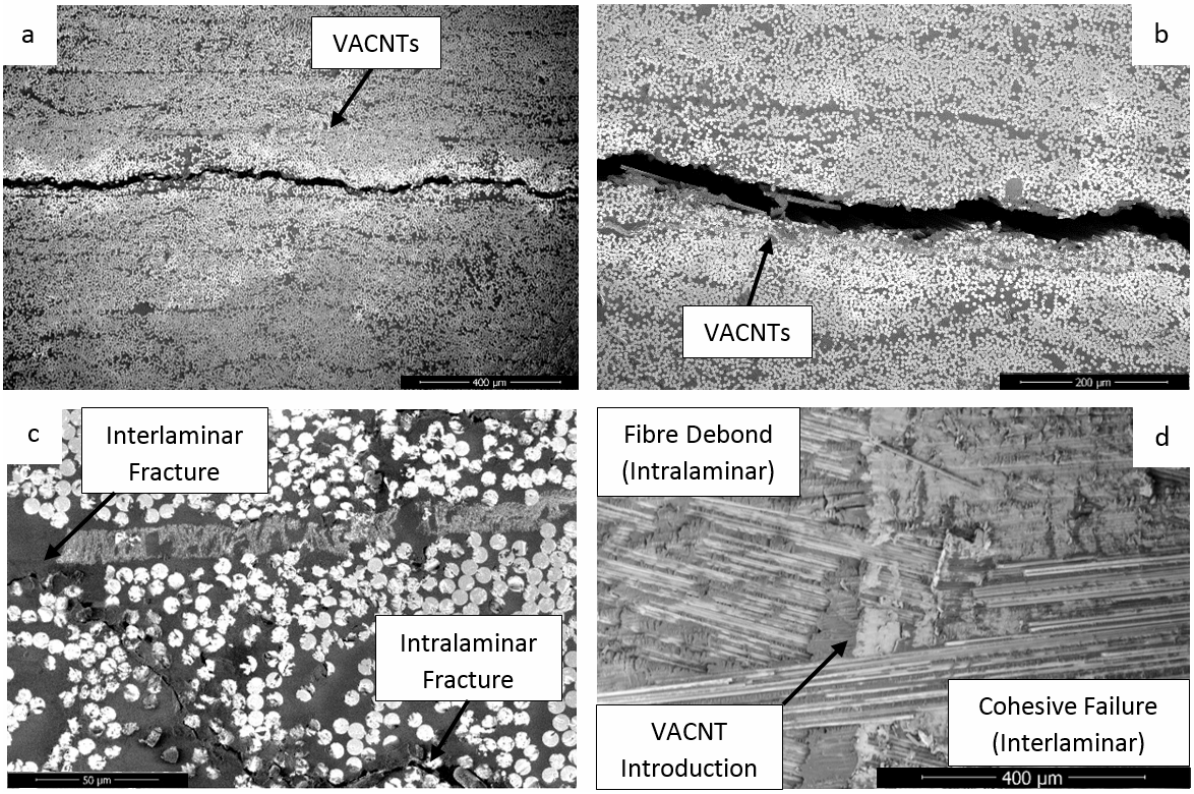

Figure 5.30: SEM images of fractured ELS VACNT interleaved specimens showing the transverse view of intralaminar fracture of the (a) Chevron and (b) CB3 specimens; (c) A magnified image of a crack transitioning from interlaminar to intralaminar delamination from the incorporation of the VACNTs, and (d) a surface view of the Chevron pattern showing failure transitioning between resin cohesive failure (associated with interlaminar delamination) and fibre debonding (associated with intralaminar delamination) at the position where the crack enters the interleaved region.

5.4 Conclusion

In this chapter, carbon fibre reinforced polymers were interleaved with VACNTs, which have a variety of nanotube densities and distributions. The aim was to investigate how distributing the nanotubes within the interleaf, either homogeneously or discretely, influences the interlaminar fracture toughness under Mode I and Mode II conditions. Three homogeneously distributed VACNT interleaves with linearly separated densities were transferred onto prepreg ply interfaces using a heated laminator method, while four discretely distributed VACNT patterned interleaves were transferred through a novel masking process. This innovative process involved cutting a film mask and placing onto a prepreg surface prior to the VACNT transfer. The mask partially inhibited contact between the nanotubes and prepreg, enabling the user to strategically distribute the nanotubes without damaging them in the process.

Microscopic analysis prior to testing showed that nanotube deformation is dependent on

their densities, with greater amounts of nanotube micro-buckling occurring for VACNTs with the lowest density. A slight reduction in geometric dimensions was observed for the patterned VACNT interleaves, which was associated with the thickness of the mask. Intermittent nanotube transfer occurred at the mask edge, however no damage to the nanotubes was witnessed.

Under both Mode I and Mode II conditions, VACNTs were found to deflect the crack from an interlaminar delamination dominated failure mode to intralaminar delamination. This resulted in the fracture toughness increasing by $15-20\%$ in Mode I and $5-10\%$ in Mode II for a homogeneous VACNT interleaf. These improvements are attributed to additional fibre bridging effects and a more torturous fracture path. The fracture behaviour was found to be independent of the VACNT density.

Fractography analysis of the patterned VACNT interleaves showed additional failure mechanisms, not previously seen for the homogeneous interleaves. For example, under Mode I conditions, secondary cracks were found to branch off from the main crack plane. These extra cracks initiated at the VACNT termination points and subsequently surrounded the interleaves, thereby creating extra surfaces and an additional contributor to the increased fracture energy. Crack branching was found to be more frequent in interleaves with smaller feature sizes, which led to the measured fracture toughness exceeding that of patterns with a larger feature size or an equivalent homogeneous interleaf with the same nanotube characteristics.

Simultaneously tracking the crack growth along both sides of a patterned VACNT interleaved DCB specimen showed that the VACNTs influence the crack growth rate. It was observed that as the crack reaches an VACNT interleaved region, the growth rate decreases, a product of the extra work required for the crack to propagate through the intralaminar region. This indicates that strategic positioning of the VACNT interleave can enable cracks to be manipulated in-plane, thereby directing them away from critical or sensitive regions, such as edges or notches.

Under Mode II conditions, interleaf patterning was found to stabilise intralaminar delamination. For homogeneous VACNT interleaves, cracks propagated unstably once reaching the nanotubes and deflected into the intralaminar region. Whilst cracks were still deflected into the intralaminar region for the patterned VACNT interleaves, they were found to propagate stably for the duration of the test.

Prologue to Chapter 6

Now that the fracture toughness properties and fracture behaviours have been well established for the VACNT interleaved specimens, the second half of this research shall focus on the application of using this interlaminar reinforcement technique on two delamination prone structures: tapered and notched composite specimens.

The aim of these studies is to *(i)* understand the achievable strength enhancements of interleaving these delamination prone structures with VACNTs; *(ii)* compare the failure mechanisms between similar structures when interleaved or left unmodified; and *(iii)* evaluate how accurately can these interleaved structures be modelled using homogeneous cohesive elements with enhanced properties.

CHAPTER 6

SUPPRESSING DELAMINATION OF TAPERED COMPOSITES THROUGH INTERLEAVING WITH VACNTS

Abstract

Delamination-prone, tapered specimens are interleaved with vertically aligned carbon nanotubes (VACNTs) at critical ply-drops and loaded in tension until failure. Two nanotube lengths are investigated (11 μm and 40 μm) and compared to an unmodified specimen, with respect to failure load and delamination onset location. Mechanical tests showed that the tensile strength of 40 μm VACNT interleaved tapered specimens increased by 7% relative to the unmodified baseline, while the 11 μm VACNTs made an insignificant difference. Global laminate stiffness was unaffected by the introduction of the VACNTs. Failure sequences were captured using a high-speed camera and it was found that the delamination onset location was unchanged when interleaved. Additional fracture behaviours were observed with the 40 μm interleaved tapered specimens, including the slippage of multiple 'stitched' plies and intralaminar crack formations, which led to greater amounts of energy dissipation. The dependence of tensile strength on nanotube length was attributed to the greater amounts of bridging at the resin pocket tip, which resisted initiation of through-thickness tension stresses and secondary delaminations. Cohesive element modelling was used to determine whether the influence of VACNTs can be captured numerically. Baseline models with material properties defined through primary data and literature, resulted in an ultimate failure load prediction within 2% of the experimental average. Cohesive element property enhancements were used to mimic the effects of the VACNTs. It was found that a good initial estimation is the hypothesis that the cohesive element strength increases by the same proportion as that of the critical strain energy release rate. This resulted in the ultimate failure load prediction being $< 0.5\%$ away from the experimental value. Preliminary models were unsuccessful at predicting the negligible tensile strength effect from interleaving tapered specimens with 11 μm VACNTs and is therefore recommended for further investigation.

6.1 Introduction

Composite materials have seen tremendous grown in the last few decades driven by their high specific stiffness and strength properties.

This chapter aims to build on the work done by Gouldstone *et al.* by investigating how VACNT length influences interlaminar delamination suppression. In order to allow for valid comparisons, a tapered composite, which fails repeatedly through delamination at a specific ply-drop, is required. Kawashita *et al.* have shown that this is achievable by tapering from a $[0/+45/0/-45]_{2S}$ layup to $[0/+45/0/-45]_S$, except for two plies that have been switched to generate a 0° ply termination closest to the thin section [43]. It was found that delamination initiated repeatedly at this ply termination and therefore this will be interleaved in this study. An unmodified baseline specimen will be compared to similar tapered composites with VACNTs interleaved around the critical ply-drop. Two nanotube lengths have been selected for these interleaves: 11 μm and 40 μm. All specimens will be tensile loaded and observed using a selection of high-speed cameras to investigate *(i)* whether the VACNTs increase the ultimate tensile strength of the tapered specimen and *(ii)* what is the failure mode and where does it initiate?

To complement the experimental work, a cohesive element model will also be developed with the aim of *(i)* predicting the tensile failure load and *(ii)* predicting the location of initial delamination for both the baseline and VACNT interleaved specimens. Multiple studies comment that further enhancements are achievable through either modifying the laminate stacking sequence or the positioning of the interlaminar reinforcement [40, 192, 237]. Therefore, it is hoped that this model will offer a simple tool that enables engineers to optimise both layup, ply termination locations and reinforcement position. Experimental results will be compared to these cohesive element models for each tapered specimen configuration.

6.2 Methodology

6.2.1 Tapered specimen fabrication

To investigate whether VACNTs are able to suppress delamination at a ply-drop and if nanotube length influences the behaviour, three tapered specimen configurations were manufactured: an unmodified baseline and VACNT interleaved specimens with nominal CNT lengths of 11 μm or 40 μm.

All tapered configurations were manufactured from HexTow® IM7/HexPly® 8552 prepreg (Hexcel Composites, Duxford, U.K.). The layup can be seen in Figure 6.1: specimens taper from a $[0/+45/0/-45]_{2S}$ to a $[0/+45/0/-45]_S$ layup, except for two plies that have been switched to generate a 0° ply termination closest to the thin section. The tapered laminates were cured as two mirrored halves, on a flat tooling using the modified cure cycle as outlined in chapter 4. These cured halves were later bonded at the symmetry plane using Redux 319 adhesive film (Hexcel

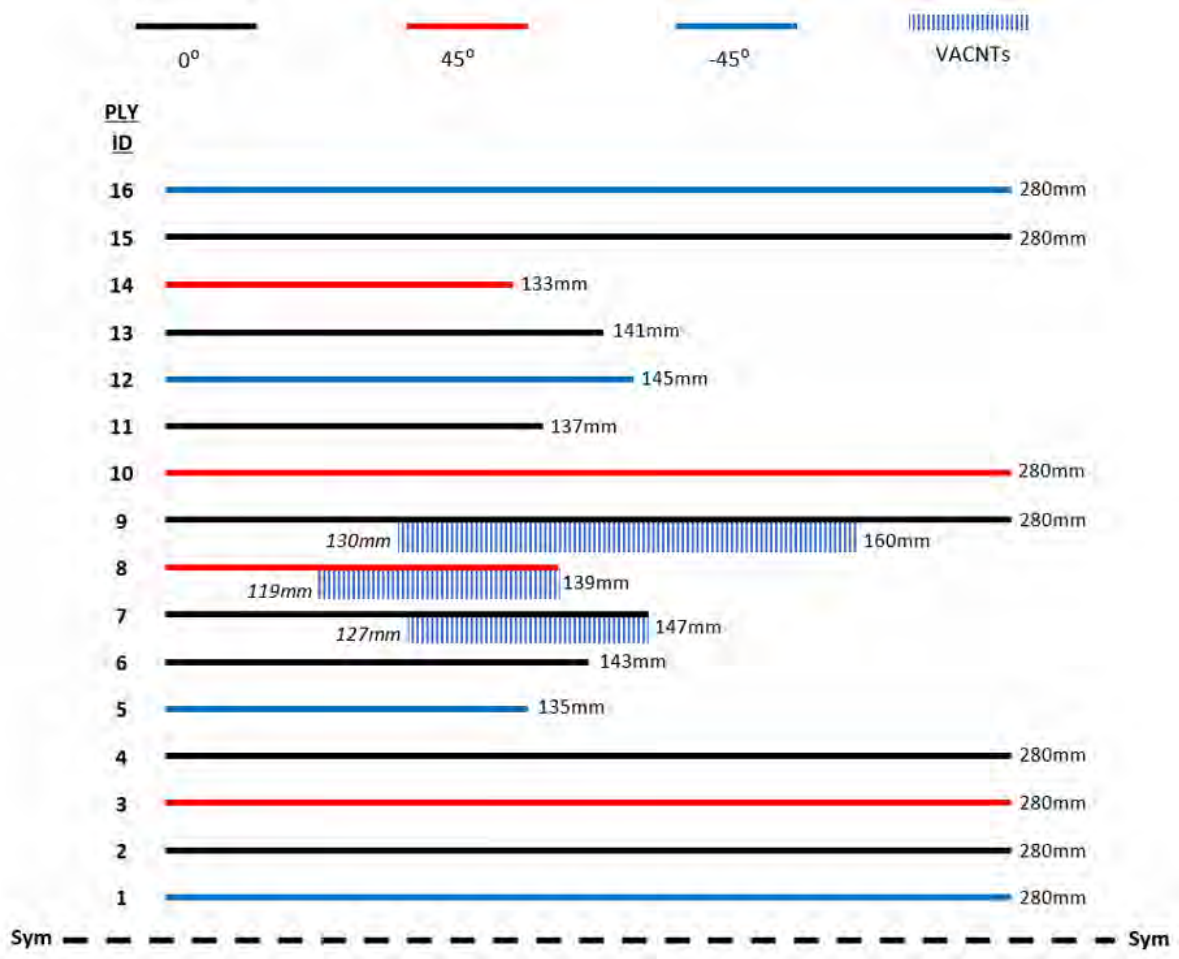

Figure 6.1: Illustration of one side of the tapered laminate with ply length and VACNT interleaf locations annotated.

Composites, Duxford, U.K.), with the inner surfaces grit blasted and cleaned to ensure a strong adhesion. The two parts were cured using the cycle recommended by the supplier (under vacuum for 2 hours at 160°C) [238].

As illustrated in Figure 6.1, ply-drops occurred at 2 mm separations, with a total of 8 ply-drops on each side, to taper the specimen thickness from 4 mm to 2 mm. Kawashita *et al.* [43] have shown that delamination initiates at the initial 0° ply termination (Ply 7 in Figure 6.1) and so this was the location selected to interleave with VACNTs. All multi-walled CNTs were grown through a proprietary continuous chemical vapour deposition (CVD) process with nominal lengths of 11 μm and 40 μm [213, 214]. Other nanotube characteristics have been outlined in Table 6.1.

To ensure good engagement between the VACNTs and the host laminate, the VACNTs were first embedded into individual plies, using a combination of heat (55°C) and pressure (vacuum) for a duration of 2 minutes. Afterwards, the substrate was removed, leaving a nanotube rich surface as shown in Figure 6.2a. The locations of the VACNT interleaves are illustrated in Figure 6.1.

Table 6.1: Geometric properties of the VACNTs investigated in this chapter.

Form (−)	Length (μm)	Diameter (nm)	Population Density ($CNTs/cm^2$)
MWCNTs	11/40 ± 4	12	1.0E+10 - 1.5E+10

An interleave zone length for the reinforced terminating plies (*i.e.* Ply 7 and Ply 8) was selected as 20 mm rather than the full substrate width (30 mm), so as to ensure minimal damage to the CNTs near the ply edge during substrate removal. Interleaf positioning was selected to ensure that VACNTs do not rest upon other VACNTs. Preliminary studies have shown that VACNTs have poor interfacial properties with other VACNTs, as they do not nest together, which would reduce the CNT's ability to suppress delamination.

Once both laminate halves were joined, 3 mm thick GFRP cross-ply end-tabs were bonded using Huntsman Araldite 2014 epoxy adhesive and cured using the supplier's recommendations (7 days at 25°C) [239]. To ensure strong adhesion, both specimen and end-tab surfaces were grit blasted prior to adhesive application. Specimens were then cut using a water-cooled diamond saw to 15 mm x 250 mm, as shown in Figure 6.2b. These dimensions were selected to match the work done by Kawashita *et al.* [43].

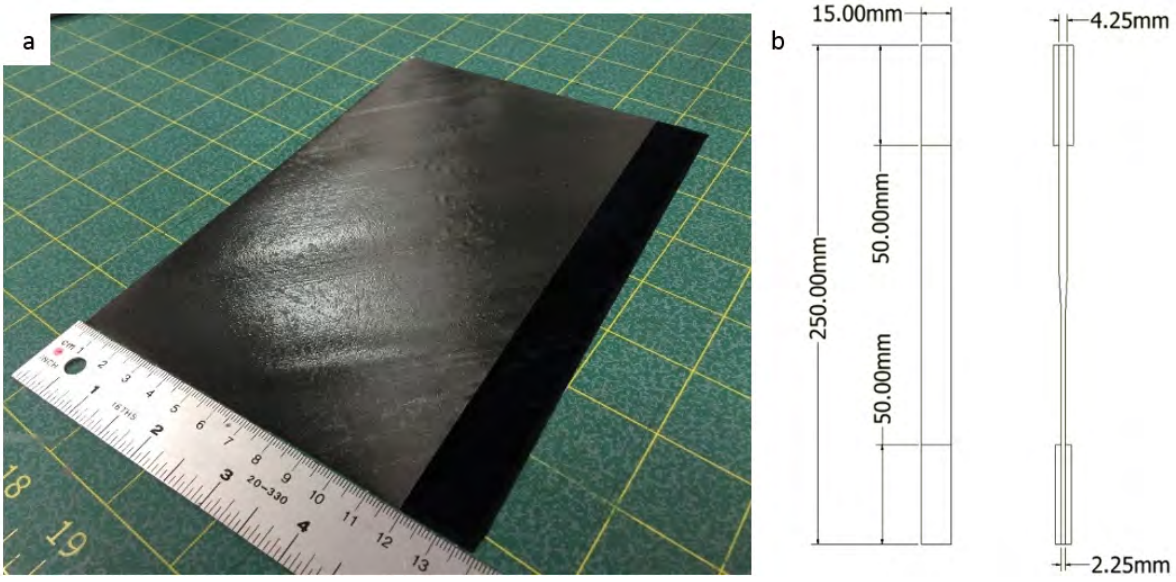

Figure 6.2: (a) Photograph of 'Ply 8' with nanotubes embedded into surface and (b) a schematic of the tapered specimen dimensions.

6.2.2 Experimental methodology

6.2.2.1 Microscopy

To determine the quality of nanotube engagement post cure at the interleaved ply-drop, all pristine specimens were imaged using a scanning electron microscope (SEM). Specimens were cut using a water-cooled diamond saw and then ground and polished to a fidelity of at least one micron. The pristine surfaces were then viewed using a Verios^{TM} XHR SEM (FEI, Oregon, USA) at magnification levels of x150 to x2500 and a voltage acceleration of 500V.

6.2.2.2 Mechanical testing

All specimens were axially loaded in tension using a calibrated Instron 8801 with a 100 kN load cell and at a displacement rate of 0.5 mm/min. A Fastcam SA-Z optical high-speed camera was used for every test to determine the mode and location of failure. Images were taken at a frame rate of 175000 fps and a resolution of 128 x 408 pixels. High intensity LED lights were directed at the surface of the laminate in order to visualise specimens clearly at the high frame rate. While the heating effects of these lights made strain measurements difficult, preliminary tests showed that failure load was not significantly affected. Failure strain measurements were not in the scope of this study and were therefore omitted from the testing procedure.

To validate the optical high-speed camera images, a Telops FAST M2K high-speed infrared camera was also used to visualise failure of the unmodified baseline specimens. Images were taken at 2880 fps and a resolution of 320 x 96 pixels. Crack formation results in a heat trace, due to the new surface generation [240]. Therefore, the location of the initial significant heat source will correspond to the failure location. The set-up of both the optical high-speed camera and high-speed IR camera can be seen in Figure 6.3.

6.2.3 Numerical methodology

6.2.3.1 Mesh generation

To predict the tapered laminates response under static tensile conditions, 2D slice cohesive element models were constructed using the commercial FE package ABAQUS®. Algorithms built on those developed by Kawashita *et al.* [43], were used to generate a ply-level mesh. High-resolution images of the pristine polished cross-section, similar to that seen in Figure 6.4, were taken for each specimen configuration to determine all the ply-drop locations along the specimen length. Resin pockets are defined through two user-defined parameters: ply-drop length (l_{PD}) and resin pocket length (l_{RP}), which are illustrated in Figure 6.5. When combined with a cosine function to produce a smooth transition, the ratio between these two parameters dictate the tapering length and severity of the terminating ply end. Overall, an average total ply-drop length (l_{PD}) of 1 mm and a resin pocket length (l_{RP}) of 0.75 mm was found to be the most representative, as shown in Figure 6.6.

The models span the full gauge length of 150 mm with a total thickness varying from 4.25 mm to 2.25 mm (Redux 319 adhesive film has a measured cure ply thickness of 0.25 mm). The element length was one ply thickness, or 0.125 mm, at the tapered region and increased to 5 mm at the specimen end boundaries, so as to reduce computational cost. The element width and thickness remained constant, corresponding to 0.25 mm and 0.125 mm, respectively. These element sizes were selected after a thorough mesh sensitivity study (carried out by Kawashita *et al.* [43]), with a maximum of three elements across the width and a minimum element length of 0.05 mm.

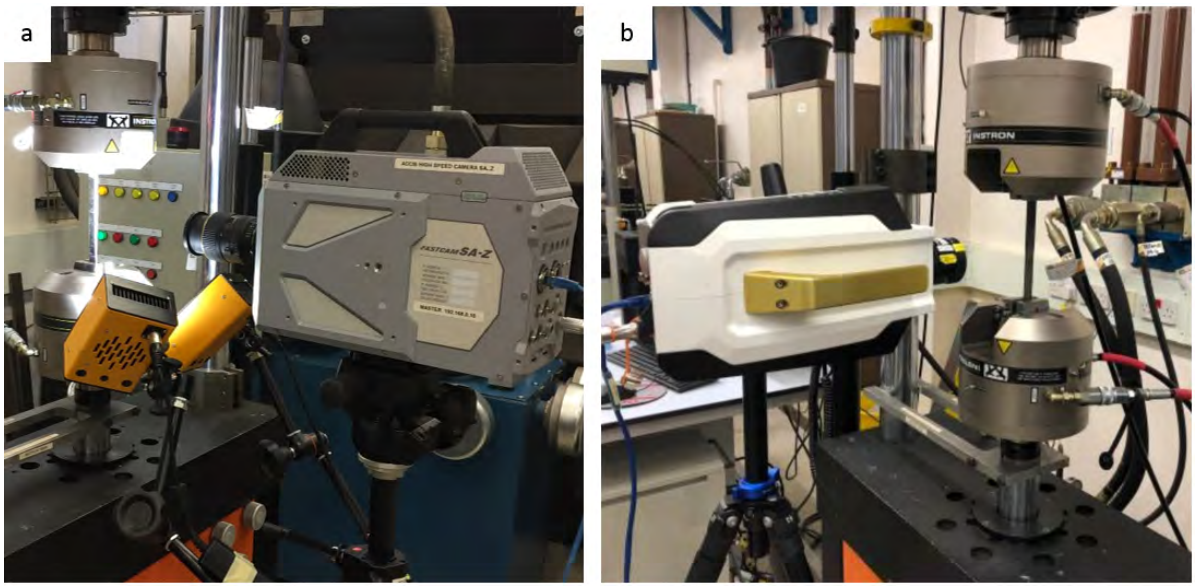

Figure 6.3: Photograph of the mechanical test set-up for the tapered specimens with (a) the high-speed optical camera and (b) the high-speed infra-red camera.

As discussed in chapter 1, interlaminar delamination is the dominant failure mode for tapered laminates subjected to a tensile load. To capture this behaviour, cohesive elements were inserted at the interfaces between plies and around the resin pockets. These cohesive elements have a thickness of 0.01 mm and followed an interlaminar failure criterion, which will be described in Section 6.2.3.3. Overall, the baseline specimen cohesive zone model consisted of 8445 eight-node brick elements for the plies, 96 eight-node brick elements for the resin pockets, 7883 cohesive elements for the interlaminar interfaces and 33704 nodes.

The mesh generation process resulted in an accurate representation of the specimen geometry, as can be seen in Figure 6.4, however surface waviness was observed, due to assumptions that the ply thickness remains constant and the resin pocket size is equal throughout. Extra refinement would be required to improve this, but this was not deemed necessary for the scope of this research.

6.2.3.2 Material properties

The elastic mechanical properties of the unidirectional IM7/8552 plies are given in Table 6.2. As this is a slice model, ±45° plies were modelled as combined with equivalent homogeneous properties, which have been summarised in Table 6.3. These have been obtained through classical laminate theory using the properties from Table 6.2. Resin pockets have been modelled as homogeneous 8552 resin, with their properties described in Table 6.4. Values have been extracted from literature and the relevant material datasheets [3, 4].

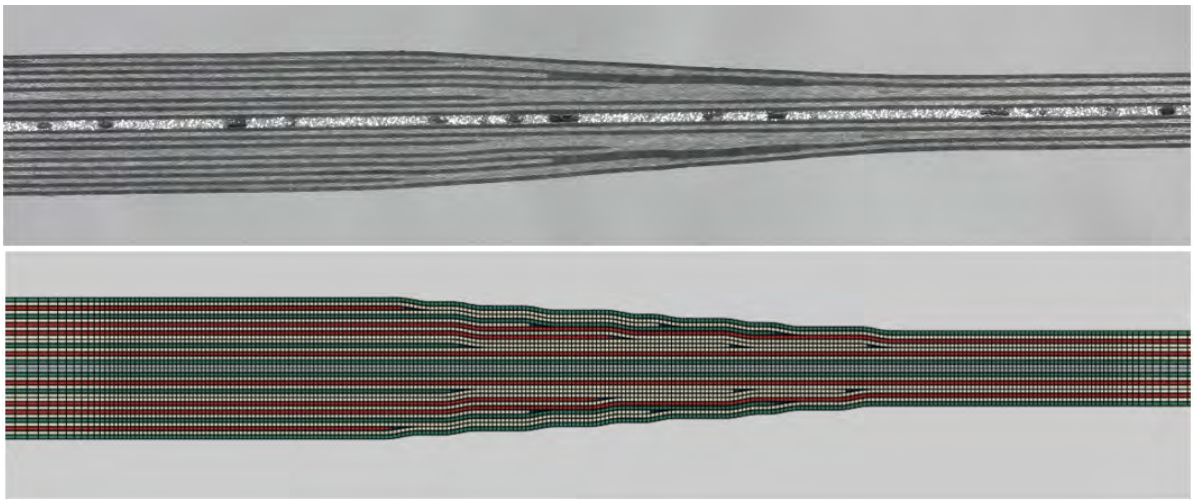

Figure 6.4: A photograph of the cross-section of a polished baseline specimen (top) with the corresponding representative finite element mode (bottom).

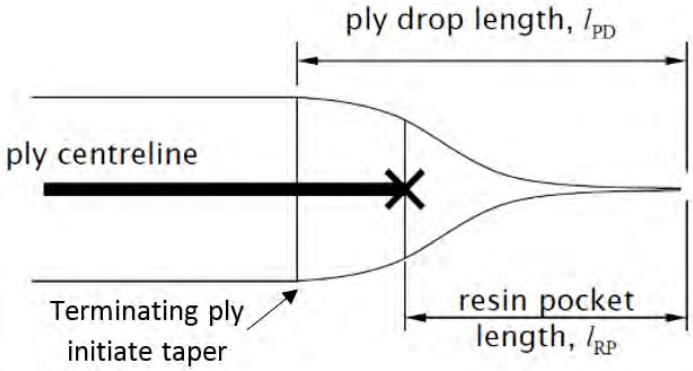

Figure 6.5: Schematic of a symmetric resin pocket formation around a terminating ply [43].

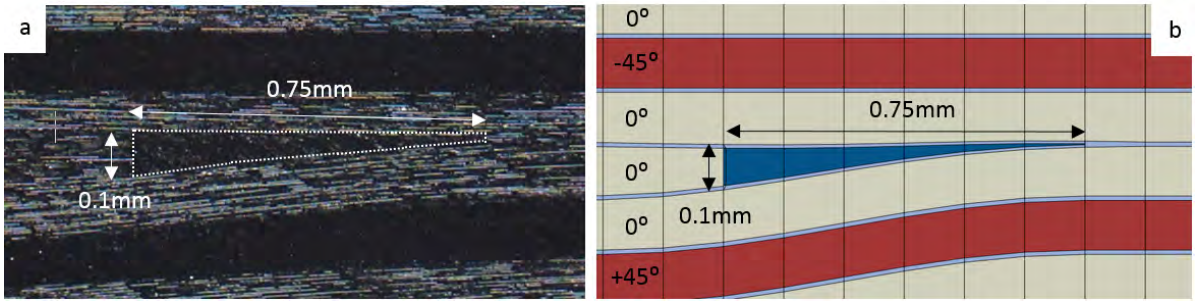

Figure 6.6: (a) An optical microscope image taken of a ply-drop within a tapered specimen and (b) a representative model ply-drop, when l_{PD} = 1 mm and l_{RP} = 0.75 mm.

Table 6.2: Material properties for a 0° unidirectional ply of IM7/8552 [2].

E_1 (GPa)	$E_2 = E_3$ (GPa)	$G_{12} = G_{13}$ (GPa)	G_{23} (GPa)	$\nu_{12} = \nu_{13}$ $(-)$	ν_{23} $(-)$
161	11.38	5.17	3.98	0.32	0.44

Table 6.3: Material properties for a ±45° unidirectional ply of IM7/8552 using classical laminate analysis.

$E_1 = E_2$ (GPa)	E_3 (GPa)	G_{12} (GPa)	$G_{13} = G_{23}$ (GPa)	ν_{12} $(-)$	$\nu_{13} = \nu_{23}$ $(-)$
18.56	13.44	41.58	4.57	0.79	0.09

6.2.3.3 Cohesive element failure criterion

Failure of the cohesive elements was captured through a mixed-mode bi-linear traction-separation cohesive formulation, developed by Jiang *et al.* [44] and Li *et al.* [45]. This formulation states that cohesive damage initiates when the pure mode stresses on the cohesive element (σ_I and σ_{II}) and

Table 6.4: Material properties for homogeneous 8552 resin [3, 4].

E (GPa)	ν $(-)$
4.67	0.37

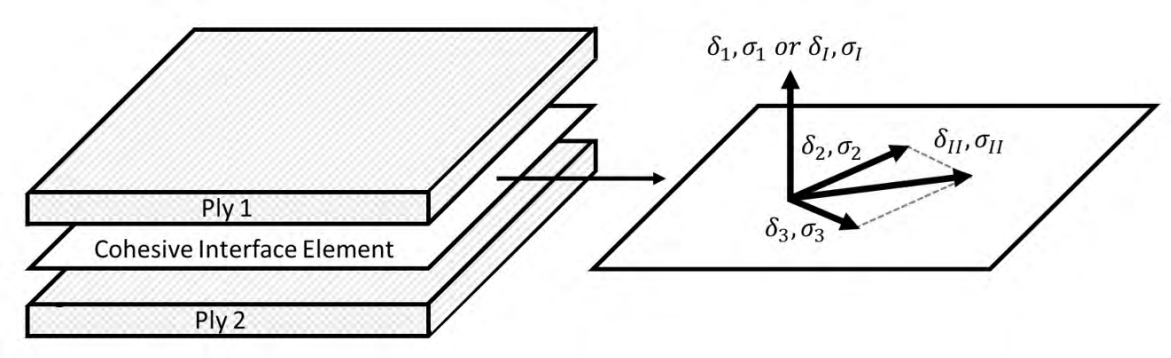

Figure 6.7: Schematic of a cohesive element between two brick elements with relative displacements (δ) and stresses (σ). Image adapted from Jiang *et al.* [44].

corresponding pure mode strengths (S_I and S_{II}) satisfy Equation 6.1. The interface relationship is assumed linear before this damage criterion is met.

$$\left(\frac{max(\sigma_I, 0)}{S_I}\right)^2 + \left(\frac{\sigma_{II}}{S_{II}}\right)^2 = 1 \tag{6.1}$$

where I and II indicate the Mode I (opening) and Mode II (shearing) components respectively. For clarity, these components are illustrated in Figure 6.7.

Once the damage criterion is met and the interface is continually loaded, the cohesive element strength is assumed to degrade linearly until complete interface failure. These relations can be described in Equation 6.2.

$$\sigma_I = (1-D)S_I; \qquad \sigma_{II} = (1-D)S_{II} \tag{6.2}$$

where D is a damage variable, defined in Equation 6.3.

$$D = \frac{\delta_m - \delta_m^i}{\delta_m^f - \delta_m^i} \tag{6.3}$$

where δ_m is the total mixed-mode relative displacement acting on the cohesive element, and the of magnitude δ_m is calculated through Equation 6.4. δ_m^i and δ_m^f are the values of δ_m at damage initiation and complete failure respectively.

$$\delta_m = \sqrt{max(0,\delta_I)^2 + \delta_{II}^2} \tag{6.4}$$

where, δ_I is the normal opening displacement and δ_{II} is the resultant shear relative displacement, which as schematically shown in Figure 6.7, can be calculated by Equation 6.5.

$$\delta_{II} = \sqrt{(\delta_2^2 + \delta_3^2)} \tag{6.5}$$

Complete cohesive failure was captured through the power law described in Equation 6.6.

$$\left(\frac{G_I}{G_{IC}}\right) + \left(\frac{G_{II}}{G_{IIC}}\right) = 1 \tag{6.6}$$

where G_I and G_{II} are the Mode I and Mode II energy release rate, while G_{IC} and G_{IIC} are the critical Mode I and Mode II energy release rates that cause crack initiation. The critical values were determined through experiments as outlined in chapter 5.

6.2.3.4 Through-thickness compression property enhancement

It has been shown in literature that the Mode II strength, S_{II}, and critical strain energy release rate, G_{IIC}, of a composite are enhanced by through-thickness compression (TTC) effects [241, 242]. This compressive loading can occur externally, such as from fasteners [243] or environmental pressure [244], or internally through residual stresses or Poisson's ratio effects. The latter is applicable in this study and should be captured when modelling the system.

Li *et al.* [29] has discussed that the enhanced Mode II strength, S_{II_E}, can be described in Equation 6.7.

$$S_{II_E} = S_{II} - \eta_S(min(0, \sigma_I)) \tag{6.7}$$

where S_{II_E} is the enhanced Mode II strength and η_S is the TTC strength enhancement factor. For the composite system investigated in this research (IM7/8552), Gan *et al.* suggested η_S is approximately 0.3 [245]. This value was measured experimentally through a double-notch shear (DNS) test and has been adopted in multiple studies [246–248], showing good consistency between numerical-experimental comparisons.

Analysis of the traction-separation law for cohesive elements, when TTC strength enhancements occur, shows that the critical strain energy release rate will also be enhanced in Mode II conditions, as visualised in Figure 6.8.

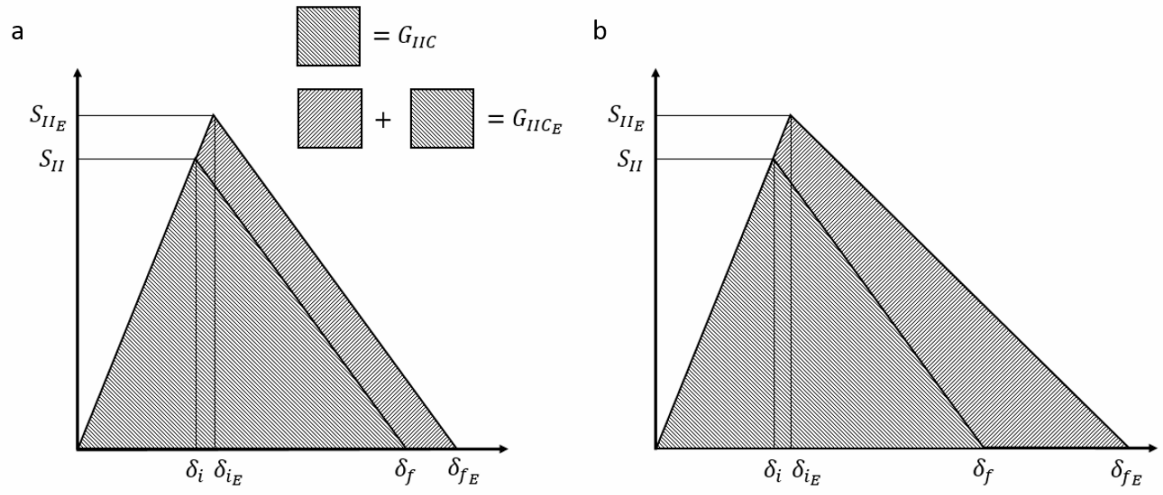

Figure 6.8: Mode II traction-separation law for a cohesive element with enhanced properties from through-thickness compression (TTC) stresses (adapted from [45]). Two damage evolution laws shown, which represent, (a) an unchanged linear softening slope when TTC stresses are included and (b) a modification to the linear softening slope when TTC stresses are included. δ_i and δ_f are the shear deformation at delamination initiation and failure respectively. δ_{iE} and δ_{fE} are the same definitions, when under TTC stresses.

There have been many studies investigating the fracture toughness enhancement factor. Li *et al.* originally proposed that its value is independent from the strength enhancement [45], and can therefore be described through the relation shown in Equation 6.8.

$$G_{IIC_E} = G_{IIC} - \eta_G(min(0,\sigma_I)) \tag{6.8}$$

where G_{IIC_E} is the enhanced Mode II strength and η_G is the TTC fracture toughness enhancement factor. This independent enhancement factor would result in the linear damage evolution law being modified relative to when TTC stresses were not included. Such a behaviour can be visualised schematically in Figure 6.8b.

Li *et al.* originally suggested a value for η_G of 0.025 MPa^{-1} for a T300/914 system [45]. This was predicted through a parametric study on η_S and η_G, using multiple experimental data sets, including sharp and shallow tapered specimens, and optimising the closest fit combination. Xu *et al.* used a similar method on cut-ply specimens manufactured from IM7/8552 and predicted a value of 0.064MPa^{-1} [246]. Catalanotti *et al.* produced an empirical estimate for a transverse crack tensile specimen, η_G as 0.0035MPa^{-1} [243] for IM7/8552, over an order of magnitude lower than that reported by Xu *et al.* This suggests that the fracture toughness enhancement factor could be either test- or layup dependent.

An alternative method, which assumes that the linear softening slope remains unchanged when TTC stresses are included, was also proposed by Li *et al.* and yielded consistent results when compared to all their experiments [45]. This assumption can be visualised schematically in Figure 6.8a. Gan *et al.* also made the same assumption, with good consistency when modelling a double-notch beam test [245].

Presuming the same softening slope allows the fracture toughness enhancement to be directly related to the strength enhancement. This relationship can be described in the form shown in Equation 6.9.

$$G_{IIC_E} = \left(\frac{S_{II_E}}{S_{II}}\right)^2 G_{IIC} \tag{6.9}$$

Owing to the lack of consistency in literature for predicting the η_G value, the author has selected to capture the Mode II critical strain energy release rate enhancement from TTC stress through Equation 6.9.

6.2.3.5 Cohesive element properties

The cohesive element properties for the unmodified baseline specimens are shown in Table 6.5. Mode I and Mode II critical strain energy release rate values correspond to that measured in chapter 5, while the strength (S_I and S_{II}) and stiffness values (K_I and K_{II}) have been directly

Table 6.5: Cohesive element properties used for the baseline model.

G_{IC} (N/mm)	G_{IIC} (N/mm)	S_I (MPa)	S_{II} (MPa)	K_I (N/mm^3)	K_{II} (N/mm^3)	η_S $(-)$
0.22 - 0.26*	0.62 - 0.67*	60 [245]	82.6 [249]	4.67e5 [245]	1.75e5 [245]	0.3 [245]

** Determined by experimental work presented in chapter 5.*

Table 6.6: Cohesive element enhanced property ranges used to model VACNT interleaved tapered specimen.

G_{IC} (N/mm)	G_{IIC} (N/mm)	S_I (MPa)	S_{II} (MPa)	K_I (N/mm^3)	K_{II} (N/mm^3)	η_S $(-)$
0.3*	0.71*	60 - 90	82.6 - 100	4.67e5 [245]	1.75e5 [245]	0.3 [245]

** Determined by experimental work presented in chapter 5.*

taken from literature [245, 249]. Cohesive elements have a geometric thickness of 0.01 mm and an out-of-plane thickness of 1 mm.

The cohesive element properties for the VACNT interleaved specimens are shown in Table 6.6. While the enhancement in the critical strain energy release rate from interleaving with VACNTs was known through the experimental work conducted in chapter 5, the use of cohesive elements to predict the enhancement of strength and stiffness was not. To determine these values, a parametric study was conducted on combinations of S_I and S_{II}. The ranges used in the study are reported in Table 6.6. Overall, nine combinations were evaluated and compared to the experimental specimens; models were evaluated against failure load and failure location. Cohesive element stiffnesses were assumed unchanged through VACNT introduction, which will be justified in the results section.

Cohesive properties were modified for interleaved regions only (shown in Figure 6.9), corresponding to the locations of the VACNTs, outlined in Figure 6.1. All other cohesive element properties matched that of the baseline model, described in Table 6.5. Resin pockets were assumed to be unaffected by the introduction of the interleaves.

6.2.3.6 Boundary conditions

Models consisted of an initial step and a dynamic, explicit step, as illustrated in Figure 6.9. In the first initial step, boundary conditions fully constrained the thick section end-face and prevented in-plane rotation throughout. In the second step, loads were applied through a uniform distributed velocity applied at the thin end and continued until failure. The internal reaction load, and therefore failure load, was determined through a load integrated output across the cross-sectional surface shortly after the fully constrained thick section end-face.

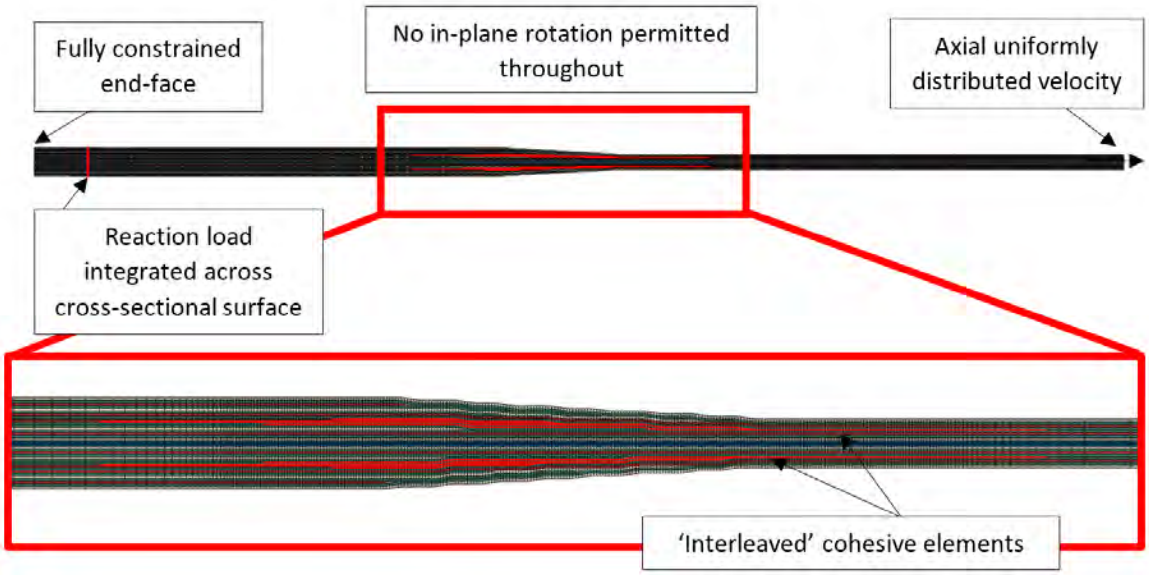

Figure 6.9: Annotated schematic of the cohesive element model for an interleaved tapered specimen showing all loads and boundary conditions applied.

6.3 Results and Discussion

6.3.1 Microscopy

SEM images of the pristine critical ply-drop when interleaved with VACNTs of lengths 11 μm and 40 μm are shown in Figure 6.10a and Figure 6.10b respectively.

In these images, the longer nanotubes were found to result in a greater amount of nanotube-fibre bridging of the resin pocket ahead of the ply termination. This happened particularly at the tip, where through-thickness tension reportedly occurs [182, 183] and cracks reportedly initiate [186, 189, 190]. The longer nanotube length also resulted in less VACNT film waviness. Overall, these characteristics result in more homogeneous property enhancements within the interleaved resin pockets.

Longer nanotubes were found to exhibit more nanotube micro-buckling at the ply interfaces surrounding the terminating ply (Figure 6.10c and Figure 6.10d), where the nanotube effective length has dropped on average by 40% for the 11 μm VACNTs and 80% for the 40 μm VACNTs. Buckling will result in additional tensile residual stresses at the ply interfaces, which could promote delamination.

A millimetre away from the interleaved ply termination position, the effective nanotube length was found to recover for both VACNT configurations (Figure 6.10e and Figure 6.10f). While micro-buckling was no longer observed for the 11 μm VACNTs, the 40 μm VACNTs still retained only 50% of their effective lengths. However, as shown in chapter 3, this behaviour is intrinsic for the longer nanotubes within this host composite system.

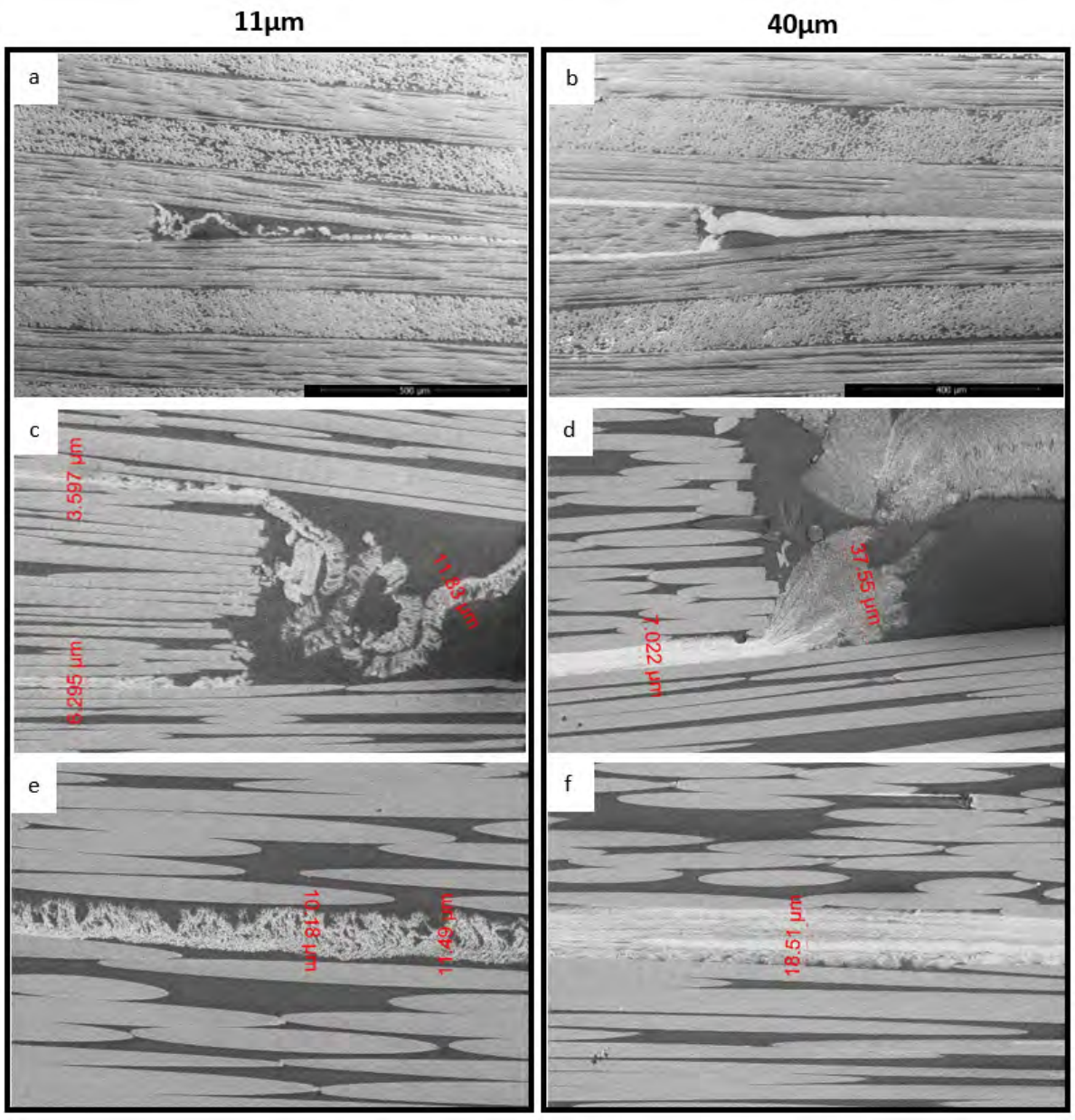

Figure 6.10: SEM images of (a) a 11 μm VACNT interleaved ply-drop, (b) a 40 μm VACNT interleaved ply-drop, (c) evidence of VACNT film waviness and VACNT buckling for 11 μm VACNTs, (d) evidence of CNT buckling for 40 μm VACNTs, (e) 11 μm VACNT length recovery and (f) 40 μm VACNT length recovery when 1 mm away from the terminated ply.

Overall, these images suggest that a compromise is required when selecting nanotube length for interleaving tapered specimens with VACNTs: the longer the nanotube, the greater amount of bridging at the resin pocket ahead of the ply termination position. However, this comes at a cost of increased levels of nanotube micro-buckling at the terminating ply interfaces, which will result in additional tensile residual stresses. The more influential behaviour shall be determined through mechanical test comparisons.

6.3.2 Mechanical testing

6.3.2.1 Tensile strength enhancement

Typical load *versus* displacement plots for each of the tapered specimen configurations tested can be seen in Figure 6.11. The corresponding average failure loads with percentage enhancements relative to the baseline specimen are displayed in Table 6.7. It can be observed from the graphs that the laminate stiffness does not appear to be affected by the selective incorporation of the VACNTs. Table 6.7 suggests that interleaving a tapered specimen with 11 μm VACNTs does not influence the tensile strength of the laminate and therefore has not suppressed delaminations. On the other hand, the 40 μm VACNTs resulted in a 7% average increase in tensile strength relative to the baseline specimen. This indicates that resin pocket nanotube bridging has a greater impact on suppressing delamination and increasing tensile strength, than the consequential increase in VACNT micro-buckling.

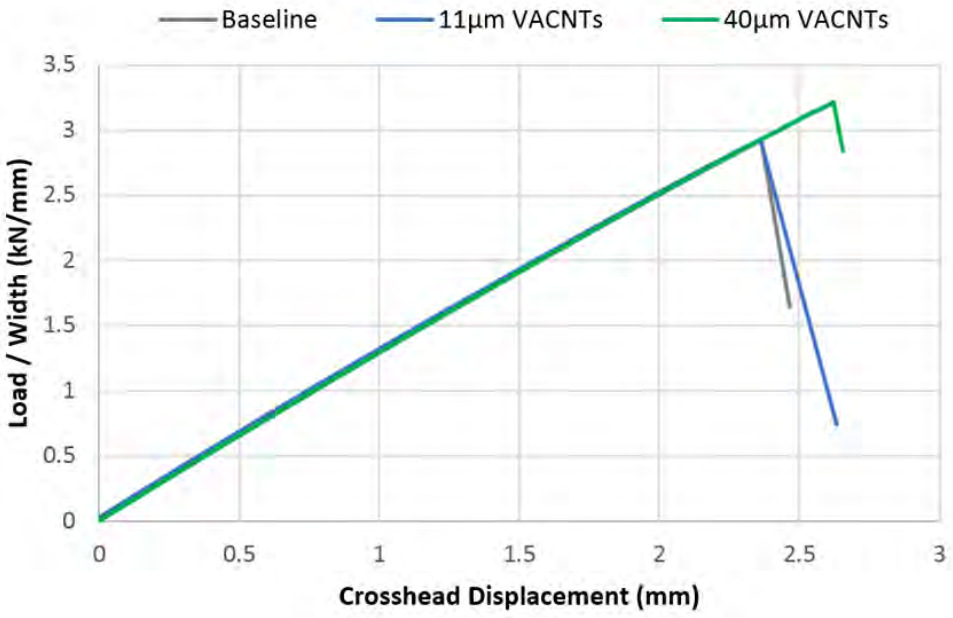

Figure 6.11: A typical load *versus* displacement plot for the unmodified baseline, 11 μm VACNT interleaved and 40 μm VACNT interleaved tapered specimens.

Table 6.7: Failure load per unit width for the unmodified baseline, 11 μm and 40 μm VACNT interleaved tapered specimens.

Baseline		11 μ**m VACNT**			40 μ**m VACNT**		
Load / Width (kN/mm)	CV (%)	Load/Width (kN/mm)	CV (%)	Enh. (%)	Load/Width (kN/mm)	CV (%)	Enh. (%)
2.89	1.46	2.89	1.18	0.02	3.09	2.15	6.96

6.3.2.2 Delamination visualisation

Post failure, all tapered specimens showed evidence of delamination along the 0° ply interfaces towards the end-tabs, as can be seen in Figure 6.12. This indicates that delamination is still the dominant failure mode for VACNT interleaved tapered specimens, and in-situ images obtained from the optical and infra-red (IR) high-speed video cameras support this conclusion.

As expected for baseline specimens, delamination was observed to initiate at the critical ply-drop ('Ply 7', as illustrated in Figure 6.1) with cracks propagating along both interfaces surrounding the terminated ply and towards the thick section. As can be seen in Figure 6.13(a-c), this subsequently caused the terminated ply to slip towards the thick section, a behaviour supported by Murri and Helmy, who found that delamination was Mode II dominated for axially loaded tapered specimens [189, 190]. Ply slippage subsequently led to the tip of the resin pocket opening and a secondary delamination event propagated towards the thin section. IR footage, as can be seen in Figure 6.14, confirms this by showing the delamination propagation directions: two cracks moving at similar rates along the interfaces surrounding the terminating ply and a singular crack propagating from the resin pocket in the opposite direction.

Typical optical high-speed camera frames, capturing the failure event, can be seen in Figure 6.15 and Figure 6.16 for the 11 μm and 40 μm VACNT interleaved tapered specimens, respectively. A similar fracture behaviour to that of the baseline specimen was observed for the 11 μm VACNT interleaved specimens, agreeing with the negligible difference in failure load. However, additional

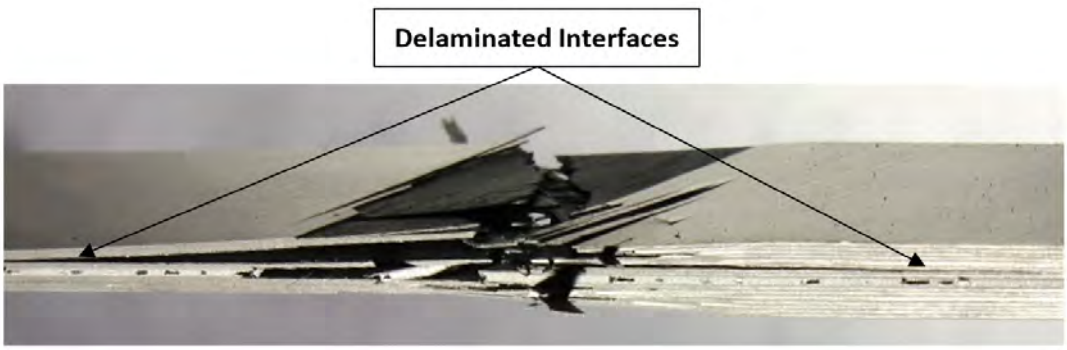

Figure 6.12: Photograph of a typical tapered specimen post-failure.

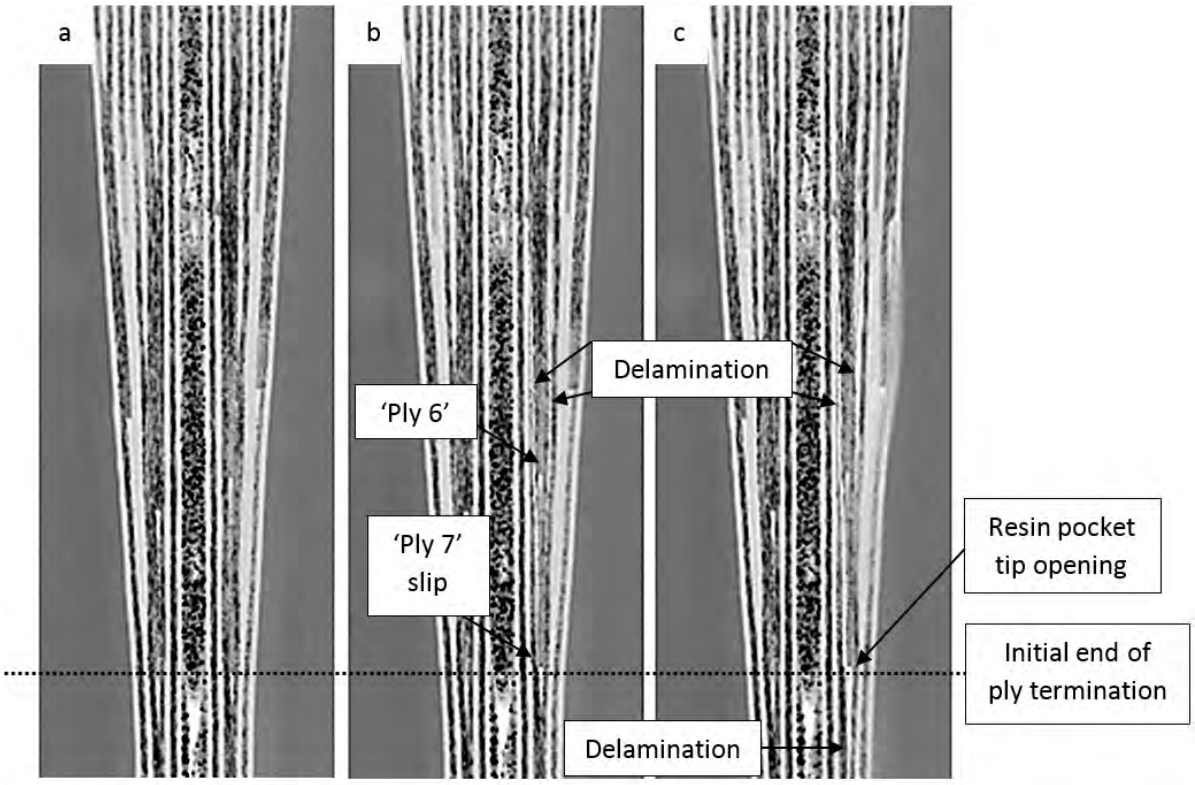

Figure 6.13: Image frames from an optical high-speed camera of the failure stages for a typical baseline specimen: (a) prior to delamination, (b) resin pocket rupture and delamination, and (c) specimen catastrophic failure.

features were observed for the 40 μm interleaved specimens. For example, footage repeatably showed the 'stitched' plies, *i.e.* 'Ply 6' and 'Ply 7', delaminate and slip in unison, rather than the critical ply alone slipping during delamination propagation. Evidence of intralaminar fracture was also observed, indicating that the interleaves were being by-passed, as concluded in chapters 3 - 5. Both of these mechanisms will result in a greater energy requirement for complete structural failure and hence a greater failure load. For two out of six specimens, structural integrity was maintained post delamination, with specimens enduring approximately 0.5 seconds after ply slippage. It is believed by the author that this is either caused by intralaminar cracks slowing crack growth, or the VACNTs at the resin pocket bridging the tip sufficiently, to temporarily resist opening loads and hence delamination growth towards the thin section.

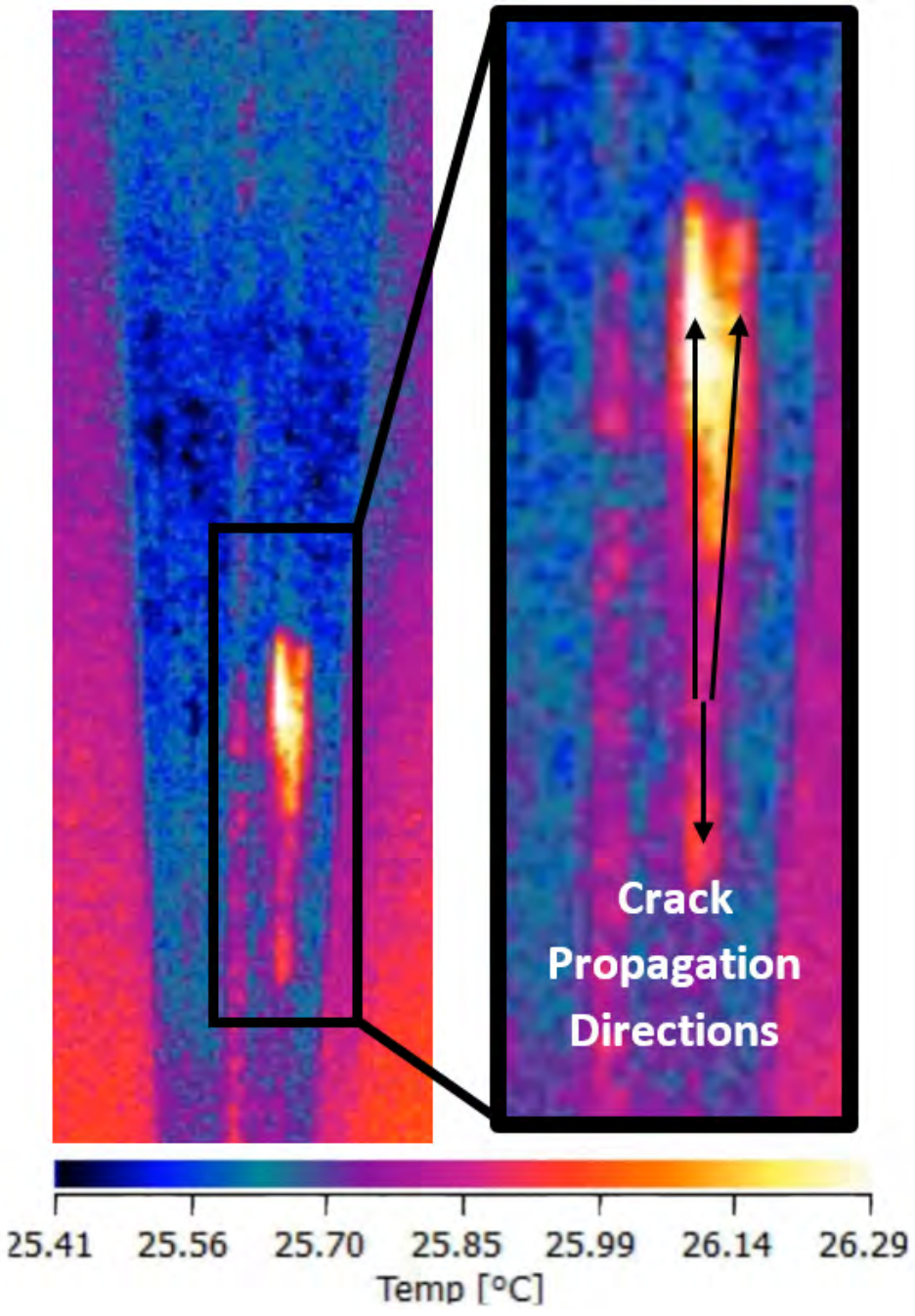

Figure 6.14: Image frame from the infra-red high-speed camera showing the temperature map recorded during delamination.

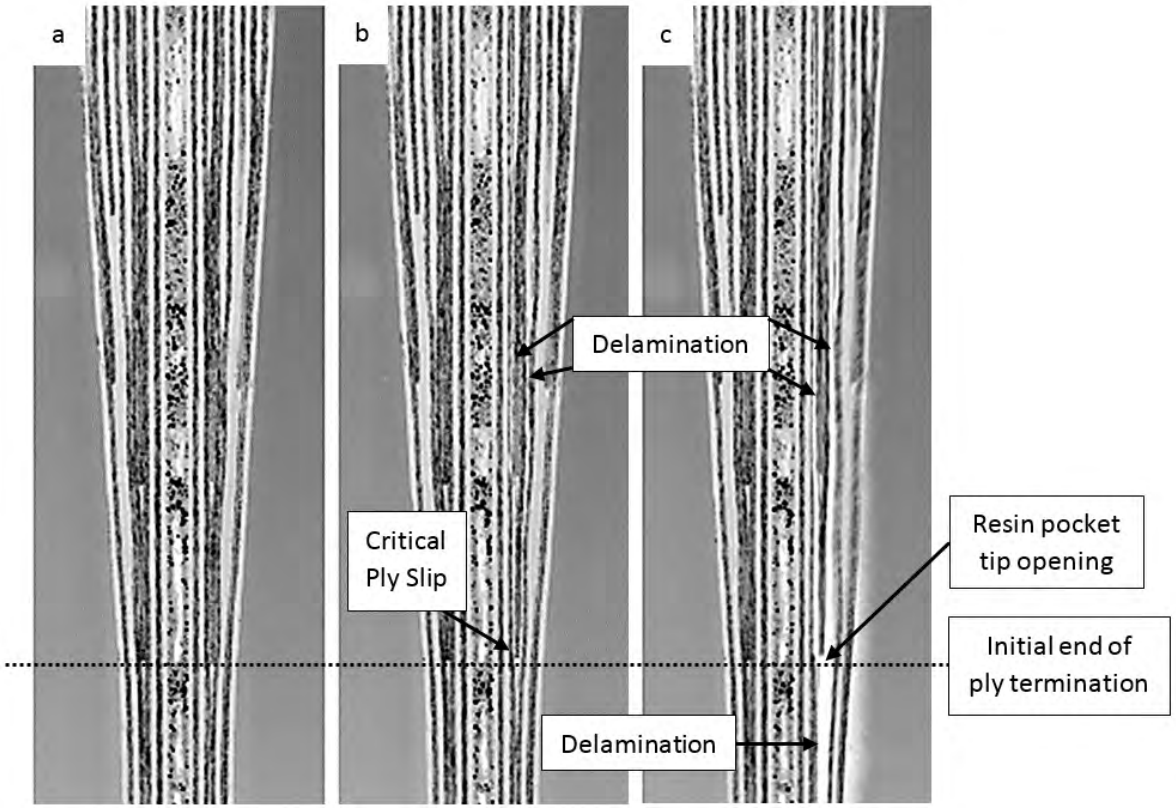

Figure 6.15: Optical high-speed camera footage of the stages of failure for a typical 11 μm VACNT interleaved specimen: (a) prior to delamination, (b) resin pocket rupture and delamination, and (c) specimen catastrophic failure.

6.3.3 Numerical modelling

6.3.3.1 Baseline comparison

To determine whether the effect arising from the VACNT interleaves on the tapered specimen tensile strength can be captured using a cohesive element model, baseline specimens were simulated and compared with their experimental counterparts. Comparisons focussed on the delamination onset location and ultimate load at failure. For this study, a delaminated interface was defined as the condition when the damage variable for the cohesive element (described in Equation 6.3) equated to 1. Figure 6.17 shows the load *versus* displacement curves for the baseline tapered specimens, when the Mode I and Mode II critical strain energy release rates are defined as that measured in chapter 5 at crack initiation (G_C) and propagation (G_{prop}). These values resulted in a predicted failure load for the baseline tapered specimen of 2.83 kN/mm and 2.95 kN/mm respectively. Comparing these values against the experimental average failure load (reported in Table 6.7), differences of -1.98% and $+2.24\%$ were identified.

Analysing the model failure sequence, as displayed in Figure 6.18, it can be seen that

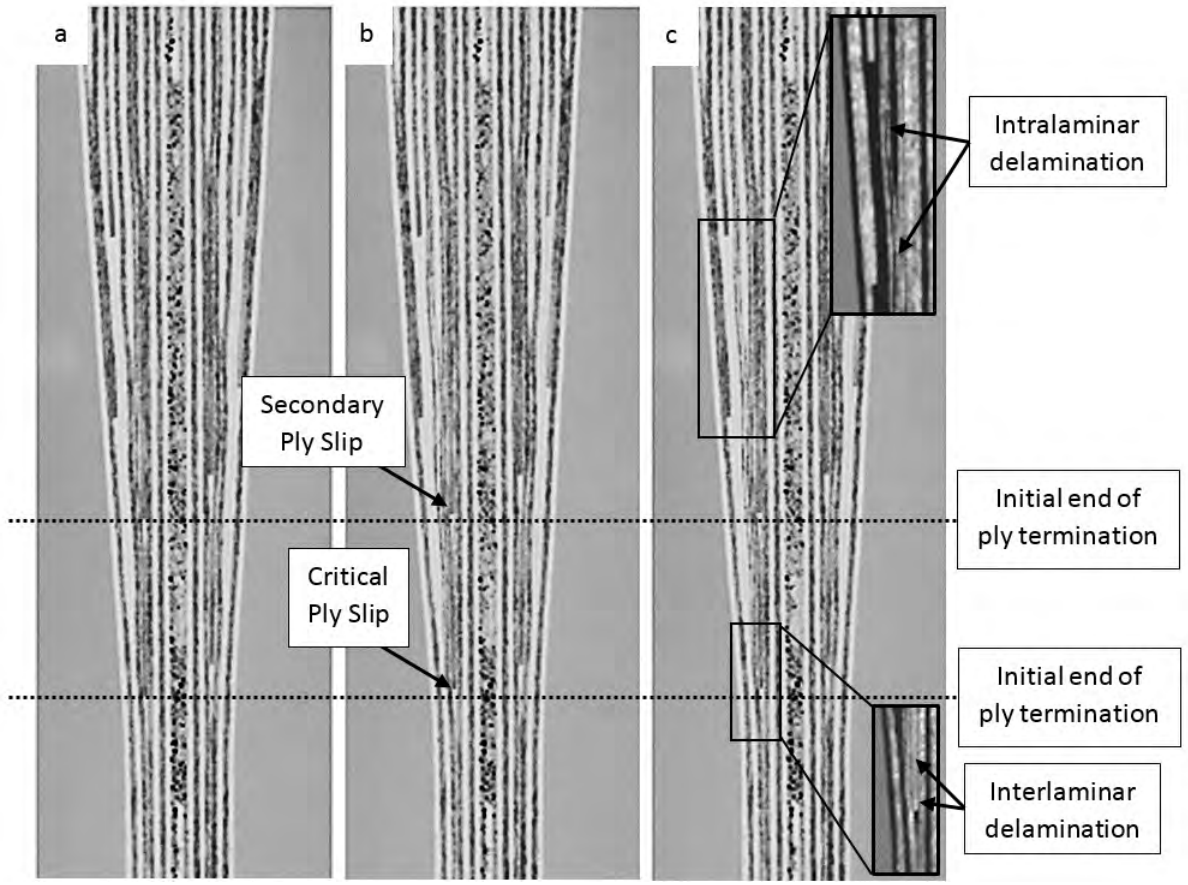

Figure 6.16: Optical high-speed camera footage of the stages of failure for a typical 40 μm VACNT interleaved specimen: (a) prior to delamination, (b) resin pocket rupture and delamination and (c) specimen structural integrity maintained after delamination with evidence of interlaminar and intralaminar fracture.

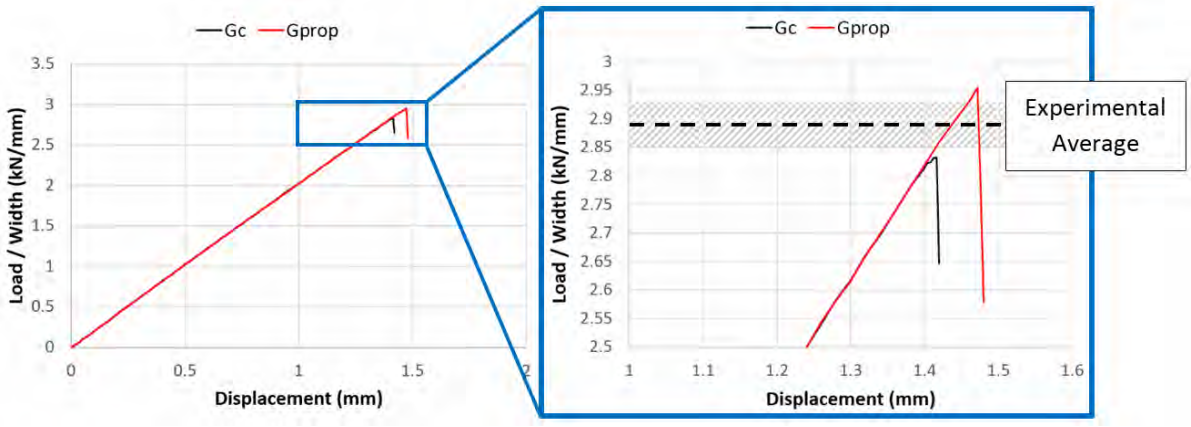

Figure 6.17: Load per unit width *versus* displacement for tapered specimens with G_{IC} and G_{IIC} defined as the initiation and propagation values measured experimentally and reported in chapter 5.

delamination onset occurred at the critical ply-drop ('Ply 7' as defined in Figure 6.1), matching observations with the optical high-speed camera footage. A similar behaviour was displayed by models defined with G_C and G_{prop} properties, with initial cohesive failure occurring in the early stages of the loading process at the interfaces adjacent to the critical terminated ply (Figure 6.18b). Delamination was then found to grow towards the thick section, whilst also initiating at the resin pocket tip. Further loading caused through-thickness tensile stress at the resin pocket tip, which, as observed by Wisnom *et al.* [182], opens the interface, causing instability and subsequently a loss in structural integrity. This simulated behaviour supports the experimental findings that interleaves comprising of longer VACNTs provide greater axial strength enhancements, as they increase the amount of bridging at the resin pocket, particularly at the tip. The orientation of the VACNTs is efficient at withstanding the through-thickness tensile stresses and therefore resists

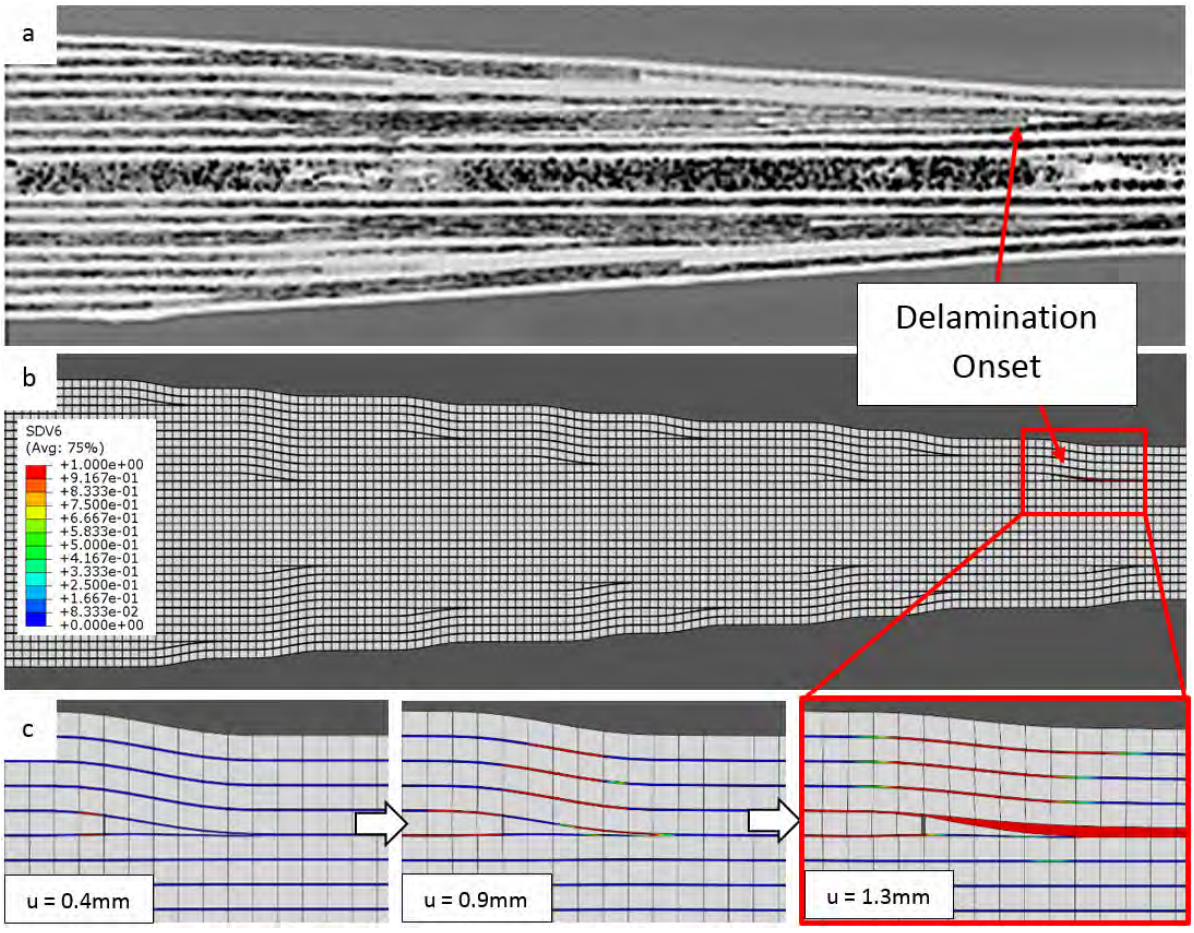

Figure 6.18: A comparison of the delamination onset location for baseline tapered specimens tested (a) experimentally and (b) numerically. (c) The failure sequence at the critical ply-drop; plotted is the damage variable (determined in Equation 6.3) at various displacements, where red is equal to cohesive element failure, or delamination, when at an axial displacement, u, of (left) 0.4 mm, (centre) 0.9 mm and (right) 1.3 mm.

unstable interface opening behaviour.

Overall, the baseline models were found to predict the failure load to within 2% of the experimental average, with the failure sequence matching the high-speed camera footage. It appears that a closer estimation is achievable by defining the cohesive strain energy release rate properties between the G_C and G_{prop} values. As it is commonplace to use crack initiation values to model composite structures, the remainder of this chapter will refer to unmodified cohesive elements with G_C properties. An identical study was conducted using G_{prop}, however similar conclusions were found. Therefore, to avoid confusion, they have been omitted from the chapter. Data tables from this complementary study have been provided in Appendix A for completeness.

6.3.3.2 VACNT interleaf comparison

To investigate whether the influence of VACNT interleaves can be captured using cohesive elements, the interfacial fracture toughness, strength and stiffness must be determined. Fracture toughness has been measured experimentally in chapter 5, although it was concluded that these values are the intralaminar fracture toughness of the host composite. In contrast, cohesive strength and stiffness are unknown. In order to estimate these enhanced properties, parametric studies will be conducted to investigate the model ultimate failure load and failure mode when different S_I and S_{II} combinations are defined. Cohesive elements, which simulate unmodified interfaces, shall be defined using the baseline model properties. For simplicity cohesive stiffness has been assumed to remain unaffected by the VACNT addition. Preliminary tests, discussed later in this section, have shown that this assumption makes an insignificant difference to the results.

The resultant failure loads for combinations of cohesive strengths are displayed in Table 6.8. Overall, it can be seen that the selected domain captures failure loads that both over- and under-estimate those measured experimentally (reported in Table 6.7). This indicates that at least one solution, which captures an identical axial strength of the interleaved tapered specimen, is within this property matrix. Comparing the interleaved model to that of the baseline model, axial strength differences can be distinguished, even when no elemental properties are changed. This is evident from Table 6.9, which displays the axial strength enhancements relative to the

Table 6.8: Failure load per unit width for combinations of cohesive element strengths. (*) shows the difference relative to the experimental value (reported in Table 6.7).

Mode II Cohesive Strength		S_{II}		
Mode I Cohesive Strength		**82.6**	**90**	**100**
S_I	**60**	2.80 (-9.50%)	3.05 (-1.37%)	3.04 (-1.63%)
	75	3.02 (-2.19%)	3.03 (-1.90%)	3.03 (-1.83%)
	90	3.14 (+1.75%)	3.13 (+1.39%)	3.11 (+0.54%)

Table 6.9: Failure load enhancement of the VACNT interleaved cohesive element model relative to the baseline model.

Mode II Cohesive Strength		S_{II}		
Mode I Cohesive Strength		**82.6**	**90**	**100**
S_I	**60**	-1.18%	7.69%	7.55%
	75	6.80%	7.11%	7.19%
	90	11.10%	10.70%	9.78%

Table 6.10: The failure load per unit width when the cohesive strength is scaled by the same proportion as the experimentally measured strain energy release rate.

Measured Strain Energy Release Rate*	G_{IC} (kJ/m^2)	G_{IIC} (kJ/m^2)
Baseline	0.22	0.62
VACNT Interleaved	0.3	0.71
Enhancement Ratio (-)	**1.36**	**1.15**

Cohesive Strength	S_{IC} **(MPa)**	S_{IIC} **(MPa)**
Baseline	60	82.6
VACNT Interleaved (Scaled)	**81.8**	**94.6**

VACNT Interleaved Cohesive Model	
Failure Load (kN/mm)	**3.10**
% Difference wrt. Experimental Average	0.26%
% Enhancement wrt. BL Model	9.47%

** As measured in chapter 5*

baseline model. Evaluating the property combination corresponding to the baseline values, *i.e.* S_I = 60 and S_{II} = 82.6, a -1.18% strength enhancement was determined. This indicates that axial strength is mesh dependent, *i.e.* it is dependent on the exact ply-drop locations, which were accounted for in each model configuration (see Figure 6.4).

Although it is not in the scope of this research to optimise the cohesive element strength to match the experimental data, it was noticed that one possible 'solution' appears to lie close to the relative strain energy release rate enhancement measured empirically in chapter 5. This enhancement ratio has been presented in Table 6.10, showing a rise of 36% in Mode I and 15% in Mode II, which corresponds to an enhanced Mode I and Mode II cohesive strength of 81.8 MPa and 94.6 MPa respectively. Applying these new values to the interleaved cohesive elements

and rerunning the model, the predicted failure mode differs from the experimental average by only 0.26%. Therefore, it can be concluded that assuming the cohesive strength enhancement is proportional to that of the critical strain energy release rate is a good initial assumption.

Reviewing the failure sequence of the interleaved models, two failure modes were observed (Figure 6.19b and Figure 6.19c). For both failure modes, initial cohesive damage occurred in a similar manner to the baseline model, with the interfaces surrounding the critical ply-drop delaminating and propagating towards the thick section. However, for higher Mode I strength configurations (when $S_I \geq 90$ MPa), the inner unmodified interface subsequently underwent unstable through-thickness tension, thereby resulting in a loss of structural integrity. This altered failure sequence is shown in Figure 6.20. It should be noted that the high-speed camera footage of the failure event did not capture this behaviour.

Overall, the cohesive modelling strategy appears to capture the enhancements in tensile strength that result from interleaving tapered specimens with VACNTs. Estimations of the strength recorded for both the baseline and interleaved specimens were comparable to the experimental results ($< 2\%$ difference) with similar failure sequences predicted to those observed in the high-speed camera footage. As an initial estimation, the cohesive strength enhancements from the VACNT interleaves are similar to that of the experimentally measured strain energy release rate enhancements. Preliminary tests to determine the effects of cohesive stiffness on tensile strength revealed that scaling the stiffness by the same proportions to cohesive strength resulted in the failure load increasing by only 0.25% (0.51% total axial strength enhancement relative to the baseline model). The operation of the high-speed camera made strain measurements difficult to achieve successfully and consequently global stiffness was not compared. Nevertheless, this simple model enables engineers to predict the initial failure load and location when strategically placing interleaves in more complex configurations and geometries.

It should be mentioned that a number of assumptions were made in the construction of these models, which should be refined if accuracy is to be increased. For example, the resin pocket shape has been meshed identically at every ply-drop, regardless of the layup or its location relative to the surface. Moreover, the ply thickness has been assumed constant throughout the laminate. These assumptions have led to high levels of surface waviness, as shown in Figure 6.4, which will result in greater interlaminar stresses forming and therefore result in an underestimation of the failure load. A limitation with cohesive element methods is that they only predict interlaminar fracture. Thus far, it has been shown that VACNT interleaves result in intralaminar delamination for stable crack growth. Hence, with a similar tensile failure load predicted for the the VACNT interleaved specimens, it is hypothesised by the author that intralaminar fracture is again present. In previous chapters, it was shown that intralaminar fracture behaviour occurs in both Mode I and Mode II conditions, for all of the nanotube lengths used in this study. This suggests that nanotube bridging of the resin pocket tip is the main contributor towards the measured increase in tensile strength. Preliminary cohesive models, which simulated poor nanotube bridging (*i.e.* the cohesive

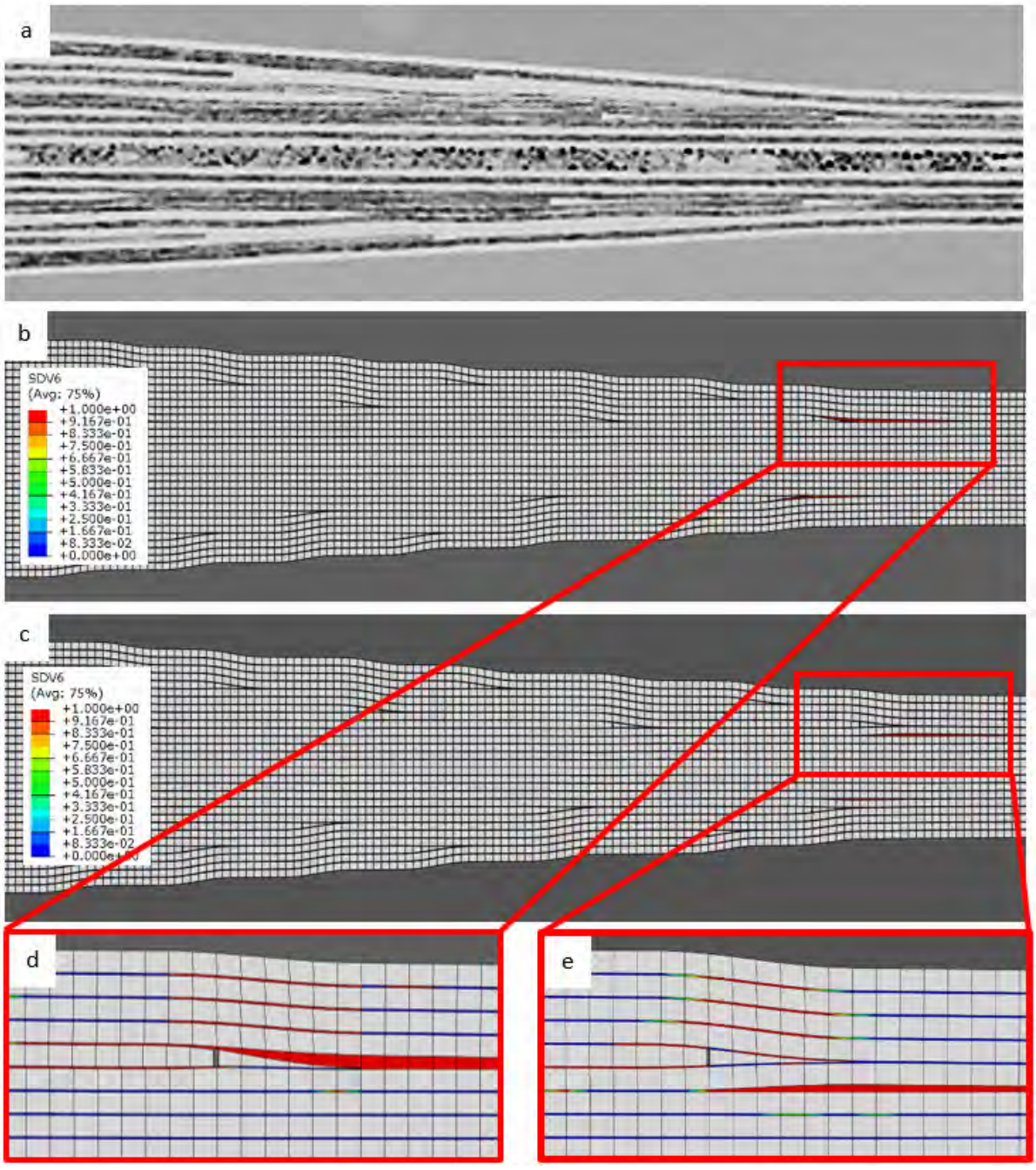

Figure 6.19: A comparison of the delamination onset location for (a) a 40 μm VACNT interleaved tapered specimen experiment and (b-c) the corresponding models. Two failure modes are observed for the interleaved models: (b) resin pocket delamination and (c) inner interface delamination, with respective magnified images (d-e) at the critical ply-drop.

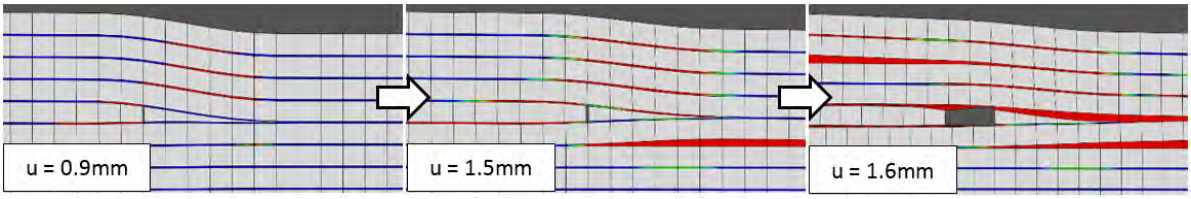

Figure 6.20: The failure sequence around the critical ply-drop for an inner interface delamination failure mode when at an axial displacement, u, of (left) 0.9 mm, (centre) 1.5 mm and (right) 1.6 mm.

element properties were not enhanced at the critical ply-drop resin pocket), were conducted to investigate whether poor bridging dominates the failure load. While a lower failure load was predicted ($\approx$ 3% reduction), it was not as substantial as that seen in experimental work. Further work into understanding the length dependency on failure load is therefore recommended.

6.4 Conclusion

In this chapter, CFRP tapered specimens, which fail repeatably through delamination, are interleaved with vertically aligned carbon nanotubes (VACNTs) at the critical ply-drops and loaded in tension to failure. Two nanotube lengths are investigated (11 μm and 40 μm) and compared to an unmodified baseline, in terms of laminate tensile strength and delamination onset location. Imaging pristine interleaved specimens showed that the longer nanotube configuration increased bridging of the resin pocket, but with the compromise of greater amounts of nanotube micro-buckling.

Mechanical tests have shown that the tensile strength of tapered specimens interleaved with the 40 μm VACNTs was increased by 7% relative to the unmodified baseline, while the introduction of 11 μm VACNTs made no significant difference; global laminate stiffness was unaffected by the introduction of the nanotubes. Optical and IR high-speed camera footage showed similar failure mechanisms for all specimens, namely, cracks initially propagating along both interfaces surrounding the terminated ply towards the thick section. This caused the terminated ply to slip towards the thick section, subsequently leading to the opening of the resin pocket tip; a secondary delamination event then propagated towards the thin section, causing complete loss in structural integrity. Additional features were observed for the 40 μm interleaved specimens, including slippage of multiple 'stitched' plies and the formation of intralaminar cracks, which led to greater amounts of energy dissipation. For a couple of specimens, structural integrity was maintained post delamination, with specimens enduring a further 0.5 seconds after the observed initial ply slippage.

Tapered specimens were modelled using cohesive elements to determine whether the influence from VACNT interleaves could be captured. Baseline models with material properties extracted from primary material characterisation data and literature, predicted an ultimate failure load

that was comparable to the experimental results (< 2% difference), with similar failure sequences observed. A parametric study was conducted to determine the cohesive strength enhancements from the introduction of VACNT interleaves. A good initial estimation was to assume cohesive strength enhancements were proportional to the strain energy release rate enhancements. This resulted in the ultimate failure load prediction agreeing (< 0.5%) with the experimental average.

It is believed by the author that the strength increases measured exclusively for the 40 μm VACNT interleaves is due to the increased bridging that occurs at the resin pocket tip. This additional bridging increases the resistance to through-thickness tension stresses and hence opening delaminations. While preliminary models showed that a lack of VACNT bridging at the resin pocket tip does reduce the ultimate strength of the laminate, the knock-down was not as severe as that measured experimentally. A number of assumptions were made with these models, such as similar resin pocket geometries and constant ply thicknesses, which will need to be addressed in future work to improve accuracy. However, it has been shown that this simple tool will enable engineers to quickly and accurately predict the failure loads and locations when strategically placing interleaves in more complex configurations and geometries.

PROLOGUE TO CHAPTER 7

The second delamination-prone structure evaluated in this research is a notched specimen, which is subjected to a tensile loading condition. In common with the work done on tapered composites (chapter 6), these notched specimens shall be interleaved with VACNTs and experimentally compared to similar unmodified baseline specimens.

The aims of this research are identical to that of chapter 6 and can be found in the prologue to chapter 6.

CHAPTER 7

SUPPRESSING DELAMINATION OF NOTCHED COMPOSITES THROUGH INTERLEAVING WITH VACNTS

Abstract

Delamination-prone open hole tension (OHT) specimens with two different layup configurations (ply-level and sub-laminate) were interleaved with vertically aligned carbon nanotubes (VACNTs) and loaded quasi-statically in tension. VACNTs with a nominal length of 20 μm were interleaved at every ply interface throughout the laminate thickness. Comparisons were made between unmodified baseline and VACNT interleaved specimens with respect to tensile strength and damage mechanisms. Damage was determined and quantified through X-ray CT scans conducted on interrupted tests, taken at a selection of load severities. A finite element model was constructed to investigate whether the effect from VACNT interleaves can be captured numerically through cohesive elements.

Mechanical tests concluded that VACNTs had an insignificant influence on either the OHT strength or stiffness, for both OHT layup configurations. Microscopy of the post-delaminated ply-level specimen edge indicated that both the baseline and VACNT interleaved specimens failed predominantly through intralaminar delamination, and therefore the interlaminar reinforcement offered by the VACNT interleaves is not suitable for enhancing tensile strength. Strength predictions from the cohesive finite element model supported this hypothesis, with the most representative model ($\approx$ 5% difference in tensile strength) being when cohesive elements are defined with intralaminar properties. The model did not capture the influence of isolated ply-splits within the laminate, which were seen to transfer damage and redistribute stress through the laminate thickness. CT scans showed similar failure mechanisms for both the baseline and VACNT interleaved specimens, however quantification of the matrix damage for each interrupted test suggested that VACNT interleaves reduced the total damaged area. It is recommended that intralaminar reinforcement techniques, *e.g.* homogeneous dispersion of nano-fillers or multi-scale fibres, may be a more appropriate means of suppressing delamination in quasi-statically loaded OHT specimens.

7.1 Introduction

The aim of this chapter is to understand how VACNTs affect the tensile strength and failure mechanisms when interleaved into a notched specimen. Using the results from the investigation carried out by Green *et al.* [194], an OHT specimen, which exhibits a delamination dominated failure mode, shall be interleaved with VACNTs and compared to an equivalent baseline. Computerised Tomography (CT) scans, similar to that used by Nixon-Pearson *et al.* [250], shall be performed on interrupted test specimens to understand the sequential damage mechanisms and quantify the damage extent for each specimen configuration. As the 'pull-out' failure mode, defined by Green *et al.* [194], also has an extensive sub-critical interlaminar damage prior to failure, a notched specimen, which exhibits a pull-out failure behaviour has also been interleaved and tested with its unmodified equivalent. This will develop an understanding of how ply stacking sequence influences the strength enhancement from VACNT interleaves.

To conclude this chapter, a supplementary investigation shall be conducted to investigate whether an interleaved OHT specimen can be accurately modelled using cohesive elements. In common with the numerical work done in chapter 6, VACNT interleaves shall be modelled as homogeneous cohesive elements with enhanced properties relative to the baseline equivalents. These cohesive element properties shall be directly taken from the values reported in chapter 6, for a tapered interleaved specimen. The model strength output and damage mechanisms shall then be compared to the experimental data to understand whether homogeneous cohesive element property enhancements are sufficient to predict the load and mode of failure of a notched, interleaved composite laminate.

7.2 Methodology

7.2.1 Laminate fabrication

All OHT specimens were manufactured out of HexTow® IM7/HexPly® 8552 prepreg (Hexcel Composites, Duxford, U.K.), with a cure ply thickness of 0.125 mm. Laminates were laid up by hand and cured using the modified cure cycle described in Chapter 4.

Two quasi-isotropic layups were evaluated in this study, which, as shown by Green *et al.* [194], fail through different modes and extensive matrix damage: a ply-level layup ($[45_2/90_2/-45_2/0_2]_S$), which fails through delamination, and a sub-laminate layup ($[45/90/-45/0]_{2S}$), which fails through a pull-out failure mode. While other layups also exhibited similar failure modes [194], these selected configurations had the minimum thickness, thereby requiring fewer interfaces to be interleaved.

VACNT interleaves were applied at every interface during the layup process. After initially being grown on to a metallic substrate through a proprietary continuous chemical vapour deposition (CVD) process [213, 214], the CNTs were transferred to the prepreg surface. This was

Table 7.1: Geometric properties of the VACNTs investigated in this chapter.

Form (−)	Length (μm)	Diameter (nm)	Population Density ($CNTs/cm^2$)
MWCNTs	20 ± 4	12	1.0E+10 - 1.5E+10

achieved *via* initially positioning the 30 mm wide VACNTs film on to the exposed prepreg surface (Figure 7.1a) and subjecting the system to vacuum pressure and heat (55°C) using a heated plate. The system was then left for 2 minutes, before the substrate was removed, leaving the VACNTs deposited on the prepreg surface, as seen in Figure 7.1b. VACNT properties were identical for all interleaved OHT specimens and can be seen in Table 7.1.

Laminate plates contained both the baseline and interleaved specimens (Figure 7.1b). Post-cure, panels were cut in half using a water-cooled diamond coated saw. GFRP end-tabs, with a nominal thickness of 3 mm, were adhesively bonded to the surface of the laminate using Huntsman Araldite 2014 and cured at 20°C for 7 days [239]. Prior to bonding, the surface of both the laminate and end-tabs were grit blasted to ensure good adhesion.

End-tabs were bonded at a distance of 63.5 mm apart, with the interleave region located centrally in the gauge length. Specimens were then cut to 15.9 mm x 163.5 mm, as shown in Figure 7.1c, using a water-cooled diamond coated saw. These dimensions were selected to be consistent to the work carried out by Green *et al.* [194] and comply with the ASTM D5766 standard requirements for OHT specimens [251].

Holes were drilled centrally using a diamond coated drill bit, which was continuously sprayed

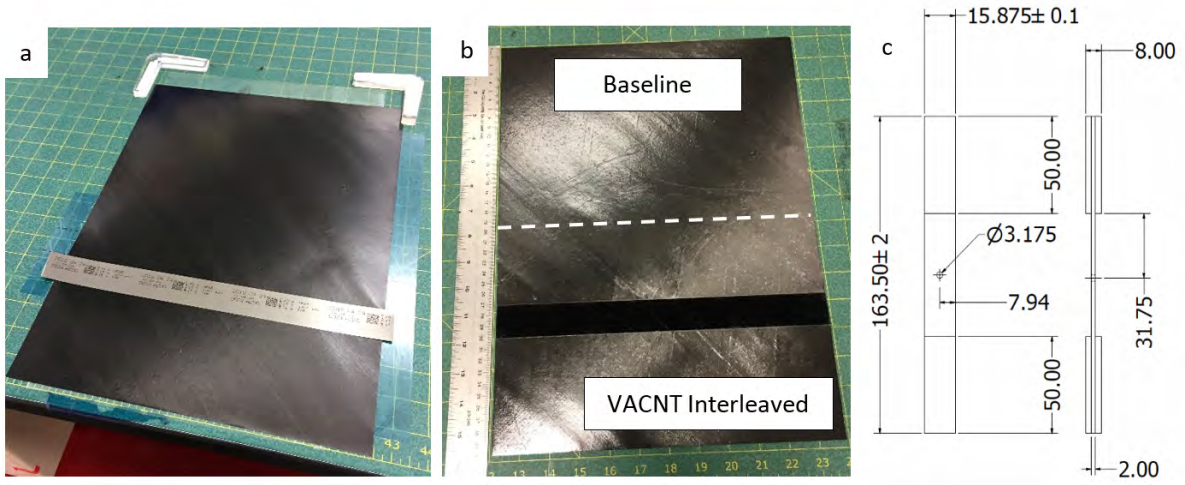

Figure 7.1: (a) −45° prepreg ply with VACNTs positioned on the surface prior to transfer, (b) −45° prepreg ply with VACNTs transferred onto the surface and annotations of the 'baseline' and 'VACNT interleaved' specimen zones and (c) a schematic of the OHT specimen with dimensions annotated (all dimensions in mm).

with a water-coolant solution. In order to mitigate delaminations from drill break-through, specimen surfaces were supported with 2 mm thick HexTow® IM7/HexPly® 8552 CFRP material. Drill speed was maximised (≈ 3000 rpm), while insert speed was minimised (≈ 1 mm/min). Visual inspection of the machined hole feature revealed little fibre breakage or local delaminations. To assess the fabrication quality of the interleaves, pristine samples were cut using a water-cooled diamond saw and ground and polished to a fidelity of at least one micron. Polished samples were then placed under a Verios^{TM} XHR SEM (FEI, Oregon, USA) at magnification levels of x75 to x3250 and a voltage acceleration of 500V.

7.2.2 Mechanical testing

All specimens were tensile loaded using a calibrated Instron 8801 with a 100 kN load cell at a constant displacement rate of 0.5 mm/min. Tests were recorded using an iMETRUM video gauge with a high-magnification lens attached to monitor ply-level damage. Both surfaces of the specimen were illuminated to improve visualisation of the hole edge. The experimental test set-up can be seen in Figure 7.2. Overall, five replicants were tested for all four specimen configurations.

7.2.3 3D x-ray computed tomography

To understand the damage mechanisms involved for each specimen configuration, interrupted tests were conducted at 60%, 80%, and 90% of the nominal failure loads. 3D x-ray computer tomography (CT) scans were performed on each interrupted test specimen. Prior to scanning, specimens were submerged in an x-ray dye penetrant solution, comprising of zinc iodide (250 g), distilled water (80 ml), isopropyl alcohol (80 ml), and Kodak Photofol® (1 ml) for a duration of 48 hours. Scans were then taken using a Nikon XTH320 CT Scanner, located at the National Composite Centre (NCC), Bristol. For each specimen, 3142 x-ray image radiographs (projections) were taken, with 2 frames averaged per projection. The scanning voltage was 75 kV (190 μA), with an image radiograph resolution of 0.025 mm/25 μm.

7.2.4 Numerical modelling

7.2.4.1 Meshing

In common with chapter 6, a numerical study was conducted, which investigated whether cohesive elements can capture the influence of VACNT interleaves. The models were constructed using the commercial FE package ABAQUS® and utilised a similar mesh to that published by Hallett *et al.* [2]. Only the ply-level, delamination dominated, layup was modelled, due to uncertainty in the fibre failure criterion implementation required to capture failure of the sub-laminate layup.

All models consisted of solid brick elements representing the plies, which were separated by cohesive interface elements. Ply-splits were simulated by additional cohesive interface elements, which ran parallel to the fibre orientation and tangential to the hole, terminating at the specimen

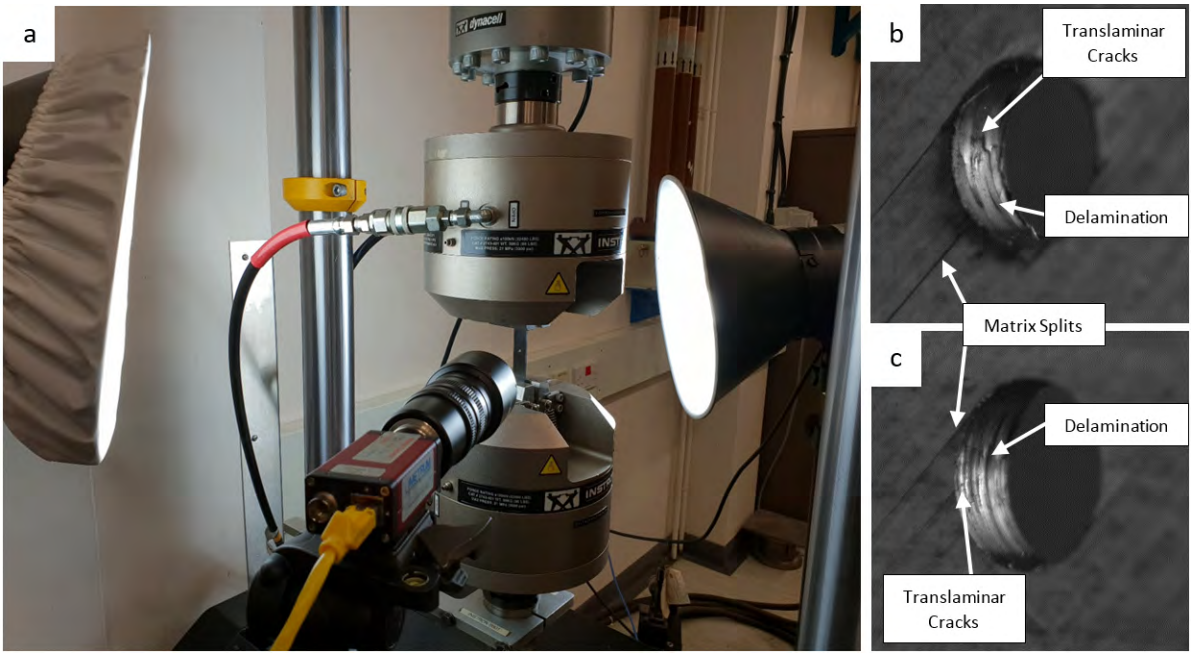

Figure 7.2: (a) Photograph of the OHT test set-up with in-situ images of the notch for the (b) block-ply and (c) sub-laminate layup baseline specimens.

edge. The exception to this was for the 90° plies, which were inserted at the locations of highest stress concentrations. This meshing method has been shown to be able to capture intra-ply splitting and interlaminar delamination [2, 252], which have been experimentally observed for these OHT laminate configurations [194]. Inserting the ply-splitting cohesive elements within the mesh resulted in degenerated elements around the hole, which were removed to leave a slightly misshapen aperture. This will alter the linear elastic stress concentrations around the hole, however, as discussed by Hallett *et al.* [2], once ply splitting initiates, the stress concentrations will be relieved, resulting in the hole geometry being less influential. Symmetry in the layup allowed for a half model to be constructed, saving computational demand.

The ply-level mesh can be seen in Figure 7.3. Mesh refinement studies were conducted by Hallett *et al.* [2], and showed that a converged solution was obtainable when the in-plane element size around the hole was in the magnitude of one to two ply thicknesses (≈ 0.125 mm - 0.25 mm). The mesh spanned the entire gauge length (63.5 mm) and specimen width (15.875 mm). Overall, the OHT model consisted of 84992 eight-node brick elements for the plies, 63744 cohesive elements for interlaminar interfaces, 576 cohesive elements for ply-splits and 174038 nodes.

7.2.4.2 Material properties

Identical material properties to those described in chapter 6 were used for the ply and interface elements. An exception to this was for the ±45° plies, which were no longer homogeneously defined (an assumption previously used to allow for modelling a slice). For completeness, all

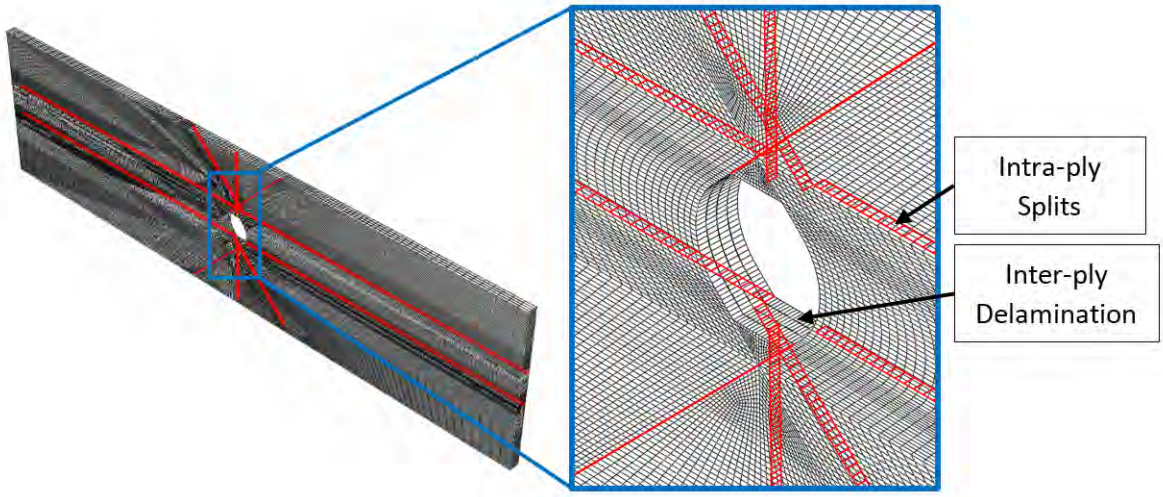

Figure 7.3: Example of the mesh with intra-ply cohesive elements highlighted for a ply-level OHT specimen.

material properties have been redefined in Tables 7.2 - 7.4. These properties were determined through either primary sourced experimental data or other relevant literature.

To model ply-level failure, cohesive elements, which captured through-thickness compression effects were used for both the interlaminar and ply-split interfaces. Assumptions and terminologies discussed in chapter 6, Section 6.2.3, were retained for all cohesive elements.

7.2.4.3 Boundary conditions

Each model consisted of an initial step and a dynamic, explicit step. The first step comprised of boundary conditions fully constraining one face and enforcing symmetry conditions to the symmetric plane. The second step contained a uniformly distributed axial velocity applied to all free-end nodes, which continued until failure. The displacement rate was selected to not induce any dynamic effects. Internal reactive loads, and therefore failure loads, were determined through a load integrated output across a cross-sectional surface a short distance away from the fully constrained end-face. These conditions can be seen in Figure 7.4. Thermal residual stresses were incorporated through applying a $-160°C$ temperature reduction before axial loading. This simulated the cool down process after curing the composite at $180°C$ and testing at room temperature ($20°C$).

Table 7.2: Material properties for a 0° unidirectional ply of IM7/8552 [2].

E_1 (GPa)	$E_2 = E_3$ (GPa)	$G_{12} = G_{13}$ (GPa)	G_{23} (GPa)	$\nu_{12} = \nu_{13}$ $(-)$	ν_{23} $(-)$	α_{11} $(°C^{-1})$	$\alpha_{22} = \alpha_{33}$ $(°C^{-1})$
161	11.38	5.17	3.98	0.32	0.44	0	3e-5

Table 7.3: Cohesive element properties used for the baseline OHT model.

G_{IC} (N/mm)	G_{IIC} (N/mm)	S_I (MPa)	S_{II} (MPa)	K_I (N/mm^3)	K_{II} (N/mm^3)	η_S $(-)$
0.22*	0.62*	60 [245]	82.6 [249]	4.67e5 [245]	1.75e5 [245]	0.3 [245]

** Determined by experimental work presented in chapter 5.*

Table 7.4: Cohesive element properties used for the VACNT interleaved OHT model.

G_{IC} (N/mm)	G_{IIC} (N/mm)	S_I (MPa)	S_{II} (MPa)	K_I (N/mm^3)	K_{II} (N/mm^3)	η_S $(-)$
0.3*	0.71*	81.8#	94.6#	4.67e5 [245]	1.75e5 [245]	0.3 [245]

** Determined by experimental work presented in chapter 5.*
 # Determined by numerical work presented in chapter 6.

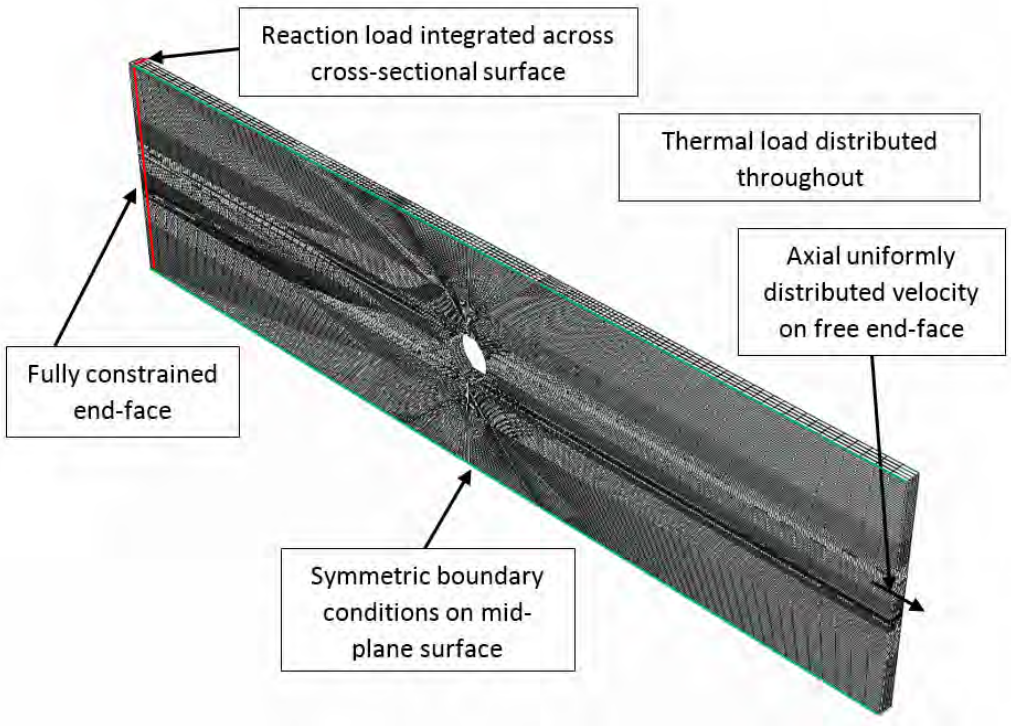

Figure 7.4: Annotated schematic of the cohesive element model for an interleaved tapered specimen showing all loads and boundary conditions applied.

7.3 Results and Discussion

7.3.1 Microscopy

Far-field and high-magnification cross-sectional SEM images of pristine ply-level and sub-laminate VACNT interleaved specimens are shown in Figure 7.5a and Figure 7.5b respectively. It can be observed that all interfaces were interleaved successfully with VACNTs. The effective CNT length varied along the specimen, with fibre interactions leading to micro-buckling behaviours. The average effective CNT length was approximately 10 μm, or 50% of the original CNT length.

Interfaces that separate same fibre orientation plies were found to lead to greater amounts of VACNT film waviness. This was evident when comparing the interfaces for the ply-level interleaved laminate (Figure 7.5a). The reasoning for the increased waviness has been attributed to fibre nesting in regions where interleaves are not present. This bridging behaviour will result in the effective ply-thickness becoming more variable. Therefore, in regions where fibre bridging is inhibited by the VACNTs, the interfaces are no longer uniform. On the other hand, for interfaces that separate plies with differing fibre orientations, such as for the sub-laminate configuration, nesting does not occur, and the average cure ply thickness remains uniform.

7.3.2 Mechanical testing

Typical stress *versus* displacement plots for the ply-level and sub-laminate OHT baseline specimens can be seen in Figure 7.6 and Figure 7.7 respectively. As reported by Green *et al.* [194], a clear difference in load profile can be seen between each layup configuration, corresponding to a delamination dominated and pull-out dominated failure modes for the ply-level and sub-laminate specimens respectively.

The ply-level load profile contains 2-3 distinct load drops, which correspond to three failure events. As discussed by Green *et al.* [194], Hallett *et al.* [2] and Nixon-Pearson *et al.* [250], these failure events consist of initial delamination of the $-45°/0°$ ply interface, followed by second delamination event at the same interface, attributed to asymmetric damage around the hole and finally $0°$ fibre failure. As the geometric integrity of the specimen was lost after the first delamination load drop, this has been defined as failure, for the purposes of this study. On the other hand, the sub-laminate load profile contained a signal and catastrophic load drop, ascribed to $0°$ fibre failure.

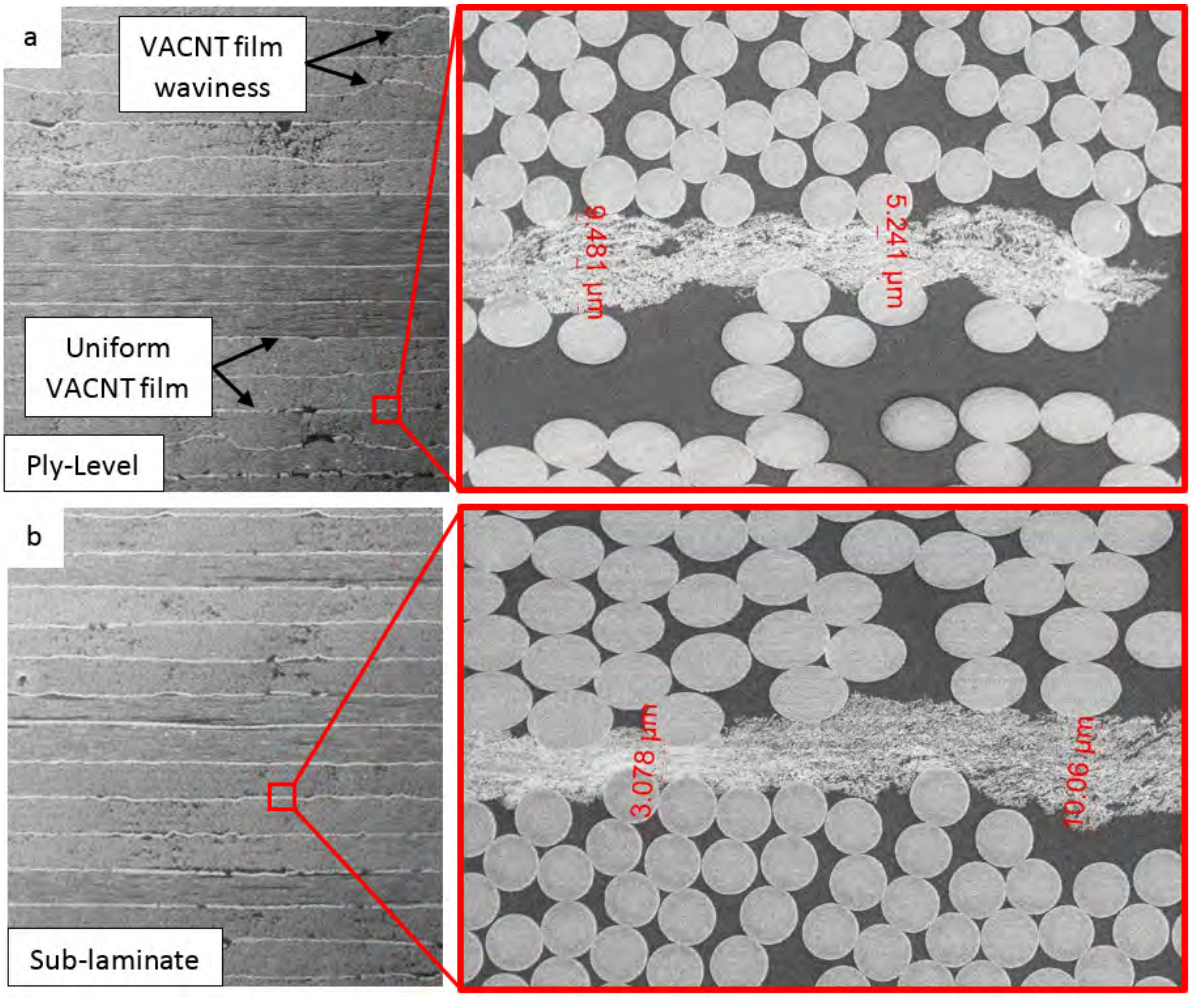

Figure 7.5: SEM images of the cross-section for (a) the block-ply and (b) sub-laminate layup when interleaved with VACNTs.

For both layup configurations, non-linearity was observed prior to the first load drop. Such behaviour is accustomed to an accumulation of damage around the hole in the form of matrix splitting, translaminar cracks and small delaminations, all of which were repeatably observed in the recorded video gauge footage, as seen in Figure 7.2b and Figure 7.2c. A more in-depth analysis into the failure sequences will be discussed in Section 7.3.3.

Typical stress *versus* displacement plots for the ply-level and sub-laminate VACNT interleaved specimens are also shown in Figure 7.6 and Figure 7.7 respectively. Comparing these load profiles with their baseline equivalents, it appears that no significant enhancements are achieved through VACNT interleaving, regardless of the layup configuration.

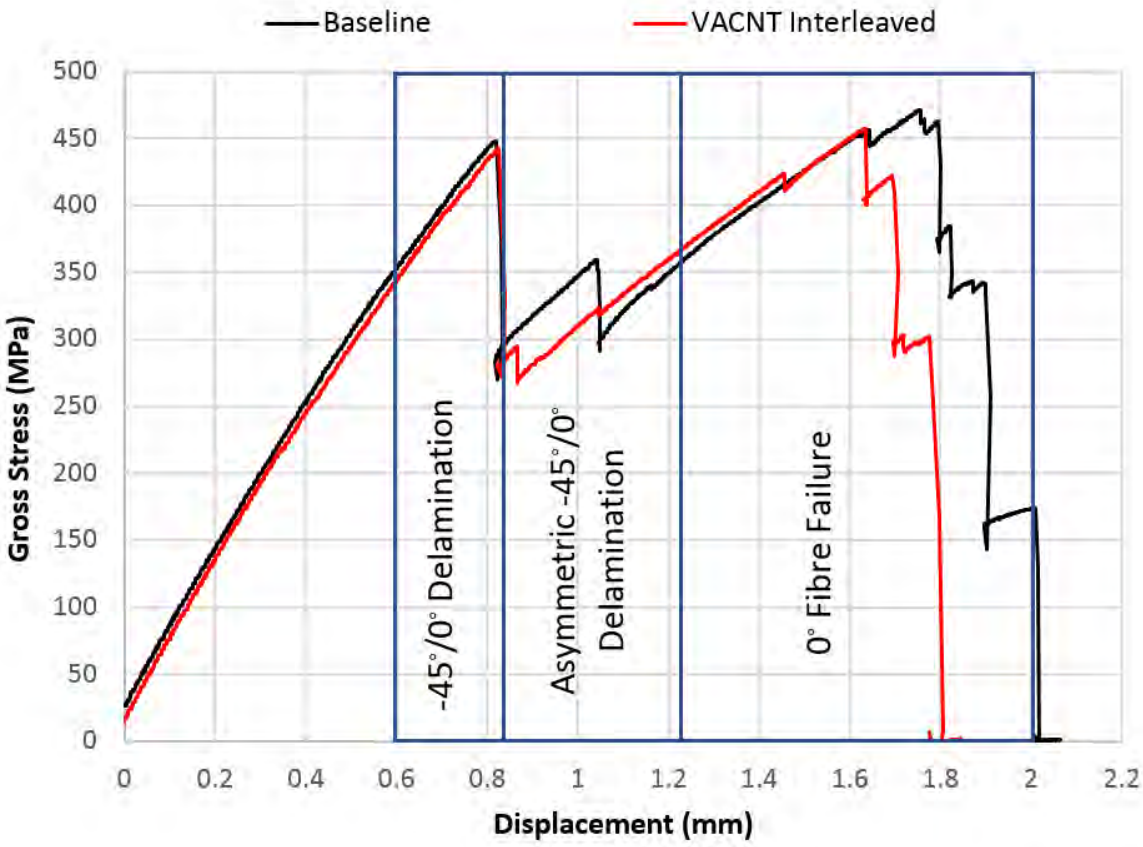

Figure 7.6: Typical gross stress *versus* displacement plots for a baseline and VACNT interleaved OHT specimen with a block-ply layup.

The average failure stress for each OHT configuration tested is displayed in Table 7.5. It should be highlighted that this is the gross average stress as calculated in Equation 7.1.

$$\sigma_f = \frac{Failure\ Load}{Gross\ Area} = \frac{L_f}{Wt} \tag{7.1}$$

where σ_f is the gross failure stress, L_f is the failure load, W is the average specimen width and t is the average specimen thickness. Specimen dimensions were determined through a digital Vernier calliper taken at three points along the specimen prior to testing.

Each laminate configuration showed good consistency, with a maximum coefficient of variance being within 5%. Overall the average baseline notched strength for the ply-level layup was approximately 455 MPa, while the average baseline sub-laminate notched strength was 546 MPa. Comparing these values to that published in literature (displayed in Table 7.6), it can be observed that the measured strengths in this study are higher. The reasoning for this is believed to be a result of machining quality; spare samples directly taken from the study by Nixon-Pearson

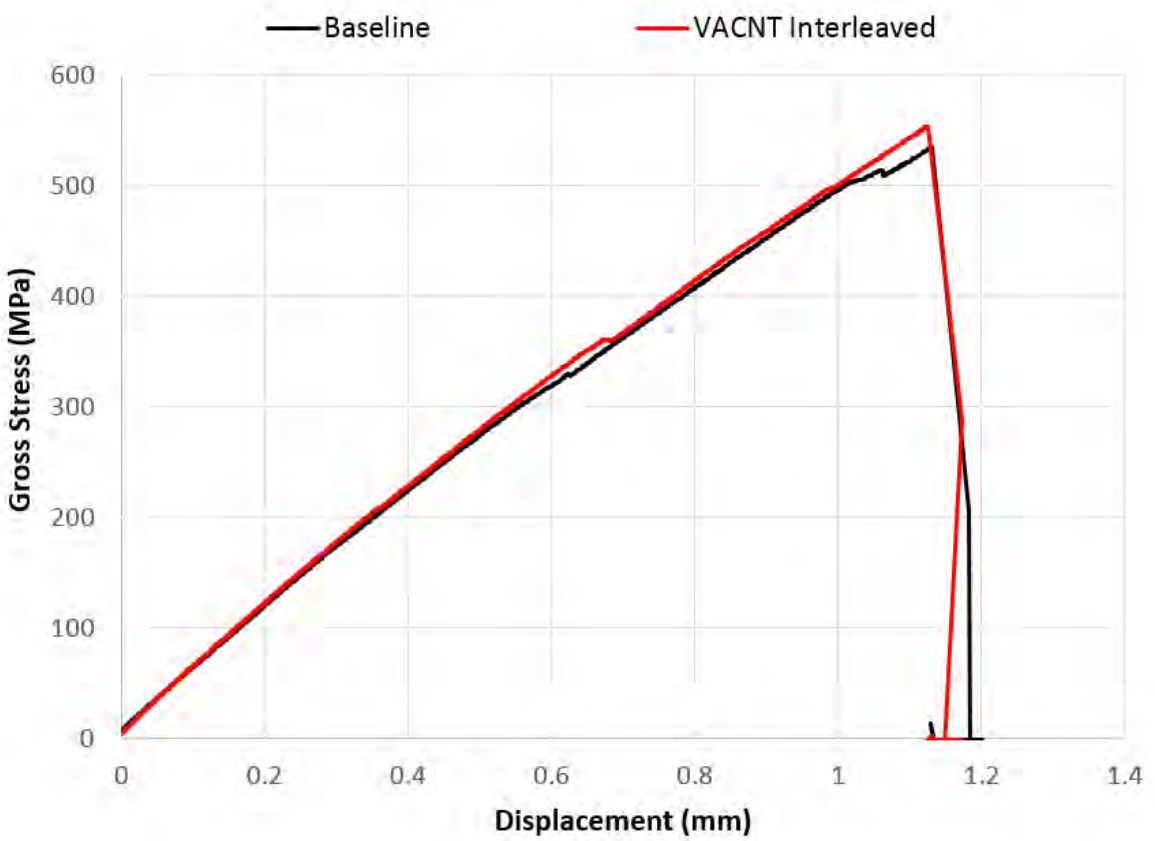

Figure 7.7: Typical gross stress *versus* displacement plots for a baseline and VACNT interleaved OHT specimen with a sub-laminate layup.

et al. [250], show a greater amount of damage around the hole prior to testing (see Figure 7.8). Although, both samples were drilled using the same procedure (outlined in Section 7.2.1), a different drill-bit type was used; this study used a diamond coated drill-bit, while all of the other studies, shown in Table 7.6, used a tungsten carbide coated drill-bit. The latter is not as durable, which leads to a greater amount of back-face delamination and matrix splits. It is therefore believed by the author that this machining damage will induce premature failure and hence be a key contributor to the lower strength measurements. Other sources of discrepancy could also be attributed to subtle changes in the fibre volume fraction, due to the modified cure cycle and batch variability (CFRP material used in this study was sourced over 5-10 years after the work published in some cited literature).

Despite the conclusive evidence that VACNT interleaves do not improve the notch strength of OHT specimens, an investigation into the damage sequences is still extremely valuable for understanding the reasoning for the lack in strength enhancement.

Table 7.5: Average net failure stress for each OHT specimen configuration.

Layup Type	**Ply- Level** $[45_2/90_2/-45_2/0_2]_S$		**Sub-laminate** $[45/90/-45/0]_{2S}$	
Configuration	Baseline	VACNT Interleaved	Baseline	VACNT Interleaved
Failure Stress (MPa)	**455**	**453**	**546**	**543**
CV (%)	1.5	3.2	3.9	4.3

Table 7.6: Average net failure stress reported in other literature investigating similar OHT laminate configurations. The difference between the literature and primary data included.

Layup Type	**Ply-Level** $[45_2/90_2/-45_2/0_2]_S$					**Sub-laminate** $[45/90/-45/0]_{2S}$		
Reference	Green [194]	Nixon-Pearson [250]			Cheung and Hallett [253]	Green [194]	Nixon-Pearson [254]	
Failure Stress (MPa)	**396**	**418**	**447**	**396**	**448**	**500**	**581**	**532**
CV (%)	5.2	6.6	3.1	5.4	5.3	4.0	2.9	3.1
Difference (%)	-12.9	-8.0	-1.7	-12.9	-1.4	-8.4	6.5	-2.5

7.3.3 Computed tomography (CT) analysis

Global damage for the ply-level and sub-laminate layups can be seen in Figure 7.10 and Figure 7.12 respectively. Displayed in each Figure are the baseline and VACNT interleaved OHT specimens when interrupted at 60%, 80% and 90% of their respective nominal failure stress.

For both layup configurations, damage can be categorised into four groups, signifying the stages to failure [194]. These groups include:

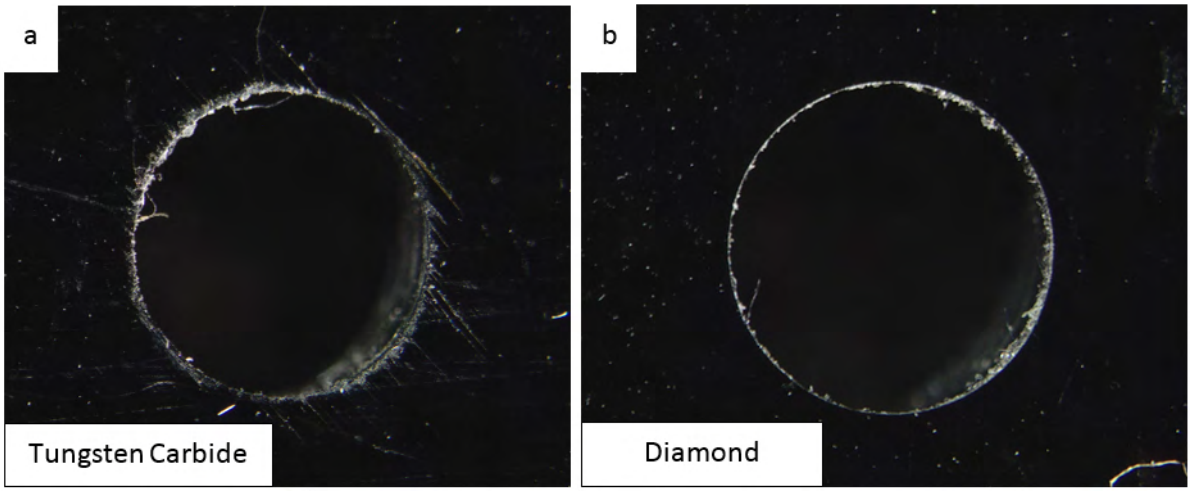

Figure 7.8: Microscope image around the notch for a hole drilled using (a) a tungsten carbide coated drill bit and (b) a diamond coated drill bit.

1. isolated damage at the hole;
2. extensive damage at the hole within the inner delamination regions (see Figure 7.9);
3. damage across the specimen width within the outer delamination regions (see Figure 7.9);
4. damage along the length of the specimen.

More detailed descriptions of the failure sequence for the ply-level and sub-laminate layup configurations are provided in Sections 7.3.3.1 and 7.3.3.2 respectively.

7.3.3.1 Ply-level failure sequence

Analysing the sequential interrupted tests displayed in Figure 7.10 and video gauge footage (Figure 7.2b), it can be observed that initial damage comes in the form of ply-splitting in the +45° surface plies and 0° central plies. These splits initiated at the edge of the hole and propagated tangentially along the fibre direction towards the specimen edge.

Isolated matrix splits in the 90° and −45° plies were later observed, which followed the +45° and 0° propagated matrix splits respectively, through translaminar cracking (seen in Figure 7.2b). The accumulation of these isolated cracks leads to small local delaminations in the inner region and at the specimen edge. With greater stress severity, the local delaminations grew into the outer region leading to delamination damage across the whole specimen width (Figure 7.10). Final failure occurred with the delamination onset of the +45°/0° interface, as also observed by Green *et al.* [194].

As seen in Figure 7.10, there are no clear differences in damage mechanisms between the interrupted baseline and VACNT interleaved OHT specimens. This suggests that while the

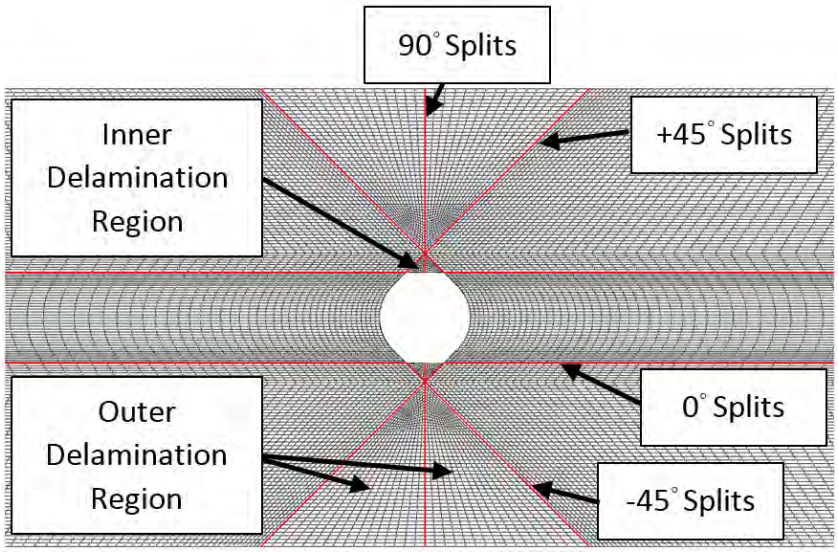

Figure 7.9: Plan view of cohesive element model with damage zones annotated.

specimens ultimately fail through delamination, failure load is dominated by the matrix splitting behaviour and the VACNTs do not provide enough of an enhancement in the interlaminar region to suppress delamination.

Optical microscopy of the OHT specimen edge was conducted for a post-delaminated baseline and VACNT interleaved specimen. These can be seen in Figure 7.11. While some evidence of interlaminar delamination was observed at the $0°/-45°$ interface (Figure 7.11a), the majority of damage displayed intralaminar delamination for both the baseline and VACNT interleaved specimens (Figure 7.11b). The lack of crack propagation through the resin rich interlaminar region explains the negligible strength enhancement measured for the OHT specimens with VACNT interleaves; the localised reinforcement does not obstruct the natural crack direction and so no delamination suppressive behaviour occurs. Therefore, it appears that failure of the ply-level OHT specimens are intralaminar delamination dominated, and hence, does not suit an interlaminar reinforcement method. Instead, the homogeneously dispersed matrix modifying techniques discussed in Section 2.2.3.1, may be more appropriate for improving the fracture toughness and tensile strength for this application.

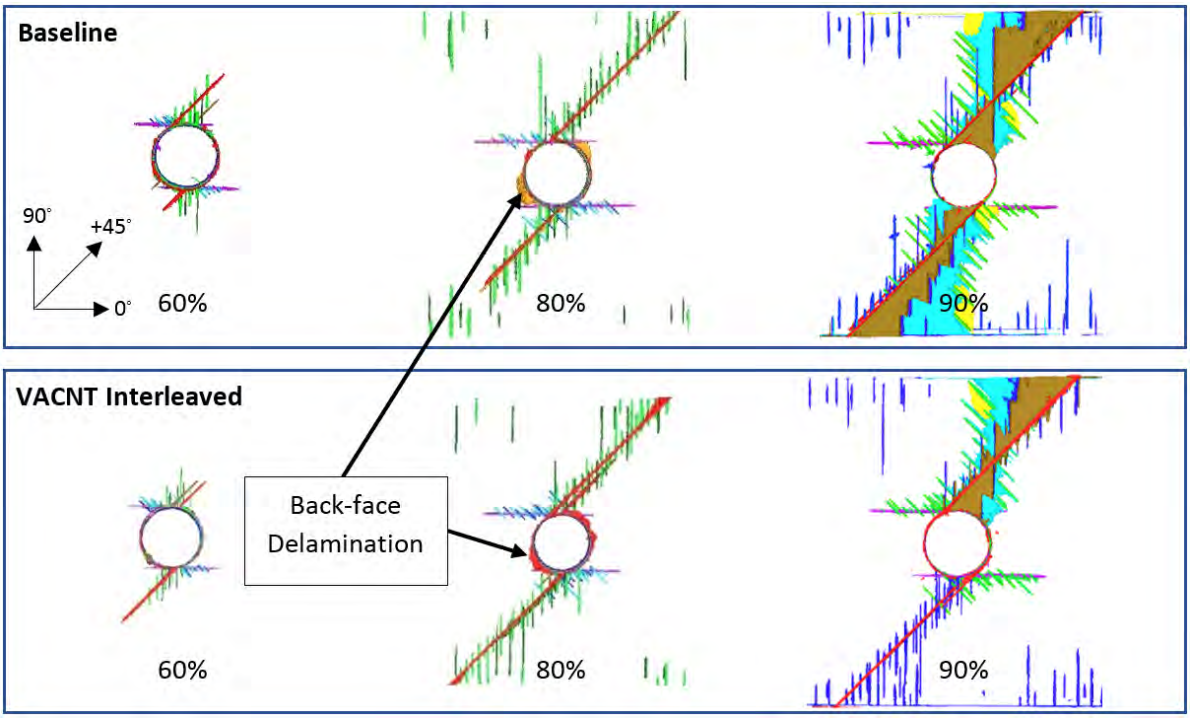

Figure 7.10: Global view from the X-ray CT scan of the interrupted tests at 60%, 80% and 90% of the nominal failure load for the baseline and VACNT interleaved OHT specimens with a block-ply layup.

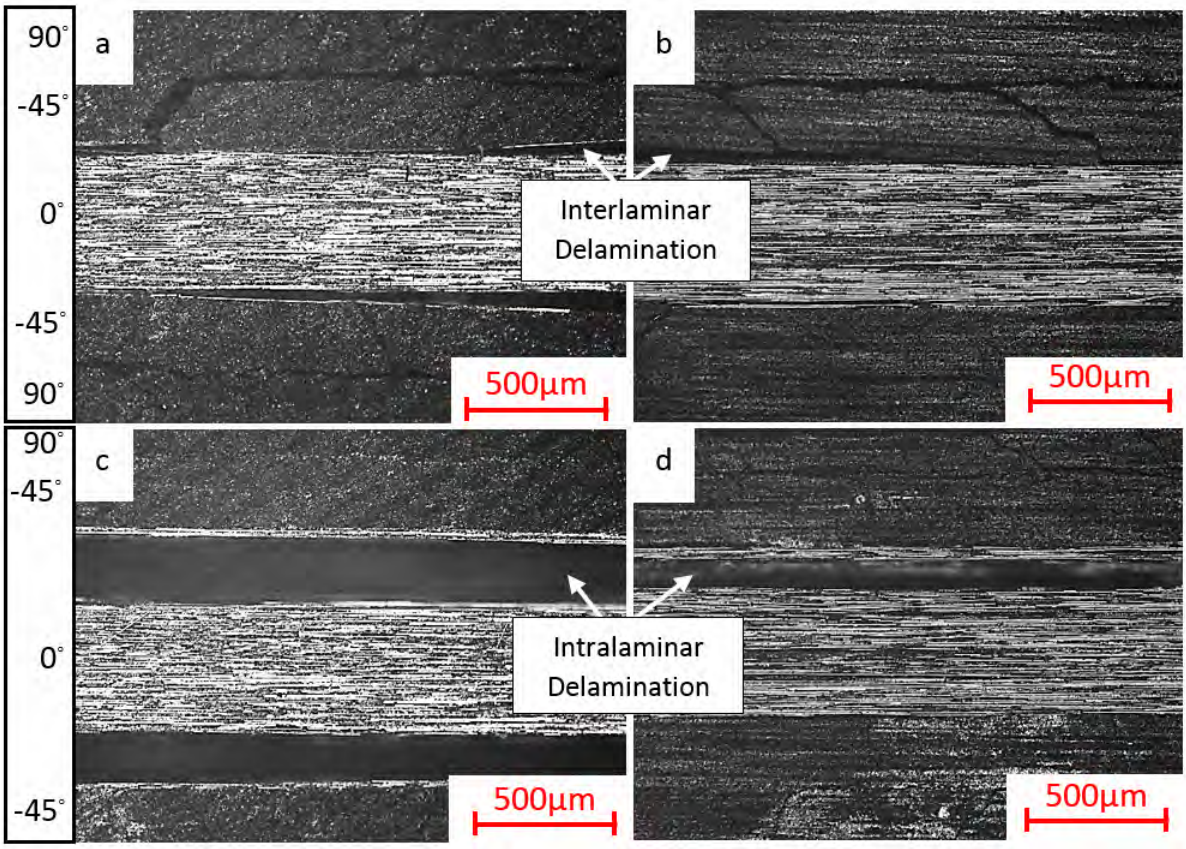

Figure 7.11: Optical microscope images of a baseline ply-level OHT specimen edge with (a) interlaminar delamination damage and (b) intralaminar delamination damage. Similar images for a VACNT interleaved ply-level OHT specimen edge with (c) interlaminar delamination damage and (d) intralaminar delamination damage.

7.3.3.2 Sub-laminate failure sequence

The damage sequence of the sub-laminate OHT specimen can be seen in Figure 7.12. Similar damage behaviours to those observed to the ply-level laminates, *i.e.* matrix splits initiating at the hole and propagating in the fibre direction, tangential to the hole for the +45° and 0° plies; isolated matrix cracks follow the matrix splits through translaminar cracking (Figure 7.2c), with their accumulation leading to highly localised delaminations. These damage mechanisms appeared in both the baseline and VACNT interleaved OHT specimens.

7.3.3.3 Matrix damage quantification

To quantify matrix damage, the raw X-ray CT scan data from each interrupted test were imported into a VG-studio max software and the damage voxels were summated. Regions of back-face delamination, caused by machining, were removed from the damage calculation.

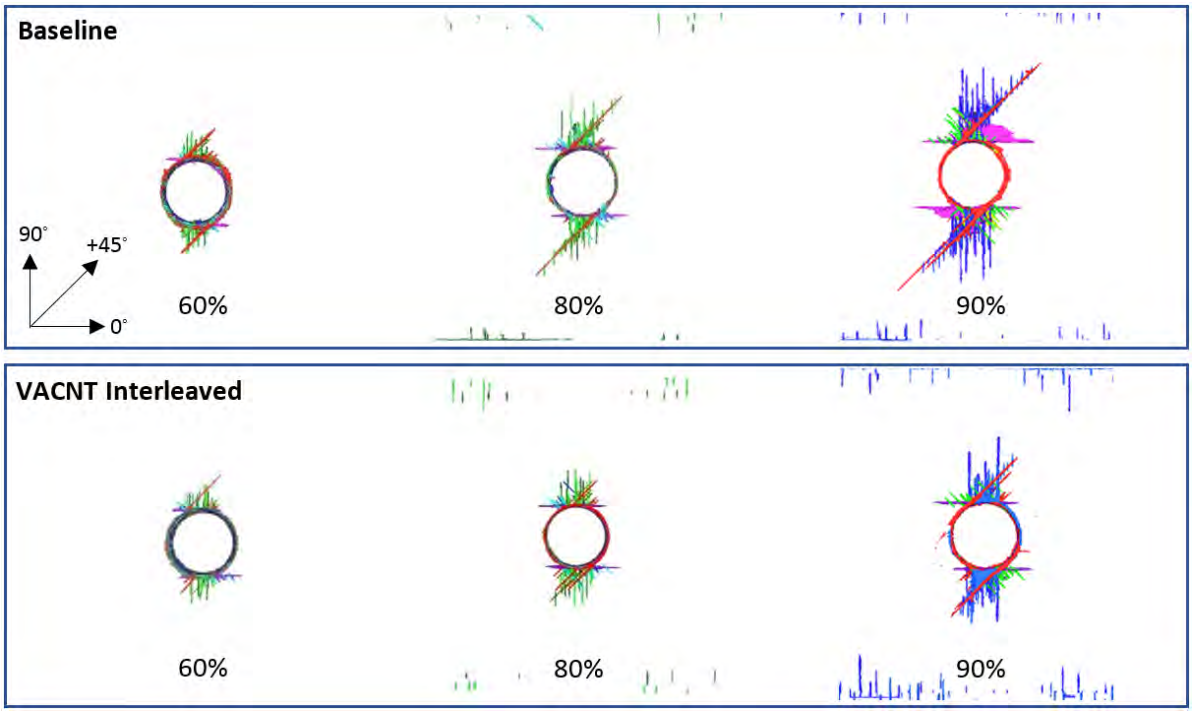

Figure 7.12: Global view from the X-ray CT scan of the interrupted tests at 60%, 80% and 90% of the nominal failure load for the baseline and VACNT interleaved OHT specimens with a sub-laminate layup.

Figure 7.13a and 7.13b shows the results for ply-level and sub-laminate OHT specimens respectively. Analysing these plots, a couple of repeatable trends appear. Firstly, for a given load severity, the sub-laminate specimens always have lesser damage than the ply-level specimens. Secondly, VACNT interleaved OHT specimens repeatably measure lesser matrix damage than their baseline equivalents. This suggests that while the strength of the laminate is not affected by VACNT interleaves, the overall matrix damage can be reduced. Therefore, VACNT interlaminar reinforcement may be more beneficial toward tensile fatigue performance.

It should be noted that while this analysis required some subjective decisions when selecting the region of interest, the calculation was evaluated multiple times, either omitting back-face delaminations or not, and consistently showed the same trends.

7.3.4 Numerical Model

Although the experimental study indicated that the VACNT interleaves provided no strength enhancement, numerical modelling is still valuable to investigate: *(i)* whether the OHT tensile strength and damage area can be captured and *(ii)* to validate whether intralaminar delamination is the predominant failure mechanism for both of these OHT configurations.

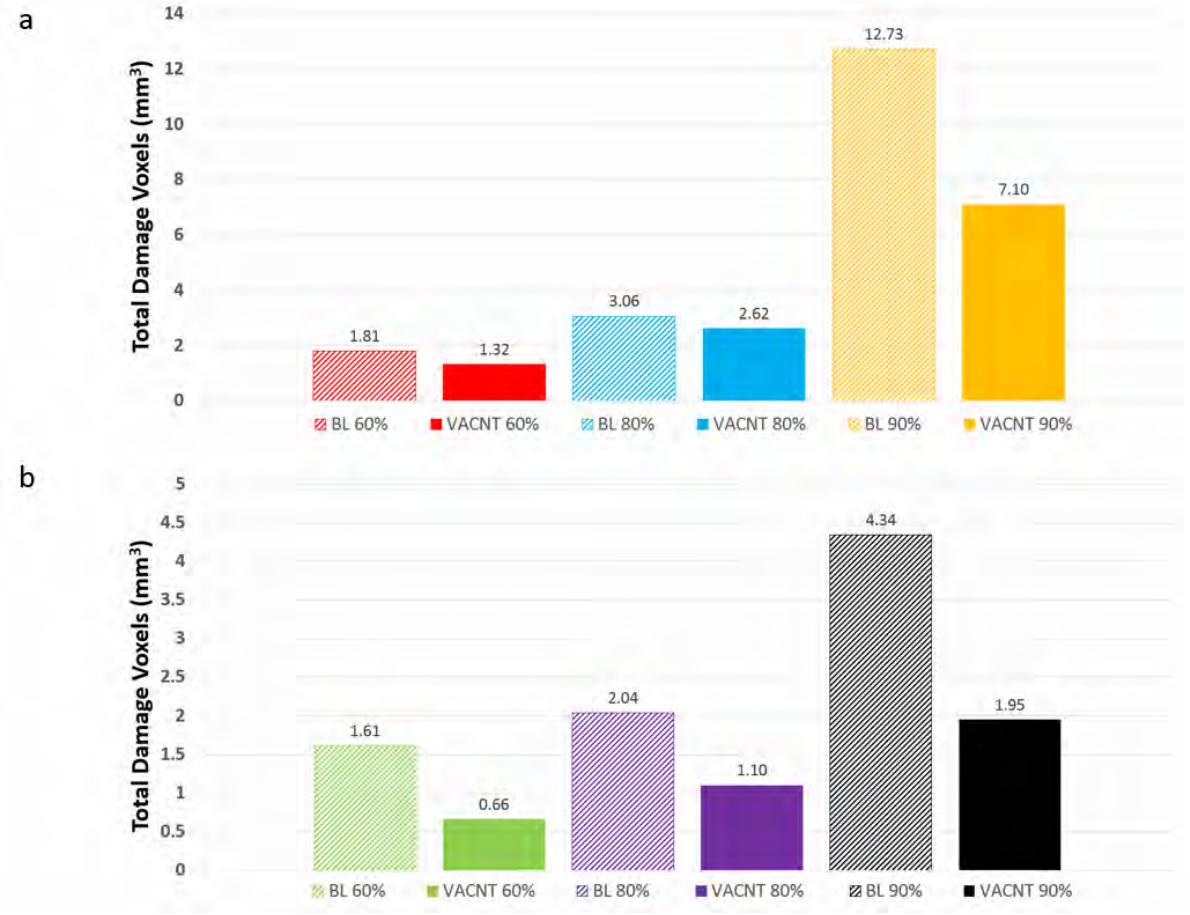

Figure 7.13: Total damage voxels summated for the interrupted baseline and VACNT interleaved specimens, at 60%, 80% and 90% of their respective nominal failure stress, for (a) the block-ply layup and (b) the sub-laminate layup.

7.3.4.1 Tensile strength comparison

The output stress *versus* extension plot for the baseline OHT model can be seen in Figure 7.14, with the corresponding strength values displayed in Table 7.7. It can be observed that when the cohesive element properties for both the interlaminar and ply-split interfaces are set to that defined in Table 7.3, the predicted failure stress is approximately 391 MPa. These contribute to a 14.1% underestimate, relative to the corresponding experimental average. On the other hand, when the interlaminar cohesive properties are defined to represent VACNT interleaves (Table 7.4), the predicted failure stress is 423 MPa, or a 7.1% underestimate relative to the experimental average. This indicates that if the baseline OHT specimens fail through interlaminar delamination, and, as concluded in chapter 5, the VACNTs induce intralaminar dominated failure, the tensile strength is expected to increase by approximately 7% from VACNT interleaving.

Table 7.7: Net failure stresses for the OHT specimen modelled with 4 different cohesive element property combinations for the interlaminar and ply-split cohesive elements.

Model	Interlaminar Properties	Ply-Split Properties	Failure Stress (MPa)	% Difference wrt. Experiments
Baseline	Table 7.3	Table 7.3	391	-14.1
BL Delam. / Intra Splits	Table 7.3	Table 7.4	402	-11.4
VACNT Interleaves	Table 7.4	Table 7.3	423	-7.1
Intra Delam. / Intra Splits	Table 7.4	Table 7.4	431	-5.3

Comparing both of these numerical strength estimations with the corresponding experimental averages, it can be seen that both underestimate the OHT specimen strength. One reason for this could be sourced from the cohesive element property definitions for the ply-splits. Currently, models assume interlaminar properties as measured for the baseline specimen in chapter 5. However, owing to the influence of the fibres within the matrix, it is believed by the author that the ply-split interfaces will require more energy to propagate a crack. In particular, it is assumed that the ply-split interface (Z axis in Figure 7.15) will require a similar energy density to an intralaminar delamination (Y axis in Figure 7.15) for a crack to initiate and propagate.

It was concluded in chapter 3 that VACNT interleaved CFRPs result in a crack being deflected into the intra-ply region, and hence the enhanced fracture toughness measured corresponded to the effective intralaminar properties of the host CFRP system. Therefore, as the CFRP system has not changed (IM7/8552), these effective intralaminar properties (displayed in Table 7.4) will also be used for the cohesive properties of the ply-split interfaces. The cohesive strength of these ply-split elements shall be assumed to be identical to that initially estimated for the tapered specimen numerical work, reported in chapter 6.

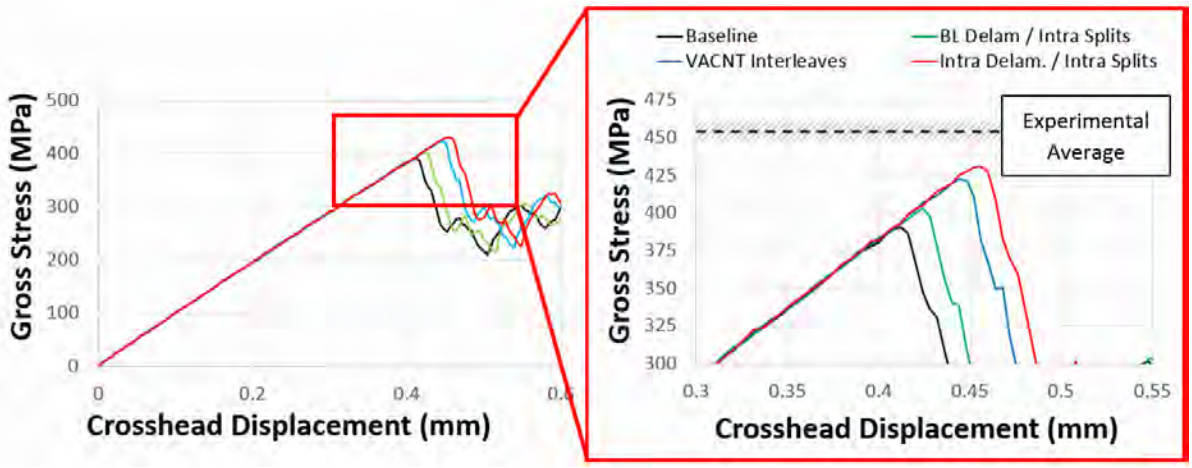

Figure 7.14: The gross stress-displacement output of the OHT cohesive element model for the interlaminar and ply-split cohesive element combinations defined in Table 7.7.

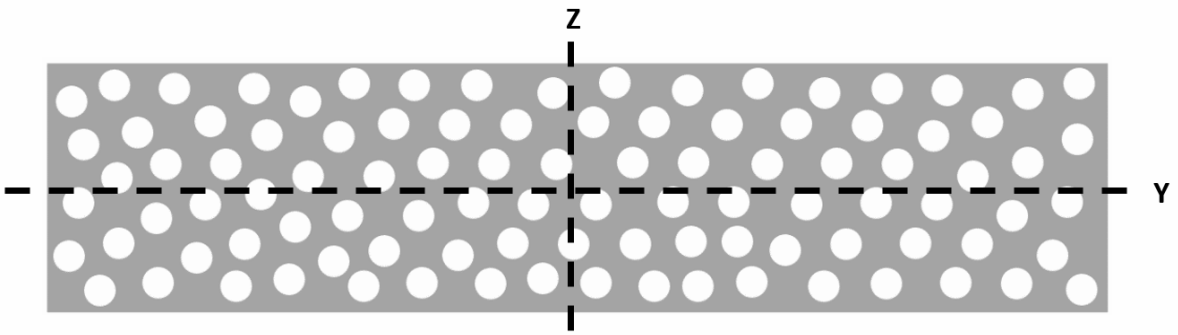

Figure 7.15: Schematic of the cross-section of a ply with two axes representing intralaminar delamination (Y) and translaminar fracture (Z).

Implementing these assumptions into the baseline and VACNT interleaved models resulted in additional enhancements to the tensile strength. As can be seen in Figure 7.14 and Table 7.7, the baseline strength rose to 402 MPa, while the VACNT interleaved strength increased to 431 MPa. This corresponded to a 11.4% and 5.3% underestimate compared to the experimental average respectively.

It is clear from the model that reinforcing the interlaminar regions should result in a tensile strength enhancement, however this was not observed in the experiments. The reasoning for the lack in strength sensitivity supports the conclusion discussed in Section 7.3.3.1, *i.e.* the baseline ply-level OHT specimen failure mode is intralaminar delamination dominated. Therefore, the most representative model for both the baseline and VACNT interleaved specimens is believed to be the VACNT model with intralaminar ply-split cohesive element property definitions. This model shall therefore be used for the damage comparisons made in the following section. The 5% strength underestimate associated with the model is believed to be a result of the non-circular hole required for effective meshing, which will lead to stress concentrations around the hole.

7.3.4.2 Matrix damage comparison

Figure 7.17 shows the interlaminar damage for ply interfaces with differing fibre orientations, when the OHT specimens are at 90% of their nominal failure load. Displayed, are the baseline and VACNT interleaved X-ray CT scans, as well as the cohesive damage output for the finite element model when both the interlaminar and ply-split cohesive properties are set to those defined in Table 7.4.

X-ray CT scans show that just prior to failure, the greatest delamination damage is at the $+45°/90°$ interface. This behaviour was also captured by the model with similar damage areas predicted. CT scans showed isolated ply-splits transferring stress through the thickness of the laminate, which lead to additional delamination events. This behaviour is most clear when observing the CT scans of the $90°/-45°$ interface, which shows damage transferred from the $+45°$ surface ply, a characteristic which was not captured by the model. These isolated

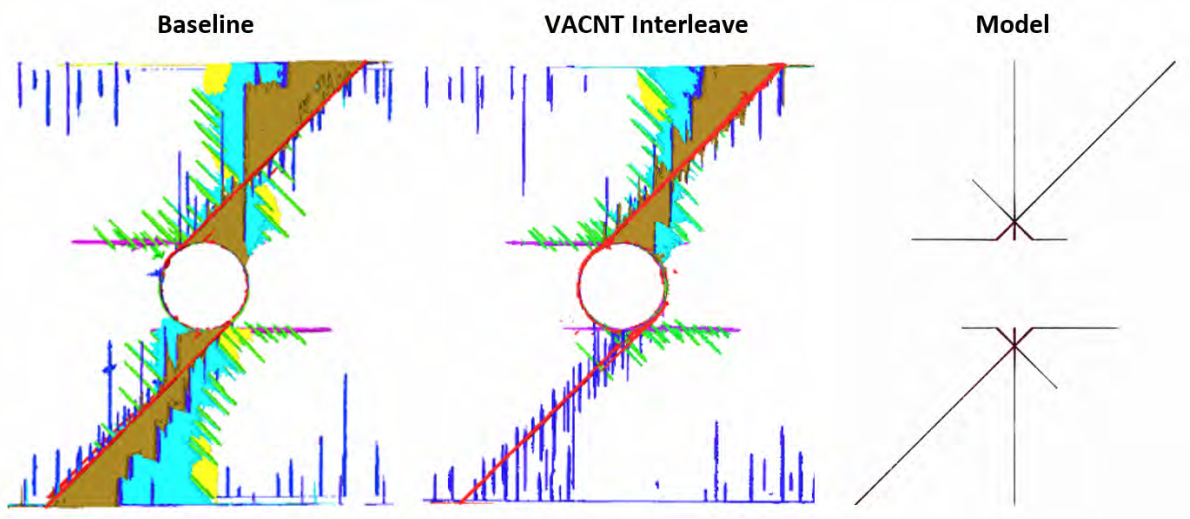

Figure 7.16: X-ray CT scans and corresponding cohesive element damage simulation of the damaged ply-splits when at 90% of the nominal failure stress.

cracks redistribute stress around the laminate, as well as dissipating energy through generating additional crack surfaces. This may therefore be another reason for the discrepancies between the numerical and experimental tensile strengths displayed in Table 7.7.

Damage at the $-45°/0°$ interface was found to be significantly greater in the model than that observed in the CT scans. This is believed to be sourced from stress concentrations developing around the corners of the non-circular hole, which lead to premature delamination predictions.

Comparing the ply-splits lengths from CT scans and the model (Figure 7.16), it can be seen that splits in the $+45°$ and $0°$ are captured well by the model, however with only two cohesive interfaces in each of the $-45°$ and $90°$ plies, the ply-splits in these directions are not representative. What is clear is that if damage is to be fully captured accurately by this model, a different meshing strategy must be adopted to allow for a circular hole and isolated ply-splits to be represented.

7.4 Conclusion

In conclusion, this chapter investigated the influence from interleaving OHT specimens with VACNTs. Two OHT layup configurations that are known to fail predominantly through either delamination (ply-level) or pull-out (sub-laminate) were interleaved with 20 μm VACNTS at every interface. Comparisons between baseline and interleaved specimens were made with respect to tensile strength and damage mechanisms. Damage was captured through video gauge footage taken during the test and X-ray CT scans on interrupted tests at load severities of 60%, 80% and 90% of the nominal tensile strengths. A cohesive element finite element model was constructed to investigate whether the effect from VACNTs can be captured numerically.

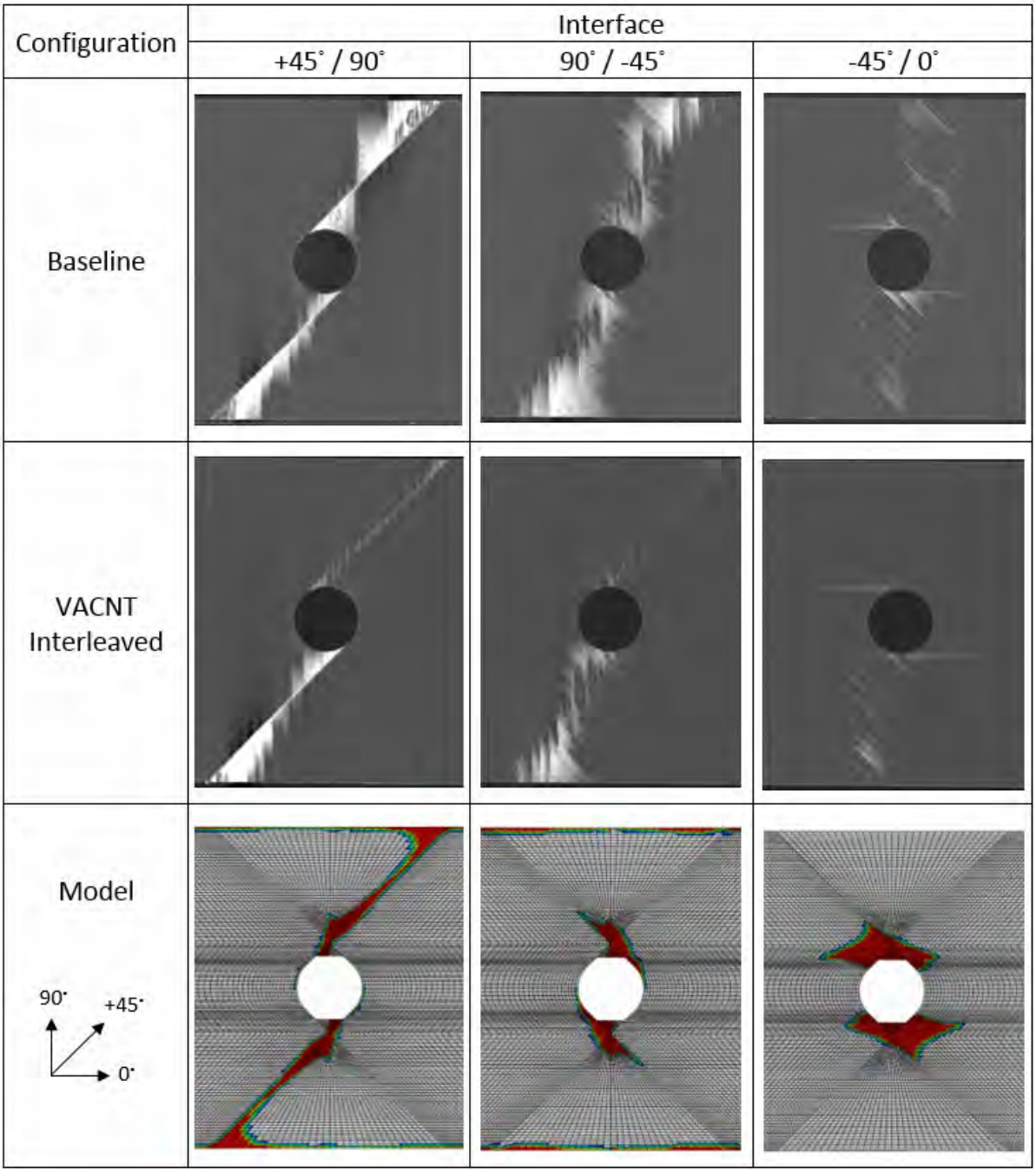

Figure 7.17: X-ray CT scans and corresponding cohesive element damage simulation at (a) +45°/90°, (b) 90°/−45° and (c) −45°/0° ply interfaces when at 90% of the nominal failure load for a baseline specimen. (Red indicates element failure).

Overall, it was found that VACNTs had an insignificant difference to both the stiffness and strength of the OHT laminate for either layup configuration. Microscopy of the post-delaminated ply-level specimen edge indicated that the ply-level layup configuration failed predominantly through intralaminar delamination and therefore the interlaminar reinforcement offered by the VACNT interleaves does not benefit the OHT application.

CT scans showed similar failure mechanisms for both the baseline and VACNT interleaved specimens; initial damage for both ply-level and sub-laminate specimens came in the form of matrix splitting in the $+45^\circ$ surface plies and 0° central plies, with splits initiating at the hole edge and propagating tangentially along the fibre direction towards the specimen edge. Isolated ply-splits formed in the 90° and -45° plies, which followed the $+45^\circ$ and 0° propagated matrix splits respectively, through translaminar cracking. Ply-level OHT configurations showed greater ply-splitting damage, with the accumulation of the isolated cracks leading to small local delaminations around the hole and specimen edge. These delaminations subsequently grew until reaching the specimen edge.

Quantification of the matrix damage for each interrupted test suggested that the overall damage area prior to failure reduced when specimens were interleaved with VACNTs. This indicates that interleaving may be more appropriate for OHT specimens subjected to fatigue conditions rather than quasi-static conditions.

Strength predictions from a cohesive finite element model supported the hypothesis that ply-level OHT specimens predominantly fail through intralaminar delamination, with the most representative model ($\approx 5\%$ difference in tensile strength) being when cohesive elements are defined with intralaminar properties. The model did not capture the influence of isolated ply-splits within the laminate, which transfer damage and redistribute stress through the laminate thickness. Furthermore, to allow for effective meshing, a non-circular hole was adopted. This led to increased stress concentrations around the hole, which is believed to be the main source of the strength underestimations made by the model.

On the whole, the author does not recommend interleaving a quasi-statically loaded OHT specimen for strength enhancement. Instead, it appears that intralaminar reinforcement techniques, such as homogeneous dispersion of nano-filler, multi-scale fibres, *etc.*, may be a more appropriate means of suppressing delamination.

CHAPTER 8

CONCLUSIONS

8.1 Thesis summary and comparison with literature

This research investigated using vertically aligned carbon nanotube (VACNT) interleaves as a technique for suppressing delamination in fibre reinforced polymer (FRP) composites. Chapter 1 discussed how the layered architecture and lack of reinforcement in the through-thickness direction, leads to delamination being the dominant failure mode in unmodified FRP composites. Chapter 2 summarised a variety of approaches to suppress delamination, including z-binder, fibre modifier, and matrix modifier techniques. Overall, a recurring relationship between interlaminar fracture toughness enhancement and subsequent degradations to in-plane mechanical properties, was established. One exception to this relation occurred for matrix modifiers with carbon-based fillers. To optimise delamination suppression performance, it was determined that such fillers should: *(i)* have a high aspect ratio and surface area; *(ii)* be highly concentrated in areas susceptible to damage; *(iii)* have good interfacial properties with the matrix; and *(iv)* be aligned with the intention to bridge the expected fracture plane. These filler characteristics led the author to an emerging interleaving technology of VACNTs.

Although VACNTs have already been investigated with respect to interlaminar fracture toughness (ILFT) enhancement, to date no work has investigated the dependence of ILFT enhancement on VACNT characteristics, such as CNT length or density. Furthermore, studies investigating VACNT interleaves have been predominantly limited to pure mode tests, for example, DCB, ENF, *etc.* As a result, the aim of this research was to evaluate how CNT characteristics influence the ability to suppress delamination in VACNT interleaved FRP composites, and to assess the effects of interleaving delamination-prone composite structures with VACNTs.

Chapter 3 began the research by studying the effect of VACNT length on the Mode I and

Mode II interlaminar fracture toughness of HexTow® IM7/HexPly® 8552 prepreg. Overall, a 17 – 20% improvement in the Mode I, and an 8 – 10% improvement in the Mode II propagation fracture toughness was measured. In comparison to the measured enhancements reported in the relevant literature (see Table 2.3), it can be seen that the values support the findings of Ni *et al.* [159], but are substantially lower that those reported in other earlier investigations [38, 39, 96]. In chapter 3, it was concluded that the measured fracture toughness improvements in Mode I and Mode II are insensitive to VACNT length, with all interleaved specimens exhibiting similar enhancement values. It is believed by the author that this is a novel finding and it indicates that VACNT interleaf characteristics are not the dominating factor influencing the maximum enhancement in fracture toughness.

Fractographic analysis of VACNT interleaved specimens showed that the VACNTs initiate a transition in the fracture mode from interlaminar delamination to intralaminar delamination. This was found to happen in both Mode I and Mode II loading conditions. A similar behaviour was also detected by Ni *et al.* [159], however, they reported that this resulted in a drop in the Mode I fracture toughness and no change in the Mode II fracture toughness. In chapter 3, it was proposed that the enhanced fracture toughness is the intralaminar fracture toughness of the host system (HexTow® IM7/HexPly® 8552). This hypothesis is supported by Czabaj and Ratcliffe [221] and Gutkin [255], who have reported a 10-25% increase between the Mode I intralaminar fracture toughness and Mode I interlaminar fracture toughness for this CRFP system. It is believed by the author that, as of yet, the Mode II intralaminar fracture toughness of the IM7/8552 CFRP system has not been measured, and therefore our 8-10% enhancement is the first reported prediction.

While other literature has reported cracks migrating into the intralaminar region when interleaves are introduced [36, 159, 176, 211], they only describe the crack running parallel with the interleaf. On the other hand, the SEM images disclosed in Chapter 3 indicate that intralaminar cracks significantly follows the topology of the VACNT film, particular under Mode II conditions. Such a behaviour suggests that the VACNTs exhibit a localised stiffening and strengthening behaviour at the interlaminar region. The SEM images further show that cracks propagate along the fibre-matrix interface, which suggests that the bonding strength between the IM7 fibres and 8552 matrix is the limiting factor that influences the maximum improvement in fracture toughness. This characteristic has not been commented on before and is a key factor when deciding whether interleaves are an appropriate through thickness reinforcement technique.

In an attempt to prevent cracks migrating into the intralaminar region, and achieve greater enhancements in fracture toughness from interleaving with VACNTs, chapter 4 investigated whether the fibre orientation of the plies adjacent to the delaminating interface influences the growth direction and hence the enhanced fracture toughness. While lots of research has been focussed on the fracture toughness and fracture mechanisms of laminates with plies oriented in multiple directions (see section 2.2.2.3), it is believed by the author that no work has been conducted on fibre orientation for VACNT interleaved specimens.

In chapter 4, it was concluded that the Mode I interlaminar fracture toughness is insensitive to the interface layup (at least up to a layup of ±15°). On the other hand, the Mode II interlaminar fracture toughness was found to increase with interface layup angle. This finding is similar to that reported in a review by Anderson and König about the dependence of fracture toughness on interface ply orientation [256]. For all interface layups tested in the chapter (±5° , ±10° and ±15°), the delaminating crack was found to migrate from the ply interface into the intra-ply region when the VACNTs were introduced. In common with chapter 3, these intralaminar cracks were found to follow the topology of the VACNT film. In order to prevent the intralaminar cracks migrating into the adjacent ply interfaces (as observed by [20, 82, 83]), three interfaces were interleaved with VACNTs (the delaminating interface and the two adjacent interfaces) rather than just one. No cracks were observed to migrate into the adjacent interfaces and predominantly followed the topology of the VACNTs at the central delaminating interface. Unlike the conclusions made by Narducci *et al.* [172], interleaving laminates along three interfaces, rather than one, made no difference to the enhanced fracture toughness in either Mode I or Mode II conditions. This is not too surprising because the crack remained within the interlaminar region.

The second part of chapter 4 investigated whether the engagement between the VACNTs and the ply fibres could be improved. Up to this point large resin pocket formations and resin rich regions between the VACNTs and fibres were regularly observed, which would result in opportunities for crack formations and growth. After discovering a paper by Hubert *et al.* [41], which investigated the cure kinetics of 8552 resin, a strategy was developed wherein the viscosity of the resin was reduced through modifying the cure cycle of the system. In particular, it was noted that removing the initial dwell period would allow the minimum viscosity of the resin to be dramatically reduced during cure. This dwell is present for reducing the likelihood of large exothermic reactions and would therefore only be problematic for thick laminates. The modified cure cycle was found to significantly improve the engagement between the VACNTs and the fibres because the resin was able to sufficiently bleed from the interleaf interface. Furthermore, thermogravimetric analysis showed that removing the initial dwell from the cycle made only a minor difference to the laminate's overall fibre volume fraction (< 1%). Along with the SEM images, this suggests that the resin rich regions at the ply interface have evenly diffused rather than exited the laminate completely. It was therefore concluded that removing the initial dwell from the cure cycle can be used as a technique for improving engagement between an interleaf and the adjacent fibres.

Chapter 5 focused on investigating the influence of interleaved VACNT distribution on the fracture toughness and fracture mechanisms. These VACNT interleaves were either homogeneously distributed or discretely distributed, i.e. patterned interleaves, and were tested under Mode I and Mode II conditions. For the homogeneously distributed interleaves, three different VACNT forest densities were tested, while the discretely distributed specimens included four patterns with either periodic or non-period pattern arrangements.

In common with chapter 3, the fracture toughness enhancement was found to be insensitive to the density of the VACNT forest. This was not surprising considering the conclusions from chapter 3, i.e. the enhancement in fracture toughness is limited by the interfacial properties between the fibres and the matrix. All homogeneously interleaved specimens were found to exhibit intralaminar delamination, however interestingly, the cracks were now found to grow in an unstable manner for the Mode II tests. It was unclear whether this behaviour was induced by the change in cure cycle, or the fewer resin rich regions at the delaminating interface.

Table 2.3 references four studies that investigated patterned interleaves. The only investigations which have focused on the Mode I and Mode II fracture toughness of patterned interleaves have predominantly involved thermoplastic interleaves [171, 172, 175], with no fracture toughness work being conducted on VACNTs. Recently, a conference paper has been published by Ni *et al.* [176], which investigated the enhancements in short beam shear (SBS) strength and double edge-notched tension (DENT) strength, when the respective specimens are interleaved with densified VACNTs. In order to densify the interleaves, *Ni et al.* compressed VACNT columns until they buckled. These buckled columns were distributed in a grid pattern and resulted in respectable strength increases, which exceeded the equivalent unbuckled homogeneous VACNT interleaved specimens. Unfortunately, the conference paper did not discuss the reasoning for this finding. It is the author's belief that no one has yet investigated the influence of either the VACNT forest density, or patterned VACNT interleaves, on Mode I and Mode II fracture toughness properties.

Chapter 5 began with a detailed description of the novel fabrication method used to produce patterned VACNT interleaves. The method involved a mask that partially inhibited contact between the VACNTs and the prepreg during the transferring stage. This method enabled the user to distribute the VACNTs strategically on to a surface of the prepreg, without causing damage to the interleaves. Experimental testing on the patterned interleaved specimens showed an undulating R-curve, which fluctuated between the interlaminar and intralaminar properties of the IM7/8552 CFRP host system. This result indicates that localised ILFT enhancement occurs in areas populated in VACNTs, while other areas exhibit baseline properties. Interestingly however, is that some patterns were found to enhance the Mode I ILFT more than the homogeneously distributed interleaves with the same VACNT forest density. Fractographic analysis showed that the reasoning for this behaviour is the presence of additional fracture mechanisms compared to similar homogeneous VACNTs interleaves. For example, in Mode I a crack branching behaviour was observed, whereby secondary cracks branched from the main fracture plane. These branching cracks were found to initiate in regions where the VACNTs were introduced, e.g. the pattern edges. The creation of extra fracture surfaces will dissipate more energy and thus lead to an enhanced ILFT fracture toughness measurement.

During the experimental testing programme of chapter 5, the crack was observed from both sides of a DCB specimen while the specimen was being opened up. The test showed that the crack

growth rate differed on each side of the specimen due to the presence of the patterned VACNT interleaves. In particular it was found that the VACNTs slowed the growth rate. The reasoning for this is because of the extra work required for a crack to propagate through the intralaminar region relative to the interlaminar region. Such a finding indicates that with strategic distribution of VACNT interleaves, cracks can be steered away from sensitive areas such as edges, joints and notches.

Finally, patterned VACNT interleaves were found to stabilise crack growth in Mode II conditions. For example, as previously mentioned, when testing homogeneous VACNT interleaves, cracks were found to propagate in an unstable manner once they entered the interleaved region. However, for the patterned VACNT interleaves, particularly those with smaller feature sizes, cracks propagated stably as they entered the interleaved region.

Part two of the research focused on the application of VACNT interleaves in delamination prone structures. Chapter 6 focused on tapered specimens under tensile loading, while chapter 7 focused on notched specimens under tensile loading.

In chapter 6, mechanical tests were conducted on tapered specimens that were shown in literature to delaminate repeatably at a specific ply termination. Overall, by interleaving the delamination susceptible ply termination with VACNTs with a length of 40 μm, an increase in tensile strength ($\approx$ 7%) was measured. This is a similar improvement to that reported by Gouldstone *et al.* [192], who tested VACNT interleaved tapered specimens loaded in a 3-point bend configuration. The tensile stiffness of the tapered specimens tested in this study were found to be unaffected by the VACNTs.

While testing the tapered specimens, optical and infrarad high-speed cameras captured the delamination event. The camera observed additional damage features for the specimens interleaves with 40 μm VACNTs. These features included multiple 'stitched plies' slippage and intralaminar crack formations. While intralaminar crack formations were also observed by Gouldstone *et al.* [192], no literature has reported interleaved plies delaminating as a sub-laminate. It is these features that are believed to increase energy dissipation and hence contribute to the increased tensile strength.

The high-speed camera footage also showed multiple tapered specimens interleaved with VACNTs with a nominal length of 40 μm maintaining structural integrity post-delamination; enduring a further 0.5 seconds after initial delamination growth. This is promising considering the fact that the VACNTs were only introduced at the interface of the critical ply termination.

As well as VACNTs with a length of 40 μm, mechanical tests were also conducted on tapered specimens interleaved with VACNTs with a length of 11 μm. The reasoning for this test was to investigate the influence of the nanotube bridging within the resin pocket ahead of the terminating ply. Overall, the tensile strength was found to be unaffected by the VACNT interleaves with a length of 11 μm. This indicates that VACNT bridging is a significant factor for suppressing delamination in tapered specimens. High-speed camera footage supported this hypothesis by

capturing the opening of the resin pocket tip ahead of the critical terminating ply. Therefore, the tensile strength enhancement measured exclusively for VACNT interleaves with a CNT length of 40 μm was attributed to the increased VACNT bridging at the resin pocket tip, which increased its resistance to through-thickness tension stresses and hence opening (Mode I) delaminations.

As outlined at the end of chapter 2, objective 4 of this research was to develop simple finite element (FE) tools to validate the experimental findings and indicate whether VACNTs can be captured through homogeneous cohesive elements. Other literature looking at modelling VACNT interleaves, e.g. Blanco *et al.* [96] and Tong *et al.* [170], have taken a mechanistic approach rather than homogenising the VACNTs within more complex structures.

The 3D slice finite element model disclosed in chapter 6 was developed to represent the unmodified and VACNT interleaved tapered specimens. The model consisted of cohesive elements to simulate the interlaminar regions, with VACNT interleaves being simulated as cohesive elements with enhanced material properties. The element properties of the baseline and VACNT interfaces were sourced from literature and the primary material characterisation data reported in chapter 5.

In general, the baseline tapered model accurately predicted the failure load and failure location. The difference between the numerical and experimental averages was approximately 2% and the location of delamination initiation matched well. Furthermore, the failure sequence in the model was similar to that capture by the high-speed cameras.

While the enhanced strain energy release rate caused by interleaving with VACNT was known from the characterisation work of chapter 3 and 5, the cohesive element strength enhancement was not known. A good initial estimation that was outlined in chapter 6 is to assume that the cohesive strength enhancement is identical to the cohesive strain energy release rate enhancement. This combination resulted in only a 0.5% difference in failure load between the experimental average and VACNT interleaved tapered model. The model also exhibited the same delamination location and failure sequence as the experiments.

Finally, in an attempt to further understand the dependency of VACNT length on the strength of tapered specimens, the interleaved model was adapted to represent VACNTs that do not bridge the resin pocket of the critical ply drop. The model suggested that VACNT bridging of the resin pocket tip ahead of the critical terminated ply increases the tensile strength of the tapered specimen. However, the lack of any significant improvement from VACNT interleaves with a nominal CNT length of 11 μm was unable to be captured by the model. This is therefore an area for future research and will be further discussed in the next and final chapter.

Chapter 7 concluded the research by investigating VACNT interleaves being applied to notched specimens under tensile loading. Following a study by Green *et al.* [194], who showed that the failure mode of an open hole tension (OHT) specimen is dependent on the hole size, specimen thickness and specimen width, two OHT configurations that exhibited delamination dominated behaviour were interleaved with VACNTs of length 20 μm. It is the author's understanding that

interleaving notched specimens with VACNTs has not be investigated before.

For both OHT configurations, the VACNT interleaves resulted in an insignificant difference in either tensile stiffness or tensile strength, when compared to an unmodified specimen. Fractographic analysis performed on the post-delaminated baseline OHT specimen edge suggested that the specimen predominantly failed through intralaminar delamination rather than interlaminar delamination. Similar behaviours were also observed for the VACNT interleaved OHT specimens. This suggests that interlaminar reinforcement is not appropriate for suppressing delamination in this application, because the cracks are not inhibited from their natural growth path.

X-ray CT scans of damaged OHT specimens, with various damage severities, showed similar failure mechanisms for both the baseline and VACNT interleaved specimens. Analysis of the CT scan data indicated that the total damage area (prior to failure) reduces when VACNT interleaves were present. This suggests that VACNT interleaves may be more appropriate for OHT specimens under fatigue conditions. Please note, initial preliminary studies investigating this hypothesis have been conducted and reported in the next chapter, along with some overarching discussion points made apparent from the results of this research.

In common with the numerical work in chapter 6, finite element models representing the baseline and VACNT interleaved OHT specimens were also developed in chapter 7. These models included cohesive elements to simulate the interlaminar and ply-split regions.

Overall, the models supported the fractographic analysis, i.e. even the baseline OHT specimens fail predominantly through intralaminar delamination rather than interlaminar delamination; The model that captured the failure load and damage area most accurately was defined with intralaminar properties throughout. It was apparent that the models did not capture isolated ply-splits or a circular hole geometry. For example, the CT scans of damaged OHT specimens showed that isolated ply-splits redistribute stress and transfer damage through-thickness, which was not observed in the numerical representation. Furthermore, the mesh required a non-circular hole to avoid degenerated elements, which led to stress concentrations forming around the hole. Both of these limitations resulted in a continual underestimation in failure load relative to the experimental averages.

CHAPTER 9

DISCUSSION AND FUTURE WORK

This final chapter discusses the overarching discoveries outlined in chapter 8, as well as highlighting the unresolved questions from the research. The chapter concludes with a selection of research opportunities, which the author recommends initially concentrating on, should future work on this topic continue.

9.1 Discussion

9.1.1 Interlaminar *versus* intralaminar properties

Throughout this research, the relationship between the interlaminar and intralaminar properties of a composite material has been discussed. A recurring conclusion from the first half of this thesis was that VACNT interleaves are limited in their toughening capabilities by the intralaminar fracture toughness of the host laminate, which in this case was HexTow® IM7/HexPly® 8552 prepreg [3].

The secondary failure mode associated with HexTow® IM7/HexPly® 8552 is intralaminar delamination for both Mode I and Mode II ILFT tests. Therefore, if the toughening enhancement from the VACNT interleaves is greater than the intralaminar fracture toughness of the host laminate, the VACNT interleaved composite will fail through intralaminar delamination rather than at the interleaf.

The intralaminar fracture toughness is dictated by the interfacial properties between the primary fibres and the matrix. Consequently, composite systems that shall gain the greatest toughening enhancements from VACNT interleaves are those with the largest difference between their interlaminar and intralaminar properties. The selection of these composites can be achieved through either a round-robin experimental programme, or if the host composite system is fixed,

the use of fibre-modifying techniques similar to those described in Section 2.2.2, to improve the fibre-matrix interfacial properties.

9.1.2 Delamination definition

Delamination is a term frequently written in literature when investigating composite failure. For the majority of cases, it refers to interlaminar delamination, whereby cracks propagate through the resin rich region between the plies. However, delamination can also imply an intralaminar fracture mode, as seen in Figure 1.2 [6], where cracks propagate through the intra-ply region and debond primary fibres away from the matrix.

Distinguishing between both delamination fracture modes is extremely important when considering interlaminar reinforcement methods, such as VACNT interleaves, to aid with suppressing delamination. VACNT interleaves will only provide fracture toughness enhancements for systems that fail at the interlaminar region. This behaviour was evident in chapter 7, where attempts were made to suppress delamination, and hence increase the tensile strength, of OHT specimens. While literature correctly reported that unmodified OHT specimens fail through ‘delamination‘, primary sourced experimental and numerical data suggested that ‘delamination‘ initiates at the intralaminar region, rather than the interlaminar region. Ultimately, this resulted in the VACNT interlaminar reinforcement having an insignificant effect on the strength of the specimen. Therefore, before any interlaminar reinforcement is selected for the purpose of suppressing delamination, confirmation must be made on whether the failure of the unmodified composite system occurs in an inter-ply fashion rather than intra-ply. Otherwise, VACNT interleaves, or any other interleaves for that matter, are not an appropriate delamination suppression technique.

9.1.3 Damage manipulation through distribution or location of VACNT interleaves

The concept of distributing VACNTs in a patterned formation has been experimentally shown to provide design flexibility for fracture manipulation. VACNT interleaves were discovered to reduce the rate of crack growth, providing opportunities for controlling crack propagation direction and guiding damage away from sensitive areas, such as notches, corners, edges, or joints. A patterned formation also produces localised unreinforced regions within the interleaved area, which increase crack path complexity and discourage intralaminar delamination.

Selective positioning of VACNT interleaves in tapered specimens has been shown to offer significant mechanical property enhancements when located at delamination-prone interfaces. It is believed that for other composites systems, which are not limited by intralaminar properties, strategic VACNT interleaf positioning will provide additional design opportunities for controlling the location of delamination initiation. For example, to aid with visual inspection and repair procedures, it is desirable for damage to first initiate towards the laminate surface, and within a

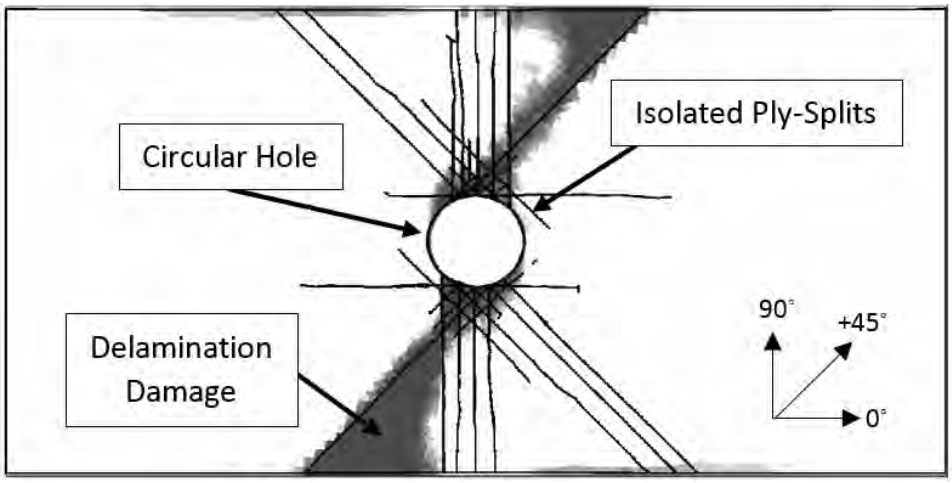

Figure 9.1: Delamination and ply-split damage at a +45°/90° interface for a ply-level OHT specimen at 85% of the numerical failure load using a simplified segment method [46].

more robust section of the structure, to prohibit catastrophic failure. VACNT interleaves could enable these requirements to be designed directly into existing composite structures through the use of finite element (FE) modelling (see Section 9.1.4), in order to increase a component's life and avoid labourious and expensive inspection programmes.

9.1.4 Capturing interlaminar reinforcement through cohesive elements

The finite element (FE) models outlined in this research suggest that enhancing the properties of cohesive elements can capture the effects of VACNT interleaves to a reasonable accuracy. Although these enhanced properties were effectively the intralaminar properties of the host composite system, estimations of the failure strength, failure location, and failure mode were captured. Therefore, this simple modelling technique enables design engineers to initially evaluate the effect that interleaves have on complex composite geometries, enabling strength optimisation and the manipulation of the location of delamination initiation.

The main limitations associated with these models arose primarily from the meshing technique adopted. For example, the mesh representing OHT specimens was unable to capture a circular hole or isolated ply-splits, which ultimately led to discrepancies when compared to the experimental data. Therefore, to progress these models further, a different meshing strategy must be adopted. One example of such a meshing strategy is the use of a simplified segment method [46], which uses multiple algorithms to sub-divide damaged elements, re-evaluate loads and stresses, and update cohesive element locations to determine crack initiation and propagation paths. This technique, as can be seen in Figure 9.1, results in multiple isolated ply-splits being captured, particularly in the 90° and −45° directions, which are more representative to the X-ray CT scan images shown in chapter 7.

9.2 Unresolved Findings and Future Work

There are multiple directions that can be taken for progressing research on VACNT interleaves as a delamination suppression technique. Examples include how ILFT enhancements from VACNT interleaves are influenced by the loading conditions (*e.g.* the load rate or cyclic loading), elevated environmental temperatures, or the host composite system. For the latter, either a new matrix and fibre combination could be investigated, or VACNT interleaves could be incorporated in unison with other intra-ply toughening techniques, such as multi-scale fibres or homogeneously dispersed matrix modifiers, to provide a synergistic enhancement to the fracture toughness. Exploration into the multi-functional capabilities of VACNT interleaves could also be investigated. For instance, VACNTs can be interleaved at every ply interface to create a conductive network through-thickness, to simultaneously provide structural, thermal, and electrical enhancements. Such systems could then be applied in other delamination-prone structures, such as pressure vessels, cornered structures, joints, and impacted cases, to quantify their benefits in suppressing delamination.

However, before further and broader studies are established, there are a number of unresolved findings within *this* research that still require further work. The first finding relates to the initial aim of this research, *i.e.* how does the CNT characteristics influence the ILFT enhancement. Owing to the unexpected crack deflection behaviour observed in chapters 3 - 5, whereby cracks migrated away from the interleaf into the intralaminar region, no dependency could be established. This study was limited to exclusively using HexTow® IM7/HexPly® 8552 prepreg as the host composite. In a supplementary study to this work, it is recommended to interleave another FRP system, one for which substantial ILFT enhancements have already been determined from other interleaf types. This will establish the full capabilities that VACNT interleaves offer for suppressing delamination, as well as whether dependencies between VACNT characteristics and ILFT enhancements exist.

The second unresolved finding corresponds to the tapered specimen study detailed in chapter 6. In this work, no tensile strength enhancement was measured for tapered specimens interleaved with VACNTs of a nominal length of 11 μm. It was hypothesised that the lack of strength increase was attributed to a lesser VACNT bridging behaviour at the resin pocket tip, directly ahead of the critical ply-drop. However, preliminary cohesive element models, which simulated no VACNT bridging at the resin pocket tip, still predicted tensile strength increases (albeit to a lesser degree when bridging was present).

To determine whether the initial hypothesis is correct, it is recommended to subject all tapered specimens to a moderate cyclic loading condition and interrupt the tests when the specimens are partially damaged. The challenge with tensile quasi-static testing, described in chapter 6, was that damage initiation and final catastrophic failure occurred in quick succession. Therefore, post-delaminated specimen fractography analysis did not reveal initial damage formations, making the detection of the fracture mechanisms difficult. On the other hand, subjecting the

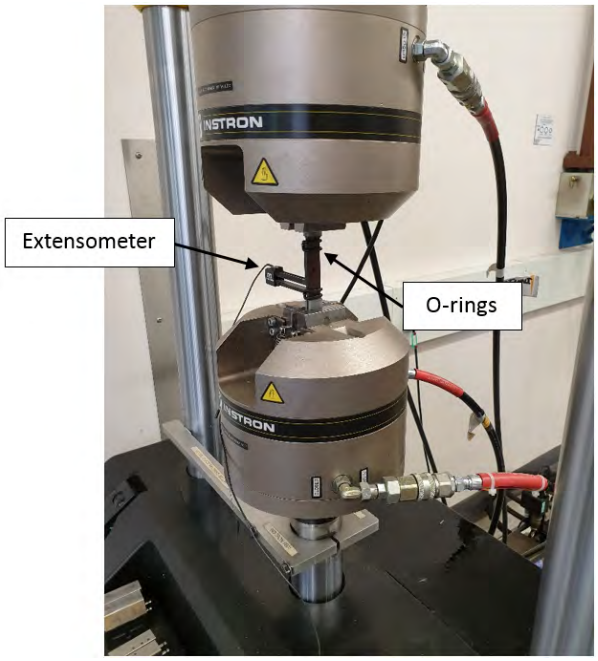

Figure 9.2: Photograph of the OHT tension-tension fatigue test set-up.

tapered specimens to a moderate cyclic load, *e.g.* 70% of the nominal failure load, will allow for an opportunity to interrupt the test prior to when catastrophic failure has occurred. To determine when to stop the test, the stiffness of the specimen should be determined in-situ through either an extensometer (similar to that seen in Figure 9.2), or a camera with tracking capabilities. A specimen can be defined as 'sufficiently damaged' when its tensile stiffness drops below a threshold value. Fractography analysis, or X-ray CT scans, on the damaged specimen could then be used to reveal the locations of initial crack formations, and hence whether resin pocket bridging is the dominating factor influencing delamination suppression behaviour in interleaved specimens. Once a deeper understanding of the damage development in interleaved tapered specimens is established, a wider range of CNT lengths between 11 μm and 40 μm can be investigated to determine whether a minimum CNT length is required to provide significant tensile strength enhancements.

The final unresolved finding follows up from the work on open hole tension (OHT) specimens, discussed in chapter 7. Within this chapter, a trend was discovered, whereby the overall area of matrix damage from ply-splits and delaminations was reduced, for specimens interleaved with VACNTs. Although this behaviour could not be captured through cohesive element modelling, the trend was supported by every interrupted specimen tested (6 pairs of OHT specimens), with differing damage severities and layup configurations. A similar finding was reported by Conway *et al.*, when investigating VACNT interleaves for impact resistance purposes [257]. In their study, it was found that for three different host composite systems (including HexTow®

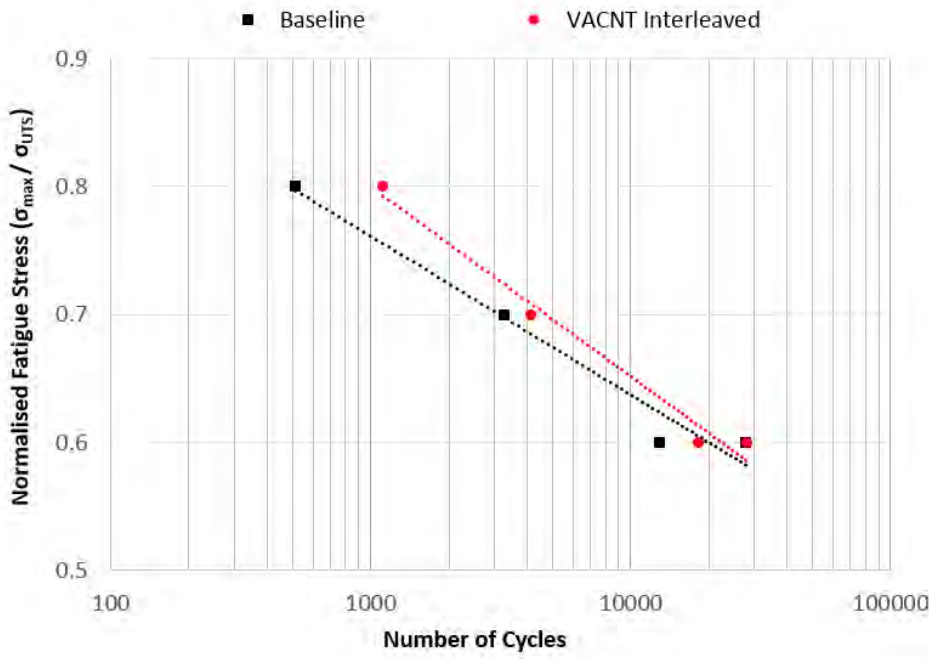

Figure 9.3: S-curve from the preliminary fatigue tests on an unmodified baseline and VACNT interleaved ply-level OHT specimens.

IM7/HexPly® 8552), the damaged area or damage severity after impact decreased, when all the ply interfaces were interleaved with VACNTs. This subsequently lead to the compressive strength of the impacted laminates increasing by between 11 – 16% [257].

To follow up on this finding, a preliminary study, which investigated whether the tension-tension fatigue life of OHT specimens can be increased through VACNT interleaves, was conducted. Theoretically, if the overall matrix damage is decreased, the fatigue life should be extended. In this preliminary study, ply-level OHT specimens, identical to the unmodified baseline and VACNT interleaved OHT specimens described in chapter 7, were cyclically loaded until failure. All OHT specimens were mechanically loaded using an Instron 8801 hydraulic test machine (see Figure 9.2), with a lateral grip pressure of 7 MPa. This pressure was selected to prevent specimen slippage during the test, while also minimising crushing damage. An extensometer was attached to the specimen surface using O-rings to measure strain throughout the test.

After the quasi-static experimental test programme described in chapter 7 was completed, four spare ply-level OHT specimens were available for both the baseline and VACNT interleaved configurations. In order to construct a preliminary S-curve and gain an initial understanding of the influence of VACNT interleaves on fatigue life, OHT specimens were subjected to three load severities, *i.e.* 80%, 70%, and 60% of the nominal quasi-static failure load. All fatigue tests were conducted under load control, using a constant amplitude, R-ratio of 0.1 and at a frequency

of 5 Hz. Failure was defined as when the tensile specimen stiffness dropped below 85% of the undamaged value. Stiffness was continually calculated through Equation 9.1.

$$E = \frac{\sigma_{max}}{\epsilon_{max}} = \frac{Pmax}{A\epsilon_{max}} \tag{9.1}$$

where E is the Young's modulus of the OHT specimen, σ_{max} is the constant maximum stress applied, ϵ_{max} is the maximum measured strain, P_{max} is the constant maximum load applied and A is the average specimen gross cross-sectional area.

Figure 9.3 shows the preliminary S-curve for both the unmodified baseline and VACNT interleaved ply-level OHT specimens. The points plotted correspond to when the specimen stiffness dropped by 15% from the initial undamaged specimen. Analysing the graph, it appears that the fatigue life of the VACNT interleaved specimens is greater than that of the unmodified baseline, which supports the hypothesis that matrix damage reduces through VACNT interleaving. However, it should be noted that similar fatigue tests on OHT specimens have shown large amounts of scatter between specimens [250], and therefore, further tests are required before a conclusive statement can be made. Regardless, literature and primary sourced data suggests that OHT specimens reinforced with VACNT interleaves offer greater performance enhancements for impact resistance and fatigue-life than compared to quasi-static performance.

APPENDIX A

APPENDIX A

Results from a complementary numerical study to that reported in Section 6.3.3.2. All values were calculated using the propagated strain energy release rate properties, G_{prop}, measured experimentally and reported in chapter 5.

Table A.1: Failure load per unit width for combinations of cohesive element strengths with G_{prop} values. (*) shows the difference relative to the experimental value. (reported in Table 6.7).

Mode II Cohesive Strength		S_{II}		
	Mode I Cohesive Strength	**82.6**	**90**	**100**
S_I	**60**	3.02 (-2.41%)	3.04 (-1.48%)	3.04 (-1.51%)
	75	3.04 (-1.73%)	3.04 (-1.46%)	3.05 (-1.26%)
	90	3.19 (+3.33%)	3.21 (+3.92%)	3.20 (+3.60%)

Table A.2: Failure load enhancement of the VACNT interleaved cohesive element model relative to the baseline model with G_{prop} values.

Mode II Cohesive Strength		S_{II}		
	Mode I Cohesive Strength	**82.6**	**90**	**100**
S_I	**60**	2.22%	3.20%	3.16%
	75	2.93%	3.21%	3.43%
	90	8.23%	8.85%	8.52%

Table A.3: The failure load per unit width when the cohesive strength is scaled by the same proportion as the experimentally measured initiation (G_c) or propagated (G_{prop}) strain energy release rate.

Measured Strain Energy Release Rate*	**Initiation**		**Propagation**	
	$G_{IC}(kJ/m^2)$	$G_{IIC}(kJ/m^2)$	$G_{Iprop}(kJ/m^2)$	$G_{IIprop}(kJ/m^2)$
Baseline	0.22	0.62	0.26	0.67
VACNT Interleaved	0.3	0.71	0.3	0.71
Enhancement Ratio	**1.36**	**1.15**	**1.15**	**1.06**
Cohesive Strength Scaling	S_{IC}	S_{IIC}	S_{Iprop}	S_{IIprop}
Baseline	60	82.6	60	82.6
VACNT Interleaved (Scaled)	**81.8**	**94.6**	**69.2**	**87.5**
VACNT Interleaved Cohesive Model	(kN/mm)		(kN/mm)	
Failure Load	**3.10**		**3.04**	
% Difference wrt. Experiment	0.26%		-1.63%	
% Enhancement wrt. BL Model	9.47%		3.04%	

** As measured in Chapter 5*

BIBLIOGRAPHY

[1] Y. Liu, M. de Araujo, and H. Hu, "Advanced fibrous architectures for composites in aerospace applications," in *Advanced Composite Materials for Aerospace Engineering* (S. Rana and R. Fangueiro, eds.), ch. 2, pp. 17–58, Woodhead Publishing, 2016.

[2] S. R. Hallett, B. G. Green, W. G. Jiang, and M. R. Wisnom, "An experimental and numerical investigation into the damage mechanisms in notched composites," *Composites Part A: Applied Science and Manufacturing*, vol. 40, no. 5, pp. 613–624, 2009.

[3] Hexcel Composites, "HexPly 8552 Product data," tech. rep., Duxford U.K., 2000.

[4] B. Zhang, G. Allegri, M. Yasaee, and S. R. Hallett, "Micro-mechanical finite element analysis of Z-pins under mixed-mode loading," *Composites Part A: Applied Science and Manufacturing*, vol. 78, pp. 424–435, 2015.

[5] "Mechanics of composite materials lab," 2019.

[6] N. Sato, M. Hojo, and M. Nishikawa, "Intralaminar fatigue crack growth properties of conventional and interlayer toughened CFRP laminate under mode i loading," *Composites Part A: Applied Science and Manufacturing*, vol. 68, pp. 202–211, 2015.

[7] M. S. Prasad, C. Venkatesha, and T. Jayaraju, "Experimental methods of determining fracture toughness of fiber reinforced polymer composites under various loading conditions," *Journal of Minerals and Materials Characterization and Engineering*, vol. 10, no. 13, p. 1263, 2011.

[8] S. Sridharan, *Delamination behaviour of composites*.
Woodhead Publishing, 2008.

[9] I. Hamerton and J. Kratz, "The use of thermosets in modern aerospace applications," in *Thermosets: Structure, Properties, and Applications* (Q. Guo, ed.), ch. 9, pp. 303–340, Elsevier, 2nd ed., 2018.

[10] A. P. Mouritz, "Review of z-pinned composite laminates," *Composites Part A: Applied Science and Manufacturing*, vol. 38, no. 12, pp. 2383–2397, 2007.

[11] A. P. Mouritz, "Three-dimensional (3D) fibre reinforcements for composites," in *Composite Reinforcements for Optimum Performance* (P. Boisse, ed.), ch. 6, pp. 157–198, Woodhead Publishing, 2011.

[12] L. Tong, A. Mouritz, and M. Bannister, *3D Fibre Reinforced Polymer Composites*. Oxford: Elsevier, 2002.

[13] L. S. Liu, P. Wang, X. Legrand, and D. Soulat, "Investigation of mechanical properties of tufted composites: Influence of tuft length through the thickness reinforcement," *Composite Structures*, vol. 172, pp. 221–228, 2017.

[14] H. Albertsen, J. Ivens, P. Peters, M. Wevers, and I. Verpoest, "Interlaminar fracture toughness of CFRP influenced by fibre surface treatment: Part 1. experimental results," *Composites Science and Technology*, vol. 54, no. 2, pp. 133–145, 1995.

[15] S. Tiwari, J. Bijwe, and S. Panier, "Polyetherimide composites with gamma irradiated carbon fabric: Studies on abrasive wear," *Wear*, vol. 270, no. 9-10, pp. 688–694, 2011.

[16] E. J. Garcia, B. L. Wardle, A. John Hart, and N. Yamamoto, "Fabrication and multifunctional properties of a hybrid laminate with aligned carbon nanotubes grown In Situ," *Composites Science and Technology*, vol. 68, no. 9, pp. 2034–2041, 2008.

[17] E. T. Thostenson, W. Z. Li, D. Z. Wang, Z. F. Ren, and T. W. Chou, "Carbon nanotube/carbon fiber hybrid multiscale composites," *Journal of Applied Physics*, vol. 91, no. 9, pp. 6034–6037, 2002.

[18] J. Andersons and M. König, "Dependence of fracture toughness of composite laminates on interface ply orientations and delamination growth direction," *Composites Science and Technology*, vol. 64, no. 13-14, pp. 2139–2152, 2004.

[19] C. Blondeau, G. Pappas, and J. Botsis, "Influence of ply-angle on fracture in antisymmetric interfaces of CFRP laminates," *Composite Structures*, vol. 216, no. March, pp. 464–476, 2019.

[20] M. Herráez, N. Pichler, G. Pappas, C. Blondeau, and J. Botsis, "Experiments and numerical modelling on angle-ply laminates under remote mode II loading," *Composites Part A: Applied Science and Manufacturing*, p. 105886, 2020.

[21] Z. Wu, C. U. Pittman, and S. D. Gardner, "Nitric acid oxidation of carbon fibers and the effects of subsequent treatment in refluxing aqueous NaOH," *Science*, vol. 33, no. 5, pp. 597–605, 1995.

[22] H. Qian, A. Bismarck, E. S. Greenhalgh, G. Kalinka, and M. S. Shaffer, "Hierarchical composites reinforced with carbon nanotube grafted fibers: The potential assessed at the single fiber level," *Chemistry of Materials*, vol. 20, no. 5, pp. 1862–1869, 2008.

[23] J. Cha, G. H. Jun, J. K. Park, J. C. Kim, H. J. Ryu, and S. H. Hong, "Improvement of modulus, strength and fracture toughness of CNT/Epoxy nanocomposites through the functionalization of carbon nanotubes," *Composites Part B: Engineering*, vol. 129, pp. 169–179, 2017.

[24] D. P. Vlasveld, W. Daud, H. E. Bersee, and S. J. Picken, "Continuous fibre composites with a nanocomposite matrix: Improvement of flexural and compressive strength at elevated temperatures," *Composites Part A: Applied Science and Manufacturing*, vol. 38, no. 3, pp. 730–738, 2007.

[25] D. Lewis, *Interlaminar reinforcement of carbon fiber composites from unidirectional prepreg utilizing aligned carbon nanotubes*.
PhD thesis, Massachusetts Institute of Technology, 2016.

[26] D. Qian, E. C. Dickey, R. Andrews, and T. Rantell, "Load transfer and deformation mechanisms in carbon nanotube-polystyrene composites," *Applied Physics Letters*, vol. 76, no. 20, p. 2868, 2000.

[27] A. F. Yee and R. A. Pearson, "Toughening mechanisms in elastomer-modified epoxies - Part 1 Mechanical studies," *Journal of Materials Science*, vol. 21, no. 7, pp. 2462–2474, 1986.

[28] L. Wang, K. Wang, L. Chen, Y. Zhang, and C. He, "Preparation, morphology and thermal/mechanical properties of epoxy/nanoclay composite," *Composites Part A: Applied Science and Manufacturing*, vol. 37, no. 11, pp. 1890–1896, 2006.

[29] L. Lavagna, D. Massella, M. F. Pantano, F. Bosia, N. M. Pugno, and M. Pavese, "Grafting carbon nanotubes onto carbon fibres doubles their effective strength and the toughness of the composite," *Composites Science and Technology*, vol. 166, pp. 140–149, 2018.

[30] Z. Li, R. Wang, R. J. Young, L. Deng, F. Yang, L. Hao, W. Jiao, and W. Liu, "Control of the functionality of graphene oxide for its application in epoxy nanocomposites," *Polymer*, vol. 54, no. 23, pp. 6437–6446, 2013.

[31] M. Hojo, S. Matsuda, M. Tanaka, S. Ochiai, and A. Murakami, "Mode I delamination fatigue properties of interlayer-toughened CF/epoxy laminates," *Composites Science and Technology*, vol. 66, no. 5, pp. 665–675, 2006.

[32] M. Hojo, T. Ando, M. Tanaka, T. Adachi, S. Ochiai, and Y. Endo, "Modes I and II interlaminar fracture toughness and fatigue delamination of CF/epoxy laminates with self-same epoxy interleaf," *International Journal of Fatigue*, vol. 28, pp. 1154–1165, 2006.

[33] B. Beylergil, E. Aktas, and M. Tano, "Enhancement of interlaminar fracture toughness of carbon fiber ‚Äì epoxy composites using polyamide - 6,6 electrospun nanofibers," *Journal of Applied Polymer Science*, pp. 1–12, 2017.

[34] Y. Zhu, C. E. Bakis, and J. H. Adair, "Effects of carbon nanofiller functionalization and distribution on interlaminar fracture toughness of multi-scale reinforced polymer composites," *Carbon*, vol. 50, no. 3, pp. 1316–1331, 2012.

[35] D. Liu, G. Li, B. Li, and X. Yang, "Establishment of multi-scale interface in interlayer-toughened CFRP composites by self-assembled PA-MWNTs-EP," *Composites Science and Technology*, vol. 130, pp. 53–62, 2016.

[36] Y. Li, N. Hori, M. Arai, N. Hu, Y. Liu, and H. Fukunaga, "Improvement of interlaminar mechanical properties of CFRP laminates using VGCF," *Composites Part A: Applied Science and Manufacturing*, vol. 40, no. 12, pp. 2004–2012, 2009.

[37] J. W. Kim and J. S. Lee, "Influence of interleaved films on the mechanical properties of carbon fiber fabric/polypropylene thermoplastic composites," *Materials*, vol. 9, no. 5, 2016.

[38] E. J. Garcia, B. L. Wardle, and A. John Hart, "Joining prepreg composite interfaces with aligned carbon nanotubes," *Composites Part A: Applied Science and Manufacturing*, vol. 39, no. 6, pp. 1065–1070, 2008.

[39] B. G. Falzon, S. C. Hawkins, C. P. Huynh, R. Radjef, and C. Brown, "An investigation of Mode I and Mode II fracture toughness enhancement using aligned carbon nanotubes forests at the crack interface," *Composite Structures*, vol. 106, pp. 65–73, 2013.

[40] K. He, S. V. Hoa, and R. Ganesan, "The study of tapered laminated composite structures: A review," *Composites Science and Technology*, vol. 60, no. 14, pp. 2643–2657, 2000.

[41] P. Hubert, A. Johnston, A. Poursartip, and K. Nelson, "Cure kinetics and viscosity models of Hexcel 8552 epoxy resin," in *International SAMPE symposium and exhibition*, no. May 2016, pp. 2341–2354, 2001.

[42] Provo Craft & Novelty Inc., "Cricut Design Space," 2014.

[43] L. Kawashita, M. I. Jones, S. R. Hallett, M. R. Wisnom, and S. Giannis, "High fidelity modelling of tapered laminates with internal ply terminations," in *18th International Conference on Composite Materials*, (Juju Island, Korea), pp. 1–6, 2011.

[44] W.-g. Jiang, S. R. Hallett, B. G. Green, and M. R. Wisnom, "A concise interface constitutive lawfor analysis of delamination and splitting in composite materials and its application to scaled notched tensile specimens," *Int. J. Numer. Meth. Engng*, vol. 69, no. August 2006, pp. 1982–1995, 2007.

[45] X. Li, S. R. Hallett, and M. R. Wisnom, "Predicting the effect of through-thickness compressive stress on delamination using interface elements," *Composites Part A: Applied Science and Manufacturing*, vol. 39, no. 2, pp. 218–230, 2008.

[46] L. F. Kawashita, A. Bedos, and S. R. Hallett, "Modelling mesh independent transverse cracks in laminated composites with a simplified cohesive segment method," *Computers, Materials and Continua*, vol. 32, no. 2, pp. 133–158, 2012.

[47] M. R. Wisnom, "The role of delamination in failure of fibre-reinforced composites," *Philosophical Transactions of the Royal Society A: Mathematical, Physical and Engineering Sciences*, vol. 370, no. 1965, pp. 1850–1870, 2012.

[48] B. Pradhan and S. K. Panda, "Effect of material anisotropy and curing stresses on interface delamination propagation characteristics in multiply laminated FRP composites," *Journal of Engineering Materials and Technology*, vol. 128, no. 3, p. 383, 2006.

[49] R. D. Adams and P. Cawley, "A review of defect types and nondestructive testing techniques for composites and bonded joints," *NDT & E International*, vol. 24, no. 2, p. 105, 1991.

[50] J. P. Davim and P. Reis, "Study of delamination in drilling carbon fiber reinforced plastics (CFRP) using design experiments," *Composite Structures*, vol. 59, no. 4, pp. 481–487, 2003.

[51] F. Cappello and D. Tumino, "Numerical analysis of composite plates with multiple delaminations subjected to uniaxial buckling load," *Composites Science and Technology*, vol. 66, no. 2, pp. 264–272, 2006.

[52] H. Suemasu, "Effects of multiple delaminations on compressive buckling behaviors of composite panels," *Journal of Composite Materials*, vol. 27, no. 12, pp. 1172–1192, 1993.

[53] Z. Aslan and F. Daricik, "Effects of multiple delaminations on the compressive, tensile, flexural, and buckling behaviour of E-glass/epoxy composites," *Composites Part B: Engineering*, vol. 100, pp. 186–196, 2016.

[54] Federal Aviation Administration, "Composite aircraft structure - AC 20-107B," tech. rep., 2009.

[55] Federal Aviation Administration, "Damage tolerance and fatigue evaluation of structure - AC 25.571-1D," tech. rep., 2011.

[56] D. Goktas, W. R. Kennon, and P. Potluri, "Improvement of mode I interlaminar fracture toughness of stitched glass/epoxy composites," *Applied Composite Materials*, vol. 24, no. 2, pp. 351–375, 2017.

[57] A. Mouritz, K. Leong, and I. Herszberg, "A review of the effect of stitching on the in-plane mechanical properties of fibre-reinforced polymer composites," *Composites Part A: Applied Science and Manufacturing*, vol. 28, no. 12, pp. 979–991, 1997.

[58] J. W. G. Treiber, *Performance of tufted carbon fibre/epoxy composites*.
PhD thesis, 2011.

[59] G. Dell'Anno, *Effect of tufting on the mechanical behaviour of carbon fabric/epoxy composites*.
PhD thesis, 2007.

[60] V. A. Guenon, T. W. Chou, and J. W. Gillespie, "Toughness properties of a three-dimensional carbon-epoxy composite," *Journal of Materials Science*, vol. 24, no. 11, pp. 4168–4175, 1989.

[61] T. Chou, "Three-dimensional textile structrual composites," in *Microstructural Design of Fiber Composites*, ch. 7, pp. 374–443, Cambridge University Press, 2nd ed., 2005.

[62] P. Chang, A. P. Mouritz, and B. N. Cox, "Properties and failure mechanisms of z-pinned laminates in monotonic and cyclic tension," *Composites Part A: Applied Science and Manufacturing*, vol. 37, no. 10, pp. 1501–1513, 2006.

[63] P. Chang, A. P. Mouritz, and B. N. Cox, "Flexural properties of z-pinned laminates," *Composites Part A: Applied Science and Manufacturing*, vol. 38, no. 2, pp. 244–251, 2007.

[64] S. Wang, Y. Zhang, and G. Wu, "Interlaminar shear properties of z-pinned carbon fiber reinforced aluminum matrix composites by short-beam shear test," *Materials*, vol. 11, no. 10, p. 1874, 2018.

[65] S. Tiwari and J. Bijwe, "Surface treatment of carbon fibers - A review," *Procedia Technology*, vol. 14, pp. 505–512, 2014.

[66] H. Qian, E. S. Greenhalgh, M. S. Shaffer, and A. Bismarck, "Carbon nanotube-based hierarchical composites: A review," *Journal of Materials Chemistry*, vol. 20, no. 23, pp. 4751–4762, 2010.

[67] Z. H. Hu, S. M. Dong, J. B. Hu, Z. Wang, B. Lu, J. S. Yang, Q. G. Li, B. Wu, L. Gao, and X. Y. Zhang, "Synthesis of carbon nanotubes on carbon fibers by modified chemical vapor deposition," *New Carbon Materials*, vol. 27, no. 5, pp. 352–361, 2012.

[68] Q. Zhang, J. Liu, R. Sager, L. Dai, and J. Baur, "Hierarchical composites of carbon nanotubes on carbon fiber: Influence of growth condition on fiber tensile properties," *Composites Science and Technology*, vol. 69, no. 5, pp. 594–601, 2009.

[69] T. Susi, A. G. Nasibulin, H. Jiang, and E. I. Kauppinen, "CVD synthesis of hierarchical 3D MWCNT/carbon-fiber nanostructures," *Journal of Nanomaterials*, vol. 2008, no. 1, pp. 37–42, 2008.

[70] S. S. Wicks, R. G. de Villoria, and B. L. Wardle, "Interlaminar and intralaminar reinforcement of composite laminates with aligned carbon nanotubes," *Composites Science and Technology*, vol. 70, no. 1, pp. 20–28, 2010.

[71] K. L. Kepple, G. P. Sanborn, P. A. Lacasse, K. M. Gruenberg, and W. J. Ready, "Improved fracture toughness of carbon fiber composite functionalized with multi walled carbon nanotubes," *Carbon*, vol. 46, no. 15, pp. 2026–2033, 2008.

[72] R. B. Mathur, S. Chatterjee, and B. P. Singh, "Growth of carbon nanotubes on carbon fibre substrates to produce hybrid/phenolic composites with improved mechanical properties," *Composites Science and Technology*, vol. 68, no. 7-8, pp. 1608–1615, 2008.

[73] H. Qian, A. Bismarck, E. S. Greenhalgh, and M. S. Shaffer, "Carbon nanotube grafted silica fibres: Characterising the interface at the single fibre level," *Composites Science and Technology*, vol. 70, no. 2, pp. 393–399, 2010.

[74] R. J. Sager, P. J. Klein, D. C. Lagoudas, Q. Zhang, J. Liu, L. Dai, and J. W. Baur, "Effect of carbon nanotubes on the interfacial shear strength of T650 carbon fiber in an epoxy matrix," *Composites Science and Technology*, vol. 69, no. 7-8, pp. 898–904, 2009.

[75] L. Zhang, N. De Greef, G. Kalinka, B. Van Bilzen, J. P. Locquet, I. Verpoest, and J. W. Seo, "Carbon nanotube-grafted carbon fiber polymer composites: Damage characterization on the micro-scale," *Composites Part B: Engineering*, vol. 126, pp. 202–210, 2017.

[76] Q. Zhang, W. Qian, R. Xiang, Z. Yang, G. Luo, Y. Wang, and F. Wei, "In situ growth of carbon nanotubes on inorganic fibers with different surface properties," *Materials Chemistry and Physics*, vol. 107, no. 2-3, pp. 317–321, 2008.

[77] V. Eskizeybek, A. Avci, and A. Gülce, "The Mode I interlaminar fracture toughness of chemically carbon nanotube grafted glass fabric/epoxy multi-scale composite structures," *Composites Part A: Applied Science and Manufacturing*, vol. 63, pp. 94–102, 2014.

[78] J. Dong, C. Jia, M. Wang, X. Fang, H. Wei, H. Xie, T. Zhang, J. He, Z. Jiang, and Y. Huang, "Improved mechanical properties of carbon fiber-reinforced epoxy composites by growing carbon black on carbon fiber surface," *Composites Science and Technology*, vol. 149, pp. 75–80, 2017.

[79] R. L. Zhang, B. Gao, Q. H. Ma, J. Zhang, H. Z. Cui, and L. Liu, "Directly grafting graphene oxide onto carbon fiber and the effect on the mechanical properties of carbon fiber composites," *Materials and Design*, vol. 93, pp. 364–369, 2016.

[80] X. Yao, X. Gao, J. Jiang, C. Xu, C. Deng, and J. Wang, "Comparison of carbon nanotubes and graphene oxide coated carbon fiber for improving the interfacial properties of carbon fiber/epoxy composites," *Composites Part B: Engineering*, vol. 132, pp. 170–177, 2018.

[81] L. Zheng, Y. Wang, J. Qin, X. Wang, R. Lu, C. Qu, and C. Wang, "Scalable manufacturing of carbon nanotubes on continuous carbon fibers surface from chemical vapor deposition," *Vacuum*, vol. 152, pp. 84–90, 2018.

[82] K. Saravanakumar, N. Farouk, and V. Arumugam, "Effect of fiber orientation on Mode-I delamination resistance of glass/epoxy laminates incorporated with milled glass fiber fillers," *Engineering Fracture Mechanics*, vol. 199, no. April, pp. 61–70, 2018.

[83] M. M. Shokrieh, M. Salamat-talab, and M. Heidari-Rarani, "Effect of interface fiber angle on the R-curve behavior of E-glass/epoxy DCB specimens," *Theoretical and Applied Fracture Mechanics*, vol. 86, pp. 153–160, 2016.

[84] A. Laksimi, A. A. Benyahia, M. L. Benzeggagh, and X. L. Gong, "Initiation and bifurcation mechanisms of cracks in multi-directional laminates," *Composites Science and Technology*, vol. 60, no. 4, pp. 597–604, 2000.

[85] Y. B. Shi and D. Hull, "Mode II fracture of $+\theta/-\theta$ angled laminate interfaces," *Composites Science and Technology*, vol. 47, no. 2, pp. 173–184, 1993.

[86] J. Li, Y. Huang, Z. Xu, and Z. Wang, "High-energy radiation technique treat on the surface of carbon fiber," *Materials Chemistry and Physics*, vol. 94, no. 2-3, pp. 315–321, 2005.

[87] J. Jang and H. Yang, "Effect of surface treatment on the performance improvement of carbon fiber/polybenzoxazine composites," *Journal of Materials Science*, vol. 35, no. 9, pp. 2297–2303, 2000.

[88] J. B. Donnet, M. Brendle, T. L. Dhami, and O. P. Bahl, "Plasma treatment effect on the surface energy of carbon and carbon fibers," *Carbon*, vol. 24, no. 6, pp. 757–770, 1986.

[89] S. Tiwari, J. Bijwe, and S. Panier, "Tribological studies on polyetherimide composites based on carbon fabric with optimized oxidation treatment," *Wear*, vol. 271, no. 9-10, pp. 2252–2260, 2011.

[90] H. Kim, E. Oh, H. T. Hahn, and K. H. Lee, "Enhancement of fracture toughness of hierarchical carbon fiber composites via improved adhesion between carbon nanotubes and carbon fibers," *Composites Part A: Applied Science and Manufacturing*, vol. 71, pp. 72–83, 2015.

[91] S. S. Wicks, W. Wang, M. R. Williams, and B. L. Wardle, "Multi-scale interlaminar fracture mechanisms in woven composite laminates reinforced with aligned carbon nanotubes," *Composites Science and Technology*, vol. 100, pp. 128–135, 2014.

[92] E. Bekyarova, E. T. Thostenson, A. Yu, H. Kim, J. Gao, J. Tang, H. T. Hahn, T. W. Chou, M. E. Itkis, and R. C. Haddon, "Multiscale carbon nanotube-carbon fiber reinforcement for advanced epoxy composites," *Langmuir*, vol. 23, no. 7, pp. 3970–3974, 2007.

[93] N. A. Siddiqui, M. L. Sham, B. Z. Tang, A. Munir, and J. K. Kim, "Tensile strength of glass fibres with carbon nanotube-epoxy nanocomposite coating," *Composites Part A: Applied Science and Manufacturing*, vol. 40, no. 10, pp. 1606–1614, 2009.

[94] A. Laachachi, A. Vivet, G. Nouet, B. Ben Doudou, C. Poilâne, J. Chen, J. Bo bai, and M. Ayachi, "A chemical method to graft carbon nanotubes onto a carbon fiber," *Materials Letters*, vol. 62, no. 3, pp. 394–397, 2008.

[95] M. A. Rafiee, J. Rafiee, Z. Wang, H. Song, Z.-z. Yu, and N. Koratkar, "Enhanced mechanical properties of nanocomposites at low graphene content," *ACS nano*, vol. 3, no. 12, pp. 3884–3890, 2009.

[96] J. Blanco, E. J. Garcia, R. Guzman de Villoria, and B. L. Wardle, "Limiting mechanisms of mode I interlaminar toughening of composites reinforced with aligned carbon nanotubes," *Journal of Composite Materials*, vol. 43, no. 8, pp. 825–841, 2009.

[97] J. K. Kim and Y. wing Mai, "High strength, high fracture toughness fibre composites with interface control - A review," *Composites Science and Technology*, vol. 41, no. 4, pp. 333–378, 1991.

[98] T. H. Hsieh, A. J. Kinloch, A. C. Taylor, and I. A. Kinloch, "The effect of carbon nanotubes on the fracture toughness and fatigue performance of a thermosetting epoxy polym," *Journal of Materials Science*, vol. 46, no. 23, pp. 7525–7535, 2011.

[99] W. D. Bascom, J. L. Bitner, R. J. Moulton, and A. R. Siebert, "The interlaminar fracture of organic-matrix, woven reinforcement composites," *Composites*, vol. 11, no. 1, pp. 9–18, 1980.

[100] D. J. Hourston and J. M. Lane, "The toughening of epoxy resins with thermoplastics: 1. Trifunctional epoxy resin-polyetherimide blends," *Polymer*, vol. 33, no. 7, pp. 1379–1383, 1992.

[101] A. J. Kinloch, S. J. Shaw, D. A. Tod, and D. L. Hunston, "Deformation and fracture behaviour of a rubber-toughened epoxy: 1. Microstructure and fracture studies," *Polymer*, vol. 24, no. 10, pp. 1341–1354, 1983.

[102] S. J. Park, F. L. Jin, and J. R. Lee, "Thermal and mechanical properties of tetrafunctional epoxy resin toughened with epoxidized soybean oil," *Materials Science and Engineering A*, vol. 374, no. 1-2, pp. 109–114, 2004.

[103] R. Bagheri, B. T. Marouf, and R. A. Pearson, "Rubber-toughened epoxies: A critical review," *Polymer Reviews*, vol. 49, no. 3, pp. 201–225, 2009.

[104] A. C. Garg and Y. W. Mai, "Failure mechanisms in toughened epoxy resins - A review," *Composites Science and Technology*, vol. 31, no. 3, pp. 179–223, 1988.

[105] A. J. Kinloch, R. D. Mohammed, A. C. Taylor, C. Eger, S. Sprenger, and D. Egan, "The effect of silica nano particles and rubber particles on the toughness of multiphase thermosetting epoxy polymers," *Journal of Materials Science*, vol. 40, no. 18, pp. 5083–5086, 2005.

[106] F. H. Gojny, M. H. Wichmann, U. Köpke, B. Fiedler, and K. Schulte, "Carbon nanotube-reinforced epoxy-composites: Enhanced stiffness and fracture toughness at low nanotube content," *Composites Science and Technology*, vol. 64, pp. 2363–2371, 2004.

[107] N. Domun, H. Hadavinia, T. Zhang, T. Sainsbury, G. H. Liaghat, and S. Vahid, "Improving the fracture toughness and the strength of epoxy using nanomaterials-a review of the current status," *Nanoscale*, vol. 7, no. 23, pp. 10294–10329, 2015.

[108] T. Imai, F. Sawa, T. Ozaki, T. Shimizu, S. I. Kuge, M. Kozako, and T. Tanaka, "Effects of epoxy/filler interface on properties of nano- or micro-composites," *Transactions on Fundamentals and Materials*, vol. 126, no. 2, pp. 84–91, 2006.

[109] K. C. Jajam and H. V. Tippur, "Quasi-static and dynamic fracture behavior of particulate polymer composites: A study of nano- vs. micro-size filler and loading-rate effects," *Composites Part B: Engineering*, vol. 43, no. 8, pp. 3467–3481, 2012.

[110] I. Ozsoy, A. Demirkol, A. Mimaroglu, H. Unal, and Z. Demir, "The influence of micro-And nano-filler content on the mechanical properties of epoxy composites," *Journal of Mechanical Engineering*, vol. 61, no. 10, pp. 601–609, 2015.

[111] R. B. Ladani, S. Wu, A. J. Kinloch, K. Ghorbani, J. Zhang, A. P. Mouritz, and C. H. Wang, "Improving the toughness and electrical conductivity of epoxy nanocomposites by using aligned carbon nano fibres," *Composites Science and Technology*, vol. 117, pp. 146–158, 2015.

[112] A. Hernandez-Perez, F. Aviles, A. May-Pat, A. Valadez-Gonzalez, P. Herrera-Franco, and P. Bartolo-Perez, "Effective properties of multiwalled carbon nanotube / epoxy composites using two different tubes," *Composites Science and Technology*, vol. 68, pp. 1422–1431, 2008.

[113] F. H. Gojny, M. H. G. Wichmann, B. Fiedler, and K. Schulte, "Influence of different carbon nanotubes on the mechanical properties of epoxy matrix composites - A comparative study," *Composites Science and Technology*, vol. 65, pp. 2300–2313, 2005.

[114] C. Ma, H.-y. Liu, X. Du, L. Mach, F. Xu, and Y.-w. Mai, "Fracture resistance , thermal and electrical properties of epoxy composites containing aligned carbon nanotubes by low magnetic field," *Composite Science and Technology*, vol. 114, pp. 126–135, 2015.

[115] R. B. Ladani, S. Wu, A. J. Kinloch, K. Ghorbani, J. Zhang, A. P. Mouritz, and C. H. Wang, "Multifunctional properties of epoxy nanocomposites reinforced by aligned nanoscale carbon," *Materials & Design*, vol. 94, pp. 554–564, mar 2016.

[116] P. C. Ma, N. A. Siddiqui, G. Marom, and J. K. Kim, "Dispersion and functionalization of carbon nanotubes for polymer-based nanocomposites: A review," *Composites Part A: Applied Science and Manufacturing*, vol. 41, no. 10, pp. 1345–1367, 2010.

[117] B. P. M. Ajayan, L. S. Schadler, C. Giannaris, and A. Rubio, "Single-walled carbon nanotube-polymer composites : strength and weakness," *Advanced Materials*, vol. 12, no. 10, pp. 750–753, 2000.

[118] L. Sun, G. L. Warren, J. Y. O'Reilly, W. N. Everett, S. M. Lee, D. Davis, D. Lagoudas, and H. J. Sue, "Mechanical properties of surface-functionalized SWCNT/epoxy composites," *Carbon*, vol. 46, no. 2, pp. 320–328, 2008.

[119] K. Song, Y. Zhang, J. Meng, E. C. Green, N. Tajaddod, H. Li, and M. L. Minus, "Structural polymer-based carbon nanotube composite fibers: Understanding the processing-structure-performance relationship," *Materials*, vol. 6, no. 6, pp. 2543–2577, 2013.

[120] S. Kim, Y.-i. Lee, D.-h. Kim, K.-j. Lee, B.-s. Kim, M. Hussain, and Y.-h. Choa, "Estimation of dispersion stability of UV / ozone treated multi-walled carbon nanotubes and their electrical properties," *Carbon*, vol. 51, pp. 346–354, 2012.

[121] S. Wu, R. B. Ladani, J. Zhang, E. Bafekrpour, K. Ghorbani, A. P. Mouritz, A. J. Kinloch, and C. H. Wang, "Aligning multilayer graphene flakes with an external electric field to improve multifunctional properties of epoxy nanocomposites," *Carbon*, vol. 94, pp. 607–618, 2015.

[122] E. Borowski, E. Soliman, U. F. Kandil, and M. R. Taha, "Interlaminar fracture toughness of CFRP laminates incorporating multi-walled carbon nanotubes," *Polymers*, vol. 7, no. 6, pp. 1020–1045, 2015.

[123] V. K. Srivastava, T. Gries, D. Veit, T. Quadflieg, B. Mohr, and M. Kolloch, "Effect of nanomaterial on mode I and mode II interlaminar fracture toughness of woven carbon fabric reinforced polymer composites," *Engineering Fracture Mechanics*, vol. 180, pp. 73–86, 2017.

[124] M. H. Wichmann, J. Sumfleth, F. H. Gojny, M. Quaresimin, B. Fiedler, and K. Schulte, "Glass-fibre-reinforced composites with enhanced mechanical and electrical properties - Benefits and limitations of a nanoparticle modified matrix," *Engineering Fracture Mechanics*, vol. 73, no. 16, pp. 2346–2359, 2006.

[125] A. Tugrul Seyhan, M. Tanoglu, and K. Schulte, "Mode I and mode II fracture toughness of E-glass non-crimp fabric/carbon nanotube (CNT) modified polymer based composites," *Engineering Fracture Mechanics*, vol. 75, no. 18, pp. 5151–5162, 2008.

[126] D. Quan, J. L. Urdániz, and A. Ivanković, "Enhancing mode-I and mode-II fracture toughness of epoxy and carbon fibre reinforced epoxy composites using multi-walled carbon nanotubes," *Materials and Design*, vol. 143, pp. 81–92, 2018.

[127] F. Mujika, G. Vargas, J. Ibarretxe, J. De Gracia, and A. Arrese, "Influence of the modification with MWCNT on the interlaminar fracture properties of long carbon fiber composites," *Composites Part B: Engineering*, vol. 43, no. 3, pp. 1336–1340, 2012.

[128] A. Godara, L. Mezzo, F. Luizi, A. Warrier, S. V. Lomov, A. W. van Vuure, L. Gorbatikh, P. Moldenaers, and I. Verpoest, "Influence of carbon nanotube reinforcement on the processing and the mechanical behaviour of carbon fiber/epoxy composites," *Carbon*, vol. 47, no. 12, pp. 2914–2923, 2009.

[129] B. Ashrafi, J. Guan, V. Mirjalili, Y. Zhang, L. Chun, P. Hubert, B. Simard, C. T. Kingston, O. Bourne, and A. Johnston, "Enhancement of mechanical performance of epoxy/carbon fiber laminate composites using single-walled carbon nanotubes," *Composites Science and Technology*, vol. 71, no. 13, pp. 1569–1578, 2011.

[130] K. N. Shivakumar, R. Panduranga, and M. Sharpe, "Interleaved polymer matrix composites - A review," in *AIAA*, (Boston, MA), pp. 1–13, 2013.

[131] F. Gao, G. Jiao, Z. Lu, and R. Ning, "Mode II delamination and damage resistance of carbon/epoxy composite laminates interleaved with thermoplastic particles," *Journal of Composite Materials*, vol. 41, no. 1, pp. 111–123, 2007.

[132] N. Sela, O. Ishai, and L. Banks-Sills, "The effect of adhesive thickness on interlaminar fracture toughness of interleaved CFRP specimens," *Composites*, vol. 20, no. 3, pp. 257–264, 1989.

[133] M. Yasaee, I. P. Bond, R. S. Trask, and E. S. Greenhalgh, "Mode II interfacial toughening through discontinuous interleaves for damage suppression and control," *Composites Part A: Applied Science and Manufacturing*, vol. 43, no. 1, pp. 121–128, 2012.

[134] J. E. Masters, "Improved impact and delamination resistance through interleafing," *Key Engineering Materials*, vol. 37, p. 317, 1989.

[135] M. Arai, Y. Noro, K. ichi Sugimoto, and M. Endo, "Mode I and mode II interlaminar fracture toughness of CFRP laminates toughened by carbon nanofiber interlayer," *Composites Science and Technology*, vol. 68, no. 2, pp. 516–525, 2008.

[136] M. Yasaee, I. P. Bond, R. S. Trask, and E. S. Greenhalgh, "Mode I interfacial toughening through discontinuous interleaves for damage suppression and control," *Composites Part A: Applied Science and Manufacturing*, vol. 43, no. 1, pp. 121–128, 2012.

[137] C. Cheng, C. Zhang, J. Zhou, M. Jiang, Z. Sun, S. Zhou, Y. Liu, Z. Chen, L. Xu, H. Zhang, and M. Yu, "Improving the interlaminar toughness of the carbon fiber/epoxy composites via interleaved with polyethersulfone porous films," *Composites Science and Technology*, vol. 183, no. September, 2019.

[138] D. W. Wong, L. Lin, P. T. McGrail, T. Peijs, and P. J. Hogg, "Improved fracture toughness of carbon fibre/epoxy composite laminates using dissolvable thermoplastic fibres," *Composites Part A: Applied Science and Manufacturing*, vol. 41, no. 6, pp. 759–767, 2010.

[139] S. Hamer, H. Leibovich, A. Green, R. Avrahami, E. Zussman, A. Siegmann, and D. Sherman, "Mode I and mode II fracture energy of MWCNT reinforced nanofibrilmats interleaved carbon/epoxy laminates," *Composites Science and Technology*, vol. 90, pp. 48–56, 2014.

[140] L. Daelemans, S. van der Heijden, I. De Baere, H. Rahier, W. Van Paepegem, and K. De Clerck, "Using aligned nanofibres for identifying the toughening micromechanisms in nanofibre interleaved laminates," *Composites Science and Technology*, vol. 124, pp. 17–26, 2016.

[141] L. Daelemans, A. Cohades, T. Meireman, J. Beckx, S. Spronk, M. Kersemans, I. De Baere, H. Rahier, V. Michaud, W. Van Paepegem, and K. De Clerck, "Electrospun nanofibrous interleaves for improved low velocity impact resistance of glass fibre reinforced composite laminates," *Materials and Design*, vol. 141, pp. 170–184, 2018.

[142] G. Mittal, K. Y. Rhee, V. Mišković-Stanković, and D. Hui, "Reinforcements in multi-scale polymer composites: Processing, properties, and applications," *Composites Part B: Engineering*, vol. 138, no. November 2017, pp. 122–139, 2018.

[143] N. Zheng, Y. Huang, H. Y. Liu, J. Gao, and Y. W. Mai, "Improvement of interlaminar fracture toughness in carbon fiber/epoxy composites with carbon nanotubes/polysulfone interleaves," *Composites Science and Technology*, vol. 140, pp. 8–15, 2017.

[144] J. A. Rodríguez-González, C. Rubio-González, C. A. Meneses-Nochebuena, P. González-García, and L. Licea-Jiménez, "Enhanced interlaminar fracture toughness of unidirectional carbon fiber/epoxy composites modified with sprayed multi-walled carbon nanotubes," *Composite Interfaces*, vol. 24, no. 9, pp. 883–896, 2017.

[145] T. Yokozeki, Y. Iwahori, M. Ishibashi, T. Yanagisawa, K. Imai, M. Arai, T. Takahashi, and K. Enomoto, "Fracture toughness improvement of CFRP laminates by dispersion of cup-stacked carbon nanotubes," *Composites Science and Technology*, vol. 69, no. 14, pp. 2268–2273, 2009.

[146] Y. Ou, C. González, and J. J. Vilatela, "Interlaminar toughening in structural carbon fiber/epoxy composites interleaved with carbon nanotube veils," *Composites Part A: Applied Science and Manufacturing*, vol. 124, pp. 1–36, 2019.

[147] S. U. Khan and J. K. Kim, "Improved interlaminar shear properties of multiscale carbon fiber composites with bucky paper interleaves made from carbon nanofibers," *Carbon*, vol. 50, no. 14, pp. 5265–5277, 2012.

[148] J. J. Stahl, A. E. Bogdanovich, and P. D. Bradford, "Carbon nanotube shear-pressed sheet interleaves for Mode i interlaminar fracture toughness enhancement," *Composites Part A: Applied Science and Manufacturing*, vol. 80, pp. 127–137, 2016.

[149] S. U. Khan and J. K. Kim, "Impact and delamination failure of multiscale carbon nanotube-fiber reinforced polymer composites: A review," *International Journal of Aeronautical and Space Sciences*, vol. 12, no. 2, pp. 115–133, 2011.

[150] R. Guzman de Villoria, P. Hallander, L. Ydrefors, P. Nordin, and B. L. Wardle, "In-plane strength enhancement of laminated composites via aligned carbon nanotube interlaminar reinforcement," *Composites Science and Technology*, vol. 133, pp. 33–39, 2016.

[151] K. L. Lu, R. M. Lago, Y. K. Chen, M. L. Green, P. J. Harris, and S. C. Tsang, "Mechanical damage of carbon nanotubes by ultrasound," *Carbon*, vol. 34, no. 6, pp. 814–816, 1996.

[152] K. Mukhopadhyay, C. D. Dwivedi, and G. N. Mathur, "Conversion of carbon nanotubes to carbon nanofibers by sonication," *Carbon*, vol. 40, no. 8, pp. 1373–1376, 2002.

[153] B. Fiedler, F. H. Gojny, M. H. Wichmann, M. C. Nolte, and K. Schulte, "Fundamental aspects of nano-reinforced composites," *Composites Science and Technology*, vol. 66, no. 16, pp. 3115–3125, 2006.

[154] V. Vahedi, P. Pasbakhsh, and S. P. Chai, "Toward high performance epoxy/halloysite nanocomposites: New insights based on rheological, curing, and impact properties," *Materials and Design*, vol. 68, pp. 42–53, 2015.

[155] R. Sadeghian, S. Gangireddy, B. Minaie, and K. T. Hsiao, "Manufacturing carbon nanofibers toughened polyester/glass fiber composites using vacuum assisted resin transfer molding for enhancing the mode-I delamination resistance," *Composites Part A: Applied Science and Manufacturing*, vol. 37, no. 10, pp. 1787–1795, 2006.

[156] F. H. Gojny, M. H. Wichmann, B. Fiedler, W. Bauhofer, and K. Schulte, "Influence of nano-modification on the mechanical and electrical properties of conventional fibre-reinforced composites," *Composites Part A: Applied Science and Manufacturing*, vol. 36, no. 11, pp. 1525–1535, 2005.

[157] Z. Fan, K. T. Hsiao, and S. G. Advani, "Experimental investigation of dispersion during flow of multi-walled carbon nanotube/polymer suspension in fibrous porous media," *Carbon*, vol. 42, no. 4, pp. 871–876, 2004.

[158] H. Ning, S. Weng, N. Hu, C. Yan, J. Liu, J. Yao, Y. Liu, X. Peng, S. Fu, and J. Zhang, "Mode-II interlaminar fracture toughness of GFRP/Al laminates improved by surface modified VGCF interleaves," *Composites Part B: Engineering*, vol. 114, pp. 365–372, 2017.

[159] X. Ni and B. L. Wardle, "Experimental investigation of interlaminar fracture micro-mechanisms of aligned carbon nanotube-reinforced aerospace laminated composites," in *AIAA Scitech 2019 Forum*, pp. 1–11, 2019.

[160] R. B. Ladani, A. R. Ravindran, S. Wu, K. Pingkarawat, A. J. Kinloch, A. P. Mouritz, R. O. Ritchie, and C. H. Wang, "Multi-scale toughening of fibre composites using carbon nanofibres and z-pins," *Composites Science and Technology*, vol. 131, pp. 98–109, 2016.

[161] K. Bilisik and E. Sapanci, "Experimental determination of fracture toughness properties of nanostitched and nanoprepreg carbon/epoxy composites," *Engineering Fracture Mechanics*, vol. 189, pp. 293–306, 2018.

[162] V. P. Veedu, A. Cao, X. Li, K. Ma, C. Soldano, S. Kar, P. M. Ajayan, and M. N. Ghasemi-Nejhad, "Multifunctional composites using reinforced laminae with carbon-nanotube forests," *Nature Materials*, vol. 5, no. 6, pp. 457–462, 2006.

[163] K. N. Shivakumar, R. Panduranga, J. Skujins, and S. Miller, "Assessment of mode-II fracture tests for unidirectional fiber reinforced composite laminates," *Journal of Reinforced Plastics and Composites*, vol. 34, no. 23, pp. 1905–1925, 2015.

[164] A. Magrez, J. W. Seo, R. Smajda, M. Mionić, and L. Forró, "Catalytic CVD synthesis of carbon nanotubes: Towards high yield and low temperature growth," *Materials*, vol. 3, no. 11, pp. 4871–4891, 2010.

[165] Y. Li, J. Kang, J. B. Choi, J. D. Nam, and J. Suhr, "Determination of material constants of vertically aligned carbon nanotube structures in compressions," *Nanotechnology*, vol. 26, no. 24, 2015.

[166] O. Yaglioglu, A. Cao, A. J. Hart, R. Martens, and A. H. Slocum, "Wide range control of microstructure and mechanical properties of carbon nanotube forests: A comparison

between fixed and floating catalyst CVD techniques," *Advanced Functional Materials*, vol. 22, no. 23, pp. 5028–5037, 2012.

[167] P. D. Bradford, X. Wang, H. Zhao, and Y. T. Zhu, "Tuning the compressive mechanical properties of carbon nanotube foam," *Carbon*, vol. 49, no. 8, pp. 2834–2841, 2011.

[168] J. R. Raney, A. Misra, and C. Daraio, "Tailoring the microstructure and mechanical properties of arrays of aligned multiwall carbon nanotubes by utilizing different hydrogen concentrations during synthesis," *Carbon*, vol. 49, no. 11, pp. 3631–3638, 2011.

[169] Y. Won, Y. Gao, M. A. Panzer, R. Xiang, S. Maruyama, T. W. Kenny, W. Cai, and K. E. Goodson, "Zipping, entanglement, and the elastic modulus of aligned single-walled carbon nanotube films," *Proceedings of the National Academy of Sciences*, vol. 110, no. 51, pp. 20426–20430, 2013.

[170] L. Tong, X. Sun, and P. Tan, "Effect of long multi-walled carbon nanotubes on delamination toughness of laminated composites," *Journal of Composite Materials*, vol. 42, no. 1, pp. 5–23, 2008.

[171] Y. Zhang, J. Stringer, A. Hodzic, and P. J. Smith, "Toughening mechanism of carbon fibre-reinforced polymer laminates containing inkjet-printed poly(methyl methacrylate) microphases," *Journal of Composite Materials*, vol. 52, no. 11, pp. 1567–1576, 2018.

[172] F. Narducci, K. Y. Lee, and S. T. Pinho, "Interface micro-texturing for interlaminar toughness tailoring: a film-casting technique," *Composites Science and Technology*, vol. 156, pp. 203–214, 2018.

[173] H. Na, J. H. Park, J. Hwang, and J. Kim, "Site-specific growth and density control of carbon nanotubes by direct deposition of catalytic nanoparticles generated by spark discharge," *Nanoscale Research Letters*, vol. 8, no. 1, pp. 1–7, 2013.

[174] J. W. Elmer, O. Yaglioglu, R. D. Schaeffer, G. Kardos, and O. Derkach, "Direct patterning of vertically aligned carbon nanotube arrays to 20 μm pitch using focused laser beam micromachining," *Carbon*, vol. 50, no. 11, pp. 4114–4122, 2012.

[175] F. Narducci, K. Y. Lee, and S. T. Pinho, "Realising damage-tolerant nacre-inspired CFRP," *Journal of the Mechanics and Physics of Solids*, vol. 116, pp. 391–402, 2018.

[176] X. Ni and B. L. Wardle, "Aerospace-grade advanced composites with buckling-densified aligned carbon nanotubes interlaminar reinforcement," no. January, pp. 1–8, 2020.

[177] S. A. Salpekar, I. S. Raju, and T. K. O'brien, "Strain-energy-release rate analysis of delamination in a tapered laminate subjected to tension load," *Journal of Composite Materials*, vol. 25, no. 2, pp. 118–141, 1991.

[178] J. C. Fish and S. W. Lee, "Delamination of tapered composite structures," *Engineering Fracture Mechanics*, vol. 34, no. 1, pp. 43–54, 1989.

[179] J. M. Curry, E. R. Ohnson, and J. H. Tarnes, "Effect of dropped plies on the strength of graphite-epoxy laminates," *AIAA Journal*, vol. 30, no. 2, pp. 449–456, 1992.

[180] W. Cui, M. R. Wisnom, and M. Jones, "Effect of step spacing on delamination of tapered laminates," *Composites Science and Technology*, vol. 52, no. 1, pp. 39–46, 1994.

[181] B. Kemp and E. Johnson, "Response and failure analysis of a graphite-epoxy laminate containing terminating internal plies," *AIAA*, 1985.

[182] M. R. Wisnom, R. Dixon, and G. Hill, "Delamination in asymmetrically tapered composites loaded in tension," *Composite Structures*, vol. 35, no. 3, pp. 309–322, 1996.

[183] A. D. Botting, A. J. Vizzini, and S. W. Lee, "Effect of ply-drop configuration on delamination strength of tapered composite structures," *AIAA Journal*, vol. 34, no. 8, pp. 1650–1656, 1992.

[184] A. Vizzini, "Influence of realistic ply-drop geometries on interlaminar stresses in tapered laminates," *Composite Materials: Fatigue and Fracture*, vol. 5, pp. 467–485, 1995.

[185] D. M. Thomas and J. P. Webber, "A design study into the delamination behaviour of tapered composites," *Composite Structures*, vol. 27, no. 4, pp. 379–388, 1994.

[186] M. R. Wisnom, M. I. Jones, and W. Cui, "Failure of tapered composites under static and fatigue tension loading," *AIAA Journal*, vol. 33, no. 5, pp. 911–918, 1995.

[187] B. Khan, K. Potter, and M. R. Wisnom, "Suppression of delamination at ply drops in tapered composites by ply chamfering," *Journal of Composite Materials*, vol. 40, no. 2, pp. 157–174, 2006.

[188] A. Weiss, W. Trabelsi, L. Michel, J. J. Barrau, and S. Mahdi, "Influence of ply-drop location on the fatigue behaviour of tapered composites laminates," *Procedia Engineering*, vol. 2, no. 1, pp. 1105–1114, 2010.

[189] G. B. Murri and J. R. Schaff, "Fatigue life methodology for tapered hybrid composite flexbeams," *Composites Science and Technology*, vol. 66, no. 3-4, pp. 499–508, 2006.

[190] S. Helmy and S. V. Hoa, "Tensile fatigue behavior of tapered glass fiber reinforced epoxy composites containing nanoclay," *Composites Science and Technology*, vol. 102, pp. 10–19, 2014.

[191] A. S. Llanos and A. J. Vizzini, "The effect of film adhesive on the delamination strength of tapered composites," *Journal of Composite Materials*, vol. 26, no. 13, pp. 1968–1983, 1992.

[192] C. Gouldstone, D. Degtiarov, and R. D. Williams, "Reinforcing ply drop interfaces using vertically-aligned carbon nanotube forests," in *SAMPE*, (Seattle, US), 2014.

[193] J. Awerbuch and M. S. Madhukar, "Notched strength of composite laminates : predictions and experiments - a review," *Reinforced Plastics and Composites*, vol. 4, no. January, pp. 3–159, 1985.

[194] B. G. Green, M. R. Wisnom, and S. R. Hallett, "An experimental investigation into the tensile strength scaling of notched composites," *Composites Part A: Applied Science and Manufacturing*, vol. 38, no. 3, pp. 867–878, 2007.

[195] D. Morris and C. Harris, "Fracture of thick laminated composites," *Experimental Mechanics*, vol. 26, no. 1, pp. 34–41, 1986.

[196] M. R. Wisnom and S. R. Hallett, "The role of delamination in strength, failure mechanism and hole size effect in open hole tensile tests on quasi-isotropic laminates," *Composites Part A: Applied Science and Manufacturing*, vol. 40, no. 4, pp. 335–342, 2009.

[197] P. Lagace, "Notch sensitivity and stacking sequence of laminated composites," in *Composite Materials: Testing and Design (Seventh Conference)* (J. M. Whitney, ed.), (Philadelphia), pp. 161–176, American Society for Testing and Materials, 1986.

[198] C. Harris and D. Morris, "A fractographic investigation of the influence of stacking sequence on the strength of notched laminated composites," in *Fractography of Modern Engineering Materials: Composites and Metals* (J. E. Masters and J. J. Au, eds.), (Philadelphia), pp. 131–153, American Society for Testing and Materials, 1987.

[199] S. R. Hallett, W.-G. Jiang, and M. R. Wisnom, "Effect of stacking sequence on open-hole tensile strength of composite laminates," *AIAA Journal*, vol. 47, no. 7, pp. 1692–1699, 2009.

[200] R. M. O'Higgins, M. A. McCarthy, and C. T. McCarthy, "Comparison of open hole tension characteristics of high strength glass and carbon fibre-reinforced composite materials," *Composites Science and Technology*, vol. 68, no. 13, pp. 2770–2778, 2008.

[201] A. Khechai, A. Tati, B. Guerira, A. Guettala, and P. M. Mohite, "Strength degradation and stress analysis of composite plates with circular, square and rectangular notches using digital image correlation," *Composite Structures*, vol. 185, no. July 2017, pp. 699–715, 2018.

[202] P. Joshi, A. Kondo, and N. Watanabe, "Numerical analysis to study the effect of through thickness reinforcement with different stitch orientations on open-hole laminates," *Plastics, Rubber and Composites*, vol. 45, no. 10, pp. 445–454, 2016.

[203] Z. Guo, X. Han, and X. Zhu, "Finite element analysis of interlaminar stresses for composite laminates stitched around a circular hole," *Applied Composite Materials*, vol. 19, no. 3-4, pp. 561–571, 2012.

[204] A. Yudhanto, N. Watanabe, Y. Iwahori, and H. Hoshi, "The effects of stitch orientation on the tensile and open hole tension properties of carbon/epoxy plain weave laminates," *Materials and Design*, vol. 35, pp. 563–571, 2012.

[205] Y. Zheng, X. Cheng, and B. Yasir, "Effect of stitching on plain and open-hole strength of CFRP laminates," *Chinese Journal of Aeronautics*, vol. 25, no. 3, pp. 473–484, 2012.

[206] A. P. Mouritz and B. N. Cox, "Mechanistic approach to the properties of stitched laminates," *Composites Part A: Applied Science and Manufacturing*, vol. 31, no. 1, pp. 1–27, 2000.

[207] A. Yudhanto, Y. Iwahori, N. Watanabe, and H. Hoshi, "Open hole fatigue characteristics and damage growth of stitched plain weave carbon/epoxy laminates," *International Journal of Fatigue*, vol. 43, pp. 12–22, 2012.

[208] R. Swain, C. Bakis, and K. Reifsnider, "Effect of interleaves on the damage mechanisms and residual strength of notched composite laminates subjected to axial fatigue loading," *Composite Materials: Fatigue and Fracture*, vol. 4, pp. 552–574, 1993.

[209] R. Guzman de Villoria, L. Ydrefors, P. Hallander, K. Ishiguro, P. Nordin, and B. Wardle, "Aligned carbon nanotube reinforcement of aerospace carbon fiber composites: substructural strength evaluation for aerostructure applications," in *53rd AIAA/ASME/ASCE/AHS/ASC Structures, Structural Dynamics and Materials Conference*, (Honolulu, Hawaii), pp. 3–10, American Institute of Aeronautics and Astronautics, 2012.

[210] Z. Sun, X. Hu, S. Shi, X. Guo, Y. Zhang, and H. Chen, "Edge delamination and residual properties of drilled carbon fiber composites with and without short-aramid-fiber interleaf," *Applied Composite Materials*, vol. 23, no. 5, pp. 973–985, 2016.

[211] C. Gouldstone, D. Degtiarov, and R. D. Williams, "Reinforcing Ply Drop Interfaces Using Vertically-Aligned Carbon Nanotube Forests," No. January, (SAMPE Seattle), 2014.

[212] N. Kobayashi, H. Izumi, and Y. Morimoto, "Review of toxicity studies of carbon nanotubes," *Journal of Occupational Health*, vol. 59, no. 5, pp. 394–407, 2017.

[213] B. L. Wardle, A. J. Hart, E. J. Garcia, and A. H. Slocum, "Nanostructure-reinforced composite articles and methods," 2006.

[214] S. A. Steiner and B. L. Wardle, "Systems and methods related to the formation of carbon-based nanostructures," 2012.

[215] ASTM D5528-01, "Standard test method for mode I interlaminar fracture toughness of unidirectional fiber-reinforced polymer matrix composites," *American Standard of Testing Methods*, vol. 03, no. Reapproved 2007, pp. 1–12, 2014.

[216] ASTM D7905, "Standard test method for determination of the mode II interlaminar fracture toughness of unidirectional fiber-reinforced polymer matrix composites," *ASTM*, pp. 1–18, 2014.

[217] BS ISO 15114, "Fibre-reinforced plastic composites - Determination of the mode II fracture resistance for unidirectionally reinforced materials using the calibrated end-loaded split (C-ELS) test and an effective crack length approach," *International Organization for Standardization*, vol. 1, no. 1, pp. 1–18, 2012.

[218] J. G. Williams, "On the calculation of energy release rates for cracked laminates," *International Journal of Fracture*, vol. 36, no. 2, pp. 101–119, 1988.

[219] A. Cao, P. L. Dickrell, W. G. Sawyer, M. N. Ghasemi-Nejhad, and P. M. Ajayan, "Super-compressible foamlike carbon nanotube films," *Science*, vol. 310, no. 5752, pp. 1307–1310, 2005.

[220] D. S. Cairns, "Static and dynamic strain energy release rates in toughened thermosetting composite laminates," tech. rep., 1992.

[221] M. Czabaj and J. Ratcliffe, "Comparison of intralaminar and interlaminar mode-I fracture toughness of unidirectional IM7/8552 graphite/epoxy composite," in *American Society for Composites*, (Arlington, TX; US.), pp. 1–18, 2012.

[222] P. Hansen and R. Martin, "DCB, 4ENF and MMB characterisation of S2/8552 and IM7/8552," tech. rep., 1999.

[223] M. Yasaee, G. Mohamed, A. Pellegrino, N. Petrinic, and S. R. Hallett, "Strain rate dependence of mode II delamination resistance in through thickness reinforced laminated composites," *International Journal of Impact Engineering*, vol. 107, pp. 1–11, 2017.

[224] T. K. O'Brien, W. M. Johnston, and G. J. Toland, "Mode II interlaminar fracture toughness and fatigue characterization of a graphite epoxy composite material," *National Aeronautics and Space Administration*, pp. 1–32, 2010.

[225] B. M'membe, S. Gannon, M. Yasaee, S. R. Hallett, and I. K. Partridge, "Mode II delamination resistance of composites reinforced with inclined Z-pins," *Materials and Design*, vol. 94, pp. 565–572, 2016.

[226] M. Todo and P. Y. Jar, "Study of mode-I interlaminar crack growth in DCB specimens of fibre-reinforced composites," *Composites Science and Technology*, vol. 58, no. 1, pp. 105–118, 1998.

[227] C. Canturri, E. S. Greenhalgh, S. T. Pinho, and J. Ankersen, "Delamination growth directionality and the subsequent migration processes - The key to damage tolerant design," *Composites Part A: Applied Science and Manufacturing*, vol. 54, pp. 79–87, 2013.

[228] C. Hwu, C. Kao, and L. E. Chang, "Delamination fracture criteria for composites laminates," *Composite Materials*, vol. 29, pp. 1962–1987, 1995.

[229] O. Allix, D. Leveque, and L. Perret, "Identification and forecast of delamination in composite laminates by an interlaminar interface model," *Composites Science and Technology*, vol. 3538, no. 58, pp. 671–678, 1998.

[230] F. Lachaud, R. Piquet, and L. Michel, "Delamination in mode I and II of carbon fibre composite materials : fibre orientation influence," in *proceedings of ICCM - 12*, 1999.

[231] M. A. Mohsin, L. Iannucci, and E. S. Greenhalgh, "Fibre-volume-fraction measurement of carbon fibre reinforced thermoplastic composites using thermogravimetric analysis," *Heliyon*, vol. 5, no. 1, 2019.

[232] P. W. Harper and S. R. Hallett, "Cohesive zone length in numerical simulations of composite delamination," *Engineering Fracture Mechanics*, vol. 75, no. 16, pp. 4774–4792, 2008.

[233] K. Song, C. Dávila, and C. Rose, "Guidelines and parameter selection for the simulation of progressive delamination," *2008 ABAQUS User's Conference*, pp. 1–15, 2008.

[234] MathWorks, "Voronoi diagram." `https://www.mathworks.com/help/matlab/ref/voronoi.html`.
Accessed: 2019-10-01.

[235] Provo Craft & Novelty Inc., "Cricut Explore Air 2," 2014.

[236] E. S. Greenhalgh, *Failure analysis and fractography of polymer composites*.
Woodhead Publishing Limited, 2009.

[237] P. Dhurvey and N. D. Mittal, "Review on various studies of composite laminates with ply drop-off," *ARPN Journal of Engineering and Applied Sciences*, vol. 8, no. 8, pp. 595–605, 2013.

[238] Hexcel, "Redux ® 319 High Performance Modified epoxy film adhesive Product Data Sheet," tech. rep., 2017.

[239] Huntsman, "Araldite 2014 A/B epoxy product datasheet," tech. rep., 2006.

[240] S. Bagavathiappan, B. B. Lahiri, T. Saravanan, J. Philip, and T. Jayakumar, "Infrared thermography for condition monitoring - A review," *Infrared Physics and Technology*, vol. 60, pp. 35–55, 2013.

[241] R. M. Christensen and S. J. Deteresa, "Delamination failure investigation for out-of-plane loading in laminates," *Journal of Composite Materials*, vol. 38, no. 24, pp. 2231–2238, 2004.

[242] S. J. DeTeresa, D. C. Freeman, and S. E. Groves, "The Effects of Through-thickness Compression on the Interlaminar Shear Response of Laminated Fiber Composites," *Journal of Composite Materials*, vol. 38, no. 8, pp. 681–697, 2004.

[243] G. Catalanotti, C. Furtado, T. Scalici, G. Pitarresi, F. P. van der Meer, and P. P. Camanho, "The effect of through-thickness compressive stress on mode II interlaminar fracture toughness," *Composite Structures*, vol. 182, no. August, pp. 153–163, 2017.

[244] K. Y. Rhee, "Hydrostatic pressure effect on the fracture toughness of unidirectional (0-deg) graphite/epoxy laminated composites," *Composite Materials*, vol. 34, no. 7, pp. 599–613, 1999.

[245] K. W. Gan, S. R. Hallett, and M. R. Wisnom, "Measurement and modelling of interlaminar shear strength enhancement under moderate through-thickness compression," *Composites Part A: Applied Science and Manufacturing*, vol. 49, pp. 18–25, 2013.

[246] X. Xu, M. R. Wisnom, X. Sun, T. Rev, and S. R. Hallett, "Experimental determination of Through-Thickness Compression (TTC) enhancement factor for Mode II fracture energy," *Composites Science and Technology*, vol. 165, no. March, pp. 66–73, 2018.

[247] Z. Zou and H. Lee, "A cohesive zone model taking account of the effect of through-thickness compression," *Composites Part A: Applied Science and Manufacturing*, vol. 98, pp. 90–98, 2017.

[248] B. Zhang, X. C. Sun, M. J. Eaton, R. Marks, A. Clarke, C. A. Featherston, L. F. Kawashita, and S. R. Hallett, "An integrated numerical model for investigating guided waves in impact-damaged composite laminates," *Composite Structures*, vol. 176, pp. 945–960, 2017.

[249] M. May and S. R. Hallett, "An assessment of through-thickness shear tests for initiation of fatigue failure," *Composites Part A: Applied Science and Manufacturing*, vol. 41, no. 11, pp. 1570–1578, 2010.

[250] O. Nixon-Pearson, S. Hallett, P. Withers, and J. Rouse, "Damage development in open-hole composite specimens in fatigue. Part 1: Experimental investigation," *Composite Structures*, vol. 106, pp. 882–889, 2013.

[251] ASTM D5766, "Standard test method for open-hole tensile strength of polymer matrix composite laminates," *ASTM International*, vol. 11, no. Reapproved 2018, pp. 1–7, 2018.

[252] O. J. Nixon-Pearson, S. R. Hallett, P. W. Harper, and L. F. Kawashita, "Damage development in open-hole composite specimens in fatigue. Part 2: Numerical modelling," *Composite Structures*, vol. 106, pp. 890–898, 2013.

[253] M. Cheung and S. Hallett, "Investigation of the effect of specimen width on open hole tensile strength," in *CompTest*, (Dayton, Ohio), 2008.

[254] O. J. Nixon-Pearson and S. R. Hallett, "An investigation into the damage development and residual strengths of open-hole specimens in fatigue," *Composites Part A: Applied Science and Manufacturing*, vol. 69, pp. 266–278, 2015.

[255] R. Gutkin, M. L. Laffan, S. T. Pinho, P. Robinson, and P. T. Curtis, "Modelling the R-curve effect and its specimen-dependence," *International Journal of Solids and Structures*, vol. 48, no. 11-12, pp. 1767–1777, 2011.

[256] J. Andersons and M. König, "Dependence of fracture toughness of composite laminates on interface ply orientations and delamination growth direction," *Composites Science and Technology*, vol. 64, no. 13-14, pp. 2139–2152, 2004.

[257] H. Conway, B. Bancroft, D. Chebot, M. Devoe, and C. Gouldstone, "Impact resistance and residual strength of carbon fiber epoxy laminates with vertically-aligned carbon nanotube interfacial reinforcement," *International SAMPE Technical Conference*, no. March, pp. 1642–1651, 2017.